DOCTOR OF PHILOSOPHY

Development of lab-on-a-chip technology

Drysdale, James Alexander

Award date:
2003

Awarding institution:
University of Wales, Bangor

Development of Lab-on-a-Chip Technology

James Alexander Drysdale

Thesis submitted to the University of Wales
in candidature for the degree of Doctor of Philosophy

December 2003

School of Informatics

Summary

This thesis describes a series of processes and devices, which have been developed to improve the functionality and ease of manufacture of micro-fluidic systems, such as lab-on-a-chip devices.

A novel fabrication technique has been developed for the production of large multilayer travelling wave electrode arrays without the use of via-holes thus significantly improving the device reliability. Also described are new processes, which have been developed for the accurate fabrication of micro-fluidic channels from low cost materials such as glass and polymers.

Both capacitive and resistive based sensors were designed and incorporated into lab-on-a-chip style devices for the measurement of fluid flow and the detection of individual particles or particle suspensions within the channel. With an aim to using these sensors in disposable devices, the complexity of the sensing element and interface electronics were minimised where possible. Through innovative electrode design, temperature compensation was incorporated into the sensor itself eliminating the need for additional components.

Continuing the desire for disposability and integration, simple device imaging systems were developed. To aid incorporation of these systems into lab-on-a-chip devices the optical components, if any, were fabricated as part of the device structure. This integration produced good quality images allowing useful measurements to be taken.

A key area of investigation in micro-fluidics is sample preparation. Computer simulation tools were used to aid in the design of a micro-fluidic system capable of automating the labour intensive process of sample conductivity reduction. This is achieved through improvements to the basic H-filter design, so facilitating the significant drop in the conductivity of whole blood necessary for dielectrophoretic measurements. The final design was tested and there was good agreement between the experimental and computational results.

Acknowledgements

I would like to thank both Professor Ron Pethig, for giving me the opportunity to study for my PhD and Dr Julian Burt for taking over as my supervisor part way through the work. I would also like to thank Professor Alan Shore for his invaluable guidance in preparing this thesis.

I would especially like to thank Melanie for her unending support and patience throughout this PhD. I would also like to thank my mum and dad for all their support over the years, without which I would not have been able to even commence this work.

For their friendship and useful discussions I would like to thank, Chris, Andy, Colin, John Tame, Sally, Xiou-Feng, Richard, Viviana and Jan. I would also like to thank all my friends in Bangor who have made my time here very enjoyable.

Thank you to the highly skilled technical staff of the engineering workshop, Miles, Ivor, Iwan, Tex and Rodney, for the high quality components they produced for use in this work and their technical advice.

Finally, I would like to acknowledge the EPSRC, for their financial support that enabled me to carry out this work.

Contents

Chapter 1

Introduction

1.1 Lab-on-a-chip

The aim of lab-on-a-chip technology is to miniaturise laboratory processes and integrate them on self contained devices, usually less than $5cm^2$ in size [1]. The use of techniques similar to those developed in the microelectronics industry allow the fabrication of micron scale fluidic channels, valves, pumps and sensors that can be used to process very small sample volumes. The main drive for the development of lab-on-a-chip technologies has come from the healthcare industry, with commercial products being developed by companies such as Calliper, Nanogen and i-Stat [2-4]. The dimensions of lab-on-a-chip devices allow rapid diagnostic analysis of small sample volumes. Additional cost benefits are achieved due to a reduction in the quantity of reagents used in processing. Overheads are also reduced due to the reduction in laboratory space required. For example the i-Stat blood analysis system [4] consists of a disposable microfabricated sensor smaller than a credit card, which is interrogated using a hand held reader. Such a disposable approach, which prevents cross contamination between samples, is common to most micro-fabricated diagnostic systems. Commercial lab-on-a-chip devices tend to contain few functional components as increased complexity increases the cost, for example the labChip™ developed by Calliper consists solely of a series of micro-channels fabricated in a glass substrate [2,5]. However, other functional components have been developed to incorporate pumping, sensing and particle separation onto the device as described in more detail in Chapter 2.

Chemistry is another area of interest for the application of lab-on-a-chip devices. It is possible to increase the yield of certain reactions above that achieved on a macro scale when they are performed on a micro scale [6]. The efficient conduction of heat from a micro-channel, due to the high surface area to volume ratio, allows highly exothermic reactions to be carried out, some of which would either be impossible or hazardous to carry out on a macro scale.

1.2 Thesis Structure

This thesis describes work that is relevant to the development of lab-on-a-chip technologies, particular attention having been paid to reducing the complexity of such devices though the use of simple device geometries and fabrication processes. Areas investigated include; methods of device fabrication, electrical sensing within micro-fluidic channels, imaging based detection systems and the design of a sample pre-conditioning stage.

Chapter 2 of this thesis provides background information on lab-on-a-chip technologies and gives an overview of some commercially available devices. The theoretical discussions of physical processes used in this thesis are included in the relevant chapters. This chapter first provides a brief overview of the concept of lab-on-a-chip technologies before discussing specific components in more detail. Firstly microfabrication approaches that can be used to produce microfluidic structures in silicon, glass and polymers are described. A range of pumping mechanisms that can be applied to sample movement within microfabricated structures are described. Chapter 5 of this thesis describes the development of a flow sensor, a range of existing flow sensors are described in this chapter in addition to a range of flow cytometers which can be used to characterise or manipulate particles in solution.

Chapter 3 describes, in detail, the standard fabrication processes that were used throughout this thesis. In addition to the protocol used, background material relevant to each process is included. The micro-electrodes used in this work were fabricated using UV photolithography to pattern gold on a glass substrate. The production of photographic masks by the photo reduction of large-scale plots is given, as well as the processes used to deposit thin films of gold onto glass through thermal evaporation. The processes used to pattern these gold films using 'print and etch' and 'lift-off' photolithography are discussed in detail. To produce multilayer electrode arrays, polyimide insulating layers were used for layer separation. The stages involved in depositing and patterning this layer are described along with the processes used to fabricate thicker insulating layers using dry film laminate resists.

The remainder of the thesis, Chapters 4 to 8 describe the experimental work undertaken which is relevant to the microfabrication of lab-on-a-chip devices.

One of the main causes of device failure in multi-layer travelling wave electrode arrays, used in the manipulation of particles through travelling wave dielectrophoresis [7] is the occurrence of electrical open circuits at via-holes [8]. The via-holes provide electrical contact between electrode layers. Chapter 4 first describes a new and simpler method for the fabrication of long travelling wave electrode arrays, which eliminates the need for via-holes. Computer simulation tools were used to compare the electric fields generated, using these electrodes, to those generated by electrodes fabricated using via-holes. The remainder of the chapter describes a series of fabrication approaches that have been developed to fabricate channel structures using polymers and glass. The methods used include photolithography and excimer laser micromachining.

There exists a wide range of sensors that can be incorporated into lab-on-a-chip devices. However, many are fabricated in silicon or are relatively complex to produce making them unsuitable for incorporation into low cost, disposable Microsystems. In this work, two main types of sensor have been produced to operate in conjunction with the channel structures developed in Chapter 4, those to measure fluid flow and those to detect particles. Chapter 5 describes the development of a microfabricated hot wire flow sensor that could be incorporated into disposable devices. Incorporating compensation into the sensing element, through the use of a Wheatstone Bridge arrangement [9], reduced the temperature sensitivity of a flow sensor. In all cases, the sensors were fabricated from thin film gold electrodes on a glass substrate. When electrodes are already incorporated into the device, for example, when performing dielectrophoretic measurements [10], these sensors can be incorporated into the same mask and produced at little extra cost. Care was also taken to minimise the complexity of the interface circuitry associated with the sensors. However, to maximise the device sensitivity it was necessary to use more complex lock-in techniques. To generate a steady flow independent of the backpressure within a micro channel, a flow sensor and pump were incorporated into a feedback loop.

In addition to measuring fluid flow within a channel it is desirable to be able to detect the presence of suspended particles. Chapter 6 describes a group of sensors that have

been developed to monitor cell suspensions within a channel or detect individual particles. These sensors rely upon measuring the dielectric properties of the material within the channel. For this reason the chapter begins with a section on dielectric theory. Particular attention is paid to the mechanisms that cause the permittivity of a dielectric to vary with electric field frequency, the formation of an electrical double layer in an ionic solution adjacent to an electrode and the dielectric properties of particle suspensions

In some applications it is necessary to visually observe particles within a lab-on-a-chip device, instead of using remote detection processes similar to those described in Chapters 5 and 6. This is typically achieved using expensive bench top microscope systems. Chapter 7 describes the preliminary development of low cost microscope and imaging systems. Devices were fabricated which incorporated the lens elements into the micro-fluidic channel structure. To assess the usefulness of these low quality images a dielectrophoresis spectra for live yeast was produced through contact imaging combined with digital image processing.

A key area of investigation in lab-on-a-chip research is sample preparation. Chapter 8 describes the development, using finite element modelling tools, of a microfluidic pre-conditioning stage for the reduction of the ionic concentration, and hence, electrical conductivity of a sample. The basic H-filter [11] is adapted to provide the large reduction in conductivity required for blood to be used in devices incorporating dielectrophoretic components. Although the emphasis of this chapter is on computer aided design, a component of the final design was fabricated and tested to check the validity of the computer model. A possible area of future work is described at the end of this chapter, whereby positive and negative dielectrophoresis is incorporated into a H-filter to selectively move particles within the device. The final chapter summarises the work undertaken and the results obtained.

1.3 References

[1] 'Future trends in diagnosis using laboratory-on-a-chip technologies' M. S. Tallary, J. P. H. Burt and R. Pethig, *J. Parasitology*. **117** (1998) S191-S203

[2] 'Caliper company web site (1/9/2002)' http://www.calipertech.com

[3] 'Nanogen company web site (1/9/2002)' http://www.nanogen.com

[4] 'i-Stat company web site (1/9/2002)' http://www.i-stat.com

[5] 'Protein sizing on a microchip' L. Bousse, S. Mouradian, A. Minalla, H. Yee, K Williams and R. Dubrow, *J. Analytical Chemistry* **73** (2001) 1207-1212

[6] 'Microfluidic technology and applications' Michael Koch, Alan Evans and Arthur Brunnschweiler, *Research studies press ltd. 2000, Hertfordshire, UK*

[7] 'Electrokinetic behaviour of colloidal particles in travelling electric fields: studies using yeast cells' Y. Hung, X-B. Wnag, J. A. Tame and R. Pethig. *J. Applied Physics D* **26** (1993) 1529-1535

[8] 'Development of biofactory-on-a-chip technology using excimer laser micromachining' R. Pethig J. P. H. Burt, A Parton, N. Rizvi, M. S. Talary and T. A. Tame, *J. Micromechanics and Micro engineering*, **8** (1998) 57-63

[9] 'Handbook of Transducers for Electronic Measuring Systems' Harry N. Norton, *Prentice Hall. 1969 London, UK.*

[10] 'Dielectrophoresis: Using inhomogeneous AC electrical fields to separate and manipulate cells' R. Pethig, *Critical Reviews in Biotechnology* **16(4)** (1996) 331-348

[11] 'Diffusion-based extraction in a microfabricated device' J. P. Broody and P. Yager. *Sensors and Actuators A* **58** (1997) 13-18

Chapter 2

Lab-on-a-chip Technologies

2.1 Introduction

The previous chapter provided an outline of the contents of this thesis. This chapter provides background information on lab-on-a-chip technologies. Section 2.2 gives an overview of some commercially available Lab-on-a-chip devices. Typically Lab-on-a-chip devices contain one or more functional parts, these include the channel structure itself, pumps to move materials around the device and some sort of sensing system. Devices of this type are also often referred to as Micro-Total Analysis Systems (μ-TAS) [1]. Some of the existing methods used to implement lab-on-a-chip functional parts are described in Sections 2.3 to 2.5. Particular attention has been given to the types of component developed in this work and described in the remainder of this thesis. The technologies and fabrication approaches used to produce lab-on-a-chip devices are also applied to other Micro electromechanical systems (MEMS) such as accelerometers [2]. As this type of component is not immediately applicable to most lab-on-a-chip devices they have been omitted from this section.

2.2 Overview of commercially available lab-on-a-chip devices

Complex analytical processes are carried out in diagnostic laboratories on a daily basis. For an organisation to remain competitive there is an obvious advantage to reducing costs, increasing throughput and decreasing the time taken to perform an analysis. This can be achieved by robotic automation of repetitive processes and the processing of an increasing number of samples in parallel using standard 96 well plates, 384 well micro plates or similar parallel approaches [3]. An alternative technology that addresses these problems, is the use of lab-on-a-chip devices. These devices, which often use technology taken from the microelectronics industry, carry out analytical processes on a microscopic scale.

A device, which is typical of many lab-on-a-chip devices currently on the market, is the LabChip™ produced by Caliper (US) [4,5] that performs DNA, RNA or protein analysis. The main part of the device is fabricated from soda lime glass, into which channels 13μm deep and 36μm wide are fabricated by chemical wet etching. A glass lid with 2mm pre-drilled holes is then thermally bonded to the substrate to form sealed

channels. As with other lab-on-a-chip devices, such as the NanoChip™ produced by Nanogen (US) [6], the small microfabricated section of the device is incorporated into a plastic holder for ease of handling. The entire device is then inserted into a dedicated machine used to control the device and perform the analysis. Figure 2.1 is a photo of the packaged caliper device and a diagram of the channels formed in the glass.

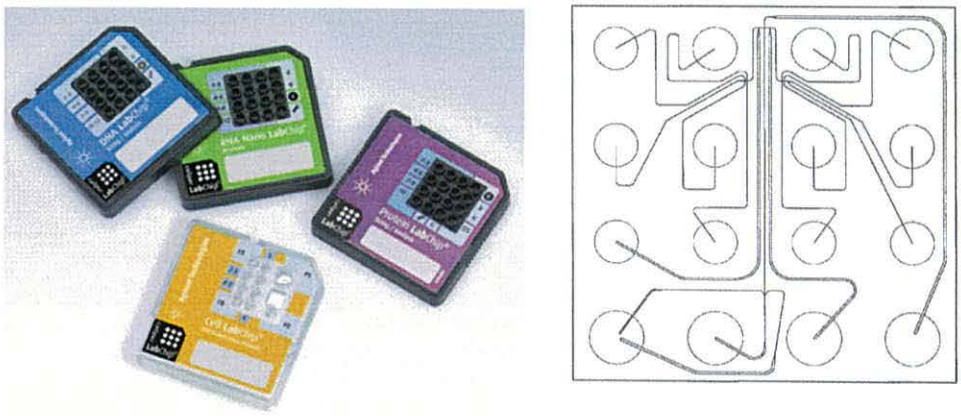

Figure 2.1 *Photograph of the LabChip produced by Caliper and a diagram of the microfabricated channel structures contained on the chip [4,5].*

The obvious advantages of lab-on-a-chip devices are the reduction in cost, due to reduced reagent costs, reduced power consumption and a reduction in the amount of laboratory space required. When performing chemical reactions on a micro-device, the reagents are in close proximity, due to the small dimensions of the channels allowing controlled diffusive mixing [7]. Another advantage of the small channel geometries is that heat transfer to and from the sample is more efficient. This can speed up processes that require the temperature to be cycled, such as the polymerise chain reaction (PCR) used to amplify a sample of DNA [8-10]. Alternatively, if the reaction is highly exothermic the heat generated can be rapidly dissipated. Such a reaction on a macro scale may be hazardous due to the high temperatures generated. The small reaction volumes and the short distances covered by a sample on a lab-on-a-chip device result in short cycle times. Samples can be processed and results produced in seconds [11].

Due to the small features of lab-on-a-chip devices, it is possible to produce a single structure that carries out a large number of operations in parallel, whilst still remaining

compact. For example, the NanoChip™ [6,12,13] has 99 test sites within an area of 0.7cm^2, which compares to the macro equivalent of a 96 well plate which typically occupies an area of 100cm^2 . Using micro-structures, it is possible to include tens of thousands of test sites within a single device [14].

The small size of lab-on-a-chip devices makes them suitable for applications not possible with macro scale systems. Microsystems can be incorporated into portable devices to allow analysis to be carried out on site in remote locations. Alternatively, systems can be combined into industrial processes to perform in-line analysis.

Lab-on-a-chip devices may contain a number of different functional parts [14,13]. These include a channel structure to hold the sample, a mechanism for moving the sample around the device and a means of detecting the result of a reaction or process. Sections 2.2.2 to 2.2.4 describe some methods that have been used to realise these functions. A raw sample will often contain contaminants. If these affect the operation of the device some sort of sample preparation may also be required. This is discussed in more detail in Chapter 8.

2.3 Fabrication of micro-channels

An important consideration when choosing the material used to fabricate a microsystem is its compatibility with the sample to be analysed and any reagents. Typically, glass and silicon, both of which are reasonably chemically inert are used to produce channels. However, polymers are increasingly being selected on cost grounds and care must be taken to ensure they are not damaged by the sample or that they leach contaminants into the device. Some common approaches used to fabricate channel structures in silicon, glass and polymers are described in this section. Once a channel has been fabricated, it is usually necessary to encapsulate it with a lid. This process should form a good seal, whilst not affecting the channel geometry.

2.3.1 Fabrication in silicon

The large majority of micro-fluidic systems and lab-on-a-chip devices fabricated in silicon, use techniques similar to those originally developed for the microelectronics industry. Typically, photolithography is used to pattern a radiation sensitive material or 'resist' deposited on the surface of the silicon or on top of a thin silicon dioxide film. Once developed, the resist acts as a masking layer to allow selective etching of the underlying substrate. The exposed areas of the silicon can be removed through either wet or dry etching. Wet etching describes the removal of the silicon using aqueous chemical solutions. Isotropic etchants remove material at the same rate in all directions and are typically acidic such as HF or HNO_3 and lead to rounded features in single crystal silicon, as shown in Figure 2.2A. Anisotropic etchants etch the substrate at different rates depending on the orientation of the crystal structure, as shown in Figure 2.2B. Typical anisotropic etchants are aqueous alkaline solutions, such as KOH and NaOH, although a variety of etchants exist [16]. Generally, isotropic etching produces channels with smoother walls, whilst it is possible to produce more complex geometries using anisotropic etching.

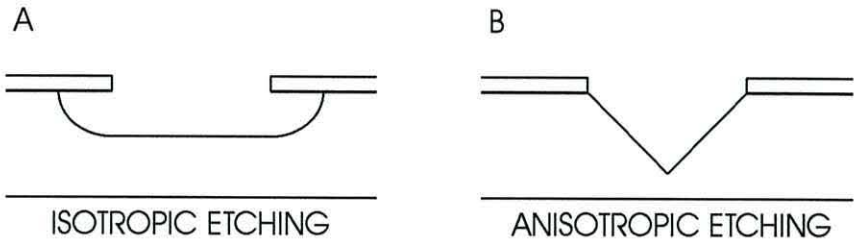

Figure 2.2 *Effect of isotropic and anisotropic etching of a substrate through a gap in a masking layer.*

An alternative approach used to process silicon is dry etching, which has particular advantages in an industrial environment, since it reduces the quantity of liquid waste. A typical dry etching technique, applicable to a wide range of substrates, is reactive ion etching (RIE) [16,17]. In this process, plasma is generated to produce highly reactive ions, which are accelerated towards a substrate using an applied electric field where they erode the substrate surface. A perpendicular approach of the ions to the substrate allows deep channels with vertical sidewalls to be produced. A limitation of reactive ion

etching is that the masking layer is removed at the same time as the substrate, this limits the maximum achievable channel depth. The purpose of the plasma in this process is to generate highly reactive ions that will react with the substrate. However, it is also possible to use a naturally reactive gas to directly etch the substrate, forgoing the need to generate plasma in a process referred to as gas phase etching [18].

Silicon is opaque at visible wavelengths, therefore it is necessary to attach a transparent lid to the channels to observe any processes on a lab-on-a-chip device. Pyrex can be directly bonded to a silicon wafer or most metals without the use of adhesives by using anodic bonding [15,19]. To form a good bond, both the silicon and Pyrex wafers must be clean and flat, since unevenness could cause fluidic channel structures to leak. Once in contact with each other a negative potential is applied to the Pyrex wafer which results in a high electrostatic field at the interface, which pulls the wafers together. The extremely high fields transport oxygen atoms out of the glass to bond with the silicon. When using this approach it is essential that the two surfaces are as flat as possible. For example, the presence of a metal track just 200nm high can result in a void extending 30μm away from the metal [15].

2.3.2 Fabrication in glass

Although there are a wide number of processes developed for use with silicon that can produce detailed structures, silicon is expensive compared to other materials such as glass. Typically micro-channels in glass are fabricated through wet etching. However, the chemical resistance of glass limits the range of etchants that can be used, typical etchants are HF, HF/HNO_3 or HF/NH_4F [20-22]. Due to the chemically aggressive nature of the etchants a polymer photoresist often does not form a sufficiently strong masking layer. Instead a metal layer, such as gold on chrome is first deposited onto the glass and patterned to act as a masking layer for the etching of the glass [21,22]. Once the glass has been etched the metal layer is chemically removed. The optimum material for the etch mask depends on the type of etchant. For example amorphous silicon forms a better mask than gold when HF is used [20].

To produce high aspect ratio (ratio of the height to the width of the channel) channels in glass, reactive ion etching can be used. A with silicon when using this approach it is necessary to produce a high quality masking layer. The steps involved in the reactive ion etching of Pyrex glass using a SF_6 plasma are illustrated in Figure 2.3 [23].

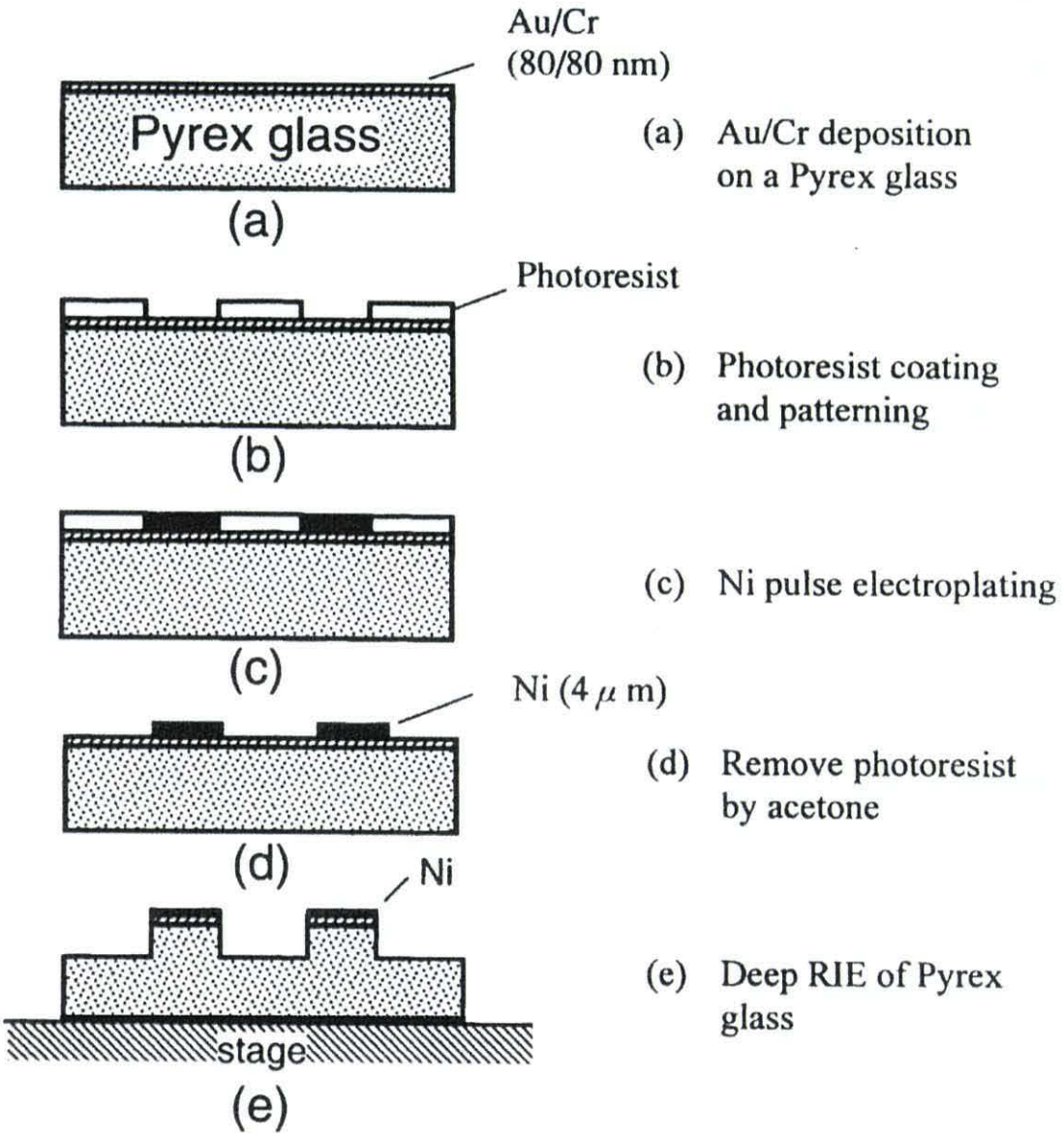

Figure 2.3 *Stages involved in the reactive ion etching of Pyrex glass using SF_6 plasma [23].*

As illustrated in Figure 2.3a a thin film of gold on chrome is deposited onto a glass substrate followed by a layer of photoresist, which is then patterned. To produce a thicker masking layer, nickel is electroplated onto the surface of the gold exposed by the

resist as shown in Figure 2.3c. Once the resist is removed, reactive ion etching is used to remove the Pyrex glass. Once the etching of the glass is complete, the metal masking layer can be removed through wet chemical etching.

As with silicon, it is possible to directly bond glass to glass without the use of an adhesive layer, allowing a transparent lid to be attached to the channel structures. This process is typically carried out using thermal bonding, as opposed to anodic bonding used with silicon. A commonly used approach is to place the two clean substrates in contact with each other and heat them to just above their annealing temperature, (typically 550-650°C) whilst applying light pressure of the order $15gcm^{-2}$[20]. However, a bond can be achieved at the much lower temperature of 90°C, if a solution of sodium silicate is spin coated onto the cover plate before it is applied to the substrate [24].

2.3.3 Fabrication in polymers

Although polymers are generally less chemically inert than silicon or glass, their low cost and wide range of properties makes them useful for the fabrication of micro-channels. Structures, such as channels, can be directly machined in polymers using lasers. For instance, the high energy UV pulses obtained from an excimer laser can be used to selectively ablate the surface of the polymer [14,25]. When an excimer laser pulse is incident on a polymer substrate it is absorbed by the material and rapidly breaks the chemical bonds, providing the energy is sufficient. This causes a mini explosion, which ejects the material from the substrate. Through the use of masks and the movement of the beam relative to the substrate it is possible to directly machine complex structures. The quality of the finished channel is dependent on the properties of the material and the intensity and repetition rate of the laser pulses. For a material to be effectively machined the energy of the UV pulse must be over the ablation threshold of the material. This property can be used to selectively machine layers of material. For example, the ablation threshold for glass is much higher than that of polyimide. Therefore, a polyimide layer on a glass substrate can be completely machined away to form a channel, without causing damage to the underlying glass substrate. Laser ablation is mainly used to machine polymers. Glass and other materials, such as metals, can be machined but a much higher energy is required.

Multiple copies of polymer structures can be produced by the well-known LIGA or related processes. LIGA from the German "lithographie, galvanoformumg, abformung", translates to "lithography, electroforming and moulding". As shown in Figure 2.4 [14], the pattern is first formed in a radiation patternable resist, which is developed to leave the structure shown in Figure 2.4B. The areas exposed between the resist are then electroplated, typically with nickel, before the resist is removed. The remaining metal structure can then be used as a precision master for moulding, embossing or extrusion [26]. The LIGA process is capable of producing structures with aspect ratios as high as 100:1.

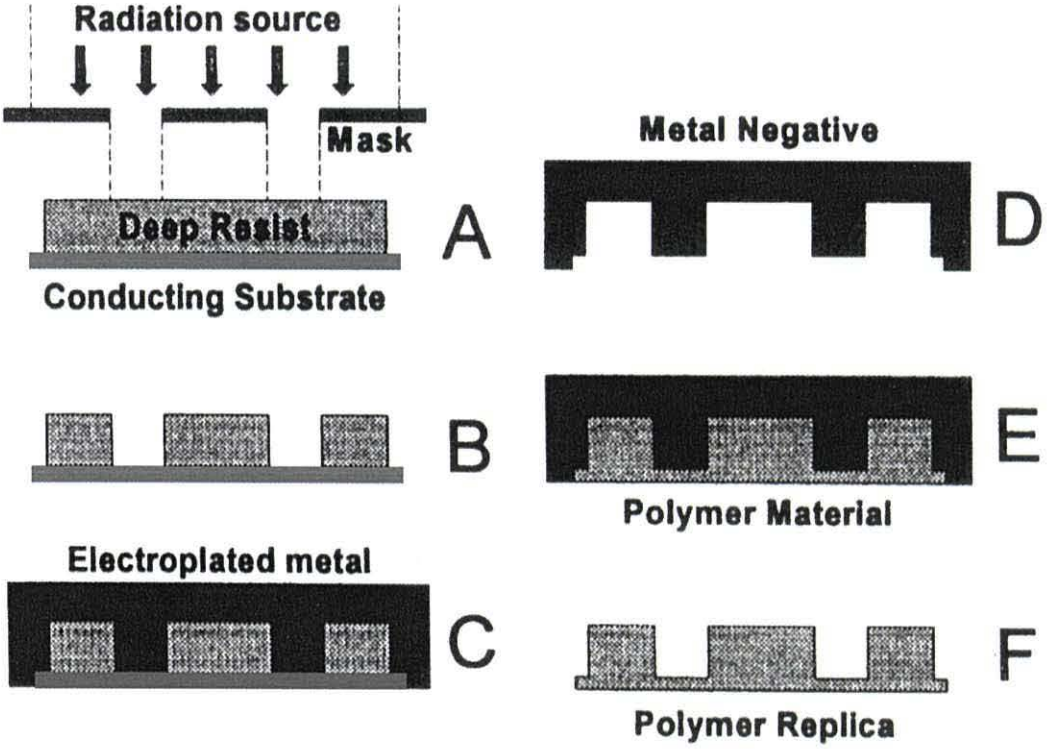

Figure 2.4 *Stages involved in the LIGA process [14].*

Originally the exposure of the deep resist was carried out using the highly collimated X-ray radiation produced by a synchrotron source. However, this is expensive and alternative processes have been developed which use UV light to expose the resist [27].

A moulding process can also be used to form channels from the elastomer PDMS (polydimethylsiloxane) [28]. To form a channel structure, uncured liquid PDMS is poured over a positive relief of the required shape that is typically fabricated using photolithography. Once the PDMS has cured, it can be released from the moulding master to reveal the channels. The curing time can be reduced from around 24 hours to 1 hour by heating the PDMS to 65°C. There is a natural adhesion between PDMS and a number of materials, such as glass and silicon, allowing temporary channel structures to be produced by simply placing the PDMS onto a flat substrate. The temporary nature of this bond allows the PDMS to be removed and reattached to the substrate multiple times. To produce a permanent bond between the PDMS and a substrate the surfaces can be exposed to oxygen plasma. When these surfaces are brought together a permanent bond is formed. Micro-lens have been fabricated in the same PDMS structure as channels, however significant deformation of the lens' has been measured due to changes in the pressure within the channel [29].

When fabricating channel structures from polymers it can be difficult to attach the lid without the use of adhesives. When using narrow channels it is possible to laminate a polymer layer directly over the surface of the channel structure. Alternatively, the patterned polymer can be placed in contact with a substrate and heated, under slight pressure, to its softening temperature for a period of time to form a strong bond. Detailed descriptions of the methods developed as part of this research for the fabrication of micro fluidic channels in polymers are provided in Chapter 4.

2.4 Sample movement within lab-on-a-chip devices

When a microsystem is used to process a fluid or particle suspension it is necessary to accurately move the sample around the device. This can be done using external pumps or features integrated into the device. The use of an external mechanical pump has the advantage that the complexity and therefore cost of the microsystem is reduced. However, care must be taken to prevent cross contamination if different microsystems are connected to the same pump. Section 2.4.1 describes a commonly used type of pump, the mechanical membrane pump and Section 2.4.2 describes some alternative pumping mechanisms that can be incorporated into lab-on-a-chip devices.

2.4.1 Mechanical membrane micro pumps

Mechanical micro-pumps normally consist of a thin membrane, which forms part of a chamber with inlet and outlet valves. Deflection of the membrane causes fluid to be pumped through the device. A generic diagram of a mechanical micro-pump is shown in Figure 2.5. Two types of inlet and outlet are shown in the diagram. For the diffuser and nozzle approach shown in the main diagram the resistance to flow depends on direction resulting in a net flow in one direction. The flap valve shown to the right physically shuts the port when the flow is reversed.

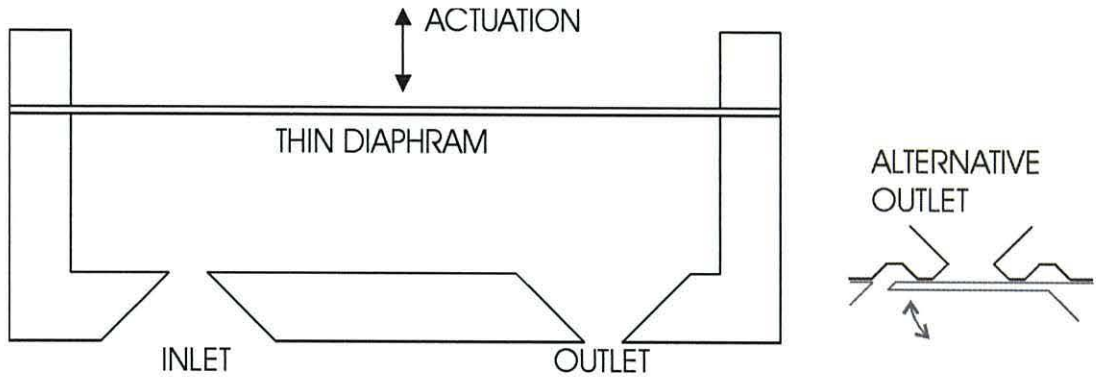

Figure 2.5 *Generic form of a mechanical micropump. The main diagram shows a nozzle and diffuser inlet and outlet[30]. The flap valve shown to the right can also be used[31].*

A wide variety of mechanical micropumps of this style have been developed, the majority are fabricated in silicon but polymer versions have also been developed[32]. The pumping is driven through the oscillation of the thin membrane shown in Figure 2.5. This has been achieved in a number ways which include,

- Piezoelectric [33-35] A piezoelectric material is bonded to the surface of the membrane. When energized it changes its dimensions and deflects the membrane.
- Thermo pneumatic [36] A confined volume is heated causing it to expand. This expansion deflects the membrane.
- Electrostatic [31] The membrane forms one side plate of a parallel plate capacitor. When a potential is applied there is an attractive force between the plates which moves the membrane.

Using mechanical membrane pumps of this type high flow rates of 16mlmin^{-1}[34] have been achieved, although in this case the back pressure was low at 1kPa. In other work [31] pumping has been carried out against a higher back pressure of 25kPa but against this pressure the flow rate was much lower at only 10µlmin^{-1}

2.4.2 Other pumping mechanisms

When a potential is applied along the length of a micro channel, which has a double layer formed at the solid liquid interface, the ions in the diffuse double layer will move under the influence of the electric field. These moving ions draw the liquid with them along the channel creating the flat fluid flow profile shown in Figure 2.7b, which is in contrast to the parabolic flow profile for pressure driven flow in Figure 2.7a. This process is referred to as Electroosmotic flow. Typically high potentials of the order 100 Vcm^{-1} are used [38]. To avoid short circuits through silicon structures, devices that use electroosmotic flow are typically fabricated from glass or have an insulating silicon dioxide layer on the walls of the channel. Using this approach flow velocities of 0.78mms^{-1} have been demonstrated for water.

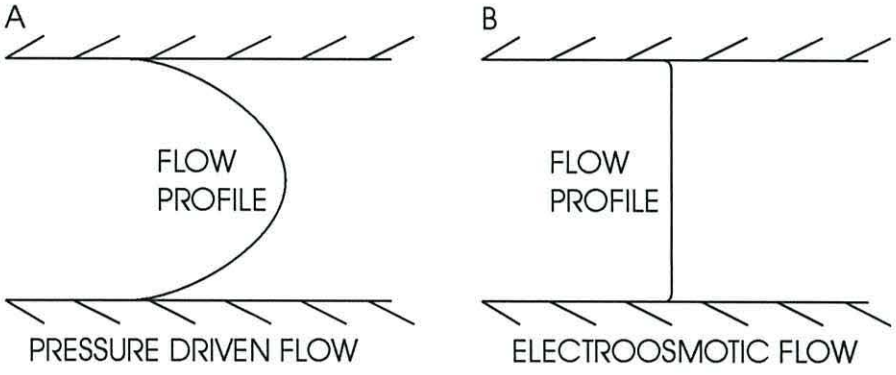

Figure 2.7 *Flow profiles generated by pressure driven flow and electroosmotic flow.*

When a current is passed through a conductor at right angles to a magnetic field a force will be exerted on the conductor. Fleming's left hand rule states that when the magnetic field is in the positive y direction and the current is in the positive x direction, the force on the conductor will be in the positive z direction as shown in Figure 2.8A. This process can be used to generate a flow in micro-channels as shown in Figure 2.8B [39].

To prevent electrolysis at the electrodes an alternating current is passed through the channel and the magnetic field is synchronised with this to ensure that the fluid flows in only one direction [40,41]. For this type of device flow velocities of 0.5 mms^{-1} for deionised water and $10mms^{-1}$ for saline solutions have been reported [41].

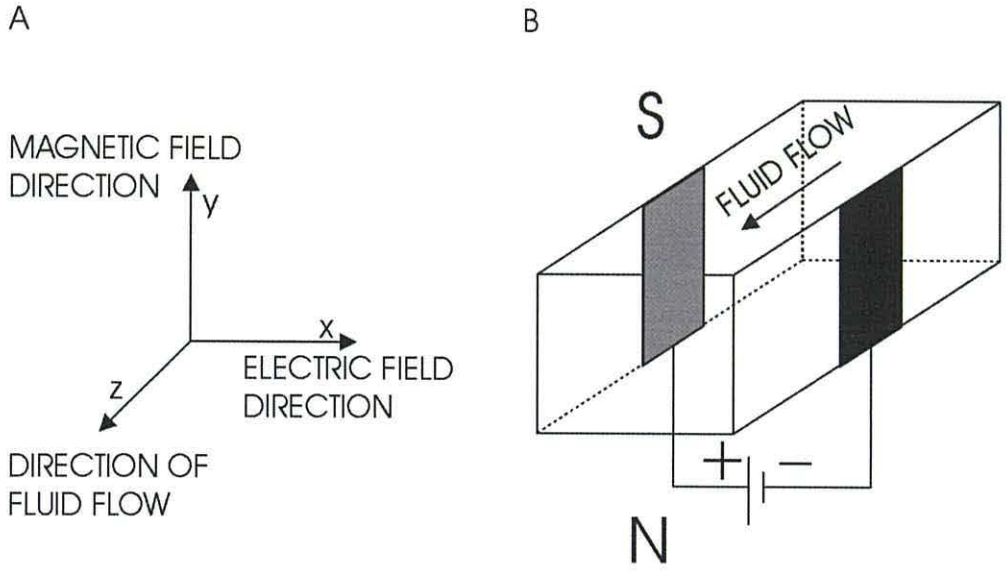

Figure 2.8 *The operation of a Magnetohydrodynamic micro pump [39].*

Electrohydrodynamic (EHD) pumps are typically used to pump low conductivity fluids in the range 10^{-8} to 10^{-10} Scm^{-1}, such as ethanol. The pumping process results from the interaction between an electric field and charges within the fluid. EHD pumps can be classified into two types, injection and induction pumping. In injection EHD pumping two grids are inserted in the fluid and a potential difference applied between them as shown in Figure 2.9. Charges are injected into the fluid as a result of high electric field strengths at electrodes. These charges move towards the other electrode drawing the fluid with them. Different electrochemical processes at the two electrodes result in an asymmetry of charge injection and therefore a net flow in one direction [15]. Using this type of pump flow rates of $14mlmin^{-1}$ have been achieved at a back pressure of 420Pa.[42].

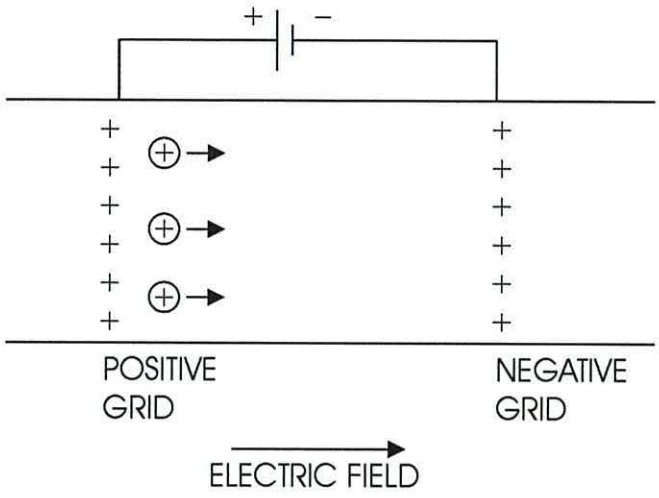

Figure 2.9 *The principle of operation of a charge injection EHD pump.*

In induction EHD pumping charges are induced in the fluid. This can be achieved through the creation of a temperature gradient in a slightly conducting fluid, such as corn oil (conductivity 10^{-8} Scm^{-1})[43]. These induced charges interact with an applied travelling electric field to form a travelling wave of charge that lags behind the applied travelling electric field. This lag between the induced charge and the applied field causes a force to be exerted on the charge, which in turn causes the fluid to flow as shown in Figure 2.11. Using this type of sensor with water of conductivity $10mSm^{-1}$ flow velocities of $250\mu ms^{-1}$ have been achieved [44].

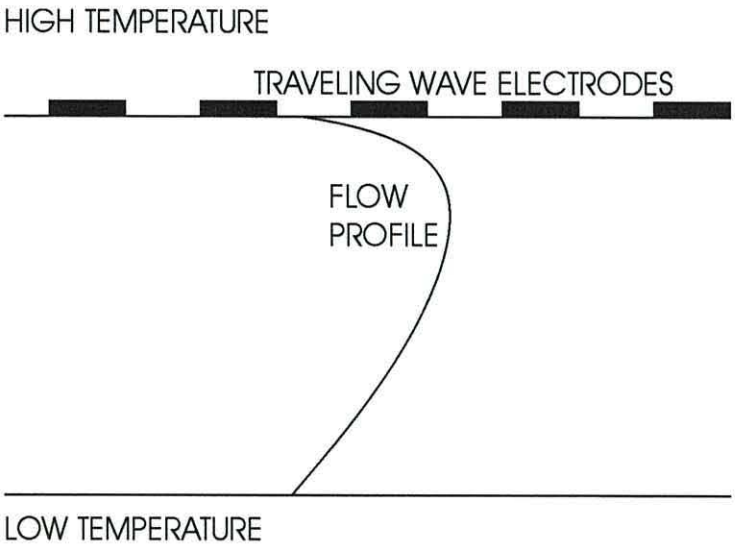

Figure 2.11 *Induced EHD flow using a temperature gradient [43].*

2.5 Sensors

A large number of micro-fabricated sensors have been developed, some of which can be applied to lab-on-a-chip type devices. Although sensors can be incorporated into lab-on-a-chip devices, this process can considerably add to production costs. The most common form of detection in commercial devices is optical based, with most of the detection system separate from the micro-device [5,6]. However, a variety of optical components such as lenses, mirrors, polarisers and gratings have been microfabricated 'on-chip' [14,15]. Optical detection techniques include measurements of absorption, fluorescence polarisation and refractive index.

The iStat^{TM} sensor [45] used to perform rapid analysis of blood to find the concentrations of selected substances, uses a series of electro-chemical sensors incorporated in the base of a micro-channel. Sensors of this type generally consist of a polymer material incorporated into an electrical circuit [46]. In the presence of a specific compound the electrical properties of the sensor change. Of particular importance in medical applications is the use of electrical measurements to detect the binding of an antibody to an immobilised antigen.

Micro fabricated sensors have also been developed to measure the properties of particles within a channel and measure flow rates of fluids in a channel.

2.6 Flow sensors

This section describes the operation of some of the types of flow sensor found in microfluidic systems. A range of different physical properties can be used to measure the flow rate of a fluid [15]. Heat transfer flow sensors measure the cooling effect of the flowing fluid on a heated sensor. Time of flight flow sensors use one upstream transducer to introduce discontinuity in the fluid flow, which is detected by a sensor down stream. The transit time is used to calculate the flow rate. The drag force or resonance that a fluid causes to structures in the channel can also be used to measure the flow rate.

2.6.1 Hot Wire flow sensors

This type of sensor measures the interaction between a heat source, a temperature sensor and the fluid. The heat source and sensor can either be two separate elements or the same structure. In structures where there is a separate heater and temperature sensor[47,48], the upstream heater heats the fluid and the downstream sensor detects the change in temperature. The temperature measured is a function of the flow rate between the sensors. An alternative approach is to heat either a metallic wire [49] or a heavily doped semiconductor [50] and then measure its temperature as a function of its electrical properties.

Thermal flow sensors can be operated in three main modes [51-53], constant temperature, constant power and time of flight, which is covered in the next section. In constant power mode the power available for heat generation is kept constant. As the velocity of the fluid increases heat is taken away from the sensor more efficiently and therefore the temperature decreases. This decrease in temperature is detected as a change in the resistance of the sensor. Alternatively, in constant temperature mode a feedback circuit is used to maintain the temperature of the sensor at a constant value. When the cooling effect on the sensor is altered by a change in the fluid flow, the feedback circuit increases or decreases the power applied to the sensor. From this change in applied power the flow velocity can be calculated. The choice between constant temperature and constant voltage hot wire anemometers depends on the application [51,52]. For example, a constant temperature anemometer is more complex than the constant power version, but as the wire is not required to change temperature it has a faster dynamic response.

Hot wire flow sensors rely on measuring temperature to measure a flow, for this reason they are susceptible to changes in ambient temperature. When a single sensor is used this effect can be minimised by increasing the overheat ratio, τ, of the sensor, which is given by the equation

$$\tau = \frac{T_w - \eta T_0}{T_0} \tag{2.1}$$

Where T_W is the wire temperature, T_0 is the ambient temperature and n is the wire recovery factor. For a sensor to be tolerant to changes in ambient temperature the over heat ratio must be near unity [53]. With a wire recovery factor of 1 and operation at room temperature the wire must operate at several hundred degrees. An alternative approach is to have a second unheated sensor that measures the ambient temperature. The signal from this sensor is combined with that from the flow sensor to give an accurate flow rate. This type of flow sensor has been widely implemented and therefore sensors exist that can measure a wide range of flow velocities. Typical flow rates for liquids in these devices can be around 1-10$\mu lmin^{-1}$ [54-56], although the majority of sensors of this type have been developed for use in a gaseous environment.

2.6.2 Time of flight flow sensors

In this type of sensor a transducer upstream in the liquid is continuously pulsed to introduce a series of discontinuities into the flow. Further down stream a sensor detects these pulses. The delay between the generation of the pulse and its detection can be used to measure the flow velocity. Typically the upstream transducer is a heater, which introduces temperature fluctuations into the flow that are detected down stream [53]. However, an alternative approach is to integrate two electrochemical cells onto the flow chamber. The up stream cell produces pulses of oxygen, which are detected by the downstream cell [57] as shown in Figure 2.13. Instead of oxygen, a sensor has been developed in which ions are injected into the flow and then detected down stream as a change in conductivity [58].

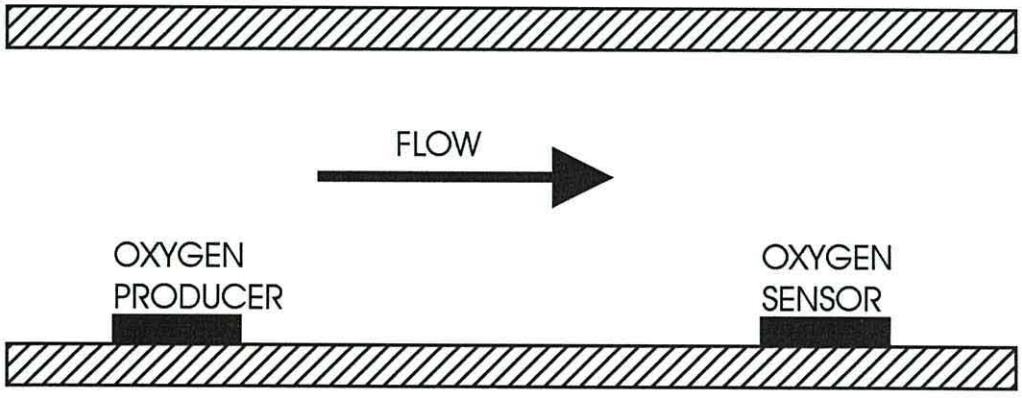

Figure 2.13 *Cross section through a time of flight flow sensor[57] formed using an oxygen producer up stream and an oxygen sensor down stream.*

A limitation of time of flight flow sensors is that as the pulse travels along the channel it disperses and reduces its peak amplitude, thus limiting the accuracy of the measurement at low flow rates. When a heat pulse is used to produce the discontinuity the energy dissipates into the channel and if the flow is low the fluid can return to its ambient temperature before the sensor is reached. This is not a problem for chemical variants of this sensor allowing them to detect much smaller flows. The minimum flows detectable for the oxygen and injected ion flow sensors were $0.75\mu lmin^{-1}$[57] and $10nlmin^{-1}$[58] respectively, compared to $10\mu lmin^{-1}$[53] for the thermal version.

2.6.3 Drag force flow sensors

When a physical structure protrudes into a fluid flow it will experience a drag force, which will increase with the flow velocity. This effect is exploited by cantilever based flow sensors [59] that consist of a cantilever beam inserted into the flow stream. The bending of the beam caused by the drag force of the fluid is then measured using a strain gauge at the base of the cantilever, as shown schematically in Figure 2.14.

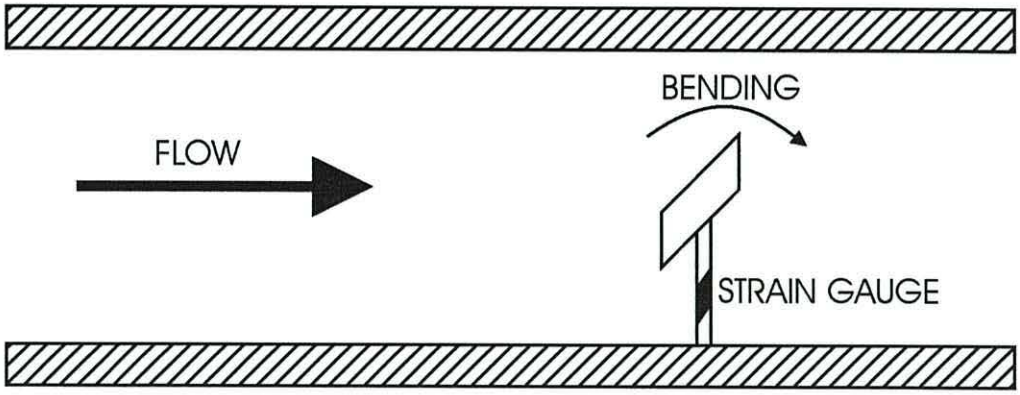

Figure 2.14 *Schematic representation of a drag force flow sensor.*

A variation on this type of sensor is to measure the damping effect of high velocity fluids on a vibrating cantilever [60]. In this type of sensor, piezoelectric actuators at the base of the cantilever are used to drive it at its resonant frequency.

2.6.4 Pressure measuring flow sensor

When a liquid flows through an aperture or along a channel a pressure drop occurs, which increases with the fluid velocity. The pressure drop also depends on the viscosity of the fluid and the physical properties of the channel. Figure 2.15 is a diagram of a flow sensor where the pressure drop is measured using a capacitive sensor [61]. One plate of the capacitor is fabricated on a thin membrane. When a pressure difference exists across the membrane, it deflects causing the distance between the plates to change and therefore the capacitance also alters.

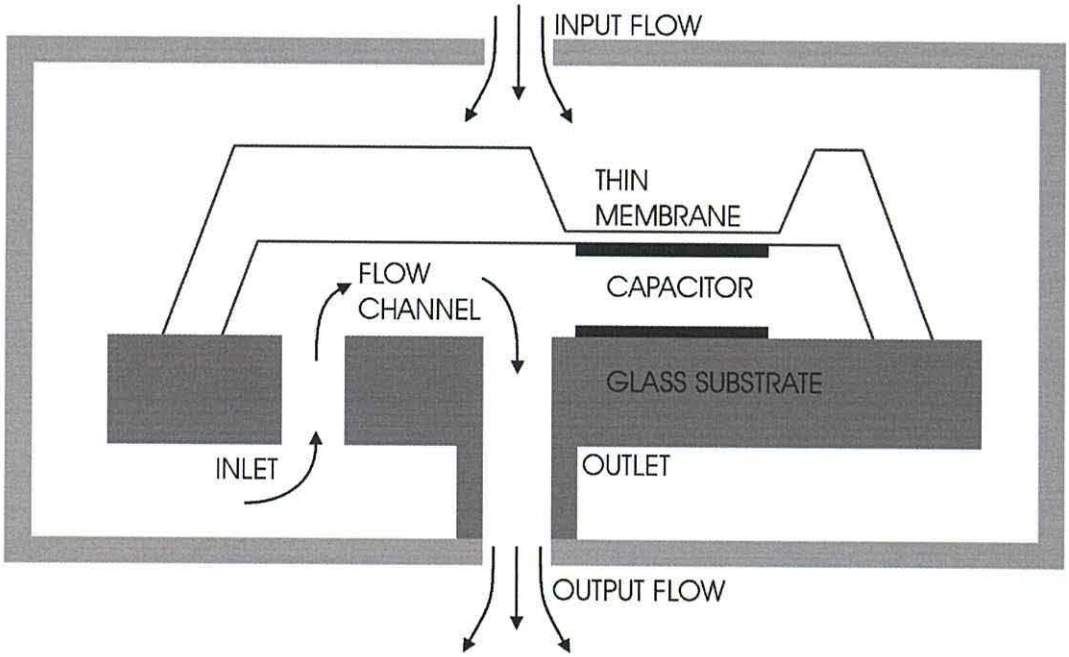

Figure 2.15 *Diagram of a differential pressure flow sensor [61]*

An alternative approach that has been used is to situate two absolute pressure sensors at either side of a channel [62] . The pressure drop over the channel can then be measured and from this the flow calculated. An advantage of this approach over the system shown in Figure 5.15 is that absolute pressure of the fluid in the system is also measurable.

2.7 Micro fabricated flow cytometers

Flow cytometers are devices that measure the properties of a suspension of cells or particles in a flowing fluid. The measurements are typically either optical or electrical. A flow cytometer can be used solely to analyse a sample, as is the case with a coulter counter where the size distribution of particles is found. Alternatively particles can be separated into sub populations, as is the case with a fluorescence activated cell sorter (FACS).

2.7.1 Particle detection

Coulter counters, both large scale and micro fabricated, detect the presence of a particle within a fluid stream by detecting the change in electrical conductivity. The basic design of a coulter counter is shown in Figure 2.6.

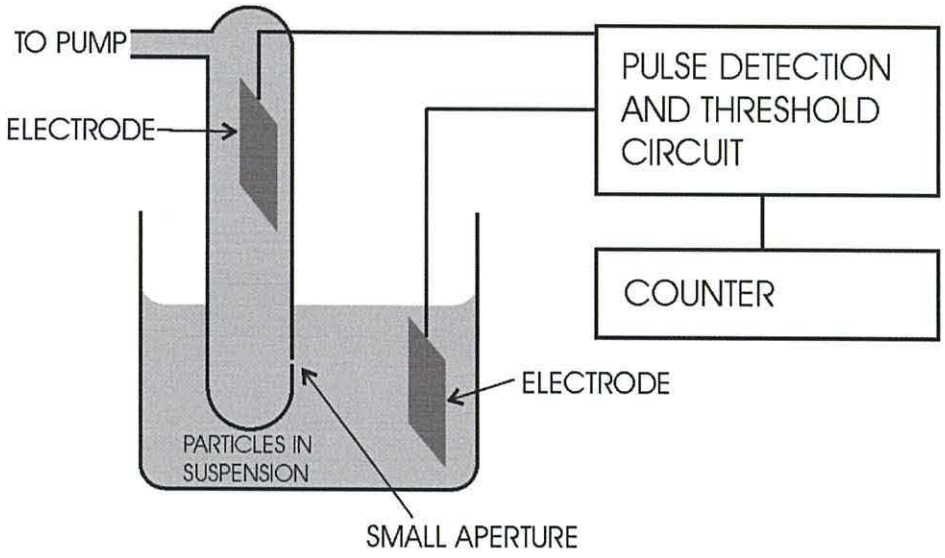

Figure 2.16 *Simplified representation of a Coulter counter.*

The system consists of a small aperture, on either side of which are electrodes between which an electrical current flows. When a particle of differing conductivity to the suspending medium passes through the aperture the resistance between the electrode changes. If the current between the electrodes is kept constant the passage of a particle results in a voltage pulse. The magnitude of this pulse depends on the size of the particle. Through the use of a thresholding circuit all the particles above a certain size

can be counted. Microfabricated coulter counters have been fabricated in silicon [63] and quartz [64], which consist of a small aperture in a channel with electrodes either side. These are used to measure the pulse change in the resistance as a particle passes through the channel.

Another approach used to detect particles within a channel is optical detection. A typical arrangement for this type of device is shown in Figure 2.16 [65]. A thin stream of particles in suspension is passed along a microfabricated channel, past two optical fibres mounted in opposite walls of the channel. One fibre illuminates the channel, whilst the other detects the light from the channel. Maximum sensitivity is typically achieved in this type of system when the particles are fluorescentley labelled and the fluorescence caused by the incident light is detected. However, these devices have also been shown to detect particles without fluorescent labelling.

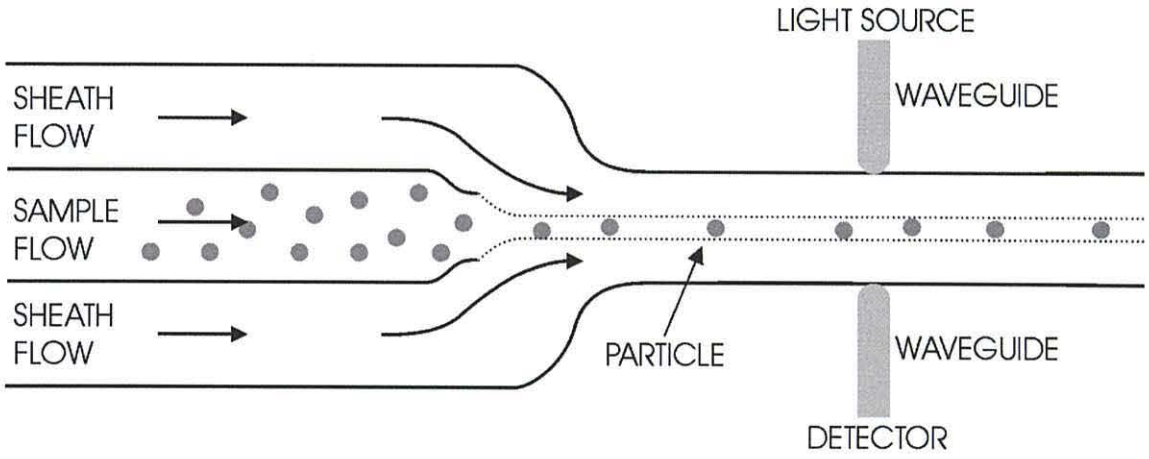

Figure 2.16 *Schematic illustrating the working principle of a cell counter[65] where the particles are hydrodynamicaly focused and then detected optically.*

To position the particles centrally in a channel and maximise the size of the particle relative to the carrying fluid, Hydrodynamic focusing [65,66] is often used. In this technique three streams of fluid are combined into one as illustrated in Figure 2.16. As a result of the greater flow volume of the outer streams, the inner stream is reduced in width. The flow rate within the device is sufficiently high that the particles do not diffuse out of the centre stream before they reach the sensor. When this approach is used in a Coulter counter the fluid making up the outer sheath is typically ultra pure water as it is non conductive, whilst the inner fluid containing the particles in suspension is more conductive. Alternatively the outer sheath can be formed from air [67]. Using this

approach it is not possible to form very thin centre streams as the flow breaks up into droplets.

2.7.2 Fluorescence Activated Cell Sorting

A Fluorescence activated cell sorting (FACS) machine is capable of measuring the fluorescence of individual particles in a stream. This information can then be used to sort particles into sub populations. Modern FACS machines are capable of operating at very rapid rates, often tens of thousands of events per second.

The two main components of this type of machine are a measurement element to detect the fluorescence of the particles and a switching element used to separate them into sub populations. A method for detecting the fluoresce of a stream of particles in a microfabricated channel has been described above. Both electrical and fluidic methods have been developed to selectively sort particles. Figure 2.17 shows the layout of a microfabricated FACS device[68]. The cells in suspension are supplied at the top of the device and then confined to a thin stream using hydrodynamic focusing. Once, the fluorescence has been measured they are sorted by switching the stream between the two outlets.

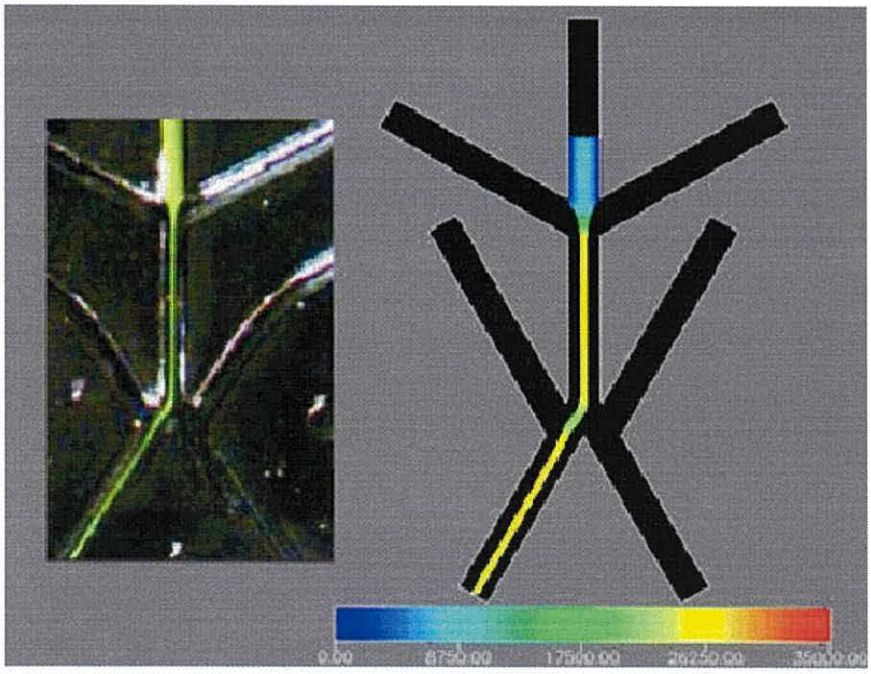

Figure 2.17 *A microfabricated fluorescence activated cell sorter (FACS)[68]*

Alternatively particles can be deflected using positive dielectrophoresis [69] that draws the particles towards high field regions. By moving a particle across the flow stream it can be selectively directed to different outlets.

2.8 AC Electrokinetic manipulation of particles

Dielectrophoresis is the movement of particles caused by electrical polarisation effects within inhomogeneous electric fields [70]. The particles do not require a net positive or negative charge and alternating current (ac) electrical fields are used to exploit the dielectric properties of the particles which vary with frequency. Dielectrophoresis can be used to separate a mixed population of particles by selectively attracting and repelling different particles from high electric field regions around energised electrodes. When a particle is exposed to a rotating electrical field of constant magnitude it will experience a torque and rotate. The speed of rotation depends on the particle and the frequency of the rotating field. This process is referred to as electrorotation. To move particles within a fluid without necessarily moving the fluid itself, travelling wave dielectrophoresis can be used. Here a particle is exposed to a travelling electrical field. The motion of the particle is dependent on the particle properties and the frequency of the travelling wave. Dielectrophoretic manipulation of particles is particularly useful when it is necessary to differentiate between particles that are optically similar but have different dielectric properties, such as dead or dormant pathogens [71].

This chapter gives an overview of existing lab-on-a-chip technologies. Chapter 3 describes the specific details of some microfabrication techniques that are used repeatedly in this research. The remainder of the thesis describes the lab-on-a-chip component parts that have been developed during this research. The theoretical discussion of the devices is in the same chapter as the description of the device and any experimental results.

2.9 References

[1] 'Introduction to micro-analytical systems: Bioanalytical and pharmaceutical applications' F. Huikko, R. Kostiainen and T. Kotiaho, *European Journal of Pharmaceutical sciences* **20** (2003) 149-171

[2] 'Silicon micro-accelerometer with mg resolution, high linearity and large frequency bandwidth fabricated with two mask bulk processes' Z. Xiao, M. Chen, G. Wu, C. Zhao, D. Zhang, Y. Hao G. Zhang and Z. Li, *Sensors and Actuators A* **77** (1999) 113-119

[3] Applied Biosystems. California, USA 'www.appliedbiosystems.com'

[4] 'Protein sizing on a microchip' L. Bousse, S. Mouradian, A. Minalla, H. Yee, K. Williams and R. Dubrow, *J. Analytical Chemistry.* **73** (2001) 1207-1212

[5] 'Caliper company web site (1/9/2002)' http://www.calipertech.com

[6] 'Nanogen company web site (1/9/2002)' http://www.nanogen.com

[7] 'A rapid diffusion immunoassay in a T-sensor' A. Hatch, A. E. Kamholz, K. R. Hawkins, M. S. Munson, E. A. Schilling, B. H. Weigl and P. Yager, *Nature Biotechnology.* **19** (2001) 461-465

[8] 'Microfabricated devices for genetic diagnostics' C. H. Mastrangelos, M. A. Burns and D. T. Burke, *Proceedings of the IEEE*, **69** (1998) 1769-1787

[9] 'Chemical amplification: Continuous-flow PCR on a chip' M.U. Kopp, A. J. de Mello and A. Manz, *Science* **280** (1998) 1046-1048

[10] 'Microfabricated structures for integrated DNA analysis' M. A. Burns, C. H. Mastrangelo, T. s. Sammarco, F. P. Man, J. R. Webster, B. N. Jhonson, B. Forester, D. Jones, Y. Fields, A. R. Kaiser and D. T. Burkes, *Preceenings of the National Acadomy of Science USA* **93** (1996) 5556-5561

[11] 'Micromachining chemical and biological analysis and reaction systems on glass substrates' D. J . Harrison, K. Fluri, N Chiem, T. Tang and Z Fan, *Sensors and Actuators B.* **33** (1996) 105-109

[12] 'Isolation of cultured cervical carcinoma cells mixed with peripheral blood cells on a bioelectronic chip' J. Cheng, E. L. Sheldon, L. Wu, M. J. Heller and J. P. O'Connell, *J. Analytical Chemistry* **70** (1998) 2321-2326

[13] 'Preparation and Hybridisation analysis of DNA/RNA from E.Coli on microfabricated bioelectric chips' J. Cheng, E. L. Sheldon, L. Wu, A. Uribi, L. O, Gerrue, J. Carrino, M. J. Heller and J. P. O'Connell, *Nature Biotechnology* **16** (1998) 541-546

[14] 'Future trends in diagnosis using laboratory-on-a-chip technologies' M. S. Talary, J. P. H. Burt and R. Pethig, *J. Parasitology.* **117** (1998) S191-S203

[15] 'Microfluidic Technology and Applications' Michael Koch, Alan Evans and Arthur Brunnschweiler, *Research studies press ltd. 2000, Hertfordshire, UK*

[16] 'Fundamentals of microfabrication' Mark Madou, *CRC press, 1997, Boca Raton, Florida, US*

[17] 'Electron beam lithography and reactive ion etching of nanometer size features in niobium films', T. T. Piotrowski, A. Piotrowaska, E. Kaminska, Z. Szopniewski, S. Kolesnik, J. Wrobel, P. Gierlowski and S. Lewandowski, *Materials Science and Engineering C* **15** (2001) 171-173

[18] 'Chemicaly assisted ion beam etching for submicron structures' J. D. Chinn, I. Adesida and E. D. Wolf, *Journal of Vacuum science and Technology* **1** (1983) 1028-1023

[19] 'Field assisted glass metal sealing' G. Wallis and D. I. Pomerantz, *Journal of Applied physics* **40** (1969) 3946-49

[20] 'Microfabrication technology for the production of capillary array Electrophoresis Chips' P. C. Simpson, A. T. Woolley and R. A. Mathies, *J. Biomedical Microdevices* **1** (1998) 7-26.

[21] 'Fabrication techniques and materials commonly used for the production of microreactors and micro total analytical systems' T. McGreedy, *Trends in Analytical Chemistry* **19** (2000) 396-401

[22] 'Micromachining of capillary electrophoresis injectors and separators on glass chips and evaluation of flow at capillary intersections' Z. H. Fan and D. J. Harrison, *J. Analytical Chemistry* **66** (1994) 177-184.

[23] 'Deep reactive ion etching of Pyrex glass using SF6 plasma' X. Li, T. Abe and M. Esashi, *Sensors and Actuators A* **87** (2001) 139-145

[24] 'Low temperature bonding for microfabrication of chemical analysis devices' H. Y. Wang, R. S. Foote, S. C. Jacobson, J. H. Schneibel and J. M. Ramsey, *Sensors and Actuators B* **45** (1997) 199-207

[25] 'UV laser machined polymer substrates for the development of microdiagnostic systems' M. A. Roderts, J. S. Rossier, P. Bercier and H. Girault, *J. Analytical Chemistry* **69** (1997) 2035-2042

[26] 'Ultra-deep LIGA process and its applications' Y. Cheng, B.-Y. Shew, M. K. Chyu and P. H. Chen, *Nuclear Instruments and Methods in Physics Research A* **467-468** (2001) 1192-1197

[27] 'UV LIGA process for high aspect ratio structures using stress barrier and C-shaped etch hole' H.-K. Chang and Y.-K. Kim, *Sensors and Actuators A* **84** (2000) 342-350

[28] 'Rapid Prototyping of Microfluidic Systems in Poly(dimethylsiloxane)' D. C. Duffy, J. C. McDonald, O. J. A. Schueller and G. M. Whitesides, *J. Analytical Chemistry* **70** (1998) 4974-4984

[29] 'Analysis of elastic micro optical components under large deformation' K. Hoshino and I. Shimoyama, *Journal of Micromechanics and microengineering* **13** (2003) 149-154

[30] 'Micronozzle/diffuser flow and its applications in micro valveless pumps' X. N. Jiang, Z. Y. Zhou, X. Y. Huang, Y. Li, Y. Yang and C. Y. Liu, *Sensors and Actuators A* **70** (1998) 81-87

[31] 'A bi-directional silicon micropump' R. Zengerle, J. Ulrich, S. Kluge, M. Richter and A. Richter, *Sensors and Actuators A* **50** (1995) 81-86

[32] 'Valve-less diffuser micropumps fabricated using thermoplastic replication' A. Olsson, O. Larsson, J. Holm, L. Lunbladh, O. Ohman and G, Stemme, *Sensors and Actuators A* **64** (1998) 63-68

[33] 'A novel micromachined pump based on thick-film piezoelectric actuation' M. Cock, N. Harris, A. G. R. Evans, N. M. White and A. Brunnschweiler, *Proceedings Transducers 1997* 353-356

[34] 'Piezoelectric micropump based on micromachining of silicon' H. T. G. van Lintel, F. C. M. van der Pol and S. Bouwstra, *Sensors and Actuators* **15** (1988) 153-167

[35] 'Micropump and sample injector for integrated chemical analysis systems' S. Shoji, S. Nakagawa and M. Esashi, *Sensors and Actuators A* **21** (1990) 189-192

[36] 'Thermopneumatic micropump based on micro-engineering techniques' H. T. G. van Lintel, F. C. M. van der Pol, M. Elwenspoek and J. H. J. Fluitman, *Sensors and actuators A* **21** (1990) 198-202

[37] 'Valveless diffuser/nozzle based fluid pump' E. Stemme and G Stemme, *Sensors and Actuators A* **39** (1993) 159-167

[38] 'Open channel electrochromatography on a Microchip' S. C. Jacobson, R. Hergenroder, L. B. Koutny and J. M. Ramsey, *J. Analytical Chemistry* **66** (1994) 2369-2373

[29] 'An AC Magnetohydrodynamic micropump' A. V. Lemoff and A. P. Lee, *Sensors and Actuators B* **63** (2000) 178-185

[40] 'Theoretical and experimental study of MHD (Magnetohydrodynamic) micropump' J. Jang, S. S. Lee, *Sensors and Actuators* **80** (2000) 84-89

[41] 'Magneto hydrodynamic (MHD) pump fabricated with ceramic tapes' J. Zhong, M. Yi and H. H. Bau, *Sensors and Actuators A* **96** (2002) 56-66

[42] 'A micromachined Electrohydrodynamic pump' A. Richter, A. Plettner, K. A. Hofmann and H. Sandmaier, *Sensors and Actuators A* **29** 1991 (159-168)

[43] 'Travelling wave bulk electroconvection induced across a temperature gradient' J. R. Melcher and M. S. Firebauch, *The Physics of Fluids* **9** (1966) 1548-1555

[44] 'Microfabricated electrohydrodynamic (EHD) pumps for liquids of higher conductivity' G. Fuhr, R. Hagedorn, T. Muller, W. Benecke and B. Wagner, *J. Microelectromechanical Systems* **1** (1992) 141-146

[45] 'i-Stat company web site (1/9/2002)' http://www.i-Stat.com

[46] 'Handbook of Chemical and Biological Sensors' Ed. R. F. Taylor and J. S. Suhultz, *Institute of Physics Publishing (1996), Bristol, UK*

[47] 'A silicon micromachined flow sensor using thermopiles for heat transfer measurements' S. Oda, M. Anzai, S. Uematsu and K. Watanabe, *IEEE Transactions on Instrumentation and Measurement* **52** (2003) 1155-1159

[48] 'Constant power operation of a two-dimensional flow sensor' K. A. A. Makinawa and J. H. Huijsing, *IEEE Transactions on Instrumentation and Measurement* **51** (2002) 840-844

[49] 'Low-cost silicon sensors for mass flow measurement of liquids and gases' N. T. Nguyen and R. Kiehnscherf, *Sensors and Actuators A* **49** (1995) 17-20

[50] 'MEMS flow sensors for nano-fluidic applications' S. Wu, Q. Lin, Y. Yuen and Y-C. Tai, *Sensors and Actuators A* **89** (2001) 152-158

[51] 'A comparative study of constant-voltage and constant-temperature hot wire anemometers: Part 2 – The dynamic response' M. A. Kegerise and E. F. Spina, *Experiments in Fluids* **29** (2000) 165-177

[52] 'A comparative study of constant-voltage and constant-temperature hot wire anemometers: Part 1 – The static response' M. A. Kegerise and E. F. Spina, *Experiments in Fluids* **29** (2000) 165-177

[53] 'Towards integrated microliquid handeling systems' E. Elwenspoek, T. S. J. Lammerink, R. Miyake and J. H. Fluitman, Journal of Micromechanics and Microengineering **4** (1994) 227-245

[54] 'Micro liquid flow sensor' T. S. J. Lammerink, N. R. Tas, M. Elwenspoke and J. H. J. Fluitman, *Sensors and Actuators* **A** 37-38 (1993) 45-50

[55] 'Hybrid-assembled micro dosing system using silicon-based micropump/valve and mass flow sensor' N. T. Nguyen, S. Schubert, S. Richter and W. Dotzel, *Sensors and Actuators A* **69** (1998) 85-91

[56] 'A MEMS body fluid flow sensor' E. Meng, S. Gassmann and Y-C Tai *Proceedings of Micro Total Analysis Systems 2001* 167-168

[57] 'Electrochemical time of flight flow sensor' J. Wu and W. Sansen, *Sensors and Actuators A* **97-98** (2002) 68-74

[58] 'Conductivity pulse time of flight flowsensor for sub-microliter/minute flow rates' C. K. Harnett, B. P. Mosier, P. F. Caton, B. Wiebenman and R. W. Crocker, *7th International Conference on Miniaturized Chemical and Biochemical Analysis Systems* 139-142

[59] 'Nanofluid handeling by microflow sensor based on drag force measurement' V. Gass, B. H. V. Schoot and N. F. de Rooij, IEEE Priceedings in Micro Electro Mechanical Systems (1993) 167-172

[60] 'Vibrating Cantileaver Mass Flow Sensor' R. E. Hetrick, *Sensors and Actuators A* 21-23 (1990) 373-376

[61] 'A high-performance microflowmeter with built-in self test' S. T. Cho and K. D. Wise, *Sensors and Actuators A* **36** (1993) 47-56

[62] 'Designing, realization and characrerization of a novel capacitance pressure/flow sensor' R. E. Oosterbroek, T. S. Y. Lammerink, J. W. Berenschot, A. van der Berg and M. C. Elwenspoek, *Proceedings in Transducers 1997* 151-154

[63] 'Design and fabrication of a micromachined coulter counter', M. Kock, A. G. R. Evans and A. Brunnschweiler, *Journal of Micromechanics and Microengineering* **9** (1999) 159-16

[64] 'Quantitative sensing of nanoscale colloids using a microchip coulter counter' O. A. Saleh and L. L. Sohn, *Review of Scientific Instruments* **72** (2001) 4449-4451

[65] 'Mocro flow cytometers with buried SU-8/SOG optical waveguides' G-B. Lee C-H. Lin and G-L. Chang, *Sensors and Actuators A* **103** (2003) 165-170

[66] 'Improved resolution and accuracy in electrical sensing zone particle counters through hydrodynamoc focusing' H. G. Merkus, H. Liu and B. Scarlett, *Particles and Particle system Characterizations*, **7** (1990) 11-15

[67] 'Use of air-liquid two-phase flow in hydrophobic microfluidic channels for disposable flow cytometers' D. Huh, Y-C. Tung, H-H Wei, J. B. Gothberg, S. J. Skerlos, K. Kurabayashi and S. Takayama, *Biomedical Microdevices* **4** (2002) 144-149

[68] 'Development of a microfluidic device for fluorescence activated cell sorting' J. Kruger, K. Singh, A. O'Neill, C. Jackson, A. Morrison and Peter O'Brien, *Journal of Micromechanics and Microengineering* **12** (2002) 486-494

[69] 'Handling of biological cells using a fluid integrated circuit' M. Washizu, T. Nanba and S. Manuda, *IEEE Transactions on Industrial Applications* **25** (1990) 352-358

[70] 'Dielectrophoresis: Using inhomogeneous AC electrical fields to separate and manipulate cells' R. Pethig, *Critical Reviews in Biotechnology* **16** (1996) 331-348

[71] 'Development of electrorotation Assay for Analytes in water' A. D. Goater (1999) *University of Wales PhD Thesis*

Chapter 3

Microfabrication Protocols Used in This Research

3.1 Introduction

This chapter describes in detail some established microfabrication techniques used repeatedly throughout this research. New protocols developed by the author during the research are described in Chapter 4. Section 3.2 describes in general terms the principles of photolithography and the photosensitive polymers that are used to transfer the two-dimensional pattern of structures from a photographic mask to the substrate. To produce structures using photolithography it is necessary to fabricate photo masks and deposit the material to be patterned. Section 3.3 details how the photo masks used in this research were produced using a photographic reduction process. The electrode structures used in this research were fabricated in gold with a chrome seed layer on a glass substrate. Section 3.4 describes the thermal deposition of gold and chrome to a thickness of 70nm.

The fabrication protocols used in this research to produce gold electrodes using 'print and etch' photolithography and 'lift off' photolithography are described in detail in Sections 3.5 and 3.6 respectively. To produce thin insulating films between layers of gold, polyimide was used. The stages in the production of photo-patterned films of polyimide are described in Section 3.7. An alternative method used to produce polymer structures, described in Section 3.7, was the use of dry film laminate.

3.2 Photolithography and photo patternable polymers

This section gives a general overview of how photolithography and photo patternable polymers are used to produce microfabricated structures. The remainder of the chapter describes the specific manufacturing protocols used.

To generate microstructures a pattern on a photographic mask can be transferred through UV exposure to a thin, or sometimes thick [1], layer of photosensitive polymer referred to as a resist. This resist is then developed to selectively remove either the exposed or unexposed polymer, depending on the polarity of the resist. Once the pattern is formed in the resist it acts as a masking layer for further etching of the substrate or the deposition of other materials.

To produce accurate structures in the resist it is necessary to have a uniform coating with the minimum of contaminants. This can be achieved by spin coating the resist onto the substrate. The substrate is held on a rotating chuck by a vacuum and covered with an excess of resist. It is then rotated at a high speed forcing the excess resist off the edge of the substrate, leaving a thin uniform film. The thickness of the film depends on the spin speed and the viscosity of the resist. At this stage in the fabrication process, the resist is baked at a relatively low temperature of the order of 100°C, to evaporate any remnants of the solvents that were used to make it fluid to allow spin coating. The baking process also anneals the resist, removing any internal stresses resulting from the spin coating procedure. Failure to properly anneal resists, especially thick resists, can lead to cracking of the resist layer or distortion of patterned structures [2].

To generate the photo mask the pattern can be first plotted at a large scale and then photographically reduced onto a glass or quartz plate, which is used as the mask. Alternatively, an electron beam or optical mask writer can directly produce the image. Typically electron beams are used to pattern a thin layer of resist on a chrome covered substrate. Once the resist has been developed the chrome is patterned through etching. This can produce finer features than the optical method. Depending on the process and resists used, the pattern on the mask will either be a negative or positive of the final structure. A mask is referred to as either light field or dark field depending on its polarity as illustrated in Figure 3.1.

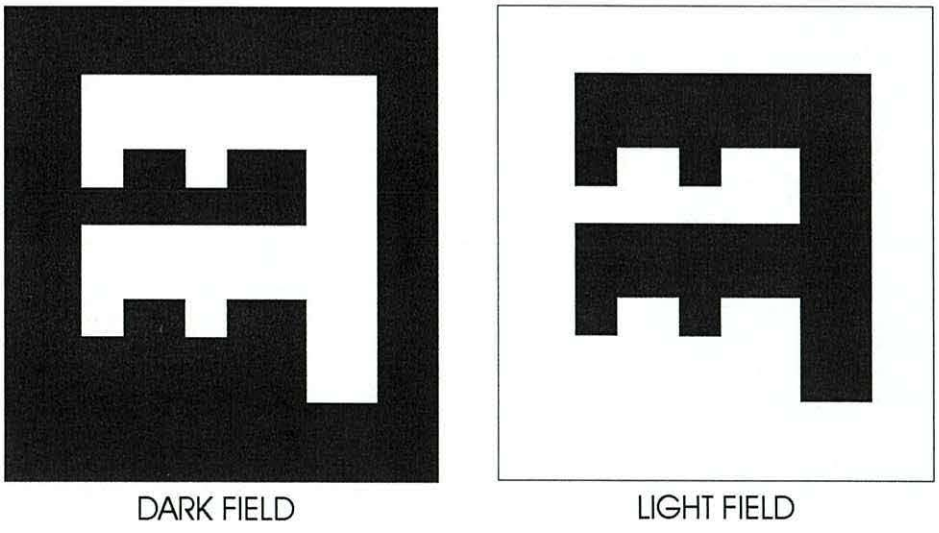

Figure 3.1 *Polarity of the image on light and dark field masks.*

Once produced the photo mask is then placed in contact, or near to, the layer of resist on top of the substrate and exposed to radiation, UV light in this research. There are two types of photoresist, positive and negative. When a positive resist is used, the exposure to UV light typically weakens the polymer by breaking chemical bonds, making it more soluble in the developer. The developed pattern in a positive resist is a copy of the opaque areas on the photo mask. When a negative resist is used, the polymer is chemically strengthened when exposed to UV light, making it less soluble in the developer, this is typically due to the formation of additional chemical bonds [3]. The developed pattern in a negative resist is a copy of the transparent areas on the photo mask. Figure 3.2 shows the patterns produced in positive and negative resists.

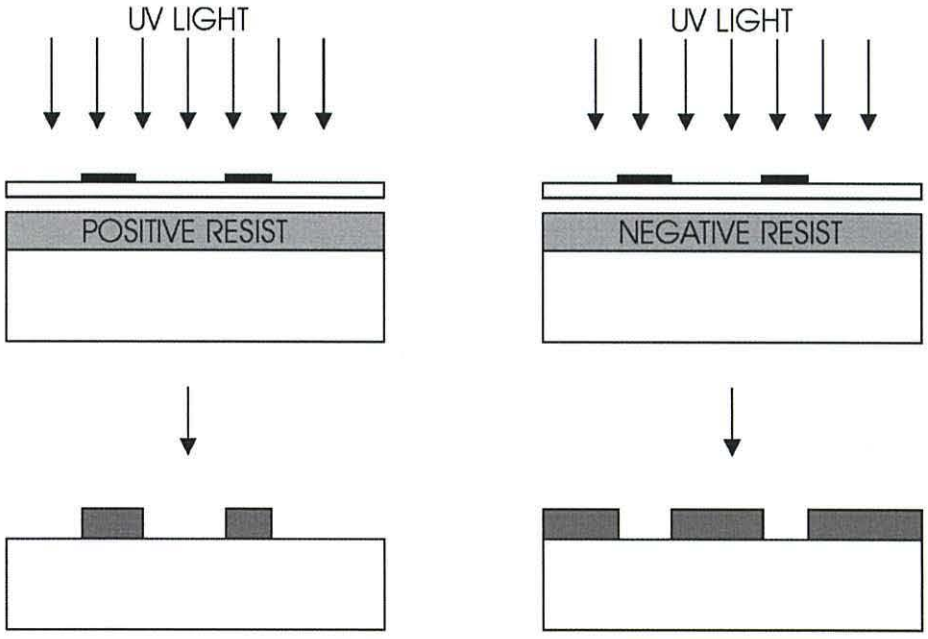

Figure 3.2 *The operation of positive and negative photoresists.*

When a resist is exposed via a mask, light is scattered within the resist and reflected from the substrate. This process generally causes the structures produced in the resist to differ slightly from the structures on the photo mask. Figure 3.3 illustrates the effect of light scattering in both negative and positive resist. The darkly shaded area in the diagram represents the partially exposed resist. The extent to which this is removed depends on the length of the exposure and development.

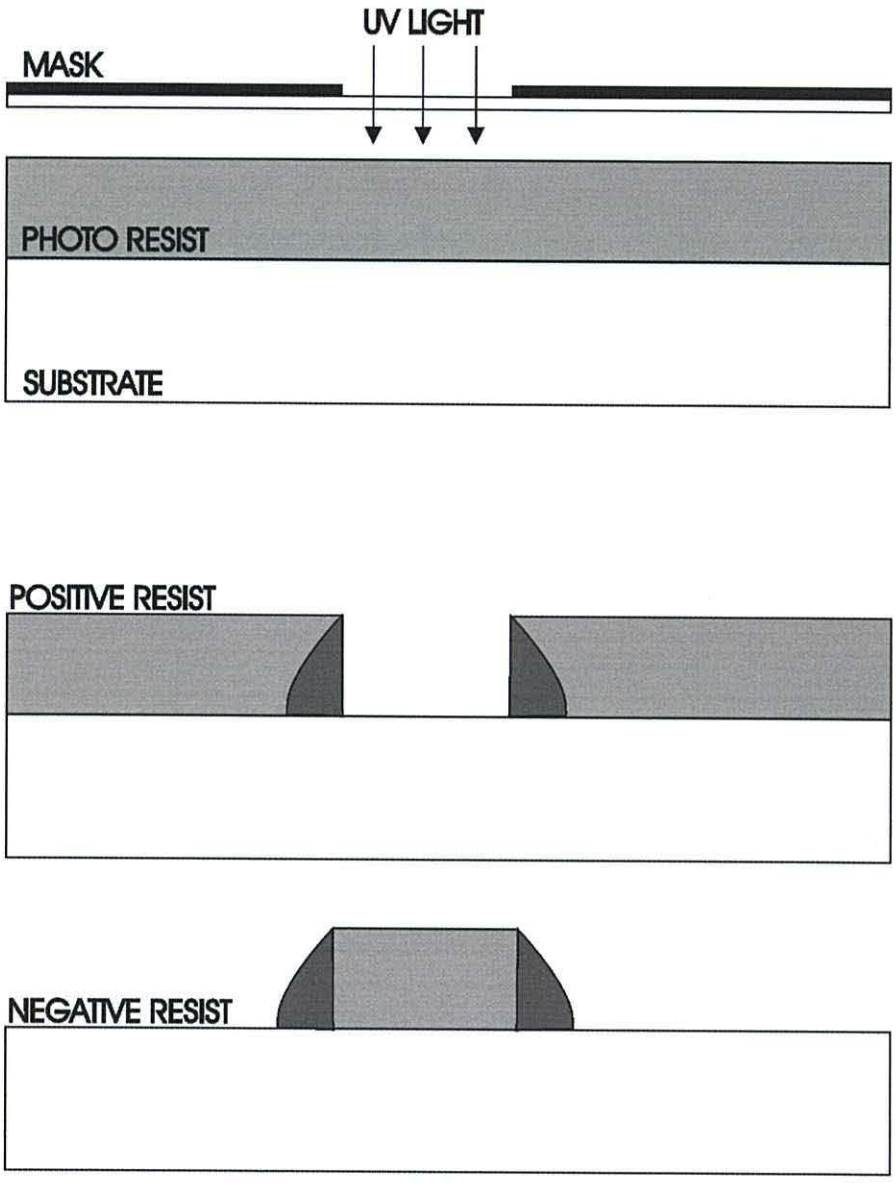

Figure 3.3 *The effect of light scattering on the patterning of a photoresist.*

Once a pattern has been produced in a resist layer either the exposed material can be removed or additional material can be deposited. The precise methods used in this research, are explained in detail in Sections 3.5 and 3.6.

3.3 Mask production

When fabricating structures using photolithography, the pattern is transferred from a mask to the resist. The mask pattern was generated 25 times larger than the final structure using a computer drawing package. This was plotted commercially onto

acetate film at a resolution of 4,000 dots per inch and then optically reduced 25 times in two stages.

Both stages in the reduction process use negative photographic emulsions. As the image is reversed twice, the image plotted on the acetate was of the same polarity as the image required on the final mask.

The first reduction stage was carried out using a process camera built in house. The original plot on acetate was backlit using a cold cathode source. An image reduced by a factor of 5 was formed via a lens on Kodalith Ortho film, type 3 (*Kodak, UK*) that was held flat on a vacuum mount. Once exposed the film was developed for 2 minutes under constant agitation in a solution of Kodalith A (50ml), Kodalith B (50ml) and ultra pure water (300ml). After development the image was fixed by agitation for 1 minute in a 1:4 solution of G333c fixer (Agfa, UK) and ultra pure water (UPW). Once washed to remove fixer the film was then placed in a drying cabinet at 60°C until dry (~30 minutes).

The second stage of reduction requires a higher degree of resolution than the first due to the smaller features on the image. This stage was carried out on a second process camera also built in house. The negative produced during the first stage was vacuum mounted onto a cold cathode light source. This was reduced by a factor of 5 onto a 2 inch square Millimask (Agfa, UK) glass plate. To ensure an in focus image is formed the lens was focused with the aid of a microscope. To reduce the distortion of the image, both the film and the glass plate were mounted with the emulsion towards the lens. The plate was then developed in a 1:4 solution of G282c developer (Agfa, UK) and UPW for 4 minutes. Once developed the image was fixed for 2 minutes in a 1:4 solution of G333c fixer and UPW, followed by a rinse and then forced hot air dried.

3.4 Thermal Evaporation of Gold films

When producing structures in gold on a glass substrate either using 'print and etch' or 'lift off' the metal was deposited through thermal evaporation. The adhesion between gold and glass is poor and therefore it is not desirable to directly deposit the gold onto the glass substrate. Instead a thin chrome seed layer, which adheres well to the glass, is first deposited. The gold, which in turn adheres well to the chrome, can then be deposited.

The first stage in producing a metal film is to clean the substrate as the adhesion to the substrate is poor, unless the glass is extremely clean. Any contaminants on the glass will prevent a uniform coating from being produced. This could lead to defects on the final device. The glass substrate was cleaned by submerging in a 1% solution of Decon 90 (*Decon Laboratories Limited, UK*) in a staining container. This was then placed in an ultrasonic bath for 5 minutes. Once removed from the Decon solution, the substrate was washed in ultra pure water (UPW) and dried under hot air.

The thermal evaporation of the chrome and gold was carried out in an Edwards Auto 302 Turbo Evaporator (Severn Science, UK), as shown in Figure 3.4. The clean glass substrates were mounted on a rotating chuck within a vacuum chamber, which also contained sources of chrome and gold.

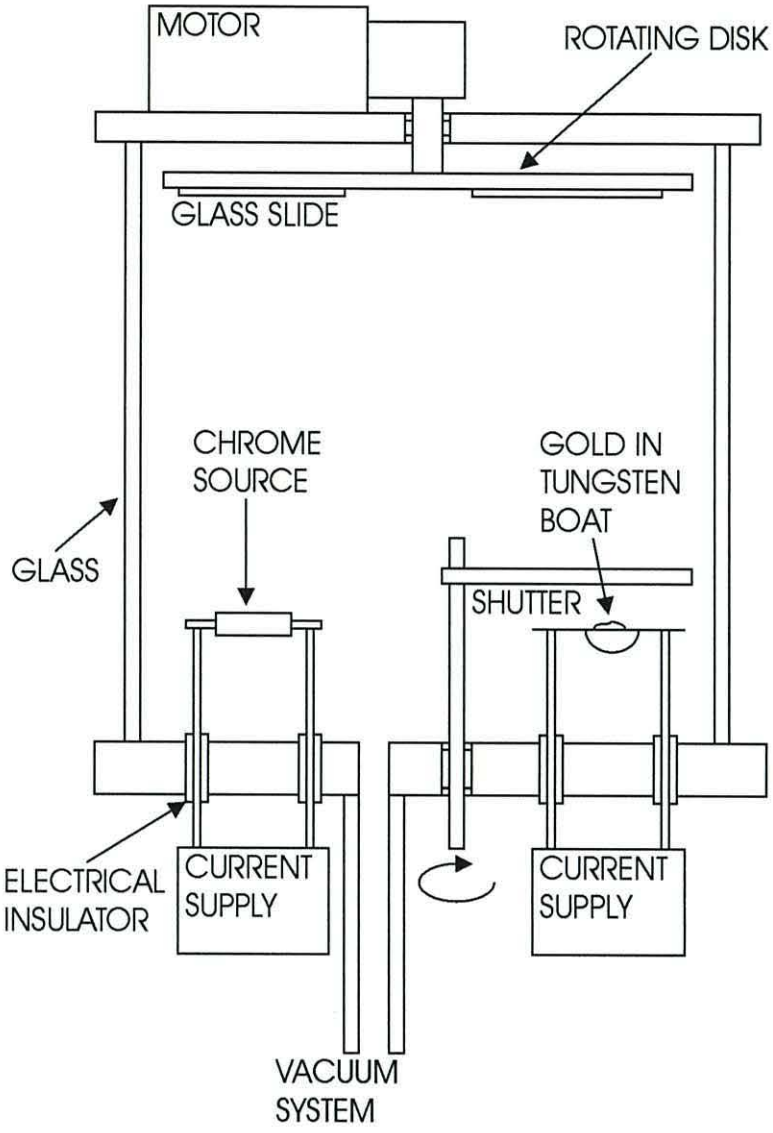

Figure 3.4 *Apparatus for the thermal evaporation of chrome and gold onto a glass substrate.*

Once the vacuum chamber was pumped down to a pressure of $8x10^{-6}$ mbar the 5nm chrome seed layer could be deposited. The source of chrome surrounded a tungsten rod through which current was passed to heat it above the evaporation temperature of the chrome. The thickness of the chrome was monitored using a quartz crystal, the frequency of which varied depending on the amount of material deposited. It is necessary to maintain the vacuum throughout the evaporation of the chrome and gold to prevent the surface of the chrome oxidising, leading to poor adhesion of the gold. To prevent cross contamination of the chrome and gold sources, a movable shutter was used to cover the source not in use. The deposition of the 70nm layer of gold was

implemented using a tungsten boat containing high purity gold. The gold was heated to above its boiling point by passing a current through the boat.

Once the apparatus had been allowed to cool for 5 minutes the vacuum system was turned off and air admitted to the chamber. At this stage the surface of the gold is very clean, therefore further fabrication steps were carried out a soon as possible.

3.5 'Print and etch' photolithography

The main types of photolithography used in this research were, 'print and etch' photolithography and 'lift off'. This section first describes how 'print and etch' is used to fabricate structures on a substrate and then describe in detail the fabrication protocol used in this research.

3.5.1 Principle of 'Print and etch' Photolithography

When using 'print and etch' photolithography the photoresist, once developed, acts as a masking layer for further etching of the substrate. Any materials to be patterned must be applied to the substrate before the resist.

Either positive or negative photoresists can be used when carrying out 'print and etch' photolithography. However, negative resists are often less expensive than positive resists and are generally used for this reason. Figures 3.5 illustrates the steps involved in making a set of gold electrodes using the 'print and etch' technique. In this example, a material is deposited onto the substrate and then etched. 'Print and etch' photolithography can also be used to directly etch the substrate.

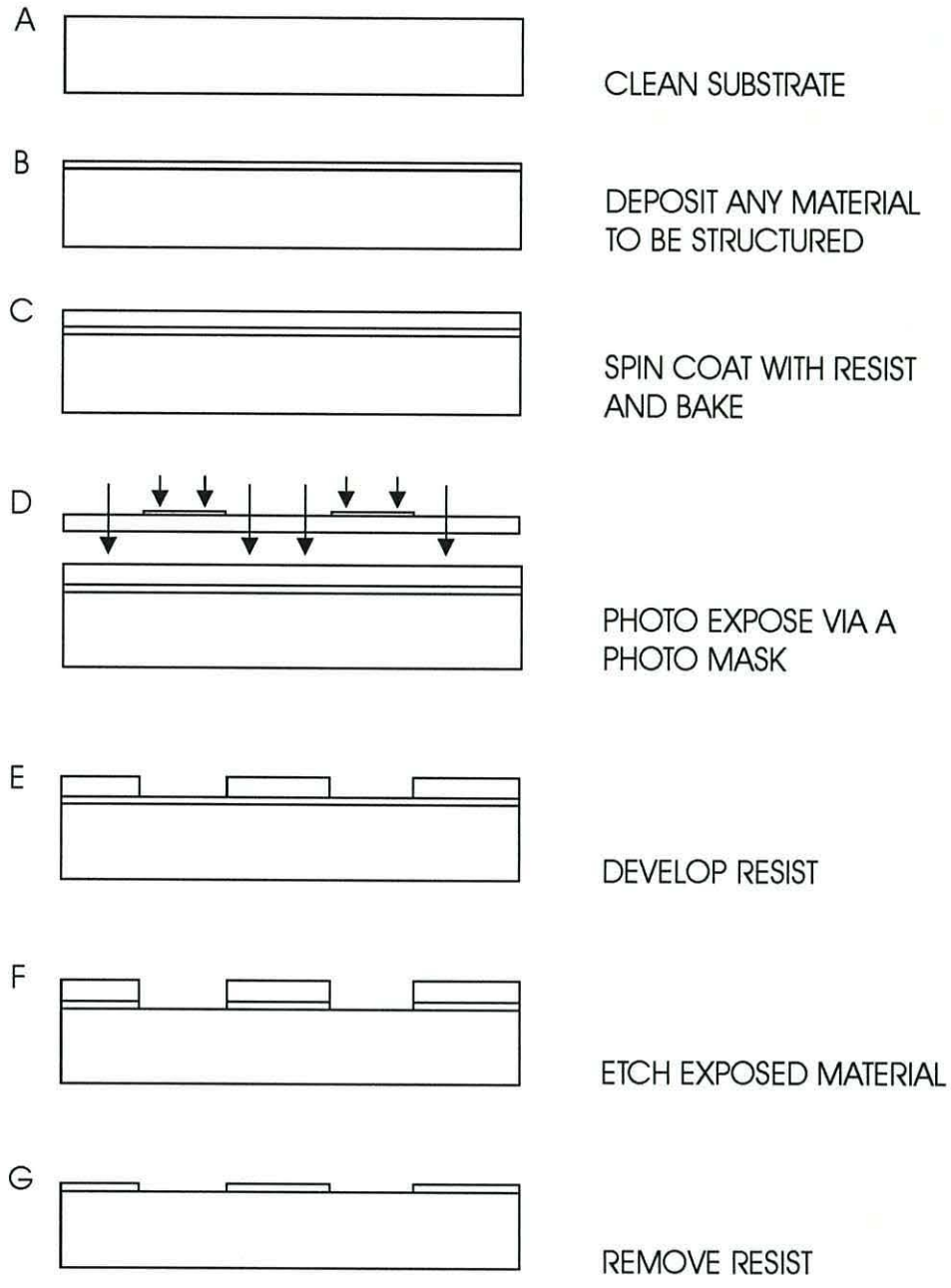

Figure 3.5 *Fabrication of structures on a substrate using 'print and etch' photolithography.*

When a negative resist is exposed the UV light is scattered within the resist, resulting in a developed pattern in the resist that is slightly larger than the negative pattern on the mask as shown in Figure 3.3. This effect can cause problems when producing narrow trenches in the resist, as the resist on either side encroaches into the trench as illustrated in Figure 3.6. It is possible to reduce this effect by changing the geometry of the mask or reducing the exposure and development times.

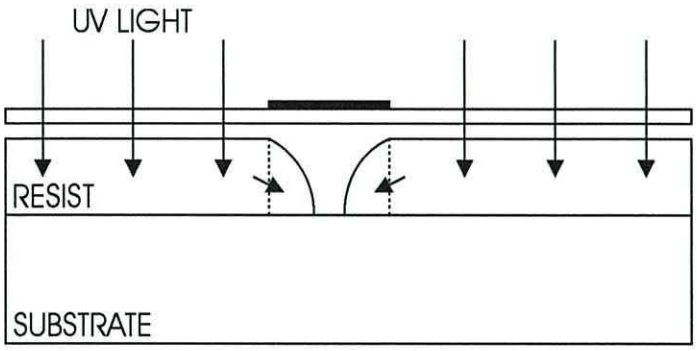

Figure 3.6 *Reduction in the width of channels in negative photoresist due to light scattering.*

If the exposure time of the resist is reduced then less light will be scattered into the resist in the channel, thus reducing the amount of material that remains after development. However, the main area of exposed resist will not have been fully polymerised and may be thinned during development. If the development time is increased more resist is removed from within the trench. This over development may also result in a thinning of the main area of the resist.

The etching of the material exposed by the resist can be either isotropic or anisotropic, depending on the material and the etchant as described in Section 3.2. If the etching process is isotropic, the uniform etch rate in all directions will result in an undercutting of the resist as shown in Figure 3.7.

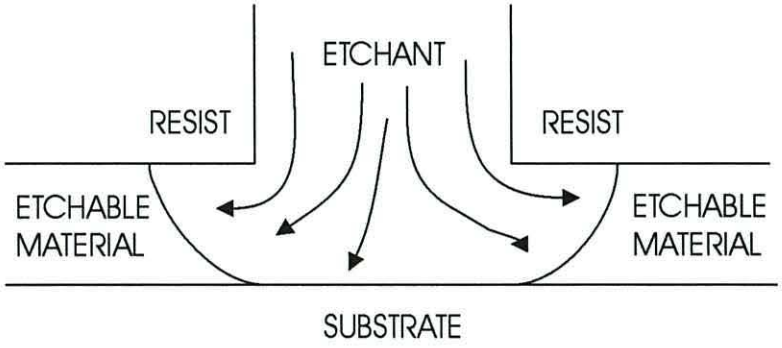

Figure 3.7 *Undercutting of the resist layer caused by isotropic etching.*

The extent of the undercut is of a similar size to the depth of the material being etched. If the device is heavily etched a large undercut could be produced causing a significant

change in the shape of the structures, which must be taken into consideration. Once the etching process is complete the resist can be removed using a solvent.

3.5.2 'Print and etch' protocol used in this work

As described in Section 3.5.1 the first stage in the 'print and etch' process is to deposit the material to be patterned. For this work, gold with a chrome seed layer is first deposited onto a glass substrate as described in Section 3.4. The specific values contained in this fabrication protocol are those normally used in this research. The exact values used are quoted. However, in most instances small changes do not significantly effect the finished device.

If the substrate is used immediately after the metallic films have been deposited, no further cleaning is necessary. However, if any contaminants were present, the surface was cleaned by submerging in a 1% solution of Decon 90 in an ultrasonic bath for 5 minutes, followed by rinsing in UPW and drying under hot air.

To provide a masking layer for the etching of the chrome and gold, a layer of S1818 positive photo resist (*Shipley Chemicals, UK)* was spin coated over the gold at 4000rpm. This was baked at 115°C for 1 minute to evaporate the solvents to leave a solid film and anneal the resist removing any internal stresses caused by the spin coating process.

Although care is taken to minimise any contamination of the substrate, some defects may be present. To reduce the device failure rate the substrate is moved relative to the mask so that any defects do not correspond to areas of fine detail. S1818 is a positive resist, therefore the areas of resist where the gold is to be removed are selectively exposed to UV light via the photo mask for 20 seconds at an energy density of $15mJcm^{-2}$. In Section 3.2 it was mentioned that negative resists are generally used for 'print and etch' photolithography due to the lower cost. However, the positive resist S1818 was used in this research as, unlike many commercial resists, it can be purchased in small volumes. The photo exposed resist is removed by agitation of the device in MF 319 developer (*Shipley Chemicals, UK*) for 40 seconds, followed by a

rinse in ultra pure water. The exposed areas of gold on chrome are then removed by etching with Aqua Rega (*75ml Hydrochloric acid (36%solution) and 25ml Nitric acid (69%solution)*) to remove the gold, followed by brief agitation in a chrome etch (*30g Ceric Amonium Nitrate, 7ml Glacial Acetic acid and 200ml Ultra pure water*) to remove the chrome seed layer. The photo resist remaining on the device is subsequently removed using acetone to leave the patterned gold electrodes.

3.6 'Lift off' photolithography

In section 3.6.1 the principle of operation of 'lift off' photolithography is described. The effect that exposure and development time has on the resist profile is also described in this section. The specific fabrication protocol used in this research is described in detail in Section 3.6.2.

3.6.1 Principle of 'Lift off' photolithography

When using the 'lift off' process, a layer of resist is spin coated onto the substrate before the layer of material to be patterned is deposited. The resist is patterned by exposure to radiation and then developed to selectively reveal areas of the substrate. A layer of material is deposited over the entire device, only coating the substrate where the resist has been removed. The resist is then dissolved, thus removing the material that is on top of it. When a multi layer device is fabricated, care must be taken not to damage the lower layers of the device when producing the upper layers. The 'lift off' process does not use any strong etchants, therefore it is especially suited to the fabrication of multi layer devices. Figure 3.8 illustrates the steps required to fabricate a structure using the 'lift off' process.

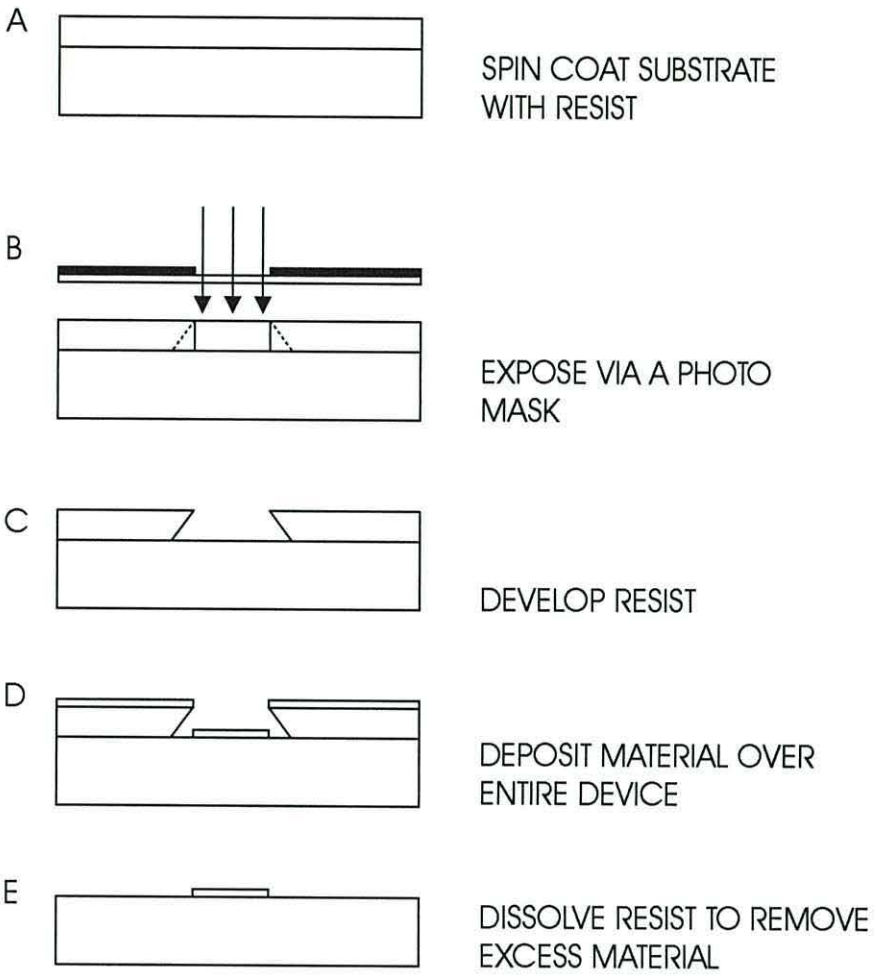

Figure 3.8 *Fabrication of structures on a substrate using 'lift off' photolithography.*

When performing the 'lift off' process it is necessary to use a positive resist, as it is not possible to achieve the undercut shown in Figure 3.7C using a negative resist. If there were no undercut on the resist, the deposited material would cover the sides of the channel making it difficult to remove the excess.

When using positive resist in 'lift off' photolithography the undercut results from the scattering of the UV light as illustrated in Figure 3.3. Depending on the degree of exposure, type of resist and the development time, the different edge profiles shown in Figure 3.9 can be achieved.

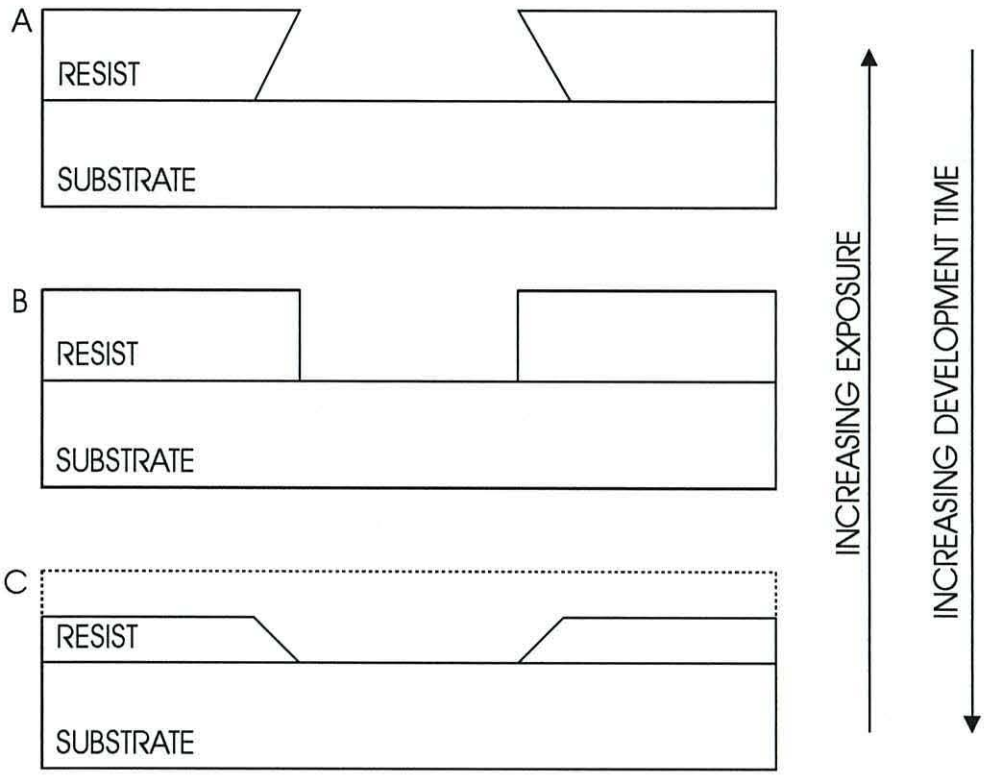

Figure 3.9 *The effect of variations in the exposure and development times on positive resist*

The profile illustrated in Figure 3.9A is the type required for 'lift off'. This profile is achieved through a high level of exposure, resulting in a large amount of light being scattered into the material. The range of the scattering increases with depth into the material, resulting in the channel being wider at the bottom than the top after development. To achieve this effect the solubility of the exposed resist in the developer must be much greater than that of the unexposed resist. The profiles shown in Figure 3.9B and 3.9C are achieved by progressively reducing the exposure time, which necessitates an increase in the development time to completely clear the channel. The long development time causes the unexposed resist to be partially eroded as shown in Figure 3.9C.

Returning to figure 3.8, once the resist is exposed and developed it has the profile illustrated in Figure 3.8C. The deposited layer of material is incident perpendicular to the substrate, resulting in a shadow being formed by the overhang in the resist as shown in Figure 3.8D. There is no physical link between the deposited layer in the channel and that on top of the resist. By dissolving the resist, the unwanted material on top can be removed without damage to the patterned structure.

When using the 'lift off' process, the final structure matches the pattern on the photo mask more closely than in the case of 'print and etch'. This is due to the scattering of the light within the resist not significantly affecting the size of the aperture in the top of the resist.

3.6.2 'Lift-off' protocol used in this work

The extent to which the substrate was cleaned before the deposition of the resist depended on the process already carried out to the device. Typically, the substrate was submerged in a 1% solution of Decon for 5 minutes in an ultrasound bath, as was the case when fabricating electrodes using 'print and etch'. The adhesion of the 'lift off' resist with the glass substrate was impaired by the presence of moisture on the substrate. To remove any absorbed moisture resulting from the cleaning process, the substrate was given a dehydration bake at 250°C for 3 minutes. To further improve the adhesion of the 'lift off' resist the device was coated in a layer of adhesion promoter, HMDS [4] (*Hexamethyldisilazane sup. Lancaster chemicals, UK*) for 30 seconds, which was then spun off before the application of the resist. HMDS negates areas that would trap water from the air, thus improving the adhesion of the resist.

The dry substrate was spin coated at 4000 rpm for 30 seconds with BPRS 'lift off' resist (*Arch chemicals, US*) and then baked at 80°C for 1 minute to evaporate the solvents and remove internal stresses. When using the 'lift off' process the areas of resist where the gold is required are removed. This is achieved through selectively exposing the resist using UV light via a photo mask for 40 seconds at an energy density of 15mJcm^{-2}. The unwanted resist is then removed by light agitation of the device in a 1:3 solution of PLSI developer (*Arch chemicals, US)* and UPW for 90 seconds. Once the resist has been developed it is washed in UPW then baked at 80°C for 1 minute to remove any absorbed moisture. To form the metallic structures, a 70 nm layer of gold with a chrome seed layer was evaporated over the entire device as described in Section 3.3. To remove the unwanted gold and chrome on top of the resist, the device is placed in acetone in an ultrasound bath, for 1 minute to dissolve the remaining resist. When the resist is dissolved, the thin film of chrome and gold breaks up into fine particles. The use of an ultrasound bath prevents these particles from being re-deposited onto the device.

3.7 Polyimide insulating layer

To produce thin insulating films, such as those used in multi-layer devices, a photo patternable polyimide can be used. In this research, the photosensitive polyimide used was Duramide (*Arch Chemicals, US*). As with the 'lift off' resist, the adhesion of the Duramide was poor unless the substrate was thoroughly clean. The substrate was first submerged in a 1% solution of Decon 90 in an ultrasound bath for 5 minutes and then submerged in chromic acid in an ultrasound bath for 1 minute to remove any organic contaminants. Once rinsed, any absorbed water was removed by a dehydration bake at 250°C for 3 minutes.

The Duramide is spin coated over the entire device in a three step process, first at 900 rpm for 6 seconds followed by a stationary hold period of 15 seconds, then 4000 rpm for 37 seconds to ensure a uniform coverage. The Duramide was baked at 100°C for 3 minutes to evaporate the solvent and leave a solid non-tacky surface and remove any internal stresses. Duramide is a negative photo polymer, therefore any areas required in the final device were selectively exposed to UV light via a photo mask for 40 seconds at an energy density of $15mJcm^{-2}$.

The photo exposed Duramide was developed by mild agitation in HDR-D2 developer (*Arch chemicals, US*) for 55 seconds, followed by 34 seconds in a 1:1 mixture of HDR-D2 and RER Rinse aide (*Arch chemicals, US*) and finally a rinse in RER. The remaining undeveloped Duramide was then spin dried at 4000 rpm. Once developed the Duramide is baked under nitrogen (flow rate $0.5lmin^{-1}$) To complete the curing process and make it more chemically inert. The temperature of the Carbolite LHT 6-60 oven (Carbolite Ltd, UK) was ramped at a rate of 4°C per minute up to a temperature of 350°C. The device was left at this temperature for 1 hour then allowed to cool naturally. The ramped temperature cycle allows uniform heating of the sample, which prevents a skin of baked material forming over the surface of the Duramide, which may trap solvents and gases so weakening the Duramide layer.

3.8 Dry film laminate

The Duramide layer fabricated in Section 3.6 was typically 1 to 2 μm thick. To produce thicker polymer structures dry film laminate was used. The 5038 dry film laminate (Ozatec, UK) used in this research was 30μm thick. To produce thicker structures several layers were applied. The laminate is supplied on rolls sandwiched between two prospective films. As illustrated in Figure 3.10, one surface is covered with a low temperature polymer to protect the surface of the laminate from damage and is automatically removed by the laminator. The other surface is covered with a heat resistant polymer that prevents the laminate from sticking to the rollers of the laminator. This must be manually removed after lamination.

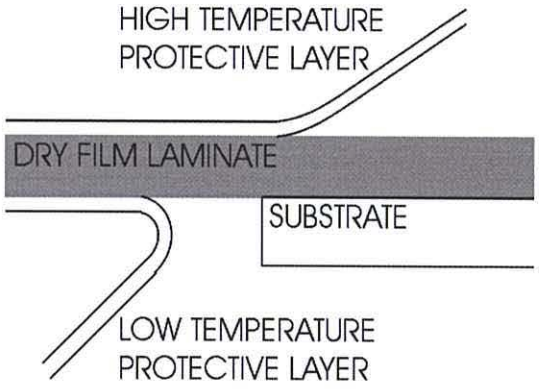

Figure 3.10 *Protective layers on Ozatec 5038 dry film laminate resist.*

As with the spin coating of polymers the adhesion to the glass substrate is improved if it is thoroughly cleaned before the laminate is applied. The substrate was cleaned using a 1% solution of Decon 90, rinsed in UPW and dried under hot air. To remove any absorbed water from the cleaning process that may cause bubbles to form under the laminate the substrate was given a dehydration bake at 250°C for 3 minutes. The physical arrangement of the laminator is illustrated in Figure 3.11.

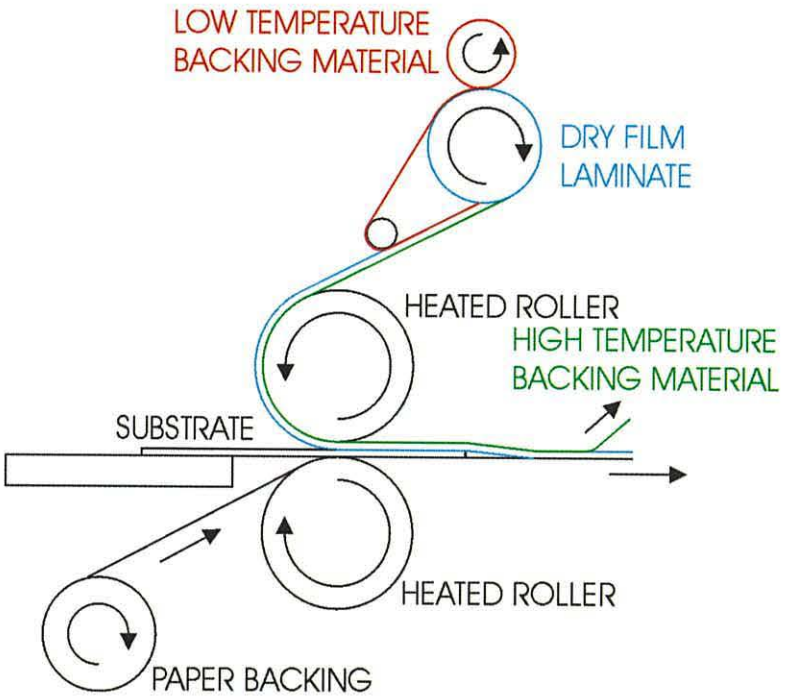

Figure 3.11 *Arrangement of dry film laminator.*

The substrate was inserted between the heated rollers operating at 110°C and automatically drawn through the machine. The paper roll below the substrate is to prevent the laminate surrounding the substrate from adhering to the lower roller.

This type of dry film laminate is a negative photo resist, therefore it is necessary to expose the areas required after development to UV light via a photo mask. The duration of the exposure was dependent on the number of layers of laminate deposited, typically an exposure time of 20 seconds per layer at an energy density of $15mJcm^{-2}$ was required.

Before the laminate can be developed, it is necessary to remove the protective coating. Once removed, the soft surface of the laminate is exposed and care must be taken to prevent mechanical damage. Unexposed areas of laminate were removed by development in a Girojet 2 (CIF, France) spray tank using a 1% by weight solution of sodium carbonate. The development time depends on the number of layers of laminate deposited and is typically 3 minutes per layer. After development, the remaining laminate is rinsed in UPW and allowed to dry at room temperature. To completely cure

the laminate it is baked at 300°C for 30 seconds. The baking process also increases the hardness and makes it more chemically inert.

The next chapter describes novel new designs and manufacturing processes developed in this research. A design and fabrication process for large area travelling wave electrode arrays that eliminate the need for via-holes is described, as well as a series of microfluidic channel designs.

3.9 References

[1] 'Ultra-deep LIGA process and its applications' Y. Cheng, B-Y. Shew, M. K. Chyu and P. H. Chen, *Nuclear Instruments and Methods in Physics Research A* **467-468** (2000) 1192-1197

[2] 'UV-Liga process for high aspect ratio structure using stress barrier and C-shaped etch hole' H-K. Chang and Y-K. Kim, *Sensors and Actuators A* **84** (2000) 342-350

[3] 'Fundamentals of microfabrication' Mark Madou, *CRC press, 1997, Boca Raton, Florida, US*

[4] 'HMDS (Hexamethyldisilazane) data sheet' available from: Lancaster chemicals, United Kingdom.

Chapter 4

Novel Device Fabrication Methods

4.1 Introduction

A well documented and reliable approach used to transport cells in suspension is travelling wave dielectrophoresis (TWD) [1-6]. Travelling wave dielectrophoresis is an electrokinetic process that relies on adjacent electrodes being out of phase. To connect several different phase signals to the electrodes of a long travelling wave array, it is typically necessary to fabricate a multi-layer device. A method is described that has been developed to fabricate multi-layer travelling wave electrode arrays, which eliminates the need to use via-holes to connect between different layers. When using electrodes to manipulate particles in a suspension it is also necessary to constrain the fluid within the device. Methods for fabricating microfluidic channels used to constrain fluids are also described.

This chapter firstly describes a standard process used to manufacture travelling wave arrays, where via-holes are used to connect between two conducting gold layers separated by a thin insulator. The connections between layers in this type of multi-layer device are often the main cause of device failure, due to the emergence of open circuits caused by breaks in the gold at the via-holes. The fabrication process described in Section 4.3 was developed to produce a set of travelling wave electrodes that do not use via-holes or require electrodes to pass over any vertical steps. In this approach, the travelling wave array was fabricated from two separate layers of electrodes, where the second set of electrodes was slightly raised above the first over its entire area on an insulating layer of polyimide. In the area of the channel, the polyimide covering the first layer of electrodes was removed exposing them to the suspending medium.

Section 4.4 outlines the requirements a channel structure should satisfy and reviews some simple methods, which have been used to form channels that can be dismantled to allow the electrodes to be cleaned. However, due to limitations in the performance of this type of channel, it was found necessary to fabricate new types of structures where the lid of the channel was permanently attached. Section 4.5 describes a channel structure that was fabricated through photolithography of dry film laminate, which was bonded to a glass substrate. The lid of the channel was attached using a UV curing adhesive, which formed a much stronger channel allowing higher pressures and flow rates to be used. When an excimer laser was used to machine channels in dry film

laminate, as described in Section 4.6, it was possible to produce channels of a much higher resolution than by using UV photolithography followed by wet chemical development. When the channel was machined using a laser, the laminate retained its adhesive properties, making it possible to directly attach a lid to the device without the use of an adhesive layer. When chemicals were used to form the channel, the upper surface of the laminate was no longer adhesive after exposure to the developer. Section 4.7 describes another method that was used to fabricate a channel using two glass substrates to sandwich a layer of UV curing adhesive. The adhesive outside the channel was cured by exposure through a photomask. The unexposed liquid adhesive from the channel was then removed by flushing through with acetone. After fabrication, it was necessary to make external fluidic connections to the channel. The approaches used to connect to these channels are described in Section 4.8. The fabrication processes detailed in this chapter all produced working microfluidic channels. The comparative merits of the channels are discussed in Section 4.9.

4.2 Fabrication of travelling wave arrays using via-holes

To generate a travelling wave in the electrode array a phase difference must exist between the electrical signals applied to each electrode [1]. The extent of the phase difference depends on the number of electrodes used to describe a 360° signal cycle. For the travelling wave to have a defined direction, there must be at least three electrodes in each repeated group. To generate a travelling wave where the electrode phase repeats every fourth electrode, each electrode is energised with an electrical signal 90° out of phase with the adjacent electrode. The phases of a typical four electrode cycle travelling wave array are illustrated in Figure 4.1

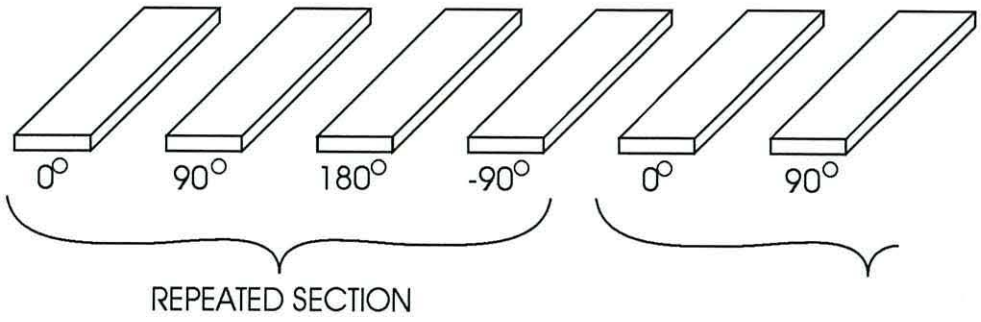

Figure 4.1 *The phases of the signals applied to a four cycle travelling wave array.*

With short lengths of travelling wave track it is possible to make a separate connection between each electrode and an interface contact at the edge of the device, as illustrated in Figure 4.2. Each external interface contact must be sufficiently large to ensure that a reliable connection is made. However, if the track consists of a large number of electrodes there may be insufficient space around the edge of the device to make individual connections. An example is the bio-factory device developed at the University of Wales, Bangor [7], which contains 6000 electrodes on a device 40mm by 53mm.

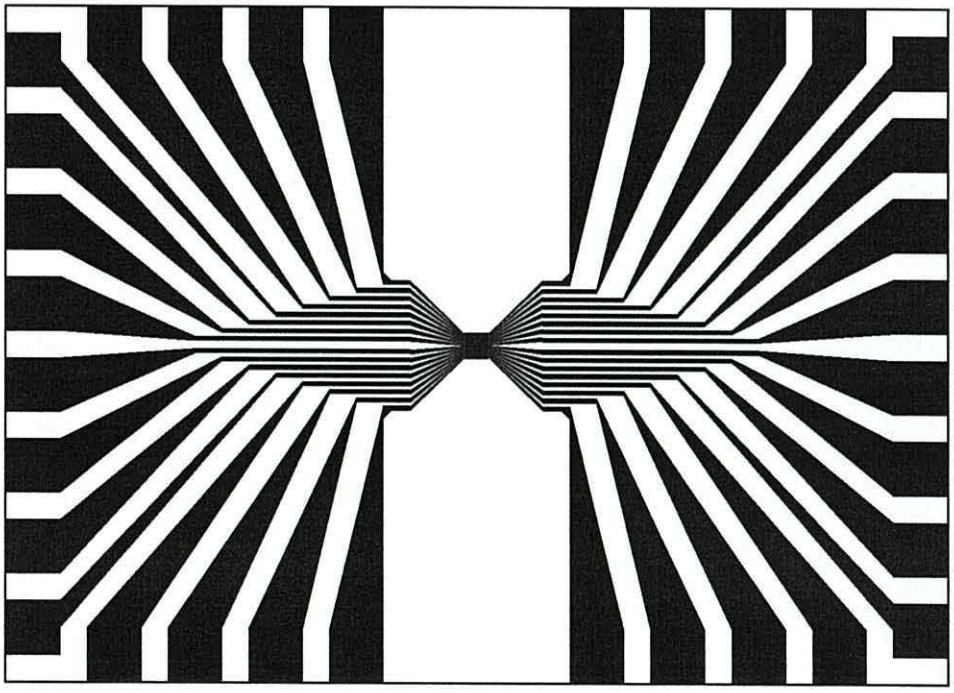

Figure 4.2 *Diagram of a single layer travelling wave track and connections fabricated on a substrate 30mm by 25mm.*

To produce a long travelling wave electrode array, it is easier to directly connect together every fourth electrode using bus bars and take just four connections off the device. Due to the physical arrangement of the electrodes, it is not possible to achieve this using a single layer device, instead a two layer device must be used. Such devices consist of two conducting layers separated by an insulator. The presence of the insulator allows conducting electrode tracks to cross without making electrical contact. If a connection between the upper and lower layers is required, a hole is fabricated in the insulating material, this is referred to as a 'via' or 'via-hole'. The stages involved in fabricating a multi-layer travelling wave electrode array are illustrated in Figure 4.3.

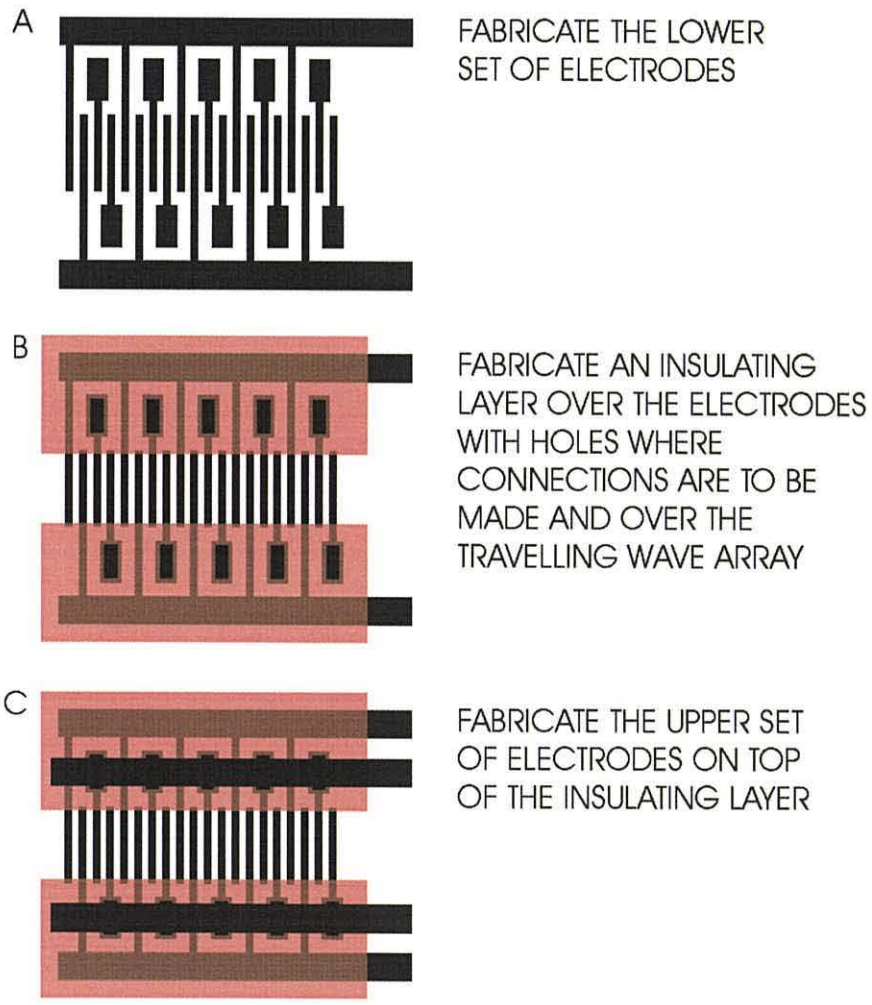

Figure 4.3 *Fabrication of a travelling wave array using via-holes.*

The approach conventionally used to connect the electrodes in a travelling wave track is to fabricate all the electrodes in a single layer of gold on a glass substrate using 'print and etch' photolithography as described in Section 3.4. On this layer external

connections are only made to two of the phases as shown in Figure 4.3A. A thin insulating layer of photosensitive polymer is then spin coated over the entire device. Using the photolithographic processes described in Section 3.6, via-holes are made in the insulating layer at the ends of the unconnected electrodes where an area is removed to expose the underlying electrodes that form the travelling wave array, as shown in Figure 4.3B. A second layer of gold is deposited and patterned to electrically interconnect the remaining two phases. These upper gold tracks run over the top of the insulating layer and only connect to the lower electrodes where a via-hole has been fabricated as illustrated in Figure 4.3C. To prevent damage to the electrodes that have already been fabricated the upper set of electrodes are fabricated using 'lift off' photolithography, as described in Section 3.5.

When using the design illustrated in Figure 4.3 connections must be made to electrodes on both sides of the travelling wave array. In some situations, such as where two travelling wave arrays are combined into one [7], it is only possible to gain access to one side of the array. This is illustrated in Figure 4.4

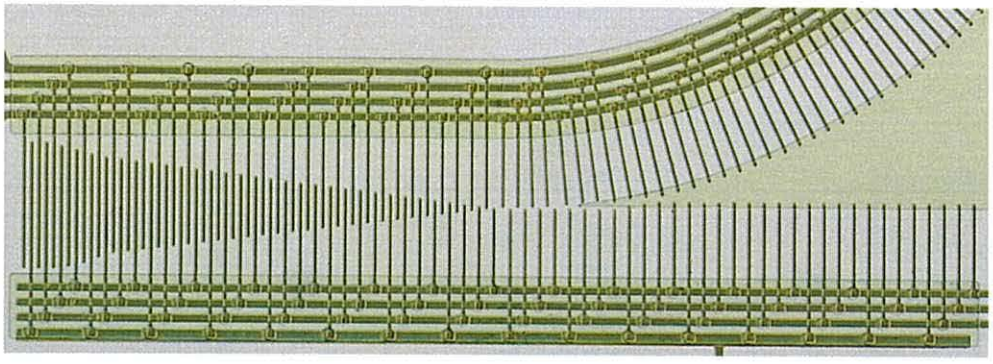

Figure 4.4 *Two travelling waves combining into one [7].*

In Figure 4.4 none of the electrodes are inter-connected using bus bars on the lower layer, but instead all individual electrodes are connected through via-holes to one of four bus bars. When every electrode is connected using via-holes the current path to each electrode is identical. Whilst it is possible to connect one phase of the travelling wave array together on the lowest level, the resistance of a direct connection can be significantly different to that of a via-hole. Therefore, the electric field generated by this

electrode set would be of a different magnitude to the other electrodes creating a distorted travelling wave.

When all the connections to the travelling wave array are made on one side of the channel there is less room for making each connection and the via-holes must be smaller in size. The reduced size of the via-holes, illustrated in Figure 4.5, makes alignment of the different layers in the device more difficult. There is also a greater chance that a small via-hole in the polyimide insulating layer will not be completely cleared during the exposure and development process, thus resulting in a poor electrical connection.

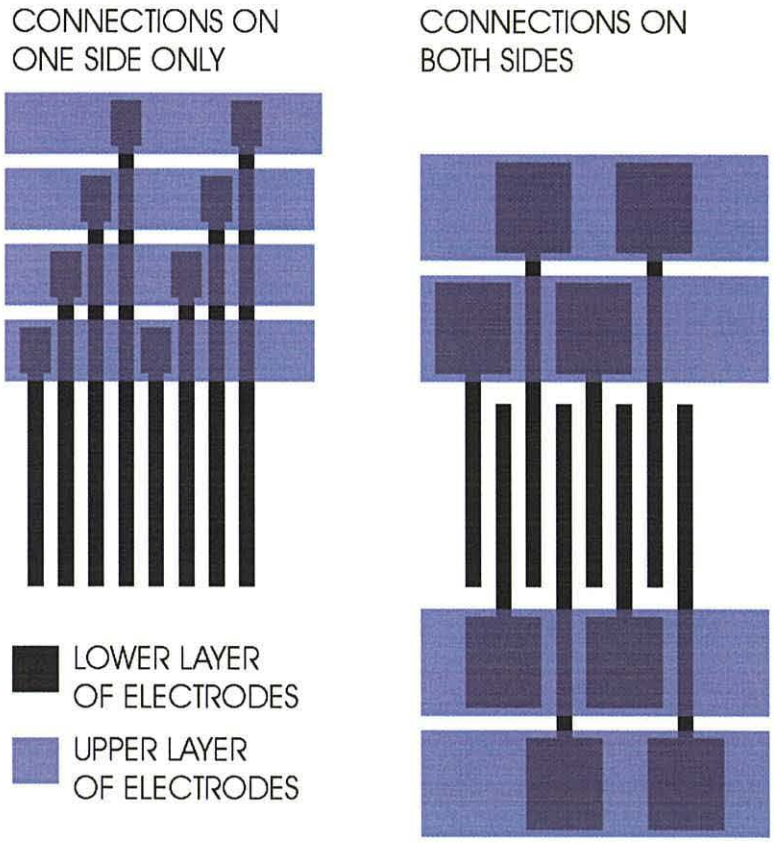

Figure 4.5 *Two travelling wave arrays, one with connections on both sides and one with them only on one, illustrating the difference in the size of the via-holes.*

A disadvantage of this fabrication approach is that the upper layer of gold must run over the edge of the polyimide insulator to make contact with the gold on the lower layer. The height of the polyimide insulating layer is of the order of 1μm. This is much greater than the thickness of the gold layer, which is 70nm in this work. The difference between the height of these two layers indicates that the upper gold layer must run a relatively long distance down the side of the via-hole. The main defect that occurs in the

fabrication of these devices are open circuits between the upper and lower gold layers. These open circuits are due either to breaks in the evaporated gold caused by poor metalisation of the via-hole wall or to the presence of polyimide residues at the bottom of the via-hole that form a thin insulating layer between the two gold films.

The layer of gold and chrome that forms the upper set of electrodes is evaporated onto the device perpendicular to the substrate. As illustrated in Figure 4.6A, if there is a slight overhang on the wall of the via-hole then a shadow will be created where no gold is deposited. This break in the gold between the top and bottom of the via-hole will result in an open circuit.

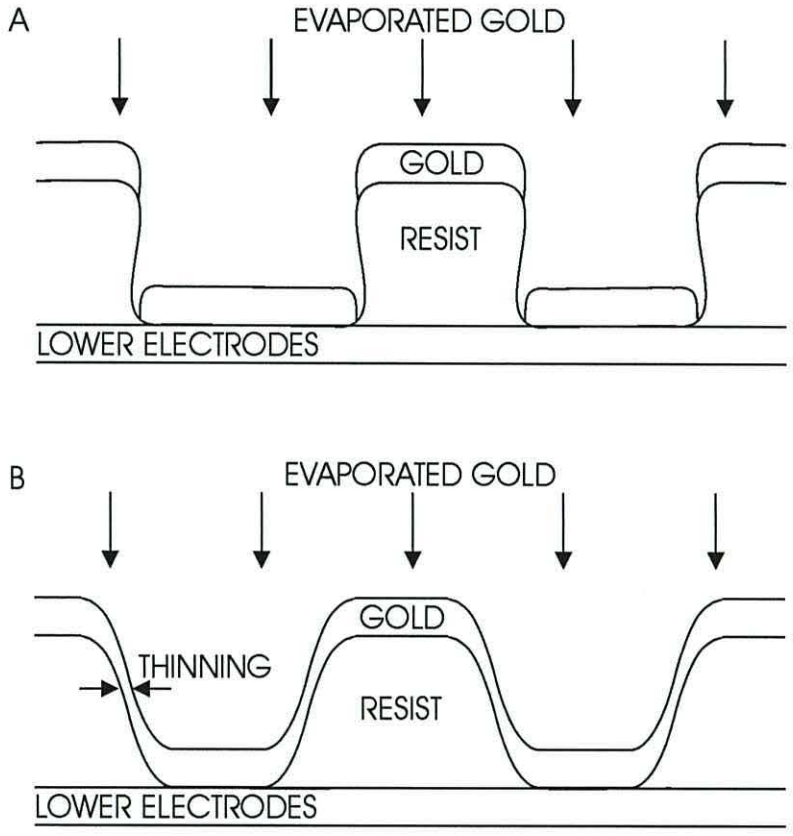

Figure 4.6 *Deposition of gold onto an uneven surface using thermal evaporation.*

The height of gold deposited over the device is uniform when measured perpendicular to the substrate. Figure 4.6B illustrates that if the walls of the via-hole are close to vertical, the gold coating will be thin despite the vertical height of the evaporated gold remaining constant. This thin coating will have a high electrical resistance and be more

susceptible to mechanical damage [7,8]. An alternative to thermally evaporating the upper layer of gold is deposition by sputtering [8,9] as illustrated in Figure 4.7.

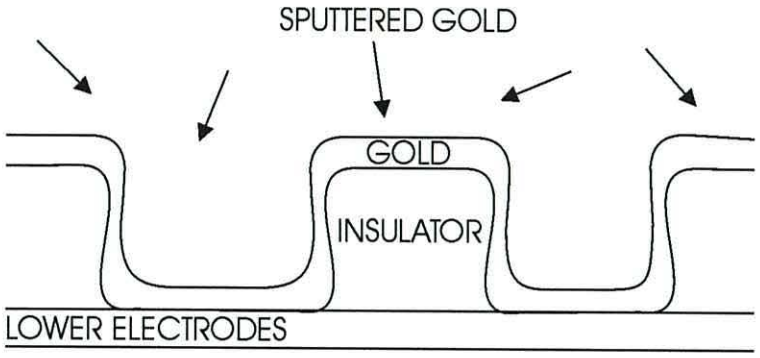

Figure 4.7 *Deposition of gold onto an uneven surface using sputtering.*

When using a sputterer the gold atoms arrive at the substrate from a wide range of different angles resulting in a better coating on the vertical sides of the via-holes. A disadvantage of using the sputtering approach is the need for a large, high purity gold target resulting in a large initial expense. The sputtering process is also slow in comparison to evaporation.

A poor connection to the electrodes can be caused by contamination of the surface of the gold at the bottom of the via-hole. These contaminants usually occur when the polyimide layer is not completely developed during the manufacturing process, leaving an insulating film at the bottom of the via-hole. This problem can be minimised by sufficient agitation of the developer solution and device after exposure to ensure that it flows into the bottom of each of the via-holes.

The via-hole faults typically effect only a few of the electrodes per device causing them either not to be connected or have connections with a high electrical resistance. Such faults are difficult to detect during manufacture, with problems only becoming apparent when the device is used, as particles do not progress uniformly along the travelling wave array.

4.3 Travelling wave arrays without via-holes

The limitations of via-hole interconnections demonstrate that it is desirable to eliminate them from the fabrication of travelling wave arrays. Using a novel electrode design this was achieved by fabricating adjacent electrodes on separate layers. In this new design, two gold films at different heights were maintained across the device. Each film incorporated the field producing electrodes, their interconnections and the external interfaces to the device. Figure 4.8 illustrates the arrangement of the electrodes. The diagram has been expanded in the vertical (z) direction to allow illustration of the thin films and wide aspect ratios used in the fabrication, the height of the gold was 70nm compared to the width of the electrodes at 10μm. The difference in height between adjacent electrodes was minimal when compared to the width of the electrodes.

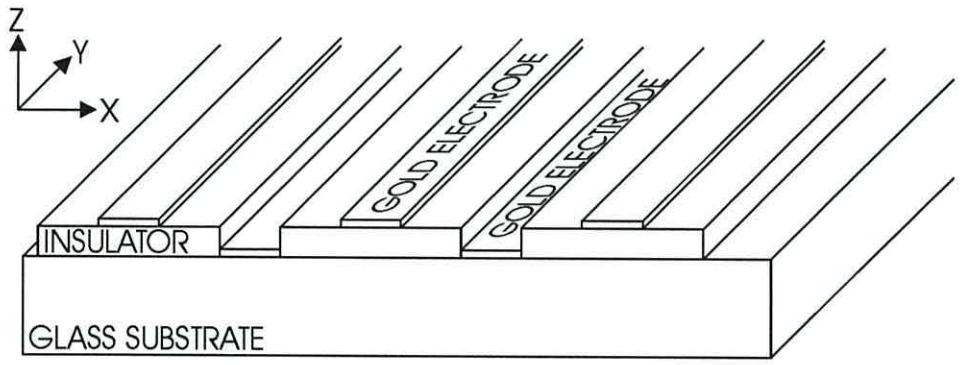

Figure 4.8 *Arrangement of the electrodes in the travelling wave array that does not use via-holes in its fabrication.*

When using the fabrication techniques described in Section 4.2 to produce a travelling wave track, the electrodes are all formed in the same layer. However, a small difference of the order of 1 to 2 μm in the height of adjacent electrodes will not significantly affect the electric field measured a comparatively long way from the electrodes. When a travelling wave array is used to move particles their levitation height above the electrodes is typically in excess of 10μm. At this distance, changes in the height of the individual electrodes of 1 to 2μm will not significantly change the field surrounding the particle.

4.3.1 Computer simulation of travelling wave electrodes

To find the extent of any change in the electric field magnitude between the different types of travelling wave dielectrophoresis (TWD) array, a finite element simulation package, FEMLAB (Comsol Ltd. Sweden) was used to model the two electrode designs. In practical use, the electric fields applied to the electrodes are constantly varying. A series of sinusoidal waveforms are applied to the electrodes, where, for a 4-phase system each electrode is 90^0 out of phase with the previous. The TWD force on a particle is related to the imaginary component of the induced dipole moment on the particle and a time dependent evaluation of the field over the electrodes is required for a full analysis if the particle behaviour [1,10]. However in this work it is only necessary to compare the TWD array developed here with those already in use. To achieve this the field over the electrodes is modelled at discrete instants in time. The simulation of the electrodes was repeated four times corresponding to successive instants in time. The phases of the first electrode at the four times are 0^0, 45^0, 90^0 and 135^0, the corresponding voltages applied to each electrode are shown in Table 4.1.

Phase of the First Electrode	**Potential of Electrode (Volts)**			
	First	**Second**	**Third**	**Fourth**
0^0	0	1	0	-1
45^0	0.7	0.7	-0.7	-0.7
90^0	1	0	-1	0
135^0	0.7	-0.7	-0.7	0.7

Table 4.1 *Potentials of the electrodes in the series of simulations to compare the field above different electrode geometries, as shown in Figure 4.9.*

Figure 4.9 illustrates the magnitude of the electric field generated by a flat travelling wave array in the left hand column. Whilst the right hand column shows the field generated when the electrodes alternate between two levels 1μm apart. The electric field plots shown are a section from the centre of a longer simulation. Neumann (symmetry) boundaries were used at the edges of the simulation area with the electrodes defined as Dirichlet (fixed voltage) boundaries.

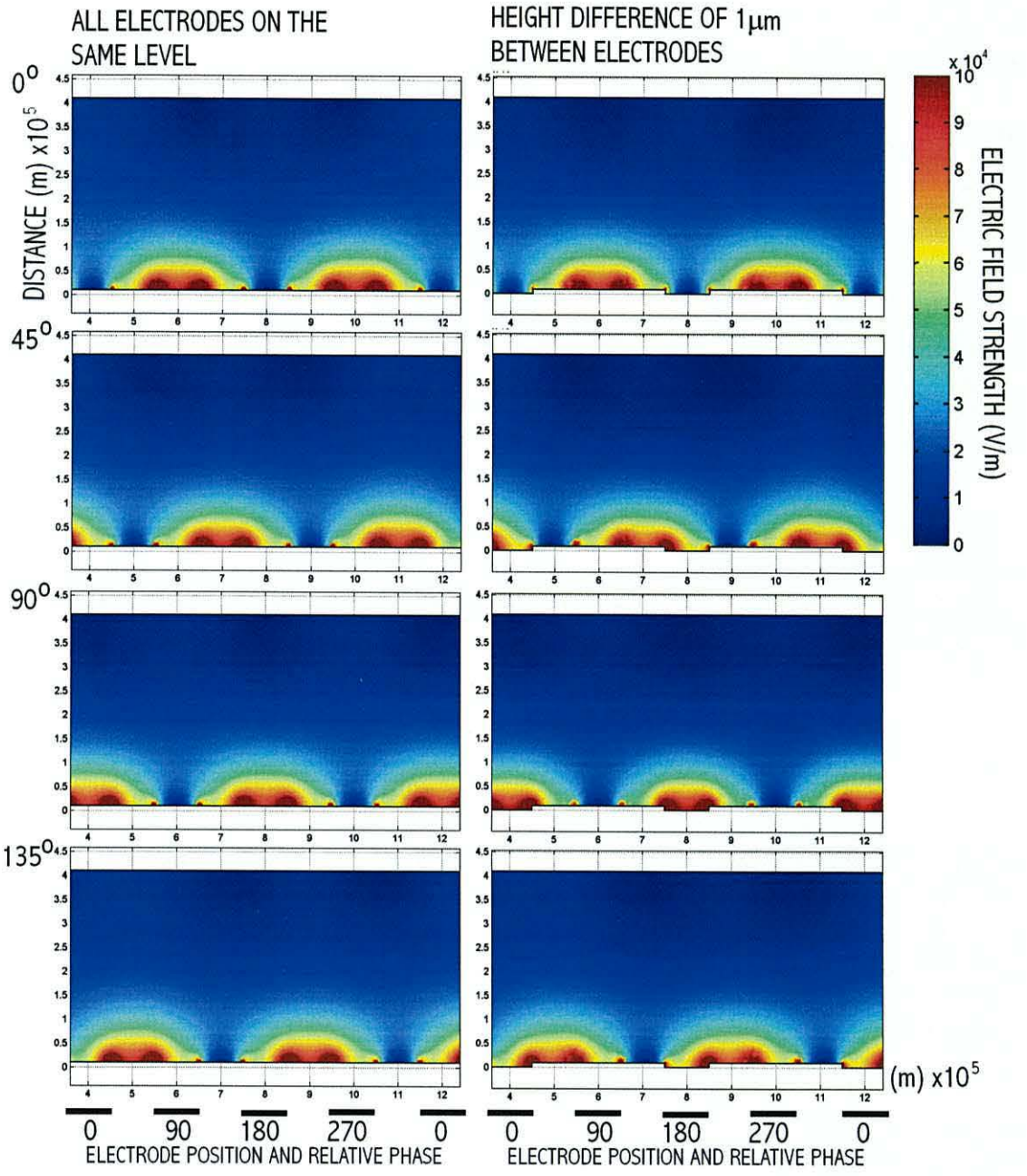

Figure 4.9 *Simulation of the electric field above travelling wave arrays. In the left hand column all the electrodes are on the same level, whilst in the right hand column there is a 1μm height difference between electrodes. The four rows correspond to successive instants in time with the corresponding phase of the sinusoidal waveform in the first electrode shown to the left.*

A slight change in the pattern of the electric field can be seen when comparing the two simulations in Figure 4.9. To provide a more quantitive representation of the change in the electric field a series of curves shown in Figure 4.10, were plotted showing the electric field at different heights above the electrodes. The heights above the electrodes used were 10μm, 20μm and 30μm.

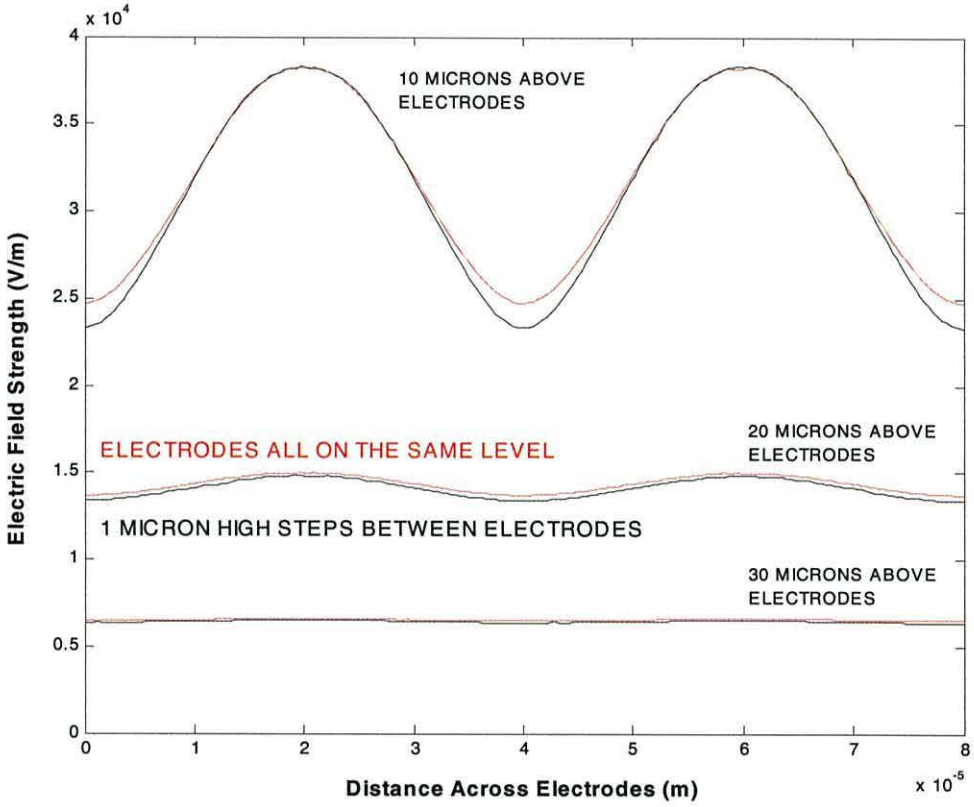

Figure 4.10 *Magnitudes of the electric field strengths at different heights above the electrodes taken from the simulation results shown in Figure 4.9.*

From Figure 4.10 it can be seen that the electric field strength above the electrodes fabricated on two levels is at most 5% lower than the case where all the electrodes are on the same level. Although there is a slight difference in the magnitude of the field the general shape is the same for both electrode arrangements. As the field strength decreases with height, the difference between the fields for the two arrangements also decreases. It is possible to largely remove this error by increasing the applied voltage to the electrode array fabricated on two levels.

4.3.2 Design of the electrodes

Figure 4.11 is an exploded view of the layers used in the manufacture of these devices. The polymer layer that separates the two sets of electrodes continues under the gold to a connection area, this eliminates all the steps in the gold that can result in open circuits. To minimise the capacitance between sets of electrodes, the areas where there are gold tracks on both sides of the polymer insulator are made as small as possible. The effect of this capacitance on the operation of the electrodes is explained in Section 4.3.4.

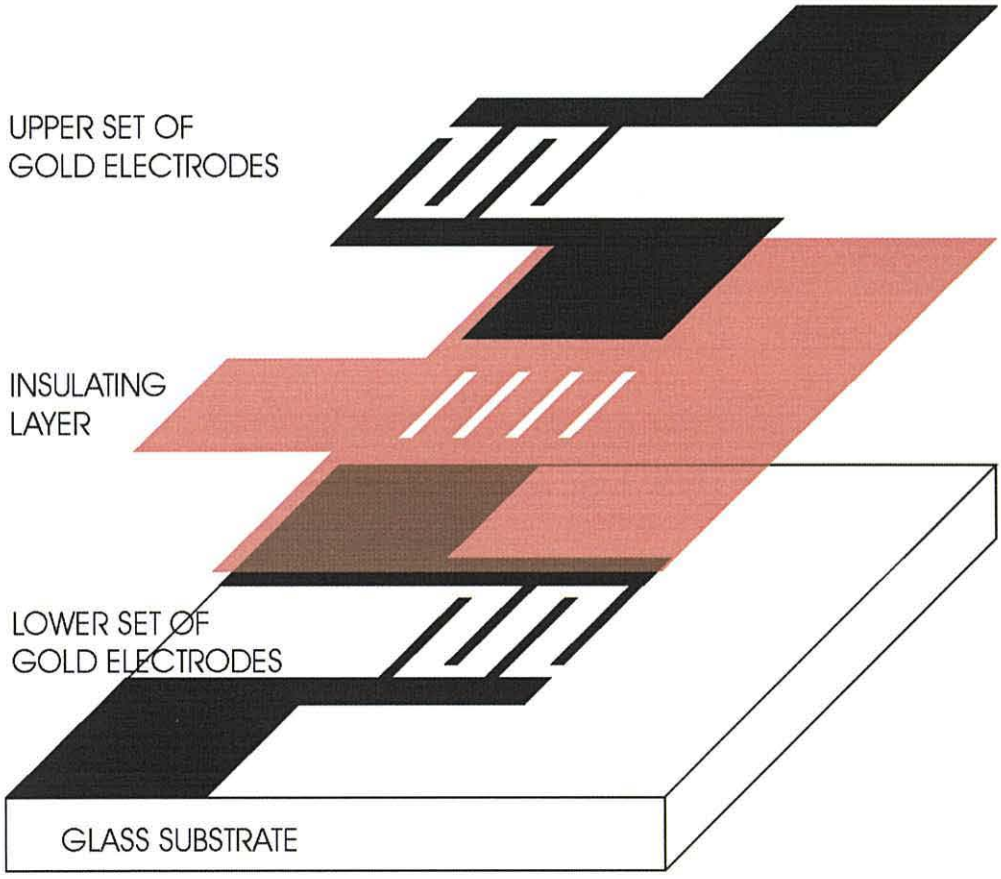

Figure 4.11 *Exploded view of the electrode layers making up a travelling wave array that does not use via-holes in its fabrication.*

4.3.3 Manufacturing process

To produce the travelling wave track, the lower set of electrodes were first produced in a 70nm evaporated layer of gold on a borosilicate float glass substrate, using 'print and

etch' UV photolithography as described in Section 3.5. The photo resist was exposed via a mask similar to that shown in Figure 4.12.

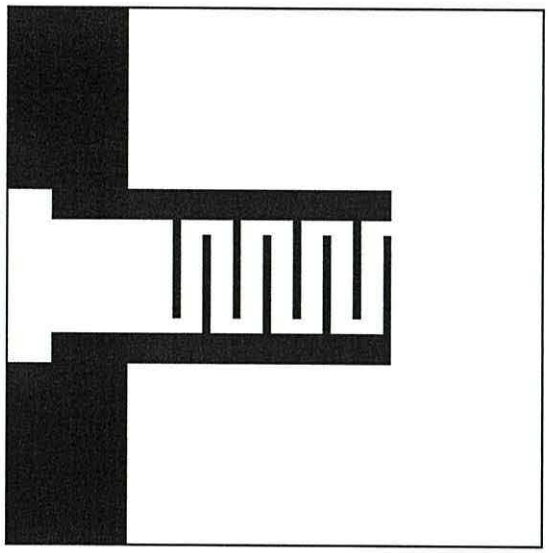

Figure 4.12 *Mask pattern used in the fabrication of the lower set of gold electrodes that make up part of a travelling wave array.*

The substrate was then coated in a layer of Duramide, a photo sensitive polyimide, which was exposed and developed to reveal the electrode fingers and the connections to the device using the process described in Section 3.7.

It can be seen from Figure 4.8 that the Duramide patterned steps must align accurately with the lower set of electrodes. Rather than use complex mask alignment techniques, accurate alignment was automatically achieved by exposing the Duramide through the underside glass substrate, causing the solid electrodes to form a mask. This process is illustrated in Figure 4.13, as Duramide is a negative photo resist, areas between the electrodes remained after development.

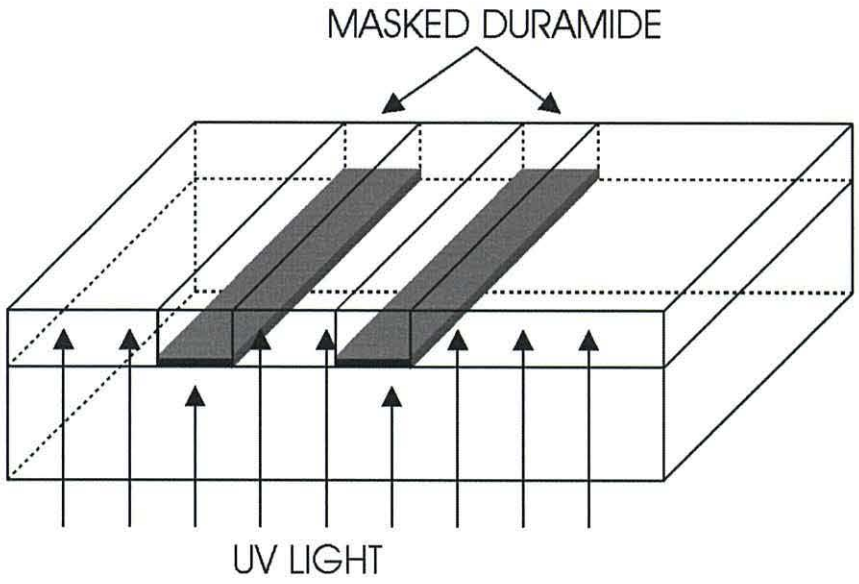

Figure 4.13 *Exposure of the Duramide insulating layer from below using the electrodes as a self aligning mask.*

Whilst exposing through the gaps in the electrodes ensured accurate alignment, it did not allow the Duramide covering the electrode connection bus bars to be exposed. To overcome this a second exposure stage from above was employed. A photomask was used to cover both the centre of the travelling wave track and the external interface connections where exposed gold would be required (Figure 4.14). Positioning of the channel above the electrode does not require a high degree of accuracy, therefore the alignment of the mask is not critical.

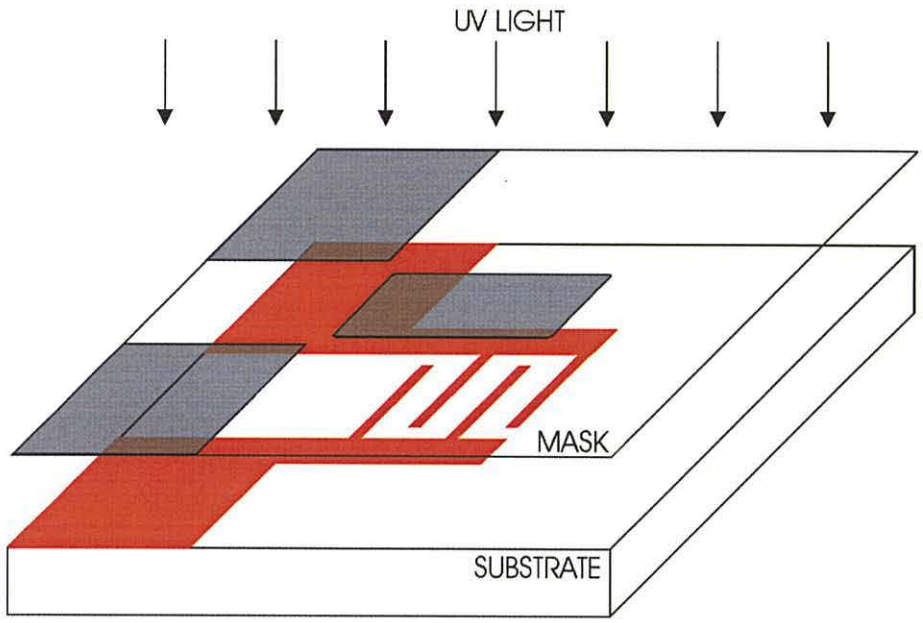

Figure 4.14 *Exposure of the Duramide from above to reveal the external interface contacts and the electrodes in the channel after development.*

The Duramide was developed as described in section 3.7. Figure 4.15 shows the areas of Duramide that remain after developing.

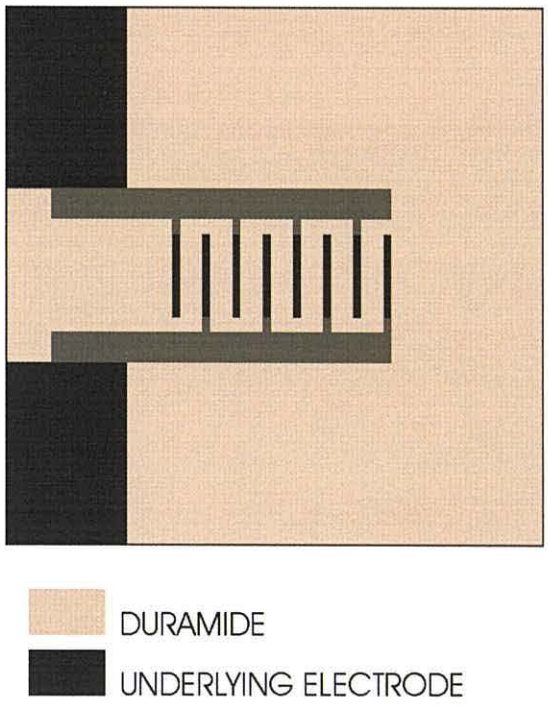

Figure 4.15 *Pattern in the developed Duramide layer.*

To gain an accurate representation of the surface of the Duramide film an atomic force microscope (AFM) image was produced as shown in Figure 4.16. When an AFM is used to generate an image the shape of the tip prevents accurate reproduction of vertical structures.

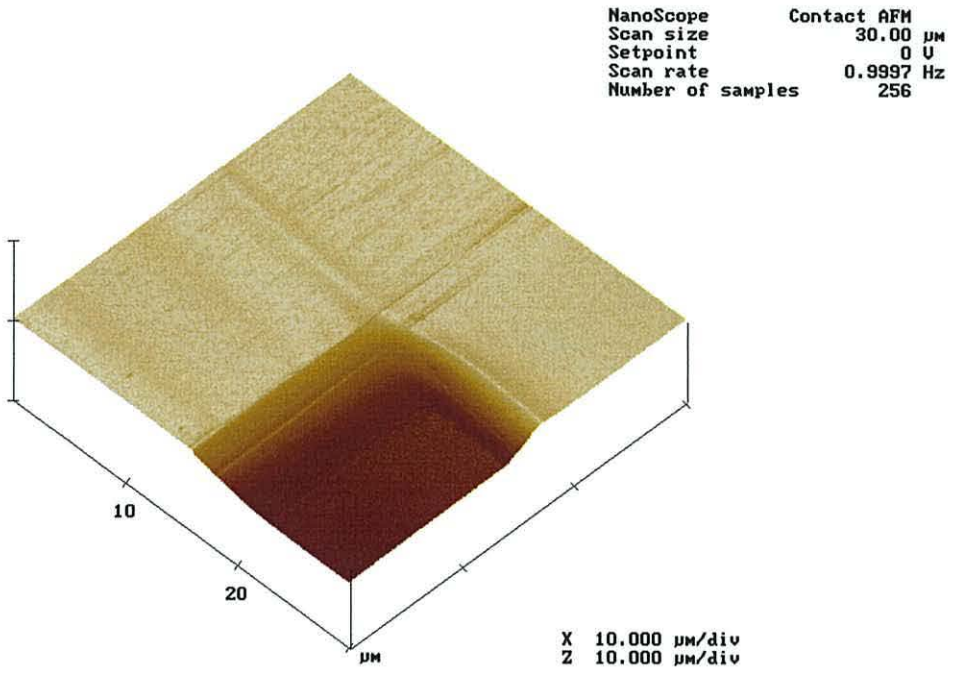

Figure 4.16 *Atomic force microscope image of a Duramide layer.*

In Figure 4.16 the electrode under the Duramide runs adjacent to the lower left hand side of the image. The parallel lines running from the lower left to upper right of the image correspond to the path taken by the AFP tip and are not features of the material surface.

It can be observed from Figure 4.16 that the step formed in the Duramide above the electrode is much steeper than that formed at the edge of the electrodes. This could be due to over exposure of the Duramide caused by reflection of the UV light from the gold surface.

At this stage in the fabrication, areas of gold forming the lower set of electrodes are exposed. Therefore, it is not possible to fabricate the second set of electrodes using the 'print and etch' approach that was used for the first layer of electrodes, as the lower electrodes would be etched away when the upper set is defined. To overcome this

problem the electrodes were patterned in a 70nm layer of gold using a 'lift off' fabrication method as described in Section 3.6.

When using 'lift off' resists to fabricate electrode structures, the resist is removed in the areas where the gold tracks are required. This is in contrast to the 'print and etch' approach used for the lower layer. In this research a positive resist S1818 was used in the 'print and etch' process. However, as described in Chapter 2 'print and etch' is normally carried out using a negative resist. If a negative resist is used in the production of the lower set of electrodes, the same mask could be used for both the lower and upper electrodes. For straight TWD arrays, rotation of the electrode pattern allows external interface connections to be formed on the other side of the device (Figure 4.17). To produce curved TWD tracks, two different masks are still required, as the channel does not possess rotational symmetry.

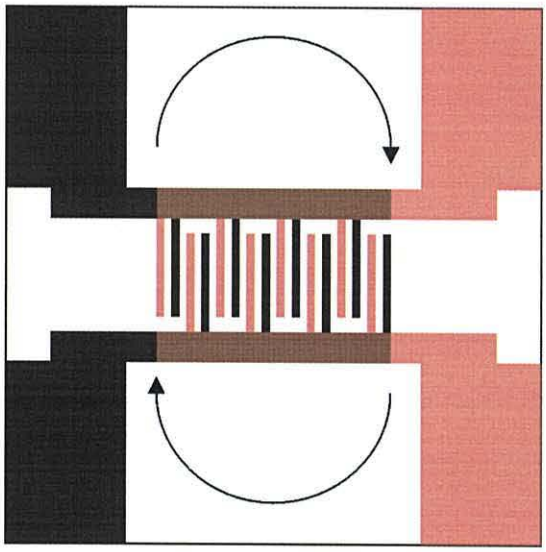

Figure 4.17 *Rotation of the mask.*

Due to the presence of the Duramide insulating layer it was not possible to clean the substrate very thoroughly before the next fabrication step. Instead, the device was placed in an ultrasonic bath in a 1% solution of Decon 90 for 1 minute to remove surface contaminants and then rinsed in ultra pure water (UPW). Exposure to prolonged ultrasonic agitation was found to cause the Duramide to lift from the glass substrate. Additionally, chromic acid was found to vigorously attack the Duramide layer. A photograph of the finished device is shown in Figure 4.18.

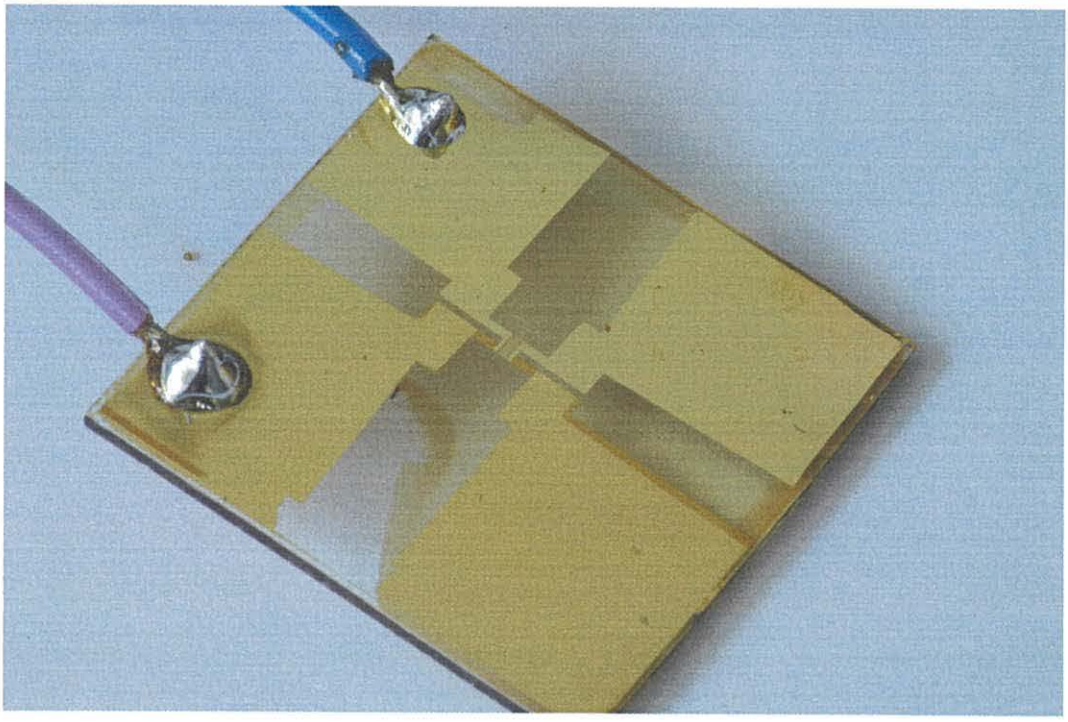

Figure 4.18 *Travelling wave electrodes fabricated without the use of via-holes.*

4.3.4 Device testing

For this manufacturing technique to be useful, devices developed in this way must perform as well as or better than devices fabricated using via-holes. As mentioned in Section 4.2 open circuits in the gold can occur around the lip of a via-hole. When electrodes are fabricated using the approach described in Section 4.2.1 both the upper and lower layers of gold are flat with no steps, so eliminating this problem. The external contact pads to the upper set of electrodes are on top of a layer of polymer. If the melting point of this polymer is less than the temperature reached by the electrodes when contacts are soldered to the device, the connection could be difficult. However, Duramide has a high melting point in excess of 350°C once fully baked and no problems were encountered when soldering to the device at a typical soldering temperature of 250°C.

When using a travelling wave array to move particles such as biological cells, the speed of travel depends on the magnitude of the applied field, as well as its frequency [1]. To take quantitative measurements of particle properties, it is necessary to know the strength of the field above the electrodes. The amplitudes of the quadrature sinusoidal

signals applied to the device were typically measured at the output of the signal generator. However, electrical losses occur within the electrical circuit leading to the electrodes. The electrical wires that run from the signal generator to the device have an inherent resistance and inductance. If the wires are kept short the inductance can be reduced to a negligible amount. The gold tracks on the device running from the contacts to the electrodes have a resistance, which can be minimised by making the tracks as wide as possible. It is also possible to reduce the resistance of these tracks by increasing their thickness, by either evaporating a thicker layer of gold or electro plating additional metal.

In multi-layer devices such as the one described, there is a capacitance between the layers where they overlap, as well as a capacitance between adjacent tracks. However, this is comparatively small because the distance between adjacent tracks is much greater than that between overlapping tracks. The capacitance between two planar electrodes is proportional to their area and the relative permittivity of the material between them (relative permittivity of polyimide = 3.4)[11]. The area where different layers overlap should be minimised to reduce the capacitance. As capacitance is inversely proportional to the distance between two electrodes, capacitance is only likely to be a problem where electrodes are close together. However, when the device is in use the total impedance between adjacent tracks must be considered. In this situation, the impedance is affected by the conductivity and permittivity of the suspending medium. Figure 4.19 illustrates the equivalent circuit for the electrodes described in this chapter.

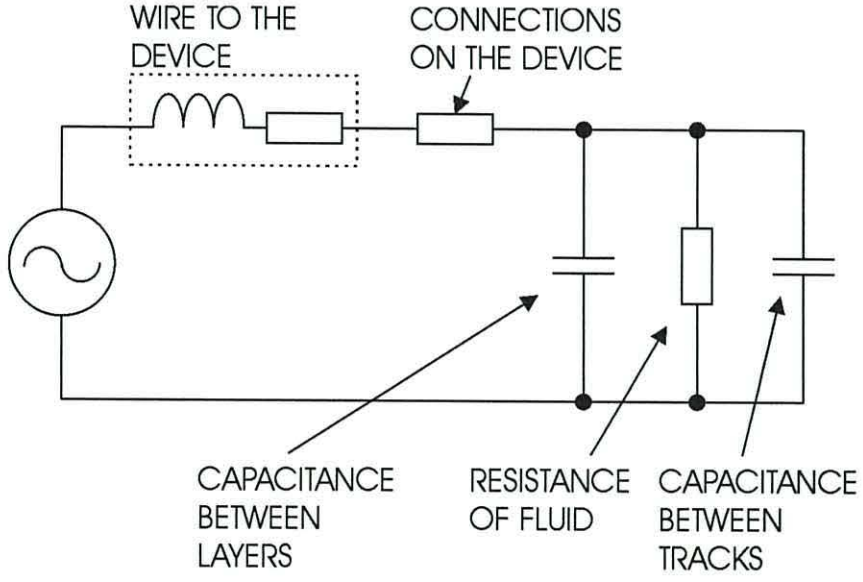

Figure 4.19 *Electronic circuit representation of a travelling wave electrode array and its connection to a voltage source.*

This circuit can be simplified to that illustrated in Figure 4.20. The tracks on the device and the wire to the device are in series and have been combined into one resistance. When comparing the combined resistance, the effect of the inductance in the wire is small justifying its removal from the equivalent circuit. The connection resistance to the device and the two capacitances in series with the resistance between the electrodes form a potential divider. As the reactance of the capacitors varies with frequency, the amplitude of the voltage at the electrodes will also vary with frequency. The extent to which this affects the performance of the device depends on the values of the resistances and the capacitance.

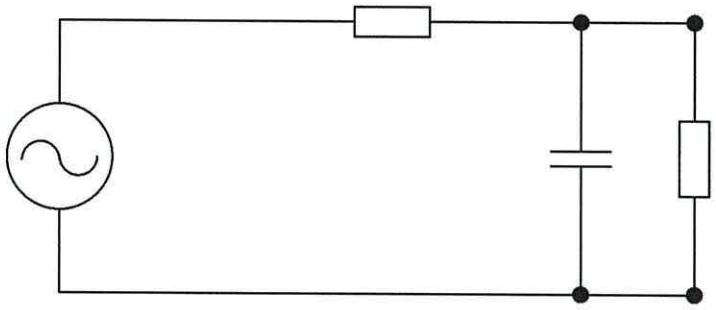

Figure 4.20 *Simplified version of the circuit diagram shown in Figure 4.19.*

The capacitance caused by the overlapping of the tracks on the two layers is independent of the properties of the fluid over the electrodes. The capacitance between adjacent electrodes depends on the permittivity of the fluid between them and the formation of the electrical double layer at low frequencies. The capacitance of this double layer depends on the current density at the electrodes, as well as the concentration of ions in the solution. The effect of the double layer on the capacitive element shown in Figure 4.20 does not depend on the fabrication approach used to produce the electrodes. A result of the fabrication approach described is that the two gold layers overlap more than was the case for travelling wave electrodes formed using via-holes. The capacitance caused by this overlap was measured with no fluid over the electrodes using an A4192A impedance analyser (Hewlett Packard, US) and is illustrated in Figure 4.21.

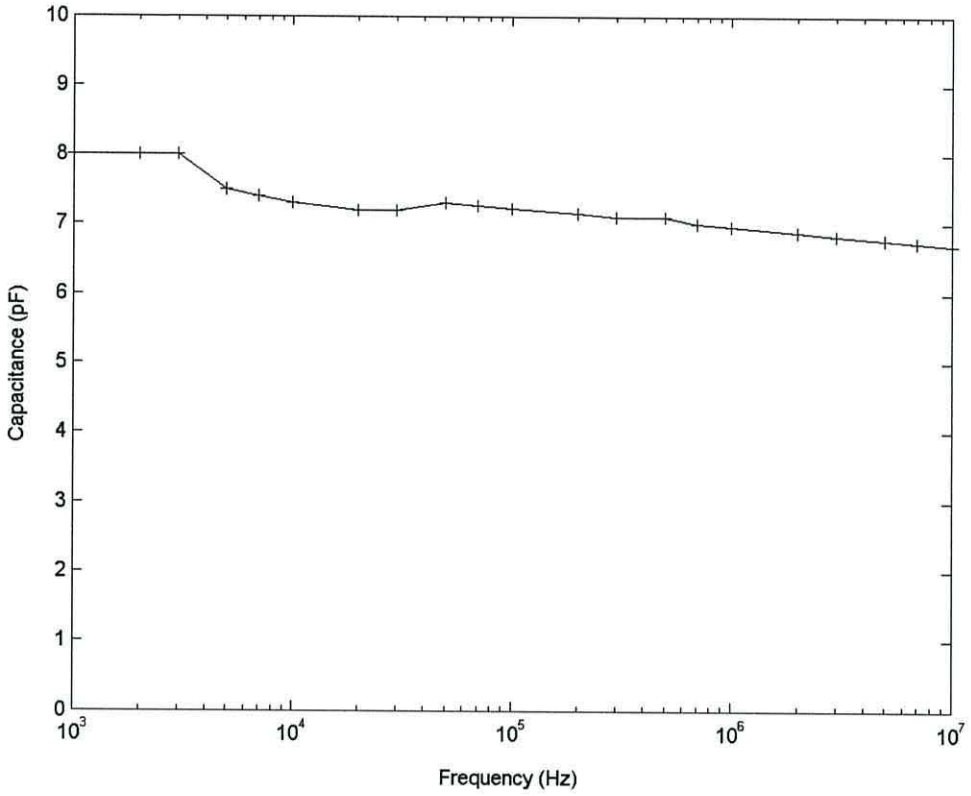

Figure 4.21 The capacitance between adjacent electrodes at different frequencies for a travelling wave electrode array fabricated without the use of via-holes.

The capacitance due to the physical structure of the travelling wave array remains reasonably constant at around 7pF over a wide range of frequencies. This small capacitance will not noticeably affect the potential measured at the electrodes as the frequency is increased. The capacitance measured between the same electrodes covered in UPW at an applied frequency of 100kHz was 230pF. The substantial difference between these values indicates that the maximum frequency that the travelling wave array can operate at is not limited by this fabrication approach.

To further test the operation of the travelling wave array 5μm latex beads in a buffer of conductivity $50\mu Scm^{-2}$ were used. The results obtained were the same as those obtained when using a travelling wave electrode array fabricated using via-holes to connect between layers.

4.4 Channel structures for use in lab-on-a-chip devices

In the remainder of this chapter a range of different fabrication processes are described for the manufacture of channel structures. The aim of this was the production of low cost structures using simple fabrication processes and materials.

Fluidic channel systems play an essential role in lab-on-a-chip devices. Primarily they act as a means for constraining and transporting a sample to desired regions of a device. In the case of TWD systems this is over the electrode arrays. Additionally, the channel structures can play an active role in other electrokinetic transport processes, such as electroosmosis [12] where the movement of charges adjacent to the channel wall cause the fluid to flow as described in Section 2.4.2.

4.4.1 Requirements for channel structures

When fabricating a fluidic channel to contain a suspension of particles or a fluid, it is necessary that the channel structure is compatible with the equipment with which it is to be used. When carrying out an experiment, particles within the device are typically observed using an optical microscope. At high magnifications the distance between the objective lens of a commercial microscope and the sample is small, of the order 1-2mm. Using an objective lens of lower magnification can increase the distance between a channel and the objective lens, but this reduces the amount of detail that can be observed. As a result of this short distance, a channel must be close enough to the upper surface of the device to allow the microscope to focus on any particles it contains. If the device is to be illuminated from below and viewed using a microscope, both the upper and lower surfaces of the device must be transparent. Any electrodes contained within the device must have exposed areas to connect to an external signal generator.

Containing the particle suspension in a transparent chamber over the array satisfies these requirements. In an approach previously used in this laboratory to produce chambers for carrying out dielectric measurements, the walls of the chamber are formed from a section of PVC electrical insulating tape. The lid to the channel consists of a microscope cover glass placed on top of the tape and held in place by surface tension.

This approach is limited to systems where there is no flow across the device, as the lid is lifted off by the pressure required to generate a fluid flow. To produce devices that operate under pressure, the cover slip is glued in place using silicone rubber. To clean such a device, the silicone rubber is pealed off and the cover slip removed. Using such structures it is difficult to produce high resolution, complex channel geometries. An alternative method which has been used is the formation of channel structures in transparent elestomer PDMS [13] as described in section 2.3.3. This approach formed good quality temporary channel structure. However, in practice the quality of permanent bonds made between the PDMS and substrate was highly dependent on environmental conditions.

4.5 Photolithographically patterned laminate channel

The device described in this section was fabricated using photolithographic techniques to increase the level of complexity and resolution possible. In summary, the channels are fabricated on a glass substrate onto which electrodes had been formed in a 70nm layer of gold using the photolithographic processes described in Chapter 3. Channel walls of a suitable depth were optically patterned in a layer of Ozatec 5038 dry film laminate (Ozatec, UK) as described in Section 3.7. To form a sealed channel, a glass lid was attached to the device using Locktite 358 UV curing adhesive (Locktite, UK). A diagram of the finished device is shown in Figure 4.22.

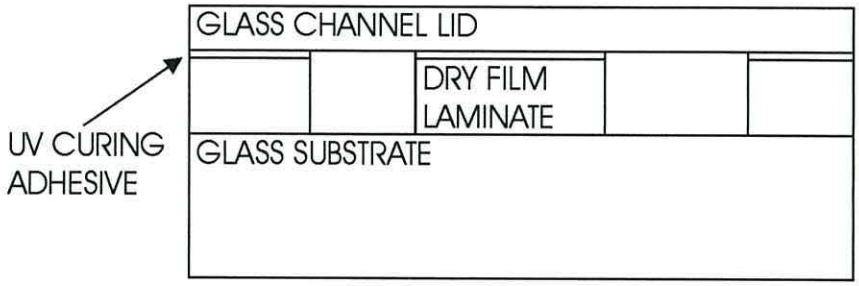

Figure 4.22 *Channel structure formed from dry film laminate with a lid attached using UV curing adhesive.*

The lid was spin coated over its entire surface with a layer of UV curing adhesive and placed on top of the channel structure. At this stage the channel became partially blocked with the liquid adhesive. To cure only the adhesive in contact with the laminate, the adhesive was selectively exposed to UV light using a photo mask. The required pattern of cured adhesive was the same as the pattern formed in the laminate and therefore the same mask was used for both exposures. The adhesive in the channel, being masked from the UV light, remained liquid and was removed by flushing through with acetone. The complete removal of the adhesive from the channel allowed unobstructed optical observations of particles within the channel to be made.

4.5.1 Manufacturing process

The electrodes to be contained within the channel were fabricated, using standard 'print and etch' photolithography on a borosilicate float glass substrate, as described in Section 3.5. Additional cleaning before the laminate was applied was not necessary as the substrate had been thoroughly cleaned and rinsed during the fabrication of the electrodes. Ozatec 5038 dry film laminate resist was applied to the surface of the slide and the channel structure formed using the process described in Section 3.7. The laminate was exposed to UV light via a light field photo mask similar to that shown in Figure 4.23.

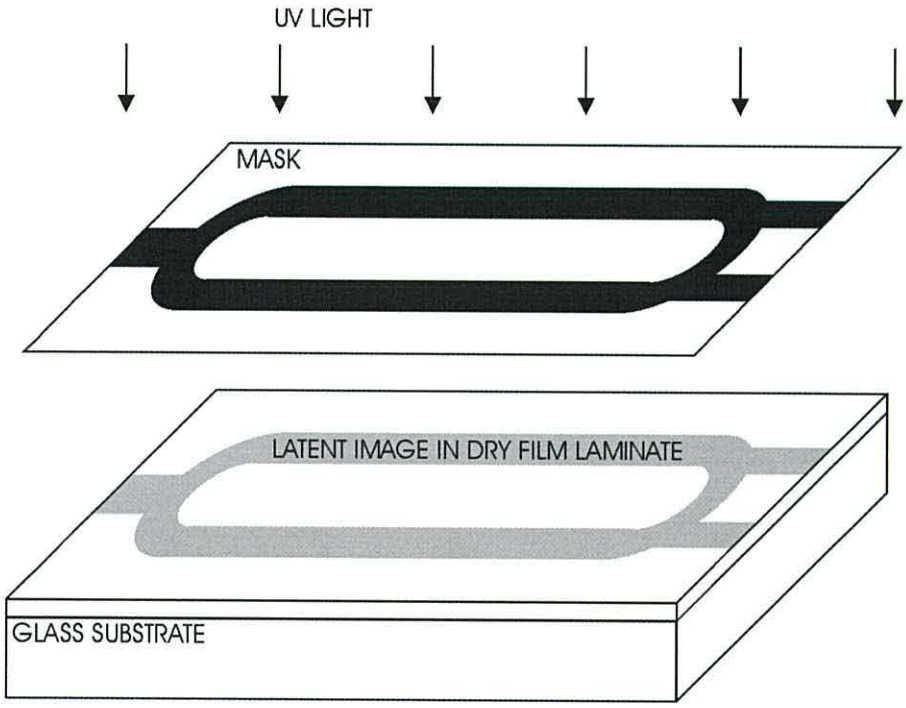

Figure 4.23 *Exposure of laminate using a photo mask.*

Figure 4.24 shows the structure of the device after development. The top surface of the laminate is slightly uneven due to the texture of the laminating roller. To form a watertight channel it is necessary to form a good seal between this uneven surface and the glass lid of the channel.

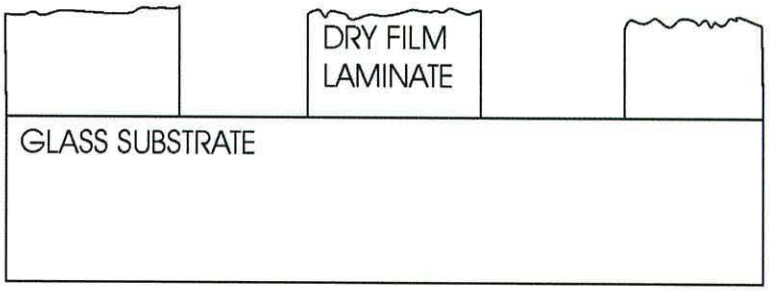

Figure 4.24 *The channel structure after development showing the uneven surface of the laminate.*

The glass slide used to form the lid of the channel was washed in a 1% solution of Decon 90, rinsed using UPW and dried under hot air. As with the base of the device, the slide was given a dehydration bake at 200°c for 5 minutes to remove any remaining

moisture. Once cool, a thick layer of UV setting glue was spin coated at 500 rpm for 30 seconds onto the glass lid. The thick layer of adhesive was used to fill the imperfections in the uneven surface of the laminate. The lid was then placed on top of the laminate and allowed to settle into position. Although the layer of adhesive was thick enough to fill the imperfections in the laminate, it was thin enough not to completely block the channel structure.

Initially, blanket exposure of the device was used to cure the adhesive. However, when the adhesive over the entire device was cured, the adhesive that remained in the channel restricted the size of the channel. Also, the uneven surface on the cured adhesive distorted the image of particles within the channel when viewed using a microscope. To eliminate this problem it was necessary to completely remove the adhesive from the channel. To cure only the adhesive outside the channel, the device was selectively exposed to UV light through a photo mask for 15 seconds at an energy density of $15mJcm^{-2}$, as illustrated in Figure 4.25. The mask was used to cover only the adhesive in the channel and so allowed it to remain liquid. The pattern of this mask is the same as that used during the exposure of the laminate, as can be seen by comparison of Figure 4.23 and Figure 4.25.

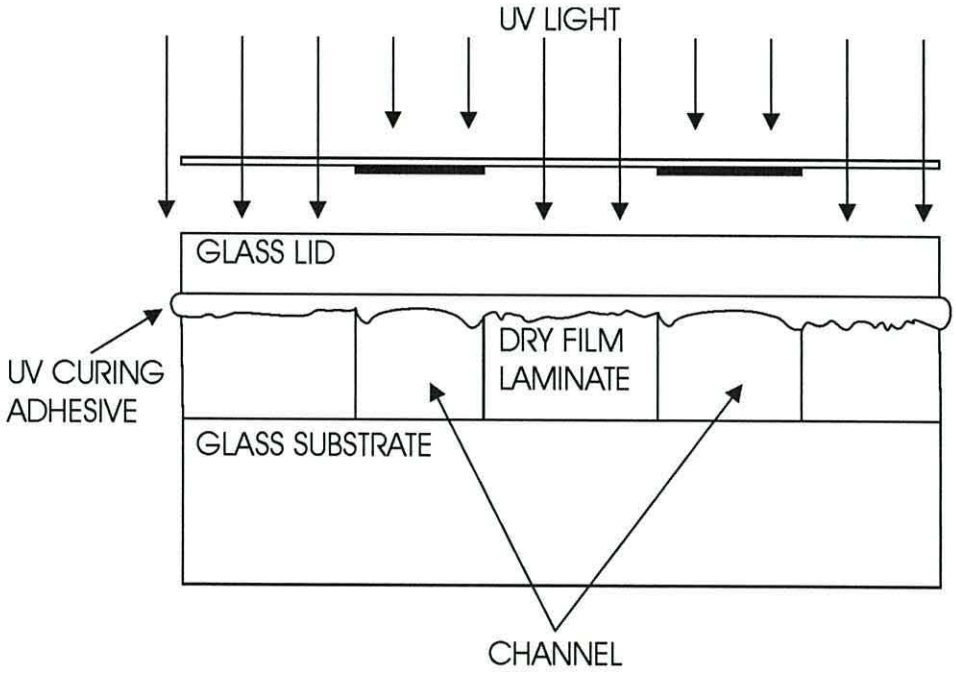

Figure 4.25 *Selective exposure of the UV curing adhesive outside the channel to attach the glass lid.*

The uncured glue in the channel was washed out using acetone to leave an optically clear channel. As the channel had not been completely blocked by adhesive the acetone could flow freely through the device. Whilst acetone did attack the cured adhesive, this process occurred very slowly taking several days to significantly damage the device. Figure 4.26 is a photograph of the completed channel. It can be seen from the photograph that the glass slide making up the lid is smaller than that used for the base, thus allowing electrical connections to be made.

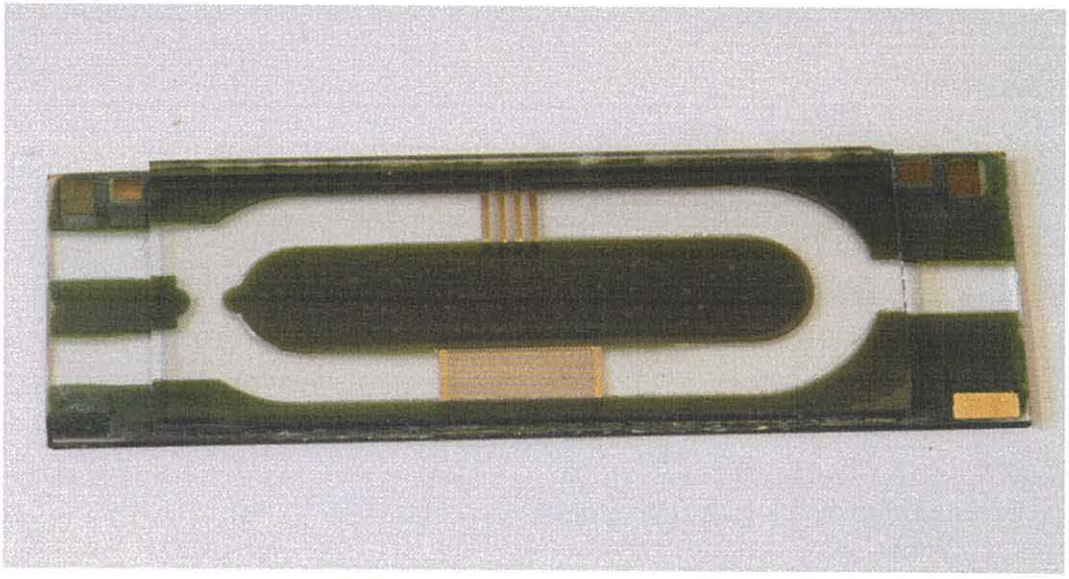

Figure 4.26 *Channel structure fabricated from dry film laminate with a lid attached using UV curing adhesive.*

4.5.2 Device testing

To test the structural strength of the device, water was passed through the channel using a syringe. For a wide aspect ratio channel 60μm high and 2mm wide flow rates in excess of $1 ml sec^{-1}$ could be achieved without damaging the channel. This flow rate is in excess of the flow rates induced during normal use, which are typically of the order of micro litres per second. However, when the device was filled with water for over 24 hours, the dry film laminate began to separate from the glass substrate. A separate device, which has not been in contact with water, has remained intact for over two years.

At this stage it is not clear what causes the laminate to separate from the substrate but it is possible that the laminate at the edge of the channel may absorb water causing it to expand. Once baked, the laminate is no longer flexible and expansion of the laminate at the edge of the channel could pull the nearby laminate away from the substrate. Swelling of resists is well documented for some organic solvents [8] and water may have a similar effect but at a lower magnitude.

4.6 Laser machining of channels

The dry film laminate used to fabricate the channel described in Section 4.5 is naturally adhesive. Once the laminate has been exposed and developed it looses its adhesive properties and will no longer easily adhere to other surfaces. If a channel can be fabricated using dry film laminate, without exposing it to the development chemicals, the upper surface of the laminate will remain adhesive. The natural adhesive properties of the laminate can then be used to attach a lid to the channel without the need for additional glues. The laminate is most flexible before it has been exposed or baked. By using the laminate to form the channel in its unbaked state, it is less likely to crack causing the channel structure to delaminate. However, a disadvantage of making the channel from unbaked laminate is that it is more likely to be damaged if solvents are passed through the channel.

Instead of using photolithography to pattern the laminate, an excimer laser (Exitech 8000 series Micromachining Workstation, Exitech Ltd, UK) was used to ablate the material in the channel. The laser is only focused on the area of the channel and therefore does not change the properties of the remaining laminate.

4.6.1 Manufacturing process

The glass substrate used to form the base of the channel was covered in a layer of dry film laminate using the process described in Section 3.8. When an excimer laser is used to machine a polymer, the ablated material is ejected in the form of a vapour and particulate debris, some of which settles around the machined area. The amount of

debris generated depends on the material being machined, the pulse repetition frequency of the laser and the energy of each laser pulse.

Each material has a unique ablation threshold, which the energy of the laser must exceed for the material to be machined. The ablation threshold for the dry film laminate used in this work is $350mJcm^{-2}$. As the energy of the laser is increased above the ablation threshold, the rate at which the material is removed is increased. The ablation threshold of glass is much higher than that of the dry film laminate. This difference in ablation thresholds allows the dry film laminate to be rapidly machined without causing any damage to the underlying glass substrate.

To produce a channel that was as optically clear as possible, it is necessary to minimise the amount of debris left in the channel when the laminate was machined. The ablation of a polymer using an excimer laser is achieved through a combination of shock waves breaking up the material and vaporisation. At low energies the removal of material is due mainly to vaporisation, resulting in a small amount of debris being produced for a given amount of material removed. As the energy of the laser is increased the amount of energy transferred to the material per pulse is increased, resulting in a greater shock wave effect. The fragmented material removed through the shock wave produces a greater amount of debris.

Through experimentation it was found that the debris was minimised when the laser was operated at a low energy and reasonably low repetition rate. To machine all the way through the laminate using these settings it was necessary to move the work piece at a slow feed rate. The energy used was $600mJcm^{-2}$ and the pulse repetition rate was 25Hz. These values are a compromise between producing a device with little debris in the channel and producing the device in a reasonable time.

Initially the laminate was machined with the protective coating, shown in Figure 3.2, removed to reduce the amount of material that had to be removed and therefore reducing the overall machining time. Using this approach, it was found that a large amount of debris was produced which was recast onto the surface of the laminate surrounding the channel. The coating of debris on the surface of the dry film laminate caused it to lose its adhesive properties, thus preventing the lid from being attached.

Debris from the dry film laminate deposited in the base of the machined channel could be removed by repeating the machining process, which can be easily achieved as the work piece is moved relative to the laser, using a precision computer controlled stage. However, debris on the surface of the laminate could not be removed in this way, as the laminate would be machined. To overcome this and to protect the surface of the laminate during machining, the channel was machined with the protective layer left in place. Once machined, the protective layer of plastic could be removed, along with the debris that had settled on it, to expose the adhesive surface of the laminate. The stages in machining the channel are shown in Figure 4.27.

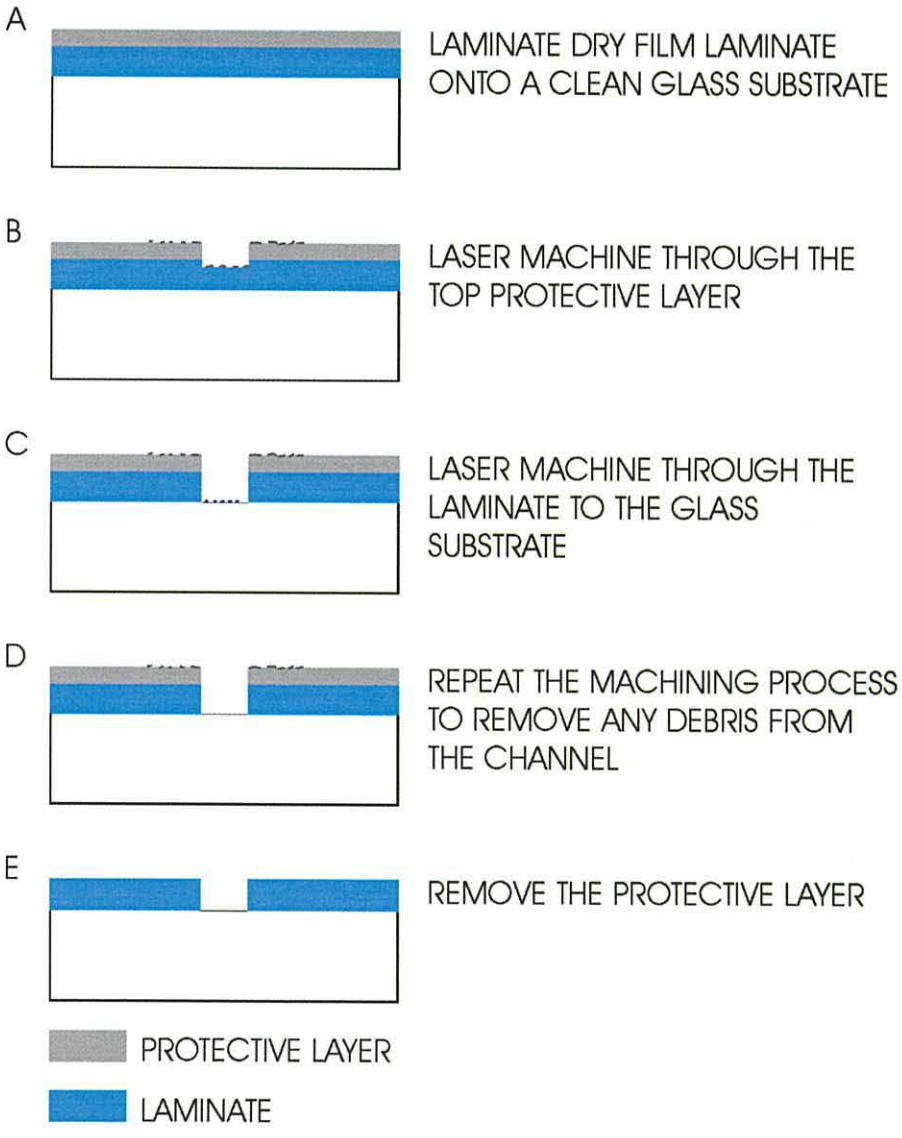

Figure 4.27 *Stages involved in laser machining a channel in dry film laminate.*

The channel structure in the laminate was machined in two stages. First, the protective layer was machined away to reveal the laminate (Figure 4.27B) and then the machining process was repeated to remove the laminate itself, along with any debris deposited in the partially formed channel (Figure 4.27C). As the laser progressed along the channel a small amount of debris was left behind on the freshly exposed glass substrate. To remove this debris the machining process was repeated a third time (Figure 4.26D). Machining the channel in a number of passes clearly takes longer than with a single pass. However, using a single pass to remove both the protective layer and the laminate caused excessive debris to be generated in the channel. Most of this debris results from the machining of the protective layer and unlike the debris from the laminate was difficult to remove by repeating the machining process.

The machining of the protective layer over the laminate was carried out much more rapidly than the machining of the laminate, as any debris deposited in the channel had to be removed when laminate was machined during the second pass.

If electrodes were to be incorporated into the channel they were fabricated on the glass slide, which forms the lid of the channel. As with the slide that formed the base of the channel, a dehydration bake at 200°C for 5 minutes was used to remove any absorbed moisture. Next the protective coating was removed from the machined dry film laminate to reveal a debris free surface (Figure 4.27E). Once the slide was applied to the laminate, slight pressure of the order of $100gcm^{-2}$ was applied and the whole device was heated on a hot plate to 70°C for 1 hour and then allowed to cool naturally. Other approaches as described below were investigated. However, these did not produce as strong a bond. When the device was heated to 70°C and bonded under a high pressure of the order of 10 $Kgcm^{-2}$, applied using a hydraulic press, the laminate deformed and flowed into the channel. At a temperature of 70°C the laminate is slightly flexible whilst keeping its shape. Under low pressure at 70°C the surface imperfections in the laminate flattened out to form a complete bond with the glass. A range of different pressures were used to attach the lid to the channel at room temperature. However, the bond formed was not as strong and there were air bubbles between the glass and the laminate. Figure 4.28 is a close up view of the bubbles that formed in the laminate when room temperature bonding was used.

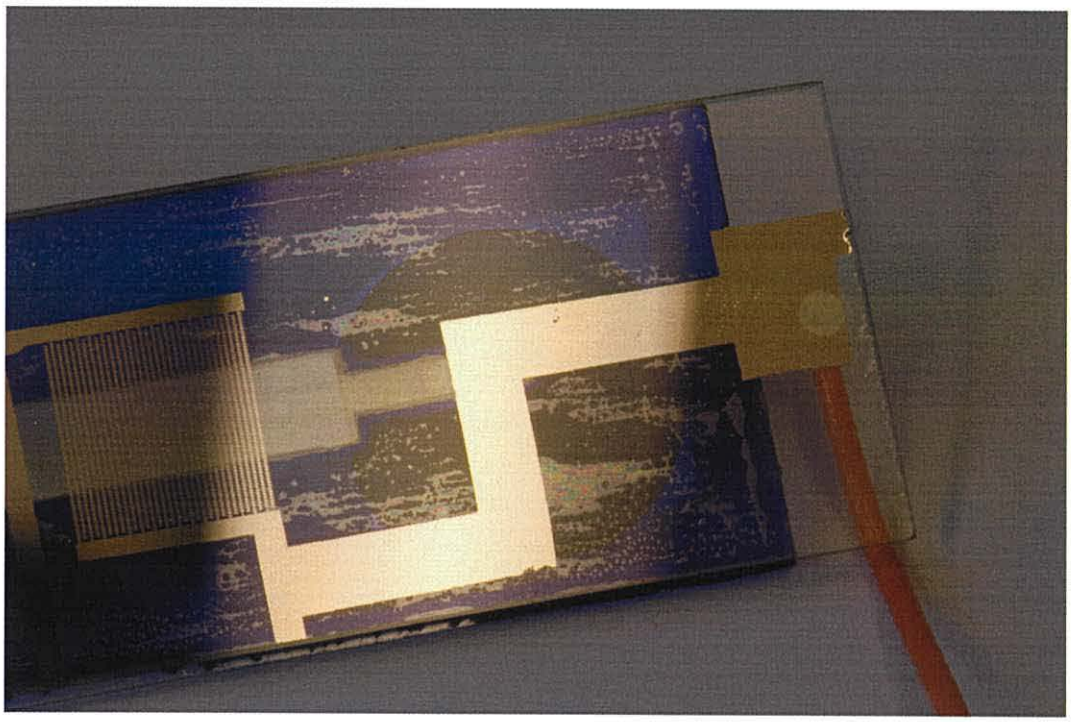

Figure 4.28 *Bubbles formed in the laminate when the lid was bonded to the laser machined dry film laminate channel at room temperature.*

When fabricating the channel structures, some devices were retained in an unexposed form until after the lid was attached, while others were exposed to ambient UV light prior to attaching the lid. It was found that a stronger bond was formed with the lid of the device if the laminate remained unexposed until after the lid was attached. Once the laminate was exposed to UV light it became more brittle and the surface less adhesive due the photo polymerisation of the short chain molecules by the UV light. The short chain molecules have a lower melting point than the long polymers, making the material more flexible and adhesive. Figure 4.29 is a photograph of a channel fabricated using an excimer laser to machine dry film laminate.

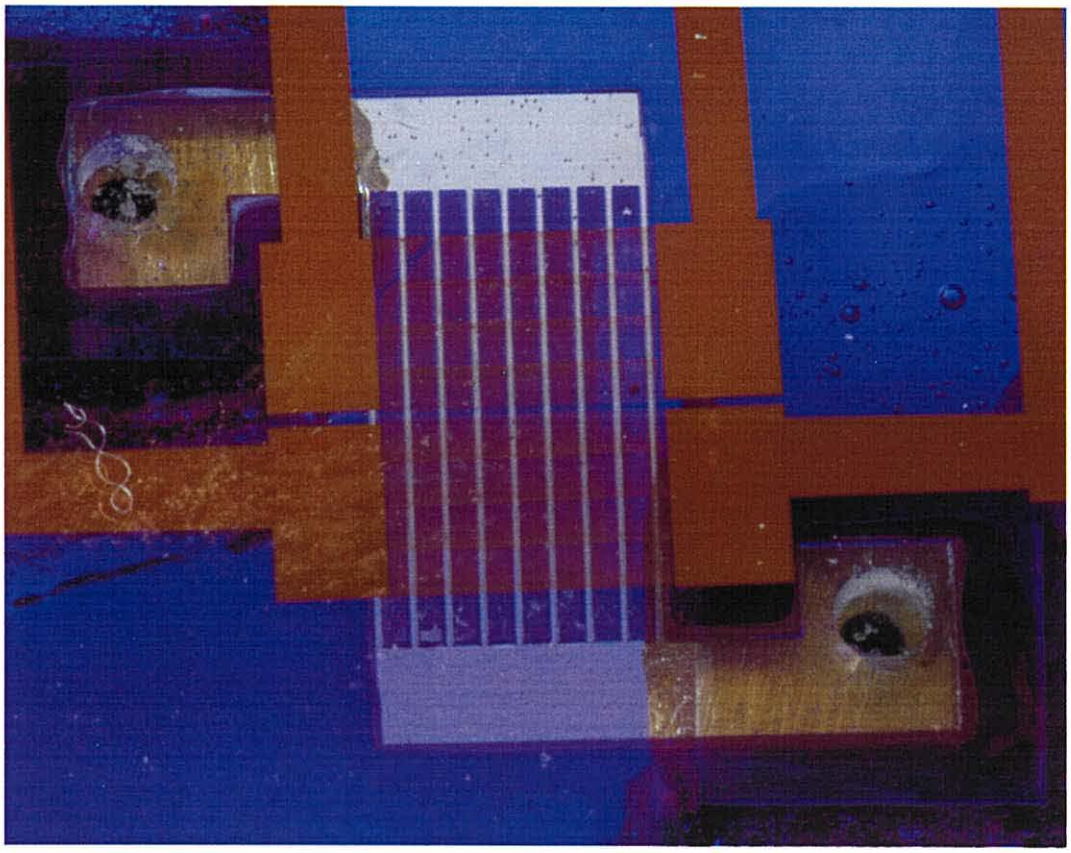

Figure 4.29 *Channel structure fabricated through laser machining of dry film laminate.*

The ablation threshold for bulk gold, as with other metals, is significantly higher than that of dry film laminate. Therefore, it is possible to fabricate a channel in dry film laminate over a set of gold electrodes. However, this is difficult to achieve as thin metal films are easily damaged. The gold is not ablated but instead peels away from the substrate. At energies slightly above the ablation threshold of the laminate this is avoided but the machining process takes a very long time.

4.6.2 Testing

To test the device, water was passed through the channel using a syringe. For a wide aspect ratio channel 60μm high, 2mm wide and 60mm, long flow rates of 0.5ml/sec could be achieved before delamination was observed. The delamination occurred both between the base and the laminate and between the lid and the laminate. A device of this type, containing a set of interdigitated castellated electrodes was filled with a

suspension of non-viable yeast cells in a medium of conductivity 100uScm^{-1}. Once filled, the channel was sealed at each end using epoxy adhesive. The dielectric behaviour of the particles within the channel remained the same for several days, indicating that the conductivity of the suspending medium was not changed significantly by chemicals leaching out of the laminate. This device has remained intact and filled with fluid for over two years. However, in some devices over a year old and not filled with fluid, the laminate at the side of the channel has begun to separate from the glass, as illustrated in the Figure 4.30. This is probably due to the laser machining process partly exposing the laminate either side of the machined channel and reducing its adhesion to the glass substrate or lid.

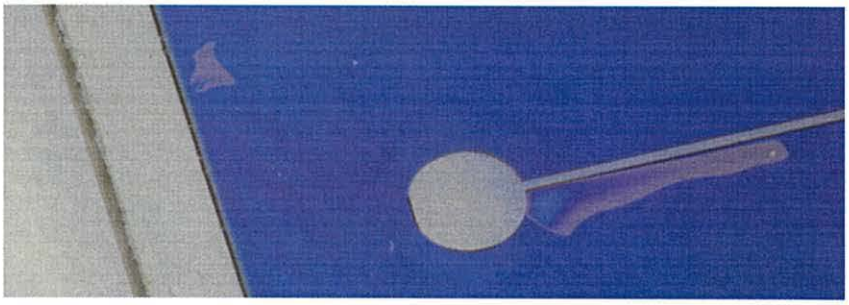

Figure 4.30 *Delamination at the edge of a laser machined dry film laminate channel.*

Although this approach produces channels that are not as strong as those produced using the process described in Section 4.5, a much finer resolution can be achieved. Figure 4.31 shows an electron micrograph of 2 channels fabricated in two layers of laminate, 60μm deep in total.

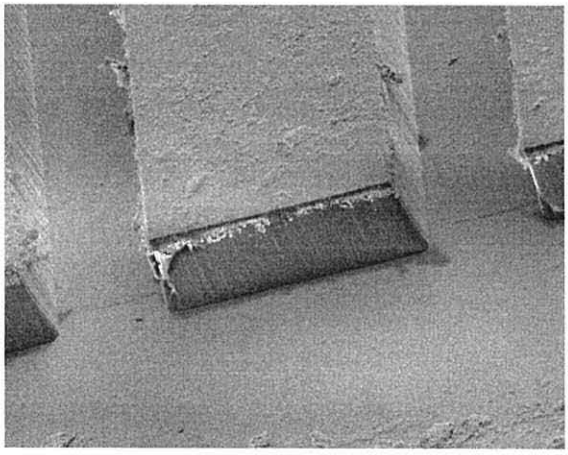

Figure 4.31 *Electron micrograph of two channels fabricated in dry film laminate 60μm deep.*

4.6.3 Channel profiles

Microfluidic channels generally have a square or rectangular profile. However, in some situations there are advantages to having a curved channel profile. The computer simulations, produced using FEMLAB, illustrated in Figure 4.32, illustrate the flow profile through three channels of different shapes. Although the channel shapes are different each channel has the same cross sectional area and total flow rate.

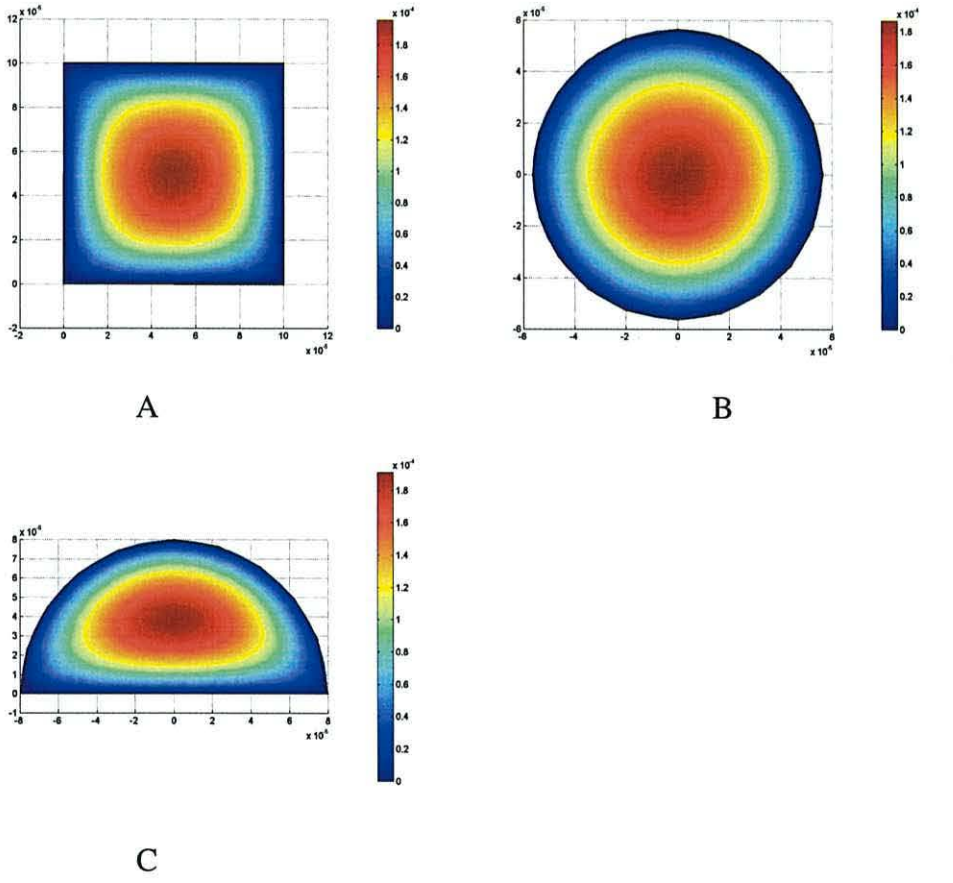

Figure 4.32 *Simulations of flow profiles through channels of square cross section (A), Circular cross section (B) and semi circular cross section (C). In each case the total cross sectional area is 0.01mm^2 and the average flow rate is 100μms^{-1}.* For all the plots the scale bar runs from 0μms^{-1} at the bottom to 180μms^{-1} at the top.

The fluid in the corners of the square channel in Figure 4.32A moves much more slowly then that in the centre. This slow moving volume increases the amount of fluid that must pass down the channel, to ensure that any particles or bubbles trapped in the corners are completely removed from the channel [14]. However, when the circular

channel in Figure 4.32B is used the simulation shows that, although the fluid is still stationary at the channel wall, the areas of slow moving fluid are reduced. For electrodes to be easily incorporated into the channel, part of the profile must be flat making a circular channel unsuitable. The third simulation in Figure 4.32C illustrates the flow profile through a semi circular channel. In this case, slow moving fluid in the lower corners has not been removed as a flat surface is required on which to fabricate the electrodes. However, the curved upper surface of the channel reduces the amount of slow moving fluid in which particles could stagnate.

When an eximer laser is used to machine a channel in dry film laminate it is possible to produce channel profiles that are not square. As illustrated in Figure 4.33 when a beam is moved across the work piece the channel will have a profile which depends on how many times the laser has fired on a given area. This process of moving a shaped beam across the work piece is called mask dragging.

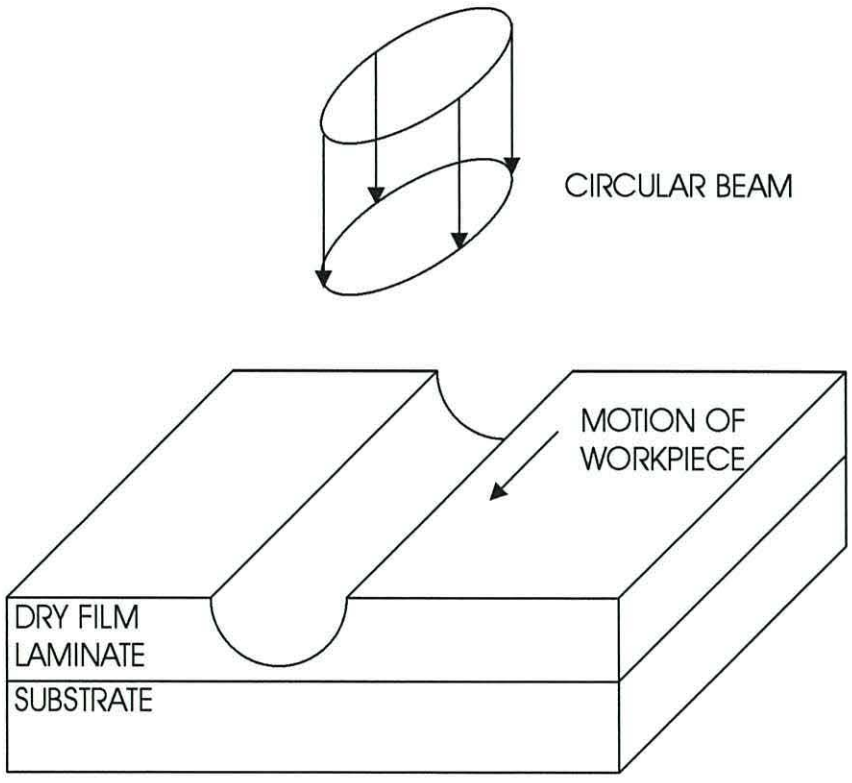

Figure 4.33 *Illustration of the mask dragging process used to produced shaped channel profiles*

By moving a circular beam across the surface of the laminate it is possible to produce semi circular channels as shown in Figure 4.34. Two of these channels can be combined to form a pipe with a circular cross section, which can be used to connect cylindrical pipes from external sources of fluid. Alternatively, one can be used to form a semi-circular channel over a set of electrodes. As the upper surface of the channel is formed from laminate instead of clear glass, it is necessary to view the channel from below.

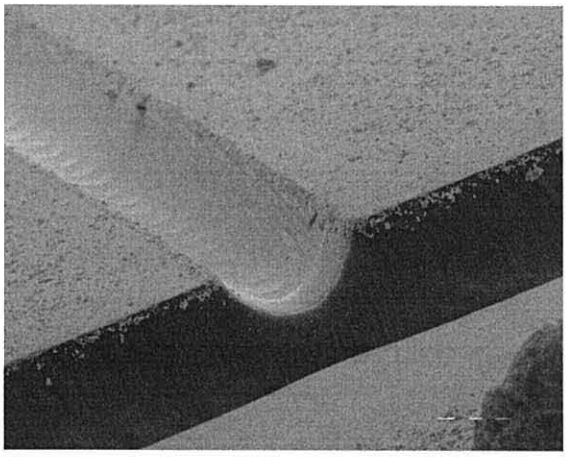

Figure 4.34 Electron micrograph of a semi circular channel formed in dry film laminate.

4.7 Fabrication of channels from UV curing adhesive

Applications such as the capacitive sensors described later in Chapter 5 require electrode arrays to be positioned on both the upper and lower surfaces of a microfluidic channel. Laser ablation is a mechanically aggressive process and can cause damage to thin film electrodes. To overcome this another channel fabrication process was developed.

Instead of using UV curing adhesive to only attach the lid over a channel as described in Section 4.4, it was also shown to be possible to construct the entire channel structure from a layer of UV curing adhesive sandwiched between two layers of glass.

4.7.1 Manufacturing process

To have electrodes on both surfaces of the channel, the electrodes were first fabricated using the processes described in Chapter 3 onto the two substrates used to form the lid and base of the channel. The fabrication process provided clean substrates and no further cleaning was necessary.

PVC, laminate or metalic shim elements were used to separate the two pieces of glass that form the top and bottom of the channel and thus control the channel height. To prevent any obstruction to the channel, the shims were placed on one glass substrate in areas well away from the path of the channel as illustrated in Figure 4.35.

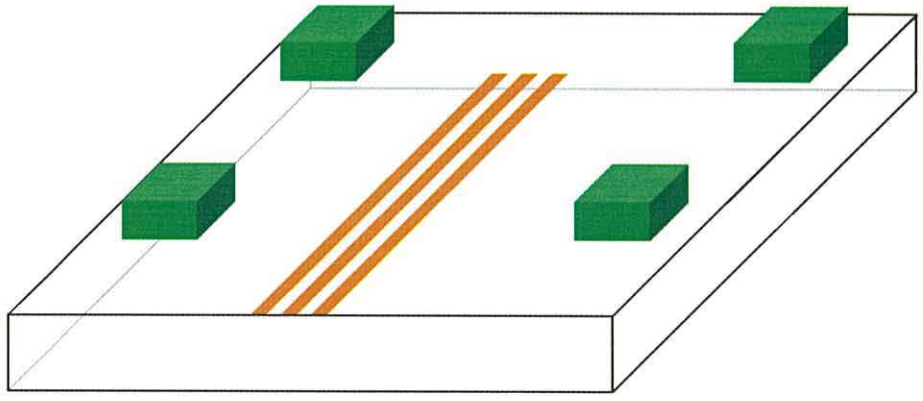

Figure 4.35 *Positioning of shims away from the channel to control its height .*

In producing a sealed channel it was necessary to ensure that no air bubbles were present in the adhesive between the two pieces of glass before it was exposed. Once the channel was formed it could leak if it intersected with air pockets. To ensure adequate coverage, the entire device was flooded with a layer of locktite 358 UV curing adhesive to a thickness greater than the height of the channel and spacers. The second glass substrate with electrodes was then placed on top of the adhesive and allowed to settle until it made contact with the spacers. To prevent the formation of air bubbles under the glass, the lid was applied one edge first and then lowered to the horizontal, as illustrated in Figure 4.36. Once in place, the upper set of electrodes were allowed to settle naturally under gravity until the glass made contact with the spacers. If excessive pressure was

applied to force the adhesive from between the glass substrates, they mechanically deformed causing air to be pulled back between the substrates when they returned to their original shape.

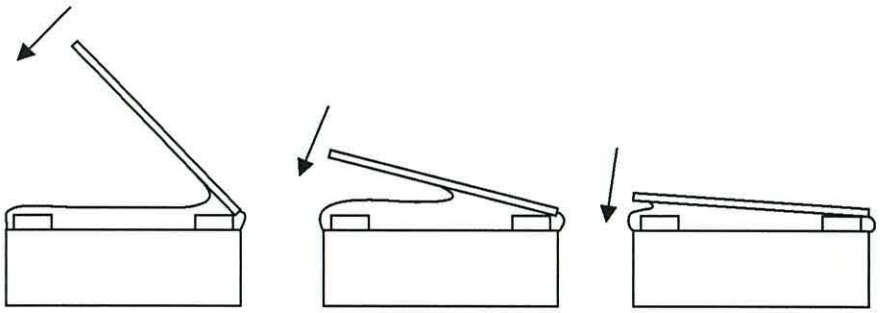

Figure 4.36 *Lowering of the channel lid from one side to prevent the formation of air bubbles.*

The channel structure was formed by selectively exposing the adhesive through a photo mask to UV light for 15 seconds at an energy density of $15mJcm^{-1}$, as illustrated in Figure 4.37. Exposed areas of the adhesive solidified to form the channel walls, whilst the unexposed adhesive occupying the channel region remained liquid.

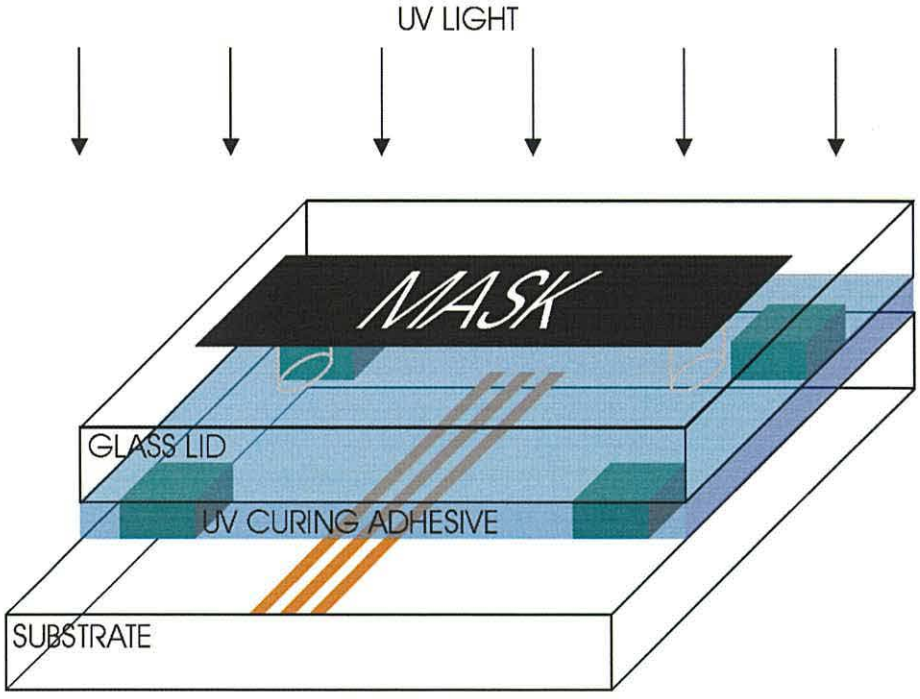

Figure 4.37 *Formation of the channel structure by exposure of the UV curing adhesive outside the channel.*

Next the channel structure was flushed through with acetone to remove the unexposed liquid adhesive. This left an optically clear channel surrounded by cured adhesive as shown in Figure 4.38. The UV light from the aligner was not perfectly parallel and as the distance between the mask and the polymer increases some loss of definition of the channel wall was observed. To improve the resolution of the channels, the upper electrodes were fabricated on a large thin cover glass of thickness 150μm, this allowed the mask to be closer to the UV curing adhesive and improved the definition. This is discussed in more detail in Chapter 8

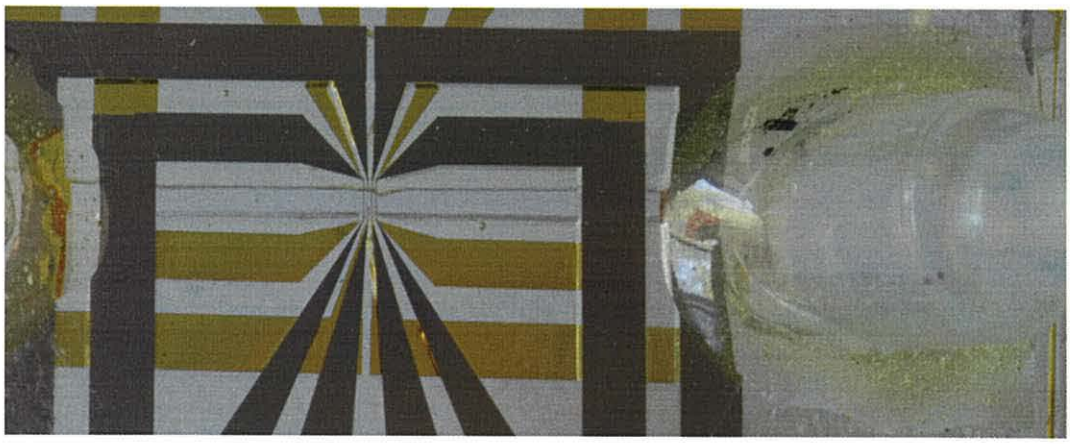

Figure 4.38 *Channel structure produced using UV curing adhesive.*

4.7.2 Device testing

As with the testing of previous devices, water was passed through the channel using a syringe. For a channel 200μm high and 1mm wide flow rates in excess of 5ml/sec were achieved. Beyond this flow rate the inlet pipe detached from the device. The flow rate of 5ml/sec is far in excess of the μl/s flow rates typical in devices of this type. A problem with the device described in Section 4.5 was that it failed when left filled with water for 24 hours. A device of the type described in this section has remained intact for over 6 months whilst filled with UPW. This is an important factor, as the complexity of some microfluidic systems makes it necessary to supply them to a customer pre-filled with a fluid.

The channel was optically clear when viewed from above and through examination with an optical microscope was found to have vertical sidewalls. Although the cured adhesive is transparent, the channel walls have a slightly matt appearance. This, and the thickness of the adhesive, prevents particles from being viewed from the side. However, the sidewalls of the channel could be used to illuminate the channel contents.

It was necessary to ensure that all the uncured UV adhesive was removed from the channel before the device was exposed to even low levels of UV light, such as that from florescent tubes. Once exposed to UV light the adhesive began to set and it was impossible to selectively remove it from the channel.

In the case where there are electrodes on both sides of the channel, the electrodes act as a mask preventing the UV adhesive in their shadow from curing. If the electrodes run continuously from the channel to the edge of the device, an additional channel will be created causing the device to leak. To prevent this it was necessary to expose the device from both above and below. Care was taken in the electrode design to ensure that no path of uncured adhesive from the channel to the edge of the device existed, as a result of the adhesive being in shadow from both sets of electrodes. The UV curing adhesive is highly viscous and only slightly soluble in acetone, therefore it was not necessary to cure the adhesive over the entire length of a path leading to the edge of the device. When the main channel is flushed under pressure, only the adhesive adjacent to the main channel will be removed, this effect is illustrated in Figure 4.39. When the device is exposed to non-collimated, ambient light the remainder of the adhesive is exposed and cured.

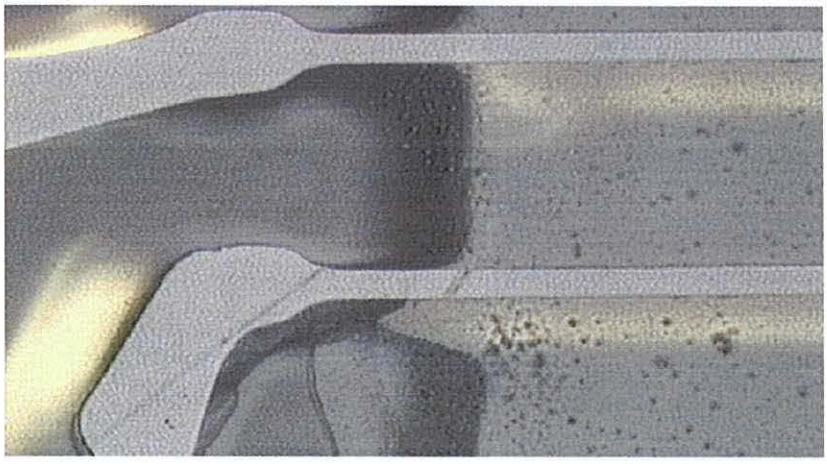

Figure 4.39 *Removal of uncured adhesive at the start of a channel created by the shadow of a set of electrodes.*

Using this manufacturing process the uncured adhesive is cleared by flushing the device through using the inlet and outlet ports. When there is more than one channel path leading between the ports, one channel may clear before the other. Acetone is much less viscous than the adhesive and will naturally flow through this cleared channel. This problem was overcome by flushing a large volume of acetone through the device at a relatively high pressure. Although the acetone moved through the clear channel, the pressure difference created by the high flow rate forced the adhesive out of the other channel. This approach was used to produce the H-Filter channel structure in Chapter 8. It was not possible to leave the device in acetone for several hours, as the cured adhesive slowly dissolved. Another approach that can be used to clear complex channel geometries is to incorporate additional outlets and channels, these are used to help clear the main channel structure and are then sealed.

4.8 Inlet and outlet ports

To pass fluid through a channel within a device it is necessary to have connections between the device and external sources, such as pumps or syringes. The process of drilling the inlets was undertaken before the device was fabricated to prevent the fine channels from becoming blocked with glass shards. To connect to the device, 1mm holes were drilled using a diamond tipped drill in either one of the pieces of glass that formed the lid or base of the channel. The area surrounding the hole was then roughened with emery paper to provide a better surface for the glue to securely adhere to. The slide was then washed in Decon 90 and dried under hot air, to remove any surface grease. Two main approaches were used to connect sources of fluid to the device. To provide a connection that could easily attach to a syringe, a blunt hypodermic needle of diameter 0.8mm was silver soldered into a hole in a small piece of brass. The part of the needle protruding through the brass was aligned with the hole and the brass block was glued to the device as shown in Figure 4.40.

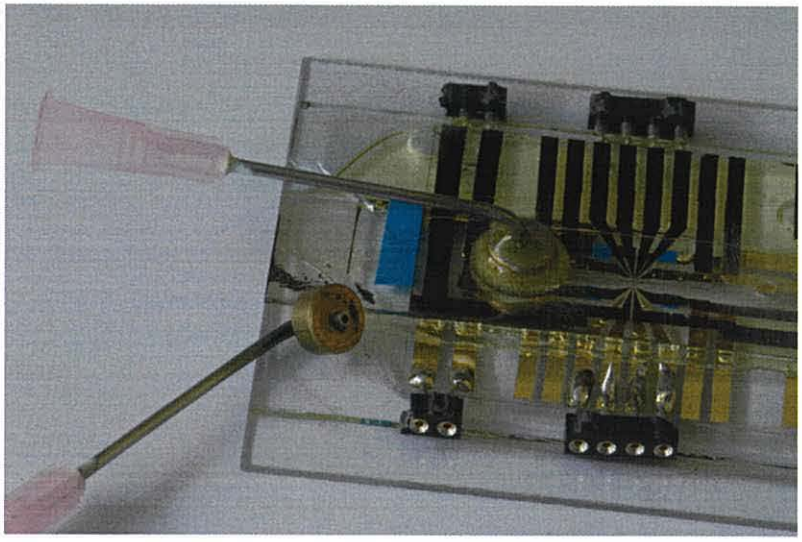

Figure 4.40 *Needle inlet used to connect to microfluidic channels.*

This design of the inlet port created very little dead volume where bubbles could form. However, its manufacture was labour intensive, as the brass block had to be produced and the needle silver soldered in place. A simpler approach used was to glue a lewer fitting directly onto the glass as illustrated in Figure 4.41

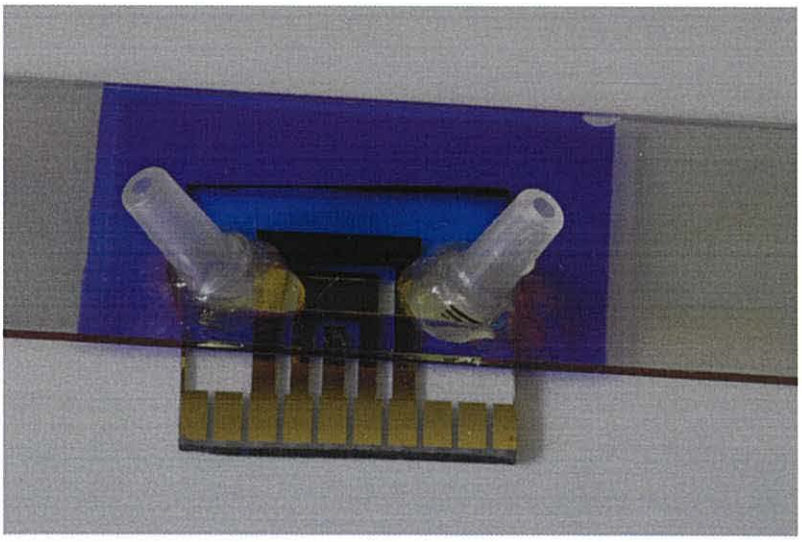

Figure 4.41 *Lewer fitting glued directly over the inlet to the microfluidic channel.*

This approach allowed pipes to be easily connected to the device. However, the relatively large diameter of the lewer fitting compared to the channel caused the formation of trapped air bubbles. When the flow from an external pump is varied, the

pressure in the pipe leading to the channel will change. This change in pressure will cause the bubble to expand or contract. The change in the volume of the bubble causes a lag between the flow rate from the pump and the flow rate in the channel.

4.9 Summary and discussion

The aim of the research described in this chapter was to develop techniques to allow the fabrication of microsystems using low cost materials, such a glass and polymers. Particular attention was paid to increasing the reliability of the devices, whilst minimising the complexity.

One approach often used to selectively move particles within a microsystem is to use TWD electrode arrays. However, this type of multilayer device is often unreliable. The main cause of failure in these devices was found to be the via-holes that connect between different layers in the device. Two approaches were investigated to overcome this problem. One approach was to produce electrode designs that were capable of selectively transporting particles but eliminated the need for multiple layers. The other approach used was to eliminate the need for via-holes. The latter was more successful and has been described in this chapter. To eliminate the need for via-holes, a design and manufacturing process was developed where alternate electrodes making up the travelling wave array were fabricated on two isolated electrode planes separated by a polyimide insulator. This design approach produced a non-planar travelling wave array. However, the variation in height of the electrodes was small compared to their width, so the electric field above them was not significantly affected. This was confirmed by computer modelling of the field strength above the electrodes. When the electrodes were tested they were found to operate as well as those fabricated using via-holes, but the reliability problem associated with the via-holes was eliminated.

As discussed, it is often necessary to produce channel structures within a lab-on-a-chip type device. An approach previously used was to fabricate the chamber walls from PVC tape with a cover glass forming the lid. However, using this approach it is not possible to produce high resolution channel structures capable of withstanding pressure driven flow. To overcome this problem a process for manufacturing accurate channels from

low cost materials was developed. To accurately structure the channel it was optically patterned in a layer of dry film laminate on a glass substrate using UV light via a photomask. Once developed and baked, the channel walls had a high degree of chemical resistance. The chemicals used to develop the laminate do not affect gold, so it was possible to fabricate electrodes in the base of the channel. A lid was secured to the channel by selective exposure of a UV curing adhesive. Unexposed adhesive remaining in the channel was then removed by flushing with acetone. Once fabricated, the channel structure is optically clear allowing observation of its contents using a microscope and is also capable of withstanding high pressure driven flows.

When the channel fabricated from dry film laminate and UV curing adhesive was left filled with water for over 24 hours it began to delaminate. An alternative approach developed to fabricate a channel was to use an Eximer laser to directly machine the pattern of the channel in the laminate. The surface of the laminate was protected from machining debris by a thin protective polymer layer, which once removed revealed an adhesive surface to which the lid could be directly attached. Channels fabricated using this approach overcame the problem of the structure delaminating when filled with water and samples of this type of channel have remained intact for over 2 years whilst filled with water. Due to the high resolution achievable through laser machining, very narrow channels can be accurately produced using this method. The mechanically aggressive nature of laser machining made it difficult to incorporate electrodes on the base of the channel. To overcome this problem the electrodes were fabricated on the lid of the device.

When a square channel is used to convey a fluid, the velocity of the fluid in the corners of the channel is significantly less than that in the centre. This increases the amount of fluid that must flow through a channel to ensure any particles at the edge of the channel are removed. This problem can be reduced by decreasing the amount of slow moving fluid within the channel, and can be achieved by using channels with a circular cross section. This was demonstrated by computer simulation of square, circular and semi circular channel profiles. To fabricate these curved channel profiles, a circular aperture in an ablating laser beam was moved across a laminate film producing a semi-circular channel profile. These channels can be placed directly on a substrate to form a semi-

circular channel over electrodes or two can be combined to form a circular channel suitable for connection to external pipes.

In some situations, such as the measurement of the impedance across a channel as described in Chapter 6, it is necessary to have electrodes on both the upper and lower surfaces of a channel. This was achieved through the development of a channel structure where the channel walls consisted of a layer of UV cured adhesive sandwiched between two glass substrates. To fabricate this structure polymer spacers were used to separate two substrates, whilst the area between them was flooded with UV curing adhesive. The channel walls were formed by selectively exposing the adhesive to UV light via a photomask. Liquid adhesive within the channel was then removed by flushing with acetone. This approach produced a strong channel capable of withstanding high pressure driven flows. As the electrodes on the substrates also formed a mask it was necessary to expose the device from both sides to prevent the formation of additional channels to the edge of the substrate. Due to the distance between the mask and the adhesive the resolution of this type of device was limited. However, an improvement in the resolution was achieved by using a thin cover glass to form the lid of the channel, thus reducing the distance between the adhesive and the mask.

The three methods of channel fabrication developed have different advantages and disadvantages. The choice of which approach to use depends on the application. The table below outlines some of the advantages and disadvantages of the different fabrication approaches.

Type of device	Advantage	Disadvantage
Baked laminate with lid attached using UV curing adhesive	• Chemically resistant channel walls • Electrodes can be fabricated on upper and lower surfaces	• Channel delaminates if left in water for over 24 hours • Comparatively low resolution
Channel walls formed from laser machined laminate	• Very high resolution • Only one manufacturing process step • Curved channel profiles can be produced	• Difficult to fabricate channels with electrodes on upper and lower surfaces • Laser machining systems are expensive to operate
Channel walls formed from UV curing adhesive	• Electrodes can be fabricated on upper and lower surfaces • Simple low cost manufacturing process	• Comparatively low resolution • Prone to leakage if not properly exposed

Once a microfluidic channel has been fabricated it is necessary to connect it to an external source, such as a pump or reservoir. Two methods were used to achieve this. If it is necessary to reduce the dead volume in a system to a minimum, a hypodermic syringe was silver soldered in place through a brass block so the ground flat tip protruded slightly. This protrusion was then located in a hole pre-drilled in the upper glass substrate that formed the channel lid and the brass block glued in place. However, if the dead volume in the system was not a significant issue a lewer fitting, of the type found on syringes was glued directly above the hole in the substrate. This provided a very simple, low cost way to attach to the device.

To monitor the fluid flow within these channels and to detect any particle movement some form of sensor arrangement is necessary. Many commercial sensors are often too bulky to incorporate within the channels described in this chapter. Chapter 5 deals with the development of small, low cost sensors that can be incorporated into these channels.

4.10 References

[1] 'Electrokinetic behaviour of colloidal particles in travelling electric fields: studies using yeast cells' Y. Huang, X-B Wnag, J. A. Tame and R. Pethig, *J. Applied Physics D* **26** (1993) 1528-1535

[2] 'Traveling-field electro-manipulation of bioparticles' J. P. H. Burt, R. Pethig, M. S. Talary and J. A. Tame, *(1995) International proceedings in precision engineering* (M. Bonis, Y. Alayli, P. Revel, P. A. McKeown and J. Corbett, Eds.) Elsevier, pp.476-479

[3] 'Electromanipulation and separation of cells using travelling electric fields' M. S. Tallary, J. P. H. Burt, J. A. Tame and R. Pethig, *J. Applied Physics D* **29** (1996) 2198-2203

[4] 'Large-area travelling-wave dielectrophoresis particle separator' H. Morgan, N. G. Green, M. M. Hoghes, W. Monaghan and T. C. Tan, *J. Micromechanics and Microengineering,* **7** (1997) 65-70

[5] 'A combined travelling wave dielectrophoresis and electrorotation device: applied to the concentration and viability determination of Cryptosporidium' A. D. Goater, J. P. H. Burt and R. Pethig, *J. Applied Physics D* **30** (1997) L65 - L69

[6] 'Design and fabrication of travelling wave dielectrophoresis structures' L. Cui and H. Morgan, *J. Micromechanics and Microengineering* **10** (2000) 72-79

[7] 'Development of biofactort-on-a-chip technology using excimer laser micromachining' R. Pethig, J. P. H. Burt, A. Parton, N. Rizvi, M. S. Talary and J. A. Tame, *J. Michromechanics and Microengineering* **8** (1998) 57-63

[8] 'Fundamentals of microfabrication' Mark Madou, *CRC press, 1997, Boca Raton, Florida, US*

[9] 'R-F sputtering processes' J. L. Vossen and J. J. O'Neill, *RCA Review* (1968) 149-178

[10] 'Simulation of travelling electric field manipulation of bioparticles' M. P. Hughes, X. B. Wang, J. P. H. Burt R. Pethig and L. R. Watkins, *2nd International conference on Computation in Electromagnetics* (1994) 48-51

[11] 'Kay and Laby, Tables of Physical and Chemical Constants 16th edition' *Longman. Essex, UK*

[12] 'Protein sizing on a microchip' L. Bousse, S. Mouradian, A. Minalla, H. Yee, K. Williams and R. Dubrow, *J. Analytical Chemistry,* **73** (2001) 1207-1212

[13] 'Rapid prototyping of microfluidic systems in poly(dimethylsiloxane)' D. C. Duffy, J. C. McDonald, O. J. A. Schueller and G. M. Whitesides, Journal of Analytical Chemistry 70 (1998) 4974-4984

[14] 'Towards integrated microliquid handling systems' M. Elwenspoek, T. S. J. Lammerink, R. Miyake and J. H. J. Fluitman, *J. Micromech. Microeng* **4** (1994) 227-245

Chapter 5

Hot Wire Flow Sensor

5.1 Introduction

The microfluidic channels described in Chapter 4 can be used in microsystems to process very small sample volumes. To monitor the fluid flow within channels, for instance in lab-on-a-chip devices, it is possible to include microfabricated sensors within a device [1-5].

When performing processes that require high purity reactants, such as the polymerase chain reaction (PCR), used to copy DNA, cross contamination between samples is a problem [6-8]. This can be resolved by using disposable micro-systems. To be viable disposable equipment must be inexpensive to produce. Chapter 4 discussed methods of producing channels from low cost materials, in this chapter the incorporation of sensors into micro channels is described. The sensors in this chapter are designed to detect the velocity of the fluid in the channel.

This chapter first considers the development of a flow sensor based on the cooling effect of a moving fluid on a metallic hot wire [9], where the temperature of the wire is found by measuring its resistance. By combining four sensing elements into a bridge circuit it was possible to reduce the output fluctuations caused by changes in ambient temperature, that were observed when a single hot wire was used to measure the flow velocity. The conventional approach to reduce the dependence on the ambient temperature is to increase the overheat ratio of the wire [10,11]. However this has limited use as too high a temperature could cause damage to biological particles within the channel.

When moving or positioning particles using a fluid it is useful to maintain a constant flow rate. By combining a flow sensor with a pump and control circuitry into a feedback loop, as shown in Section 5.3, the flow velocity was maintained at a steady value despite changes in the back pressure at the channel outlet.

5.2 Flow measurement using a hot wire anemometer

When a constant current is passed through a thin wire to provide a source of heat, the equilibrium temperature of the wire will depend on the cooling effect of the material surrounding the wire. The heating of the metallic wire caused by the current passing through it will cause its resistance to increase. As the current is constant, this change in temperature and resulting change in resistance can, via Ohm's law, be measured as a change in the potential difference across the wire [9].

When a thin electrically heated wire is placed in a stationary fluid, the area in close proximity to the wire will be heated, this will reduce the temperature difference between the wire and its surroundings and as a result reduce the rate of heat flow from the wire. When the fluid is moving, the heated fluid surrounding the wire is replaced with fresh, colder fluid. The greater temperature difference between the wire and its surroundings results in a greater rate of heat flow from the wire. The cooling effect of the fluid on a hot wire is greater if the fluid is moving, than if the fluid is stationary. This results in the wire having a higher temperature when in stationary fluid, which in turn results in a higher resistance and therefore higher potential difference across the wire when a constant current is applied [5,9,10].

Cooling of an object is more efficient as its size decreases and its surface area is large in comparison to its volume [12]. To produce a sensitive hot wire anemometer it is necessary to maximise its surface area to volume ratio, therefore maximising the cooling effect of the fluid on the wire, therefore it is necessary to use as thin a wire as possible. The wire must also be small enough not to obstruct the flow of the fluid and particles through the channel in which it is incorporated.

5.2.1 Fabrication of anemometer wires

Using photolithography it is possible to produce metallic tracks of much smaller cross sectional areas, than would be possible with conventional wire. As described in Chapter 3, photolithography can be used to produce a thin gold track on one of the two glass substrates that form the lid and base of the channels used in this research. The

thickness of the gold is typically 70nm whilst the with of the track is variable. Microfluidic channels are typically less than 200μm in height making the use of conventional wire difficult. For a channel structure fabricated on a silicon substrates thin wires have been suspend wires in the middle of the channel supported on beams of silicon nitride [13]. In this work, if other gold electrodes are used in the device, for example those used to manipulate cells by dielectrophoresis, then thin gold tracks can be fabricated at the same time at little extra cost by incorporating them onto the same mask as the other structures.

5.2.2 Flow measurement using a single thin electrode track

A single gold track 10μm wide, similar to that illustrated in Figure 5.1, was fabricated in a 70 nm layer of gold using print and etch photolithography, perpendicular to the flow direction on the base substrate of a 2mm wide and 200μm high fluidic channel. On either side of the channel the track was connected to large gold contact pads running to the side of the microscope slide. The large pads have a small resistance compared to the thin gold track so confining most of the heating effect to the thin track. A relatively large channel depth of 200μm was used to allow relatively large volumes of water to be used to generate a specific flow velocity. These larger volumes of fluid were easier to measure, thus increasing the accuracy to which the flow velocity could be measured.

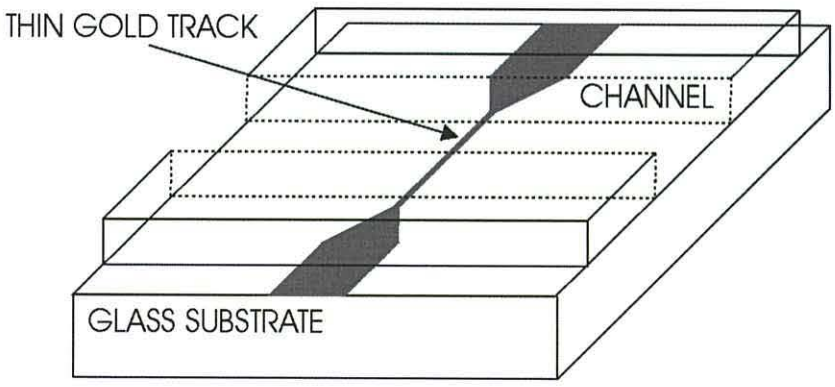

Figure 5.1 *Arrangement of a single 10 μm track across a channel used to measure fluid flow.*

The current through the track must be large enough to provide sufficient heating without melting the wire. As a guide to finding the required current, the current flux density in a piece of 5A fuse wire was calculated for its rated current. For a piece of copper fuse wire of area $0.039mm^2$ there is a current density of 125 Amm^{-2}. The same current density for the gold heater track, of cross sectional area $0.7x10^{-6}$ mm^2, gives a current of 87μA. As the gold wire is submerged in water and is much smaller than the fuse wire, it will be able to dissipate heat more effectively and therefore be able to conduct much larger currents. Allowing for the improved heat dissipation an initial current of 1mA was used.

A Wilson Current Mirror shown in Figure 5.2 capable of providing a stable output for varying loads was used to provide the constant current across the wire [14].

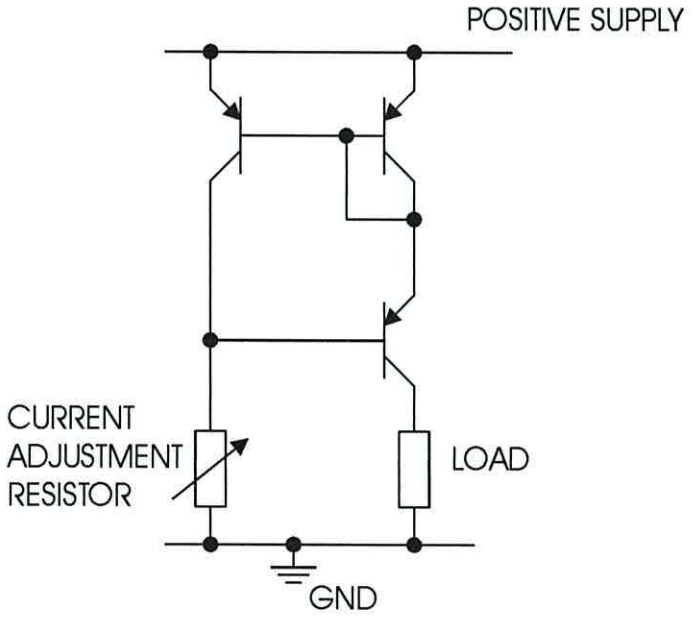

Figure 5.2 *Wilson Current Mirror used to provide a constant current across the thin track used to measure fluid flow.*

A constant current was applied across the gold track positioned perpendicular to the direction of flow. The voltage drop across the track was amplified by a factor of 10 using a 741 operational amplifier [14] in a simple inverting amplifier arrangement, then measured using a digital multi meter. A variable flow rate was produced using a Miniplus 3 Peristaltic Pump (Gilson, France), this pump was calibrated by weighing the amount of water delivered in a fixed time. It was possible to achieve a greater accuracy

by weighing the water, than would have been possible with a measuring cylinder. The flow velocity in the channel was varied from 0 to 20 mms^{-1}.

Using this arrangement it was difficult to accurately measure any changes in the output voltage with flow, as the output drifted with time. This was probably due to variations in the temperature of the fluid. As will be seen later in Section 5.2.7 the temperature of the wire at these currents is very low (low overheat ratio) making it particularly susceptible to temperature ambient temperature fluctuations as explained in Section 2.6.1.

5.2.3 Flow measurement using hot tracks in a bridge circuit

To reduce the sensitivity to temperature, four hot wire sensors were arranged in a Wheatstone Bridge [15] within the channel as illustrated in Figure 5.3. A similar approach has been used elsewhere [16] but in this case the heating elements in the design were physically separate from the temperature sensing elements. The design consisted of four heaters surrounded by four thermopile temperature sensors.

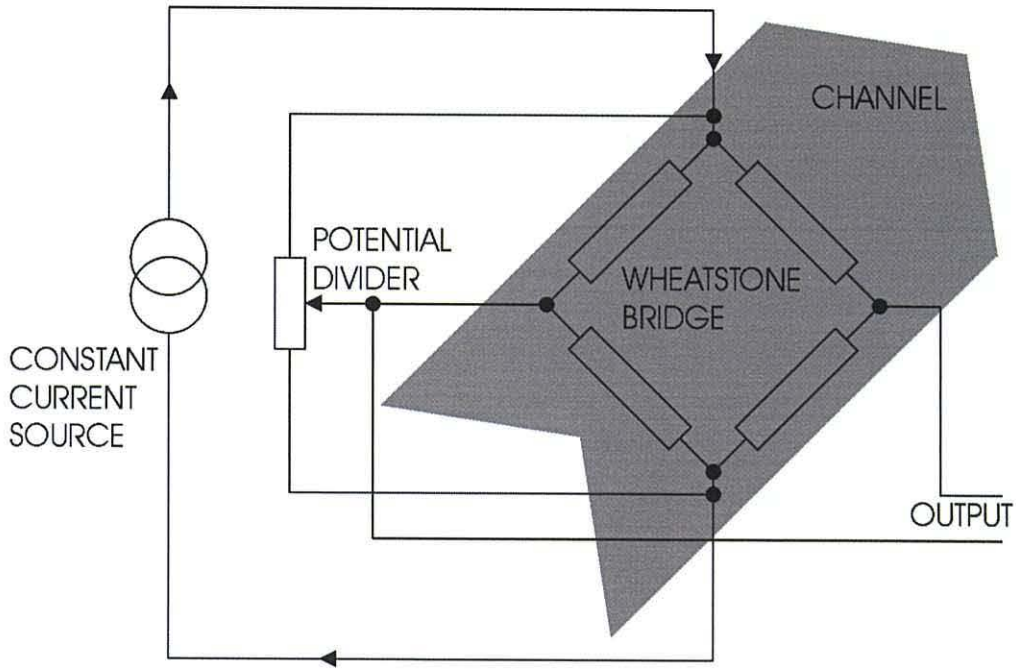

Figure 5.3 *Arrangement of 4 thin tracks in the channel to form a Wheatstone Bridge.*

In this circuit the four wires that form the Wheatstone Bridge are in the fluid flow, two opposite each other are parallel to the flow and the other two are perpendicular to the flow. A constant electrical current flows between opposite corners of the bridge and the potential difference is measured across the other two corners. For a hot track perpendicular to the fluid flow the heated fluid is removed from the vicinity of the track. However, if the direction of flow is parallel to the track the heated fluid is moved along its length reducing the portion of the track that is exposed to fresh, colder fluid. The heat loss from the tracks perpendicular to the flow is more efficient due to the greater temperature difference between the metal and the fresh fluid, than the heat loss from the tracks parallel to the flow. This difference in the rate of heat loss causes the tracks to have different temperatures and therefore different resistances. When the fluid is stationary all the tracks heat to the same temperature and have the same resistance, there is no potential difference across the bridge as it is balanced. The potential divider (Figure 5.3) is used to correct any small voltage drop caused by physical differences between the four sensing tracks. The resistance of the potential divider was 100KΩ compaired to 30Ω for the tracks so having minimal effect on the operation of the sensor. If a fluid flow is induced across the bridge the resistances of the tracks change by different amounts. As the bridge is no longer balanced a potential difference can be measured, the magnitude of which depends on the flow rate.

The important feature of this design is that a chance in the resistance of the wires caused by a change in the ambient temperature affects all the tracks equally resulting in no change in the output. Therefore a symmetrical bridge of this type is tolerant to changes in ambient temperature even at low overheat ratios.

When a single track was used to measure fluid flow the small variation in voltage with flow rate was superimposed onto a comparatively large constant voltage drop across the track. This resulted in a small percentage change in the measured voltage. This can be rectified through the use of an offset circuit but this introduces another noise source. However, when the bridge circuit in Figure 5.3 is used to measure fluid flow, the output voltage drop across the bridge is zero when there is no flow. As the output signal increases from zero it is possible to amplify the signal by a large factor without saturating the amplifier. The output is measured as the voltage difference between two points; it is therefore necessary to use a differential amplifier. The instrumentation

amplifier circuit [17] illustrated in Figure 5.4 was chosen because it has a high common mode rejection ratio (CMMR), this reduces the error caused by changes in temperature when both outputs change together. The common mode rejection ratio is a measure of the ability of a differential amplifier to produce no change in output when the two inputs vary together. The Wilson Current Mirror in Figure 5.2 was used to provide the constant current across the bridge.

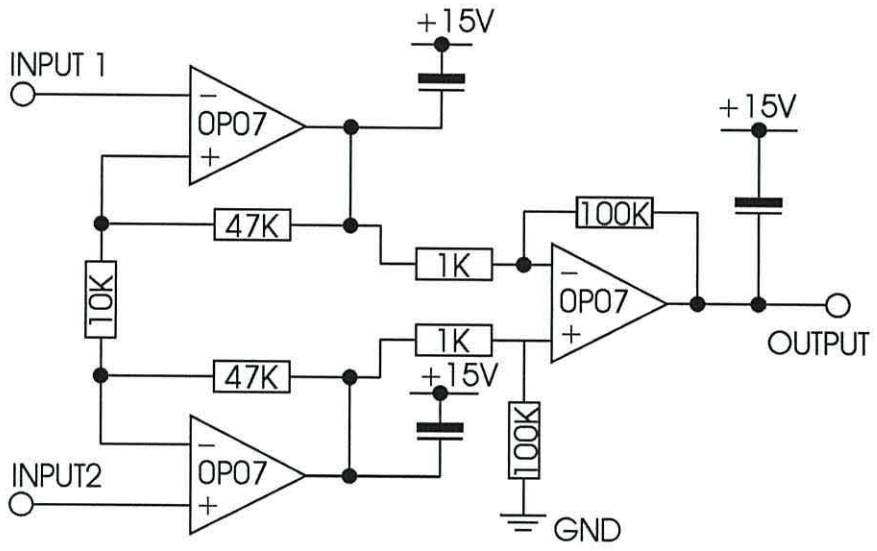

Figure 5.4 *Circuit diagram of an instrumentation amplifier used in this research.*

5.2.4 Serpentine electrode arrangement

As the length of a thin track increases, its resistance increases. If the current is kept constant, the voltage drop across the track will increase due to the increased resistance in accordance with ohms law. The magnitude of the voltage drop across the bridge for a given flow rate increases as the length of the tracks increases and as the voltage drop across each individual track increases. To increase the length of the thin tracks that make up the bridge without increasing the overall size of the device, the tracks were looped back on themselves as shown in Figure 5.5. This should not significantly effect the operation of the sensor, providing there is sufficient distance between the wires for the heat from the upstream section of wire to dissipate into the fluid before it reaches the downstream section.

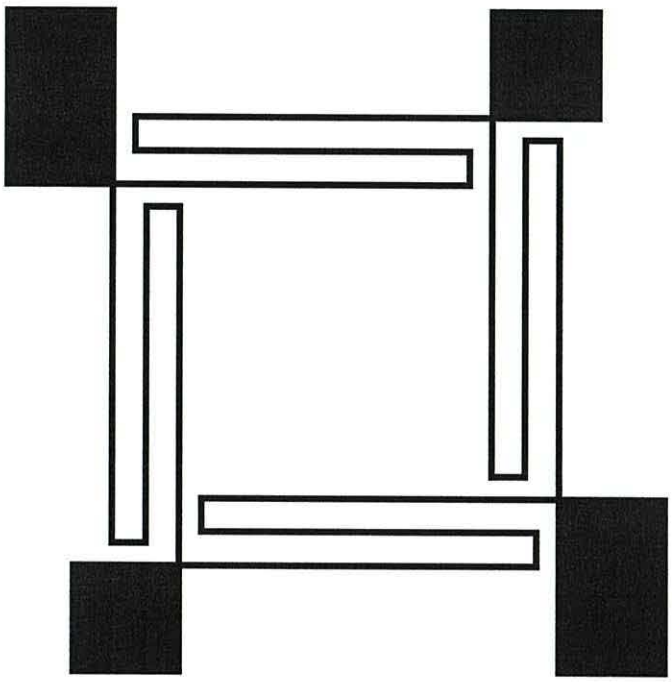

Figure 5.5 *Serpentine electrode arrangement used to increase the length of the tracks in the channel.*

The electrode tracks were fabricated using the same approach described in Section 5.2. The bridge circuit was made up of four sets of 10μm wide tracks, each 5 mm long, looped back on themselves 5 times. The overall size of the sensor was 1mm by 1mm. A 200μm high and 2mm wide channel was fabricated using the processes described in Chapter 4. A constant current of 1mA was applied across the bridge and the output voltage was increased by a factor of 1000 using the differential amplifier shown in Figure 5.4. The output of this amplifier was measured using a Keithly 602 Electrometer (Keithly Instruments, Germany).

When a peristaltic or gear pump is used there are oscillations in the flow rate caused by the cogging of the pump mechanism. A steady pulse free flow of ultra pure water was achieved by using gravity feed from a head of water. The flow rate was calibrated by weighing the amount of water that passed through the system in a given time period, this was repeated for several different heads of water.

5.2.4.1 Results

The flow rate through the device is proportional to the head of water at the inlet to the device, as illustrated in Figure 5.6.

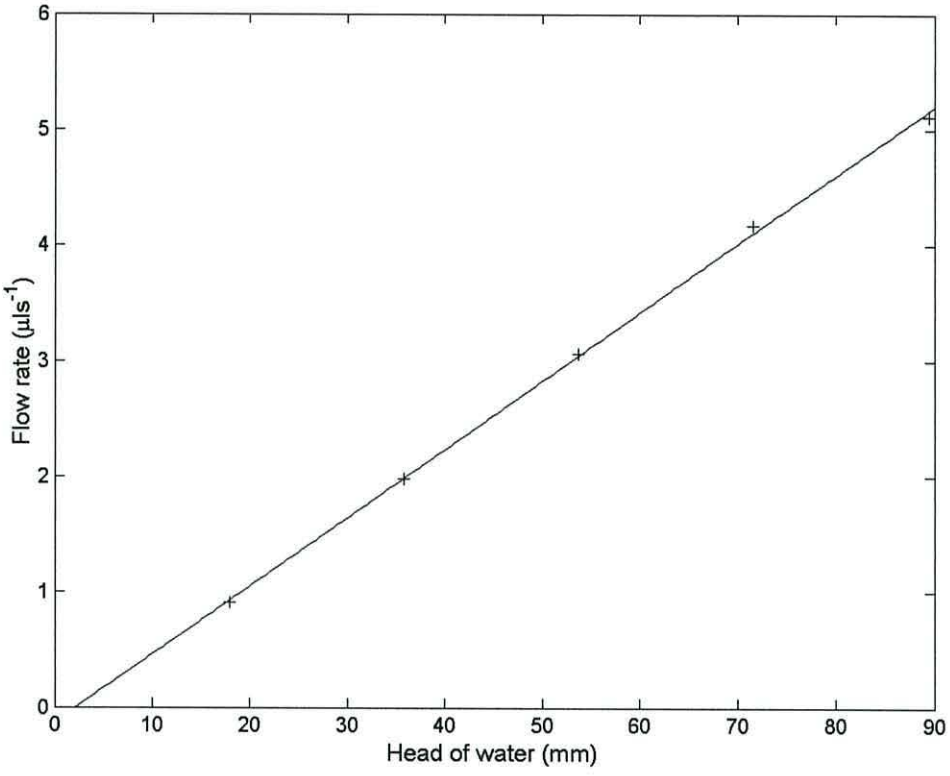

Figure 5.6 *Flow rate through the micro channel against the head of water at the inlet.*

Figure 5.7 shows the output from the bridge for different flow rates. The current across the bridge was kept constant at 1mA. It was found that the output voltage from the sensor increased as the flow rate was increased. Oscillations in the sensor output voltage resulted from oscillations in flow caused by the formation of droplets at the outlet. By submerging the outlet pipe it was possible to remove these oscillations. The formation of droplets resulted in a variation in the output of ~5% for an average flow rate of 1.5 mms^{-1}, this gives an indication of the resolution of the sensor as this corresponds to a change in flow velocity of $75\mu ms^{-1}$. The oscillations in the output correspond to a flow velocity typical of microfluidic devices [5]. However flow velocities of several mms^{-1} quite large and only found in some applications.

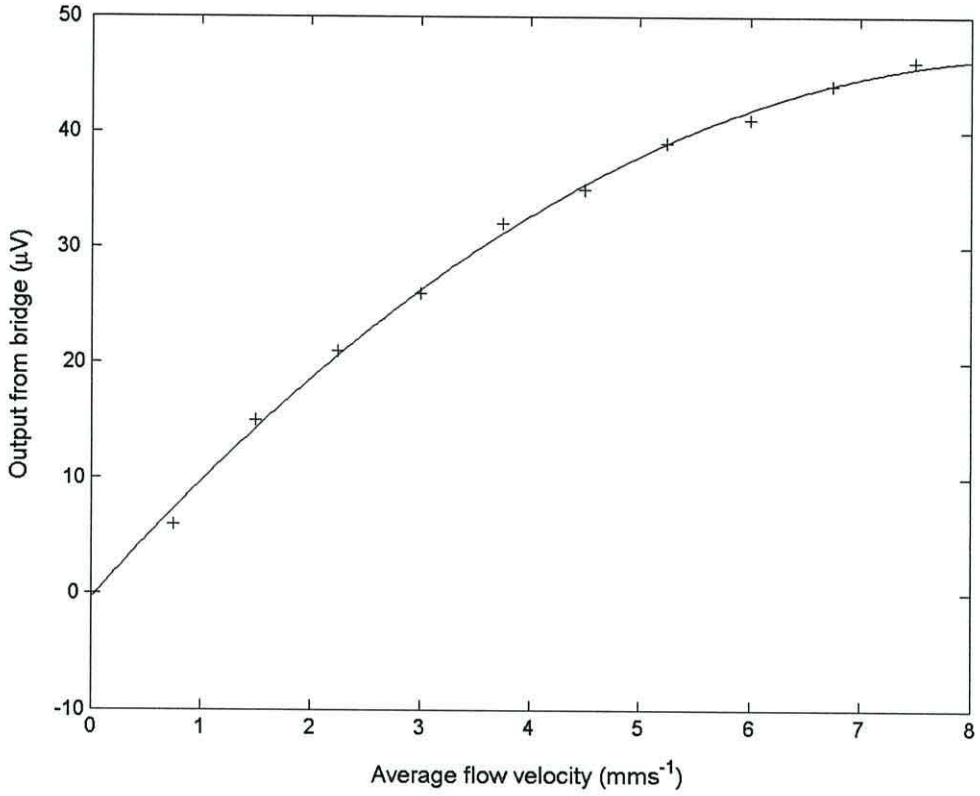

Figure 5.7 *Output from the Wheatstone bridge formed from serpentine electrode tracks against flow rate.*

5.2.5 Straight electrodes

With the serpentine electrodes there is a voltage drop along the length of the tracks, which causes adjacent bends in the track to have different electrical potentials. As the current is increased the potential difference along the wire and between adjacent bends increases. The high potential difference or such a short distance (50μm in this case) can results in electrolysis of the water and causes damage to the electrodes. This problem can be overcome by using straight electrodes. However, this reduces the length of the wires and decreases the sensitivity for a given current and flow rate. The layout of the sensor using a straight wires is illustrated in Figure 5.8.

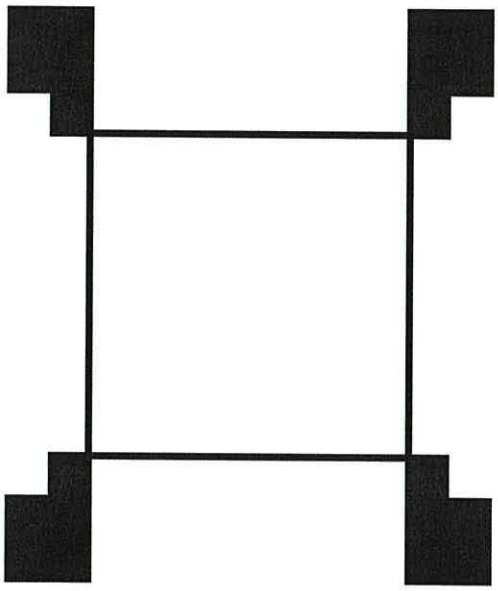

Figure 5.8 *Wheatstone Bridge flow sensor fabricated from straight tracks.*

The electrode tracks were fabricated using the same approach as those described in Section 5.2.4. The bridge circuit was made up of 4 sets of 10μm wide tracks, each 1 mm long and contained within a 200μm deep channel, 2mm wide.

Measurements were taken with constant currents from 1mA to 10mA, in 1mA steps flowing through the bridge. The output voltage was increased by a factor of 1000 using a differential amplifier then measured using an electrometer. A steady pulse free flow of ultra pure water was achieved using gravity feed from a head of water at the inlet of the device as described in Section 5.2.4.

5.2.5.1 Results

Figure 5.9 illustrates the output voltage from the bridge against the flow velocity for 11 different values of current across the bridge, ranging from 2mA to 10mA. Below 1mA it was difficult to take measurements, as the measured signal was of similar amplitude to the noise (approximately 0.5μV). It can be seen that output of the bridge is not proportional to the flow rate. If a linear response is required this could be achieved through the use of additional circuitry or the use of a look-up table implemented either in hardware or software.

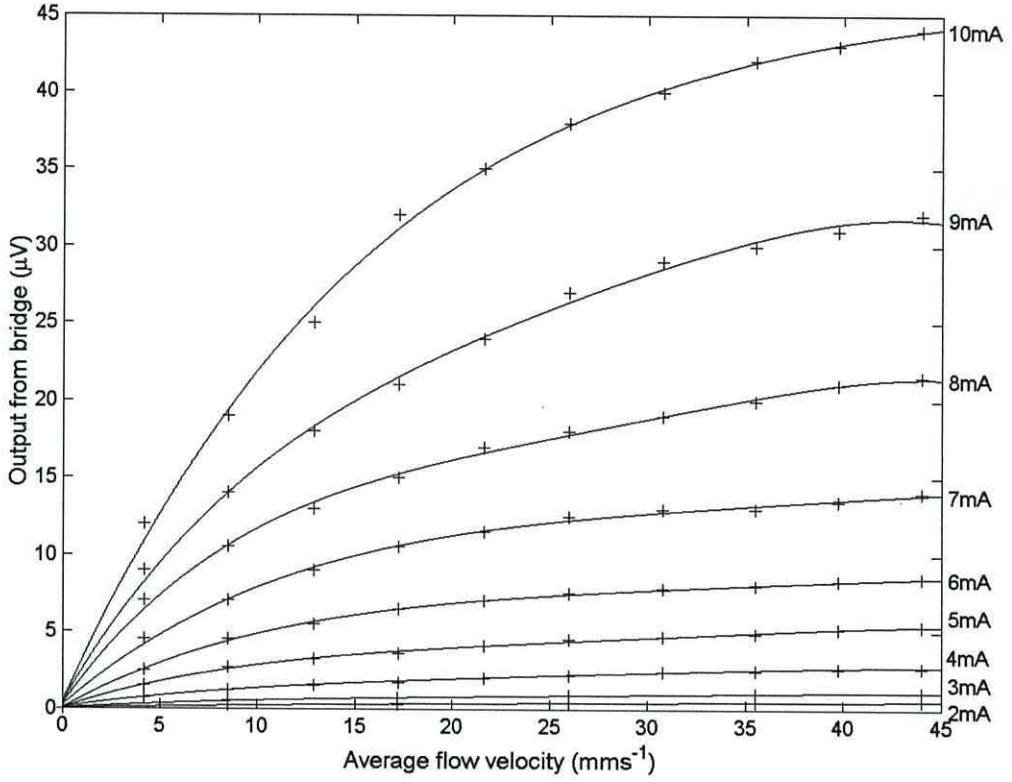

Figure 5.9 *Output from the Wheatstone Bridge formed from straight electrode tracks against flow rate. The measurements were repeated for a range of currents applied across the bridge ranging from 2mA to 10mA.*

The results in Figure 5.9 are presented on a linear scale to provide a clear indication of how the output from the Wheatstone Bridge varies with flow velocity and current. However, using this approach it is difficult to compare the effects at the extremes of high and low currents. Figure 5.10 contains the same data as Figure 5.9 but plotted using a logarithmic axis to show the small currents more clearly.

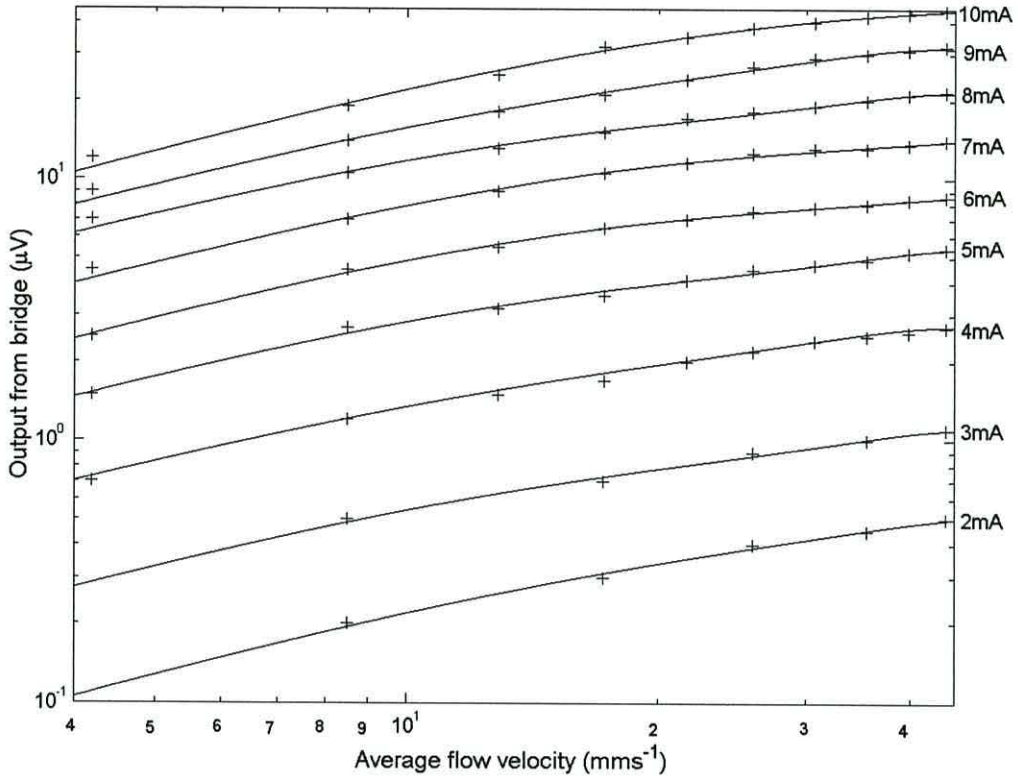

Figure 5.10 *Output from the Wheatstone Bridge formed from straight electrode tracks against flow rate plotted on logarithmic axis. The measurements were repeated for a range of currents applied across the bridge ranging from 2mA to 10mA. The data contained in the graph is the same as that presented in Figure 5.9.*

Figure 5.11 illustrates the output voltage from the bridge against the flow velocity, when a constant current of 5mA is applied across the bridge. The experiment was performed three times to assess the repeatability of the measurements. Each time a measurement was taken the flow rate was reduced to zero and then increased to the value for which a measurement was being taken. As can be seen from the graph in Figure 5.11 the measurements were repeatable. The variation in the values is probably caused by cumulative errors in taking measurement from the electrometer and errors in setting the head of water used to produce the flow. The maximum variation between repeated measurements for this data set was 13% although this dropped for higher flow rates.

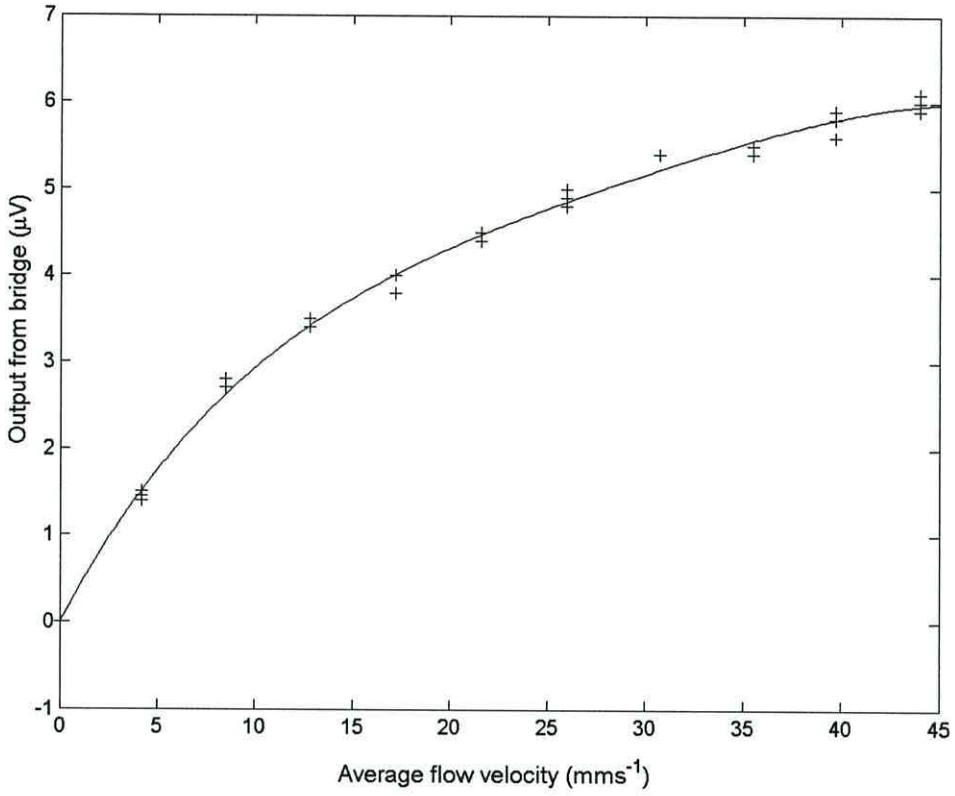

Figure 5.11 *Output from the Wheatstone Bridge for a range of different flow velocities. The current through the bridge was kept constant at 5mA and the measurements repeated 3 times to access their repeatability.*

Figure 5.12 shows the output of the bridge circuit when different currents are applied across the bridge. The flow rate was kept constant at $5\mu ls^{-1}$, which corresponds to a flow velocity of 12.5 mms^{-1}.

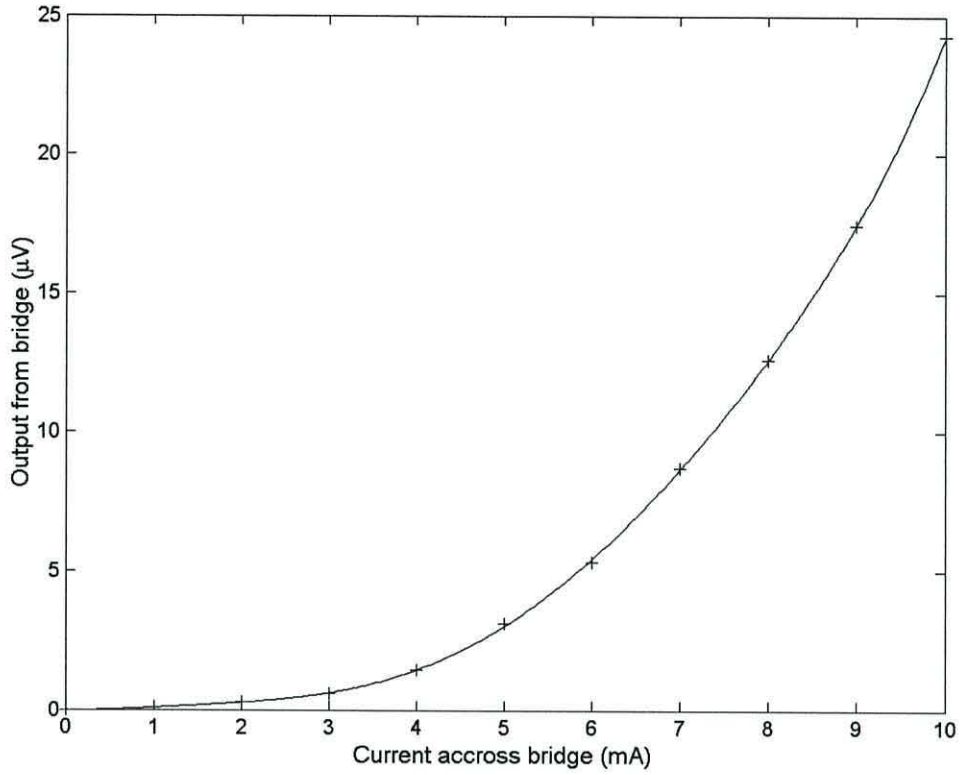

Figure 5.12 *Output from the Wheatstone Bridge for a range of different applied currents. The flow through the channel was kept constant at 5μls^{-1}, which corresponds to a flow velocity of 12.3 mms^{-1}.*

5.2.6 Measurements using a Lock-in amplifier

The sensitivity of the hot wire anemometer, bridge circuit, described previously in this chapter is limited by its susceptibility to background electrical noise. Locating the sensing element in a screened enclosure can reduce interference but this makes measurements more difficult. Lock-in amplifiers reduce the effect of electrical interference by using phase sensitive detection to only measuring the component of the signal that is at the same frequency as the excitation waveform [18,19]. Figure 5.13 illustrates how the bridge circuit is connected to the lock-in amplifier. The constant current source shown in Figure 5.3 is replaced by a sinusoidal voltage source from the lock-in amplifier, which is connected across opposite corners of the bridge. The remaining corners of the bridge are connected to the inverting and non-inverting inputs of the phase sensitive detector section of the lock-in amplifier.

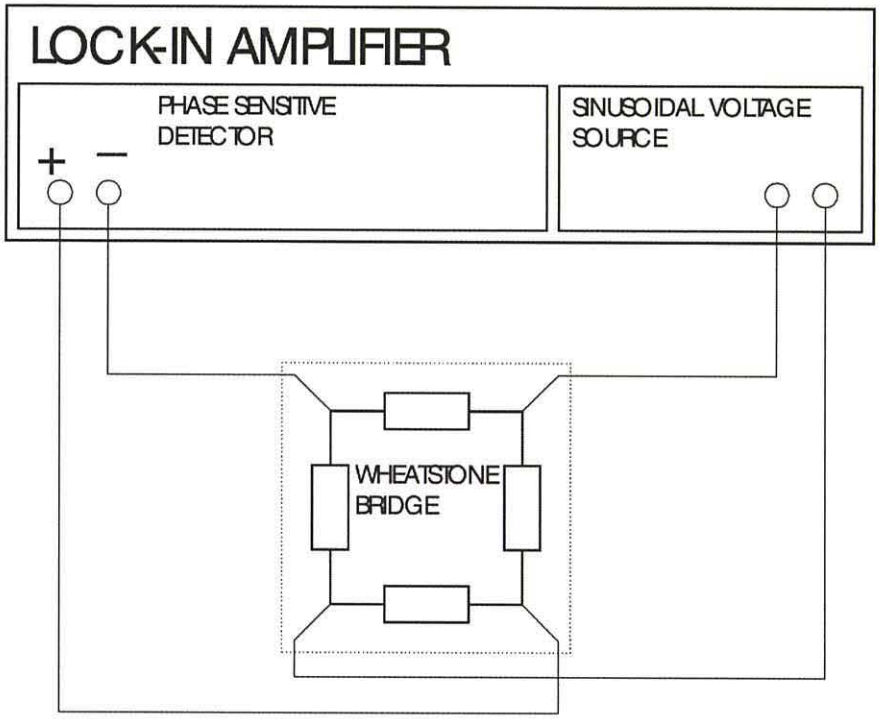

Figure 5.13 *Connections between the lock-in amplifier and the Wheatstone bridge flow sensor.*

Any offset in the output of the bridge when there was no fluid flow was removed using a potential divider connected across the bridge, as previously shown in Figure 5.3.

It is difficult to accurately control low flow rates by varying the head of water, as the pressure difference and therefore height difference between the inlet and outlet is small. To overcome this problem the flow was provided using a Syringe pump (Razel Scientific Instruments, UK). At low settings on the syringe pump the cogging of the mechanism resulted in a highly pulsatile flow. To minimise this effect the pump was only operated at flow rates greater than 10% of the maximum setting. Low flow rates were achieved through the use of a 50µl Hamilton syringe, this gave a reduction in flow of 135 times compared to the 5ml syringe specified for used with the pump.

The lock-in amplifier used to take the measurements was a Model SR830 DSP Lock-in amplifier (Stanford Research Systems, US). To allow measurements to be taken continuously the lock-in amplifier was interfaced to a computer via a GPIB (IEEE 488) interface (National Instruments, US). The control algorithm was implemented in the software package Matlab (MathWorks, Inc, US) and the accompanying instrument

control toolbox. Using this approach it was possible to take several readings of both the magnitude and phase each second.

When using a lock-in amplifier it is possible to vary the frequency of the driving signal, in this case a sinusoidal voltage source. For these measurements a frequency of 1KHz was used. At higher frequencies the lock-in amplifier was unable to provide the necessary current to drive the bridge circuit. Whilst the frequency could be reduced below 1KHz and still provide sufficient current, the lower the frequency the more likely the electrodes are to be damaged through erosion in the high electrical field.

To change the flow velocity from the syringe pump it was necessary to change the setting using a rotary switch. Each time this was done there was a brief transient, possibly due to vibration, before the output settled to a steady value. When taking the measurements the values were logged continuously at a rate of approximately 5Hz, whilst the flow rate was adjusted manually. The steady state output for a given flow rate was then measured from the resulting graph.

5.2.6.6 Results

Figure 5.14 shows the output voltage magnitude from the bridge against flow velocity for different r.m.s. voltages across the bridge. When using lock-in techniques the phase can also be measured but these measurements were noisier. This was probably due to the small reactive content of the circuit. In previous experiments a constant current had been used instead of a constant voltage. However, the measurements shown later in this chapter in section 5.2.7 illustrate that there is only a small change in the resistance of the bridge from the lowest to highest operating temperature. This small change in resistance results in a correspondingly small change in the current through the bridge. The resistance between opposite corners of the bridge and connecting tracks was measured to be 56ohms. Therefore an applied voltage of 0.5v corresponds to a current of 8.9mA ignoring thermal effects. However, as the operation of the device depends upon the tracks getting hot it is obviously unacceptable to ignore thermal effects, these are considered in Section 5.2.7.

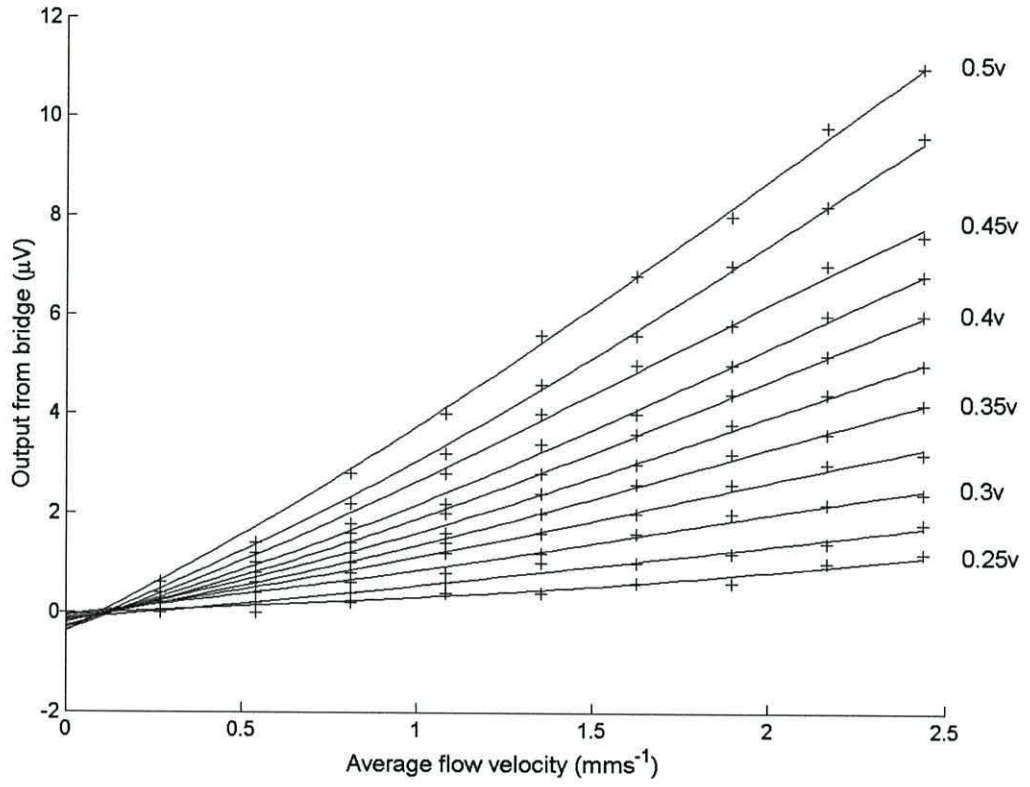

Figure 5.14 *Output of the Wheatstone Bridge flow sensor against flow rate measured using a lock-in amplifier. The measurements were repeated for a range of r.m.s. voltages applied across the bridge ranging from 0.25v to 0.5 volts.*

The results in Figures 5.14 were measured over a range of flow velocities ranging from 0 to 2.5mms-1. These flow velocities are quite large for a micro-fluidic system, where the dimensions are of the order of 10-100µm. However, in applications such as the separation cells by balancing a dielectrophoretic force with a viscous drag [20] flow rates of this magnitude and greater are used. Also the flow rates in micro-fabricated flow cytometers [21,22] are of a similar magnitude or larger. To measure lower flow rates, a 50µl syringe replaced the 1ml syringe previously used with the syringe pump. Figures 5.15 shows the output voltage magnitude from the bridge measured for lower flow velocities. To increase the sensitivity of the bridge the applied voltage has been increased to cover the range 1 to 2.5 volts, this corresponds to a maximum current of 45mA.

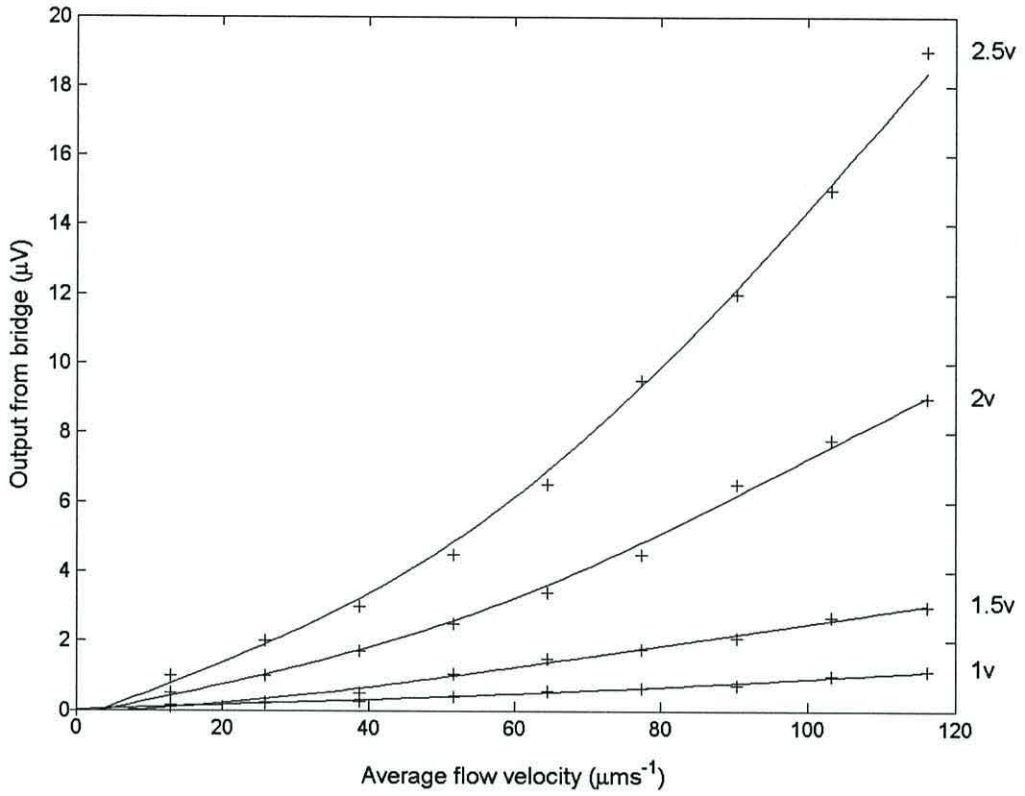

Figure 5.15 *Output of the Wheatstone Bridge flow sensor against flow rate measured using a lock-in amplifier. The measurements were repeated for a range of r.m.s. voltages applied across the bridge ranging from 1 to 2.5 volts.*

From Figures 5.14 and 5.15 it can be extrapolated that the sensitivity of the Wheatstone Bridge flow sensor could be further improved by increasing the voltage, thus increasing the current and operating temperature. However, the lock-in amplifier used to take these measurements is incapable of providing additional current, this problem could be overcome through the use of a power amplifier. In addition to this, as will be shown in the next section, if the current is increased further the temperature of the wires making up the sensor could rise to unacceptable levels. At these high temperatures damage could be caused to any biological particles within the system. Figure 5.19 shown later in this chapter gives output of the sensor against time for a flow velocity of 0.65μms^{-1} The amplitude of the noise at a current of 45mA is approximately 0.1μV. In addition to this noise the output drifted over a range of approximately 1μV limiting the resolution of the sensor.

5.2.7 Measurement of the sensor temperature

As with all metals the resistance of the gold tracks that make up the sensing element increases as the temperature increases. This section describes the calculation of the maximum temperature reached by the sensor by measuring the change in the resistance of the device as the current is increased.

To find the resistance of the flow sensor over a range of currents the I-V characteristic was plotted. A voltage ramp was generated using an auxiliary voltage output on the lock-in amplifier and the corresponding current was measured using a 197 Autoranging Microvolt DMM (Keithly Instruments, Germany). Figure 5.16(A) shows the variation in current with applied voltage and Figure 5.16(B) shows the corresponding change in resistance with applied voltage. The variations in the calculated resistance at low temperatures are a result of the small values of the voltage and current used in the calculation.

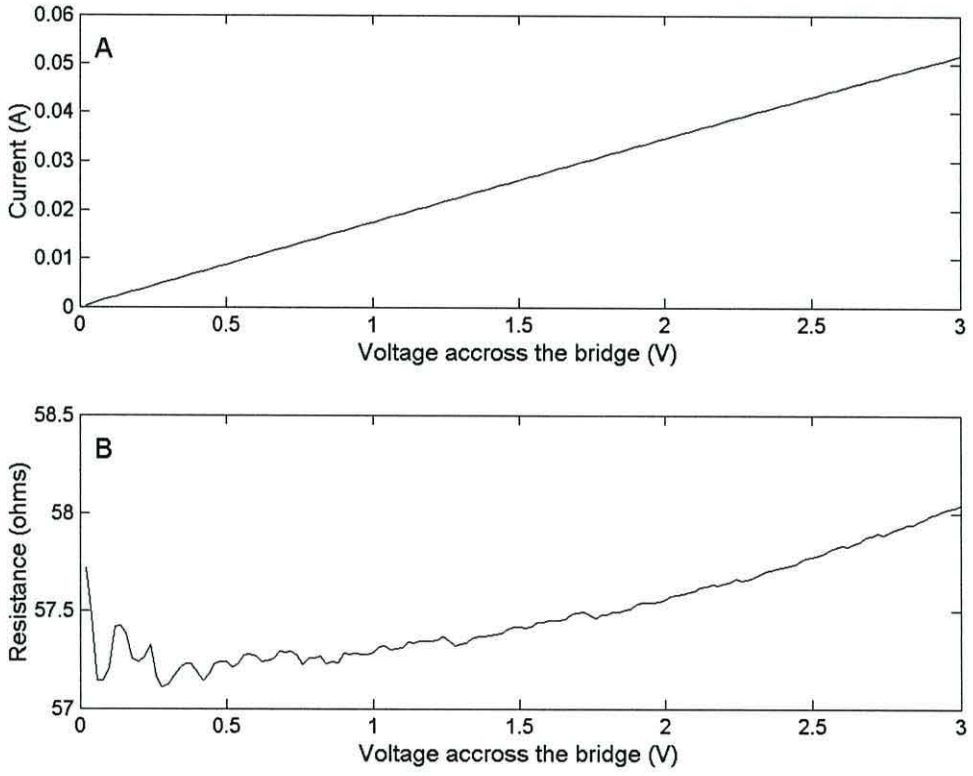

Figure 5.16 *Variation in, (A) the current through the bridge with applied voltage and (B) the resistance of the sensor with applied voltage.*

The graphs in Figure 5.16 show the change in the resistance of the whole device with applied voltage. However, the heating of the device is not uniform due to the difference in the dimensions of the wires making up the sensor and the tracks leading to the sensor. The worst-case scenario, in terms of heating, is that all changes in resistance are due to heating of the sensor wires, whilst the connections to them remain at a constant temperature. To calculate the change in temperature from the change in resistance, it is necessary to calculate how the resistance is distributed. It is not possible to directly measure the resistance of the thin gold wires due to their size. Instead the resistance between opposite corners of the bridge and the resistance across one side was measured. From this the separate resistances can be calculated. The measurement points and the equivalent electrical circuits are shown in Figure 5.17. The resistance of each thin gold wire making up the sensor is R_W and the resistance of each gold track and wire leading to the sensor is R_C. The two measured resistances are R_1 and R_2.

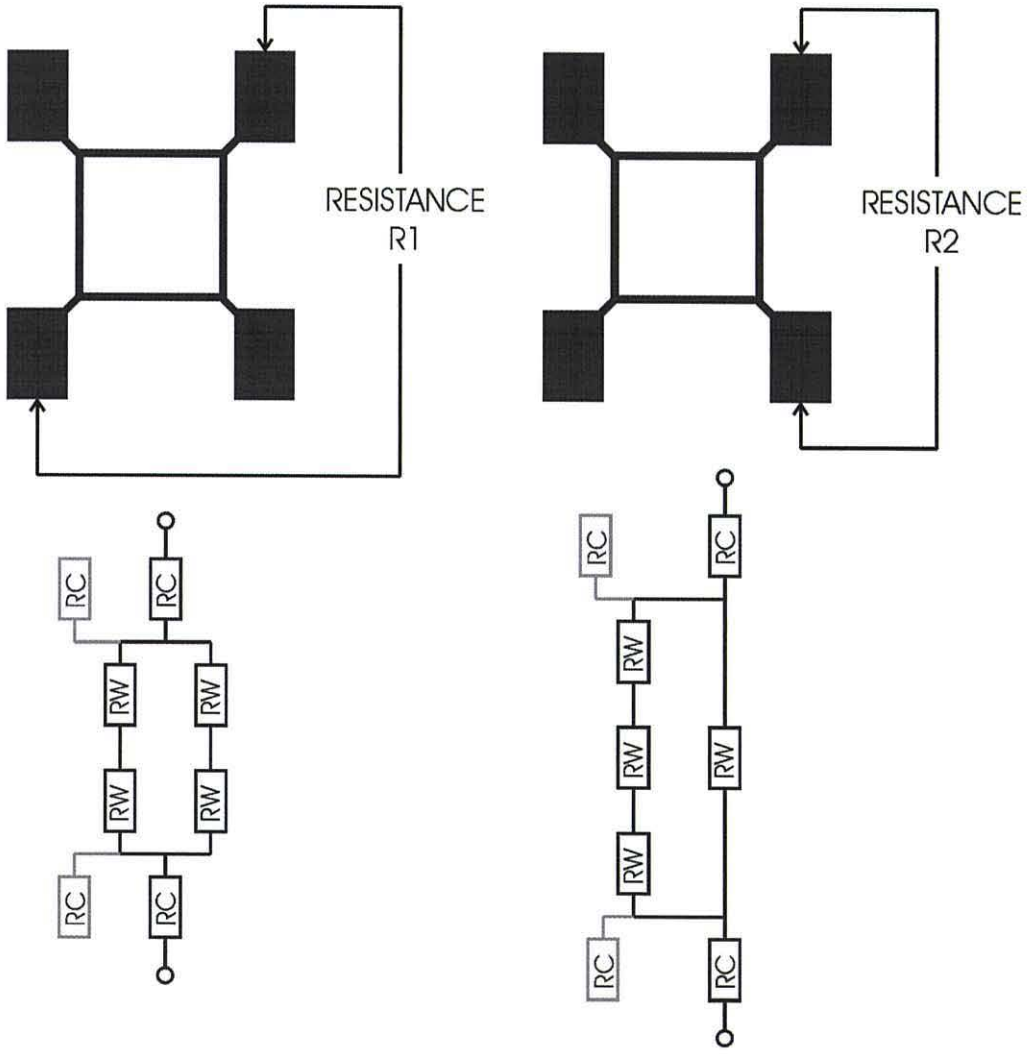

Figure 5.17 *Resistance measurements taken on the bridge circuit and the corresponding equivalent electrical circuits.*

The measured values of the resistances shown in Figure 5.17 are R_1=56ohms and R_2=48.7ohms. By considering the two equivalent circuits the expressions for R_1 and R_2 are.

$$R_1 = 56\Omega = 2R_C + R_W \tag{5.1}$$

$$R_2 = 48.7\Omega = 2R_C + \frac{3R_W \times R_W}{3R_W + R_W} \tag{5.2}$$

By solving this pair of simultaneous equations it was possible to find values for the resistance of the thin wires R_W and the connecting tracks R_C. The values a were R_W=29Ω and R_C=13Ω. The temperature coefficient of resistance of gold at 20°C is 0.34%°C^{-1} [23]. If the change in resistance shown in Figure 5.17 is due solely to a change in the temperature of the thin tracks making up the sensor, the change in temperature with applied voltage can be found as shown in Figure 5.18. The measurement of resistance at low applied voltage is noisy in Figure 5.16. Therefore 57Ω has been taken as the resistance when no voltage is applied.

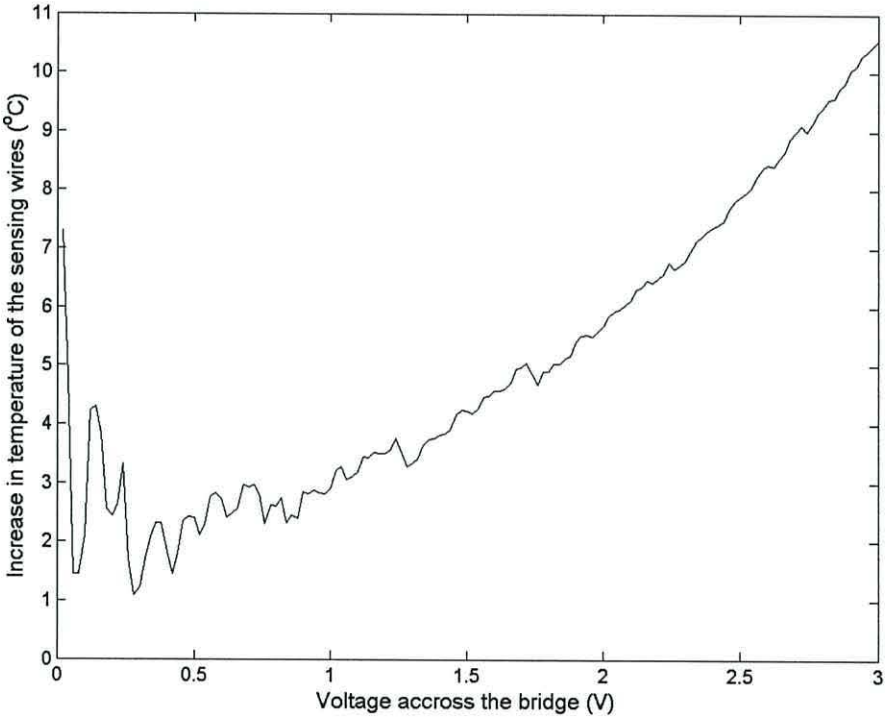

Figure 5.18 *The increase in the temperature of the sensing wire in the Wheatstone Bridge flow sensor as the voltage across the device is increased.*

From Figure 5.18 it can be seen that there is an increase in temperature of the sensing wire of approximately 7.5^{o}C at the maximum applied voltage of 2.5volts. Assuming that the liquid in the channel is normally at 25^{o}C, this results in a maximum temperature of 32.5^{o}C. If there is any significant increase in the voltage applied across the bridge and therefore an increase in the temperature, damage may be caused to any biological particles within the channel. This temperature is the maximum temperature reached; any heat will be rapidly lost down stream in a micro-fluidic system because of the small dimensions of the channel compared to the substrate [24].

5.2.8 Detection of pulsatile flow

As has been mentioned previously in this chapter the syringe pump used to generate the fluid flow was not used at settings below 10% of its maximum value. At low settings the cogging of the stepper motor used to drive the syringe forward resulted in a pulsatile flow. Figure 5.19 shows a short section of the output of the sensor when the syringe pump was used at 0.5% of its maximum value, in conjunction with a 50µl Hamilton syringe. This corresponds to an average flow velocity of 0.65µms^{-1}.

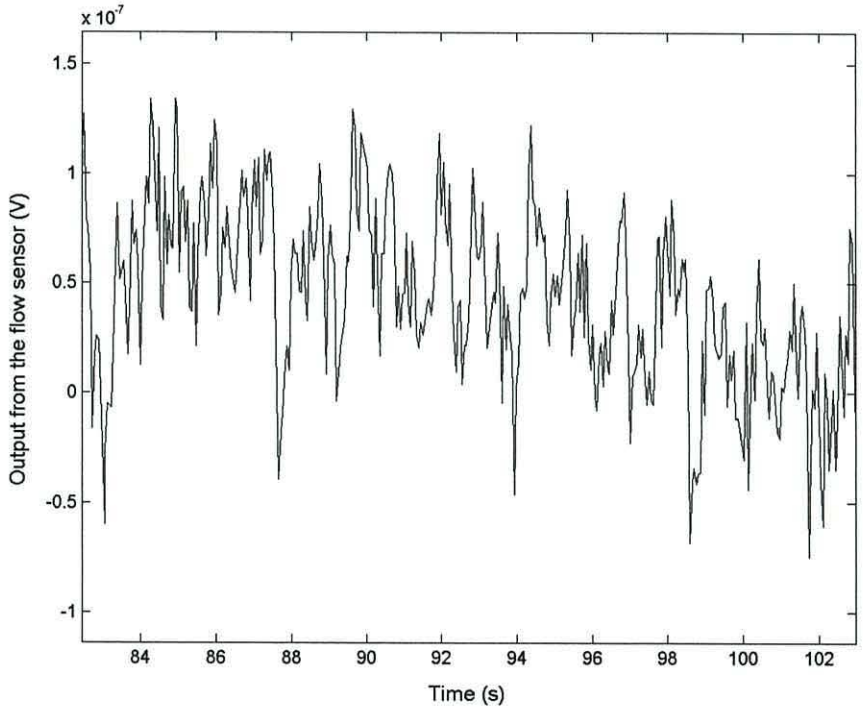

Figure 5.19 *Output of the Wheatstone bridge flow sensor against time when the syringe pump is used at 0.5% of its maximum value in conjunction with a 50µl Hamilton syringe. This corresponds to an average flow velocity of 0.65µls^{-1}.*

From the graph shown in Figure 5.19 it is not possible to accurately measure the flow rate. Although the signal appears to consist of random noise, it is possible to clearly see the cogging of the motor when the data is transferred to the frequency domain as shown in Figure 5.20. To maximise the quality of the spectrum achieved in the frequency domain the signal was pre-processed as follows before a fast Fourier transform was carried out using Matlab. Firstly, subtracting the mean value of the waveform from each point centred the signal on zero. If a Fourier transform is performed on a block of samples with an abrupt start and finish, extra frequency components are introduced due to the square shape of the sample window. This effect was minimised by multiplying the sample block by a hamming function, with the effect of tapering each end of the sample window [25]. Only the low frequency end of the Fourier transform has been shown, as there are few components at higher frequencies.

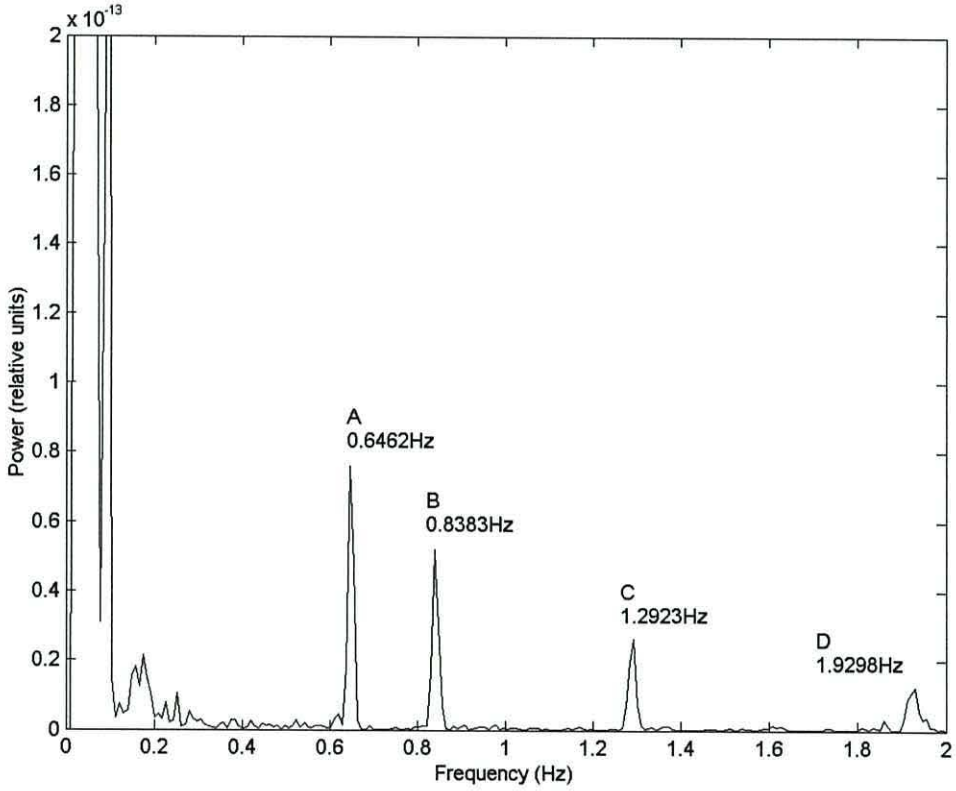

Figure 5.20 *Fourier transform of the Output of the Wheatstone bridge flow sensor when the syringe pump is used at 0.5% of its maximum value in conjunction with a 50µl Hamilton syringe.*

Ignoring the very low frequency components there are 4 main peaks in the Fourier transform of the output of the flow sensor. Peaks C and D are the second and third harmonics of peak A, whilst peak B is from a second unknown source. The absence of

any harmonics for peak B suggests it is a result of some sinusoidal interference. Direct measurement from the syringe pump confirms that peak A corresponds to an oscillation in the flow, resulting from the cogging of the pump mechanism. The experiment was repeated with the syringe pump running at 1% and 0.1% of its maximum flow rate. The Fourier transforms of these signals are shown in Figure 5.21.

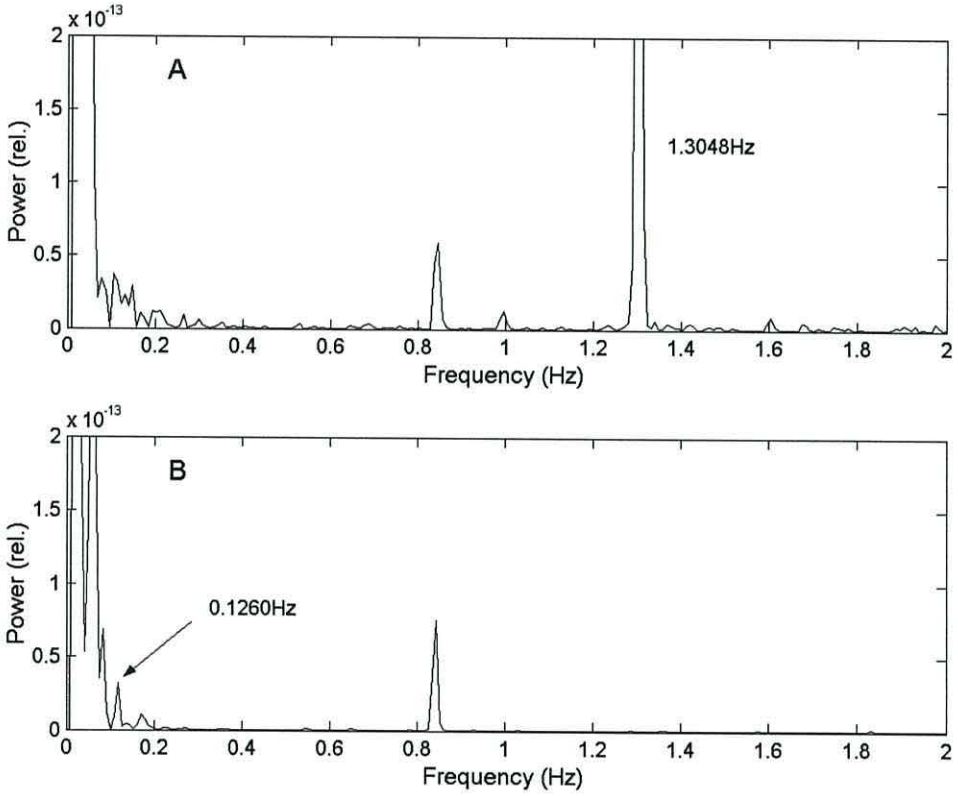

Figure 5.21 *Fourier transform of the Output of the Wheatstone bridge flow sensor when the syringe pump is used at A 1% and B0.1% of its maximum value in conjunction with a 50μl Hamilton syringe.*

The cogging frequency of the syringe pump when it is run at 1% of its maximum value can be seen clearly in Figure 5.21(A). The frequency of 1.34Hz corresponds to twice the frequency measured when the pump was operated at 0.5% of its maximum value as is expected. At the lower pumping rate, Figure 5.21(B), of 0.1% of the maximum value there is a peak at 0.12Hz but this is too close to the low frequency components to be of use.

5.3 Feedback control of fluid flow

One method of separating different cell types from a mixed population is to induce a fluid flow over a set of dielectrophoresis (DEP) electrodes [20]. If the DEP force on the cells is greater than the viscous drag of the fluid then they will remain stationary. As the DEP force is reduced, each cell type with different dielectric properties will be washed away in turn. For the cell types to be accurately separated the velocity of the fluid in the channel must be constant.

To generate a steady flow in a micro-channel a sensor, pump and control circuitry were combined into a closed loop system [26]. A schematic illustrating this system is given in Figure 5.22.

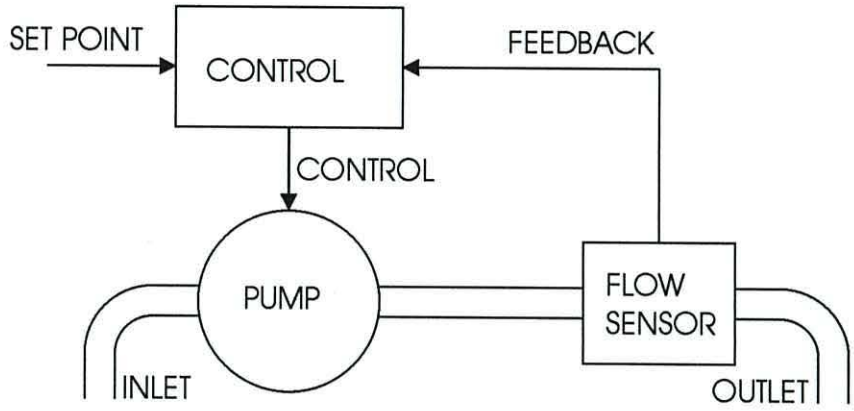

Figure 5.22 *Block diagram of a feedback control system used to control the rate of flow in a micro channel.*

A sensor consisting of 4 hot wires in a Wheatstone Bridge arrangement as described in Section 5.2.5 was used. The sensor produces a dc output voltage that could be fed directly to the analogue control circuitry, making it easy to incorporate into a feedback

When a peristaltic pump is used to generate a fluid flow there are small periodic variations in the flow velocity caused by the periodic spacing of the rollers that compress the pipe. The sensor connected to the control circuitry will detect the variations in the flow velocity. The control circuit will then adjust the speed of the pump to compensate for these variations. Due to the finite response time of the system, there will be a delay between the actual change in flow velocity and the correction to the

speed of the pump. If this delay corresponds to an 180° phase shift between the oscillations in the flow rate and the supply voltage to the pump, the pump will increase the flow rate when it is already high and reduce it when it is already low. This process of positive feedback will cause the magnitude of the oscillations to increase. To reduce the chance of the feedback system oscillating it is important that the pump produces a steady flow. The small centrifugal pump shown in Figure 5.23 was made. The flow produced by this pump was found to be less pulsetile than a gear or peristaltic pump.

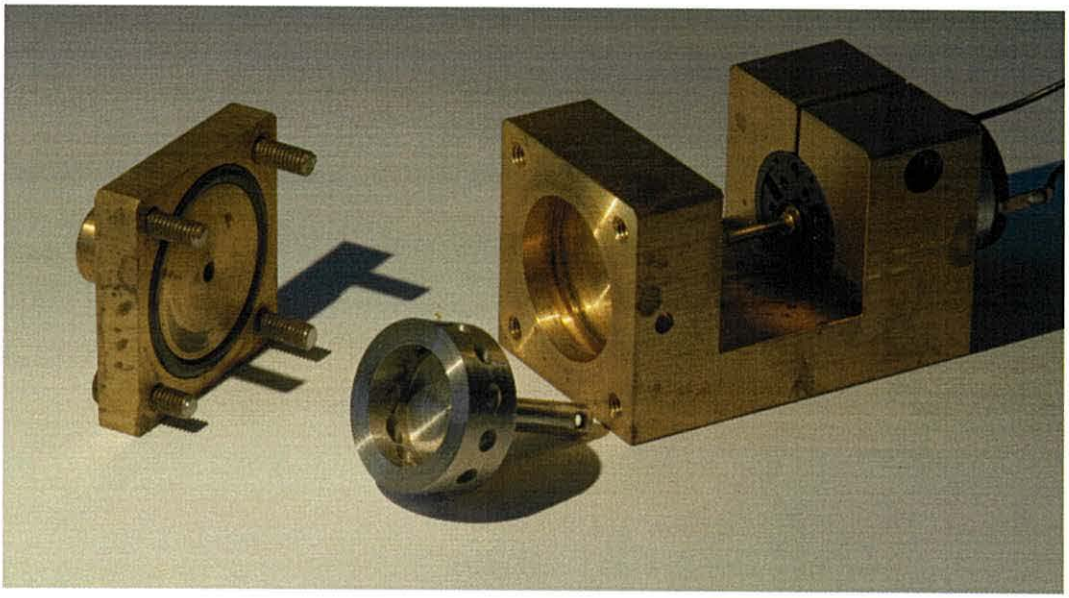

Figure 5.23 *Photograph of a miniature centrifugal pump used to produce small none pulsetile flows.*

In the feedback loop illustrated in Figure 5.22 the desired flow rate, or the set point, is represented by a constant dc voltage. The output from the sensor is fed to an operational amplifier comparator, where it is compared to the set point. The applied voltage to the pump was adjusted by the control circuitry to return the flow rate to the set value.

If the pump were to run in reverse the direction of fluid flow for the centrifugal pump would not change and the sensor would only detect the magnitude of the flow. If the flow velocity were higher than the desired set point, then the control circuitry would reduce the applied voltage. A reduction in the negative applied voltage would further increase the speed of the motor instead of decreasing it. Any corrections to the speed of the motor when it was running in reverse would be in the wrong direction. The control

circuit was such that the supply voltage to the pump was always positive, resulting in the motor always turning in the same direction.

To test the feedback circuit the head of water at the outlet was varied to change the backpressure to the pump. When the head of water at the outlet was increased the speed of the centrifugal pump increased to maintain the flow rate. As the head of water increased the voltage to the motor increased, until limited by the power supply voltage. If the head of water was increased beyond this point the flow rate fell, as the motor could not provide any additional pressure because it was already operating at maximum speed. The system stops functioning properly when the amplifier is saturated, it is therefore necessary to ensure that the initial set point is sufficiently low so that any reduction in the flow can be compensated for by an increase in the speed of the motor.

5.4 Discussion

The aim of the work described in this chapter was to develop simple flow sensors that could be incorporated into the microfluidic channels described in Chapter 3. The requirements of a fluid flow sensor depend on the application with which it is used. For instance in a system which handles biological particles, the sensor must not cause damage to the particles. This research has worked towards developing hot wire flow sensors that can operate accurately in conjunction with biological materials.

In a conventional hot wire anemometer the extent to which the sensor is affected by changes in eternal temperature is governed by the overheat ratio [10,11], which is a measure of the wire temperature relative to its surroundings. This property is covered in more detail in Chapter 2. However in summary, the higher the overheat ratio the less the sensor will be affected by changes in ambient temperature. When a single wire is heated to near 100°C in a gaseous system, changes in ambient temperature can still affect the output [27,28]. To be unaffected the temperature must be several hundred degrees.

If the channel contains biological cells then the temperature is limited to around 40°C for human cells. At these low overheat ratios the sensor will be significantly affected by changes in ambient temperature [10]. To investigate the effectiveness of a simple hot

wire anemometer with a low overheat ratio, a thin gold track was fabricated on a glass substrate that formed one side of a channel. Typically in exiting anemometers the sensing wire is suspended in the centre of the flow [13,27-29]. However, these structures are significantly more difficult to fabricate.

In conventional hot wire anemometers the sensitivity to the ambient temperature can be corrected for by using a second unheated wire or sensor to monitor the fluid temperature [27,28]. This information is then used to correct the measurement from the hot wire. Alternatively a single hot wire can be operated at two different overheat ratios and from the two results the corrected flow can be found [30,31]. Using this approach the error decreases as the difference between the two temperatures increase, This difference would be limited due to the upper temperature limit imposed by biological particles.

In this research compensation for the temperature of the fluid has been incorporated into the sensor itself. This was achieved by constructing a Wheatstone Bridge circuit consisting of four thin gold tracks on one wall of the channel. The tracks parallel to the flow were cooled less efficiently by the fluid than those perpendicular to it, resulting in a voltage drop across the bridge.

Initially the serpentine electrodes shown in Figure 5.5 were used to maximise the length of the wire and therefore the sensitivity of the bridge. This approach was not viable at high currents, as the DC voltage drop along the track caused the electrode to erode at the corners, where the potential difference between adjacent tracks was large. To overcome this problem the sensor was constructed from four straight tracks. By comparing the results for the serpentine electrode tracks and the straight electrode tracks it can be seen that both have similar shaped responses. Although the tracks for the straight electrodes are shorter, high levels of sensitivity can be achieved by increasing the current.

The required sensitivity of a flow sensor depends on the application in which it is to be used. In applications such as flow cytometry [21,22,32] the throughput of the sensor is typically improved by increasing the flow rate past the sensing element resulting in relatively high flow velocities. In contrast the flow velocity produced by some Electrohydrodynamic (EHD) micropumps [33] is measured in tens of μms^{-1}.

The initial approach used was to pass a constant DC current between opposite corners of the bridge and measure any asymmetry in the resistances, by measuring the potential between the other two corners of the bridge. As the flow rate increases, heat is taken away from the electrodes parallel to the flow with greater efficiency, the heat loss from the electrodes perpendicular to the flow is already highly efficient. This cooling of the whole device reduces the rate at which the output voltage increases as shown in Figure 5.9. The near exponential increase in output with increasing current through the bridge is illustrated by the near even spacing of the plots in Figure 5.10.

Figure 5.11 shows some variation in the output when the experiment is repeated. However, this variation is not large and is probably due to errors in carrying out the experiment, such as errors in the height of the head of water. It can be seen from Figure 5.12 that the output of the device increases rapidly as the applied current is increased. This increase in sensitivity is due to both the increase in temperature of the electrodes and greater potential differences across each wire. The rate of heat loss of an object is proportional to the temperature difference between it and its surroundings, so as the temperature of the wire increases the rate of heat loss increases. The amount of power dissipated by a resistor is proportional to the square of the current through the resistor and therefore the increase in sensitivity is non linear. Using this arrangement of current through the bridge it was necessary to use high flow rates to produce a signal significantly larger than the noise threshold.

As the current and therefor sensitivity of the bridge is increased, the DC voltage drop along each wire is also increased. The presence of this high DC potential difference increases the likelihood of damage to the electrodes due to erosion caused by electrolysis in the high fields. This problem increases as the conductivity of the liquid increases. Driving the electrode using an alternating signal decreases the likelihood of damage.

To reduce the effect of interference to a minimum, a lock-in amplifier was used. Using this technique only signals at the same frequency as the excitation waveform are detected. The results in Figures 5.14 and 5.15 show that flow rates in the range $2500\mu ms^{-1}$ down to $10\mu ms^{-1}$ were measurable. This lower limit was imposed by the

syringe pump and syringe available but these are adequate flow velocities for many lab-on-a-chip type micro fluidic devices.

The mechanism for the change in amplitude of the signal when a lock-in amplifier is used is the to the case for a DC current being used to drive the bridge. The voltages quoted in the results are all r.m.s values and have an identical heating effect on the wires as the corresponding DC voltage.

The cross sectional area of the channel used in this work is 2mm by 0.2mm At these dimensions an average flow velocity of $100\mu ms^{-1}$ corresponds to a volume of $0.08\mu ls^{-1}$. This volume is well below the flow velocity delivered by pumps used in microfluidic drug dosing systems [1,34]. These pumps are typically capable of delivering flow rates of several μls^{-1}.

The large majority of hot wire anemometers have been developed for use in gaseous environments and measure velocities of several meters per second [27,29,30]. Those that have been developed for use with liquid flows cover a wide range of flow rates. In a system consisting of a hot wire fabricated on a thin membrane forming one side of a channel, relatively high flow rates in the range $5mms^{-1}$ to $2ms^{-1}$ were measured [35]. A sensor developed as part of a micro dosing system [34] has been shown to measure flow rates in the range of 1 to $80\mu lmin^{-1}$. These flow rates are of a similar magnitude to those achieved in this research, However, the dimensions of the channel surrounding the flow sensor were not recorded so it is not possible to compare the flow velocity. Using silicon fabrication techniques it is possible to construct small sensing wires supported on thin membranes. Using this approach sensors capable of detecting flow rates of the order of $100\mu ms^{-1}$ have been developed [36].

The sensor arrangement developed in this work has been shown to operate over a wide range of flow velocities form $45mms^{-1}$ down to velocities of $10\mu ms^{-1}$ The range of the same sensing element has been varied by adjusting the current through the bridge.

When using hot wire anemometers in systems containing biological particles it is important to ensure high temperatures in the vicinity of the wire do not damage the

particles. Section 5.2.7 of this chapter deals with the measurement of the temperature of the Wheatstone Bridge at different currents. At the maximum current used in this research of 45mA the upper limit of the temperature increase was calculated to be 7.5°C. With this small increase in temperature it is unlikely that any damage will be caused to particles within the cannel.

The detection limit of the sensor was approximately $10\mu ms^{-1}$. at this flow velocity the background noise was of a similar magnitude to the signal from the bridge. Section 5.2.8 shows that by converting the signal from the time domain into the frequency domain using a Fourier transform is possible to detect pulsatile flows with an average velocity as low as $0.65\mu ms^{-1}$.

5.5 Summary

The main aim of this chapter is to develop simple sensors that can be incorporated into the micro-channels described in Chapter 3 to detect the presence of fluid flows. In addition to producing simple sensor elements care was taken, where possible to minimise the complexity of the associated detection circuitry.

When simple interface circuitry was used in conjunction with the microfabricated sensor, the sensitivity was limited to flow velocities measured in mms^{-1}. Through the use of a lock-in amplifier and phase sensitive detection techniques, flow velocities in the range $2500\mu ms^{-1}$ to $10\mu ms^{-1}$ were measured. These flow velocities are comparable with or an improvement upon most previously published research. A lock-in amplifier is a complex and expensive piece of equipment. This is at odds with the desire to reduce the complexity of the detection circuitry. However, a lot of the complexity and cost is due to the versatility of the equipment and for a given problem, relatively simple phase sensitive detection circuits can be produced [18]. At flow velocities below $10mms^{-1}$ it was difficult to directly measure the flow velocity. However, it was possible to detect the pulsatile nature of the flow from the syringe pump by transforming the signal into the frequency domain using a Fast Fourier Transform.

In addition to detecting fluid flow within micro-systems it can also be useful to detect the presence of particle suspensions and individual particles in flow cytometers [21,22]. The next chapter contains a description of a number of sensors that have been developed to do this.

5.6 References

[1] 'Towards integrated microliquid handling systems' M. Elwenspoek, T. S. J. Lammerink, R. Miyake and J. H. J. Fluitman, *Journal of Micromechanics and Microengineering* **4** (1994) 227-245

[2] 'Monolithic flow sensor for measuring millilitre per minute liquid flow' C. Yang and H. Soeberg, *Sensors and Actuators A* **33** (1992) 143-153

[3] 'A mems body fluid flow sensor' E. Meng, S. Gassmann and Y-C. Tai, *Micro Total Analysis Systems 2001* 167-168

[4] 'MEMS flow sensor for nano-fluidid applications' S. Wu, Q. Lin, Y. Yuen and Y-C Tai, *Sensors and actuators A* **89** (2001) 152-158

[5] 'Microfluidic Technology and Applications' Michael Koch, Alan Evans and Arthur Brunnschweiler, *Research Studies Press ltd. 2000. Hertfordshire, UK.*

[6] 'Biology, third edition' Neil A. Campbel, *The Benjamin/Cummings Publishing Company, Inc. 1993 California, US.*

[7] 'Chemical Amplification: Continuous-Flow PCR on a chip' M. u. Kopp, A. J. de Mello and A. Manz, *Science* **280** (1998)1046-1048

[8] 'Microfabricated structure for integrated DNA analysis' M. A. Burns, C. H. Mastrangelo, T. S. Sammarco, F. P. Man, J. R. Webster, B. N. Johnson, B. Foerster, D. Jones, Y. Fields, A. R. Kaiser and D. T. Burke, *Proceedings of the National Acadamy of Science USA* **93** (1996) 5556-5561

[9] 'Instrument Transducers, An Introduction to their Performance and Design' Hermann K. P. Neubert, *Clarendon Press 1975 Oxford, UK.*

[10] 'A comparative study of constant-voltage and constant-temperature hot wire anemometers. Part 1: The static response' M. A. Kegerise and E. F. Spina, *Experiments in Fluids* **29** (2000) 154-164

[11] 'A comparative study of constant-voltage and constant-temperature hot wire anemometers. Part 2: The dynamic response' M. A. Kegerise and E. F. Spina, *Experiments in Fluids* **29** (2000) 165-177

[12] 'Microrobots and micromechanical systems' W. S. N. Trimmer, *Sensors and actuators* **19** (1989) 267-287

[13] 'Micro-liquid flow sensor' T. S. J. Lammerink, N. R. Tas, M. Elwenspoek and J. H. J. Fluitman, *Sensors and Actuators A* **37-38** (1993) 45-50

[14] 'The Art of Electronics, second edition' Paul Horowitz and Winfield Hill, *Cambridge University Press 1989 Cambridge, UK.*

[15] 'Handbook of Transducers for Electronic Measuring Systems' Harry N. Norton, *Prentice Hall. 1969 London, UK.*

[16] 'Constant power operation of a Two-Dimensional Flow Sensor' K. A. A. Makinwa and J. H. Huijsing, IEEE Transactions on Instrumentation and Measurement 51 (2002) 840-844

[17] 'OPO7A component data sheet' *Precision Monolithics.*

[18] 'Electronics, noise and Signal Recovery' E. R. Davies *Academic Press 1993 London, UK*

[19] 'SR830 Lock-In Amplifier Operating Manual and Programming Reference' *Stanford Research Systems 2001 California, US.*

[20] 'Dielectrophoretic separation of cells: Continuous Separation' G. H. Markx and R. Pethig, *Biotechnology and Bioengineering* **45** (1995) 3376-343

[21] 'Micromachined flow cytometers with embedded etched optic fibers for optical detection' C-H. Lin and G-B Lee, *Journal of Micromechanics and Microengineering* **13** (2003) 447-453

[22] 'Development of a microfluidic device for fluorescence activated cell sorting' J. Kruger, K. Singh, A. O'Neill, C. Kackson, A. Morrison and P. O'Brien, *Journal of Micromechanics and Microengineering* **12** (2002) 486-494

[23] 'Kaye and Laby, tables of physical and chemical constants, sixteenth edition' *Longman, Essex, UK*

[24] 'Future trends in diagnosis using laboratory-on-a-chip technologies' M. S. Talary, J. P. H. Burt and R. Pethig, *Parasitology* **117** (1998) S191-S203

[25] 'The Fast Fourier Transform and its applications' E. O. Brigham, Prentice Hall 1988 London, UK

[26] 'Feedback control of dynamic systems' G. F. Franklin, J. D. Powell and A. Emami-Naeini 1994 *Addison Wesley Wokingham, UK*

[27] 'A digital anemometer' K. Okamoto, T. Ohhashi, M. Asakura and K. Wananabe, *IEEE Transactions on Instrumentation and Measurement* **43** (1994) 116-120

[28] 'A thermistor anemometer for low-flow-rate Measurements' H. Fujita, T. Ohhashi, M. Asakura M. Yamada and K. Wananabe, *IEEE Transactions on Instrumentation and Measurement* **44** (1995) 779-782

[29] 'Theoretical and experimental studies of micromachined hot-wire anemometers' F. Jiang and J-C. Tai

[30] 'Hot wire anemometer with temperature compensation using only one sensor' R. P. C. Ferreira, R. C. S. Freire, G. S. Deep, J. S. R. Neto and A. Oliveira, *IEEE Transactions on Instrumentation and Measurement* **50** (2001) 954-958

[31] 'Performance evaluation of a fluid temperature compensated single sensor constant temperature anemometer' R. P. C. Ferreira, R. C. S. Freire and G. S. Deep, *IEEE Transactions on Instrumentation and Measurement* **52** (2003) 1554-1558

[32] 'Micro flow cytometers with buried SU-B/SOG optical waveguides' G-B. Lee, C-H. Lin and G-L. Chang, *Sensors and Actuators A* **103** (2003) 165-170

[33] 'Microfabricated Electrohydrodynamic (EHD) pumps for liquids of higher conductivity' G. Fuhr, R. Hagedorn, T. Muller, W. Benecke and B. Wagner, *Journal of Microelectromechanical Systems* **1** (1992) 141-146

[34] 'Hybrid assembled micro dosing system using silicon based micropump/valve and mass flow sensor' N. T. Nguyen, S. Schubert, S. Richter and W. Dotzel, *Sensors and Actuators A* **69** (1998) 85-91

[35] 'A liquid velocity sensor based on the hot-wire principle' a. J. van der Wiel, C. Linder, N. F. de Rooij and A. Bezinge, *Sensors and Actuators A* **37-38** (1993) 693-697

[36] 'Low cost silicon sensors for mass flow measurements of liquids and gases' N. T. Nguyen, R. Kiehnscherf, *Sensors and Actuators A* **49** (1995) 17-20

Chapter 6

Particulate Detection

6.1 Introduction

The previous chapter described some methods developed during this research for the measurement of fluid flow within a micro-fluidic channel. Often micro-fluidic channels are used to transport suspensions of particles, as is the case for micro fabricated flow cytometers of fluorescence activated call sorters (FACS)[1-5]. This chapter describes methods that have been developed to measure both suspensions of particles and individual particles within micro channels.

The sensors described in this chapter detect the presence of particles by measuring changes in the impedance between electrodes in a fluidic channel. Some of the detection mechanisms described are based around direct current (dc) measurements, so the impedance is purely resistive and no capacitive or inductive component is measured. However, some measurements are carried out using alternating signals (ac) so the impedance is complex and both real and imaginary components can be measured. The impedance of the sensors used in this research depends on the dielectric properties of the material in the channel. A background to the dielectric theory applicable to this work is given in Section 6.2.

Through the use of electrodes on either side of the channel it is possible to measure the overall effective permittivity of the dielectric material in the channel. Section 6.3 describes a sensor that detects groups of particles suspended in the channel by monitoring changes in the permittivity. In addition to detecting suspensions of particles within a micro-system it is also desirable to detect individual particles. To detect single particles, changes in the impedance within the channel were measured. In the research described in section 6.4 a constant current is applied across the channel and the voltage pulse caused by the passage of a large particle detected. In an alternative approach described in Section 6.5 a lock-in amplifier is combined with a four point probe electrode arrangement, to detect the passage of individual yeast cells.

6.2 Dielectric theory

This section deals with the dielectric properties of the materials as relevant to the remainder of the chapter. As an introductory point, a discussion is presented on how the capacitance of a parallel plate capacitor depends on its dimensions and the permittivity of the dielectric material between the plates. Section 6.2.2 explains how the properties of a dielectric change with temperature and the frequency of an applied field and the concept of complex permittivity is introduced in Section 6.6.3. When a dielectric consists of an aqueous solution of ions, an electrical double layer will form at an electrode at low frequencies,. The formation of this double layer and its properties are explained in Section 6.2.4. A suspension of cells in a channel forms a dielectric of more then one material, this is discussed in Section 6.2.5

6.2.1 Parallel plate capacitor

If the two conductors forming a parallel plate capacitor are connected to separate terminals of a voltage source, such as a battery, charge will flow until the capacitor plates possess the same electrical potential as the terminals to which they are connected. The capacitance of a system is defined as the charge present on the conductors, per unit of potential difference between the plates [6].

$$C = \frac{Q}{V} \tag{2.1}$$

Where C is capacitance in Farads, Q is charge in Coulombs and V is potential difference in volts between the plates. In a parallel plate capacitor, ignoring edge effects, the charge is distributed evenly across the plates and the electric field between the plates is uniform. According to Gauss' law the electric field strength between the plates is proportional to the charge density on the plates.

$$E = \varepsilon_o \frac{Q}{A} \tag{2.2}$$

Where E is the electric field strength (Vm^{-1}), Q is the charge (C) and A is the area (m^2) which the charge is distributed. The term ε_o is the permittivity of free space ($\varepsilon_o = 8.855 \times 10^{-12}$ Fm^{-1}) and is the constant of proportionality. As a parallel plate capacitor is being considered, the electric field strength, E, between the plates can also be found by the expression:

$$E = \frac{V}{d} \tag{2.3}$$

Where d is the separation of the capacitor plates. By substituting Equations 2.2 and 2.3 into Equation 2.1, the following expression for the capacitance of an ideal, parallel plate capacitor can be derived.

$$C = \varepsilon_o \frac{A}{d} \tag{2.4}$$

The volume between the plates of a capacitor is usually filled with a dielectric material with a permittivity greater than that of free space. In this case Equation 2.4 takes the form:

$$C = \varepsilon_o \varepsilon_r \frac{A}{d} \tag{2.5}$$

Where ε_r is the relative permittivity of the dielectric. The capacitance is defined solely by the geometry of the system and the permittivity of the dielectric material through which the electric field passes.

6.2.2 Dielectric polarisation

When a dielectric material is placed between the plates of a capacitor, charge on the capacitor plates attracts local charges of opposite polarity within the material and the dielectric becomes polarised [7]. These charges do not allow a current to flow through the material, as they are localised in the form of fixed dipoles. In simple terms, the

dipoles form an effective 'chain' between the two plates of the capacitor, as illustrated in Figure 6.1. The charges at either end of the chain cancel out the charges on the capacitor plates, reducing the potential between the plates and allowing more charge to flow onto the capacitor plates.

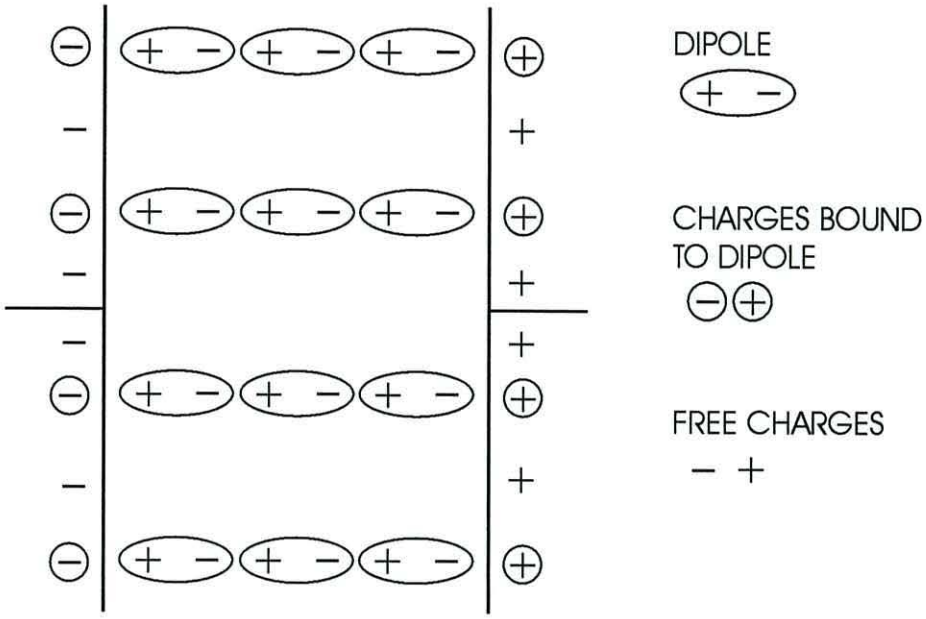

Figure 6.1 *Alignment of dipoles within a dielectric material.*

The extent to which the charges on the plates are cancelled out and therefore, how much extra charge can accumulate, depends on the polarisability of the dielectric material. The polarisation of the dielectric results from the orientation of dipoles with the applied field and the distortion of localised charge distributions. Four key mechanisms of polarisation are illustrated in Figure 6.2 [7].

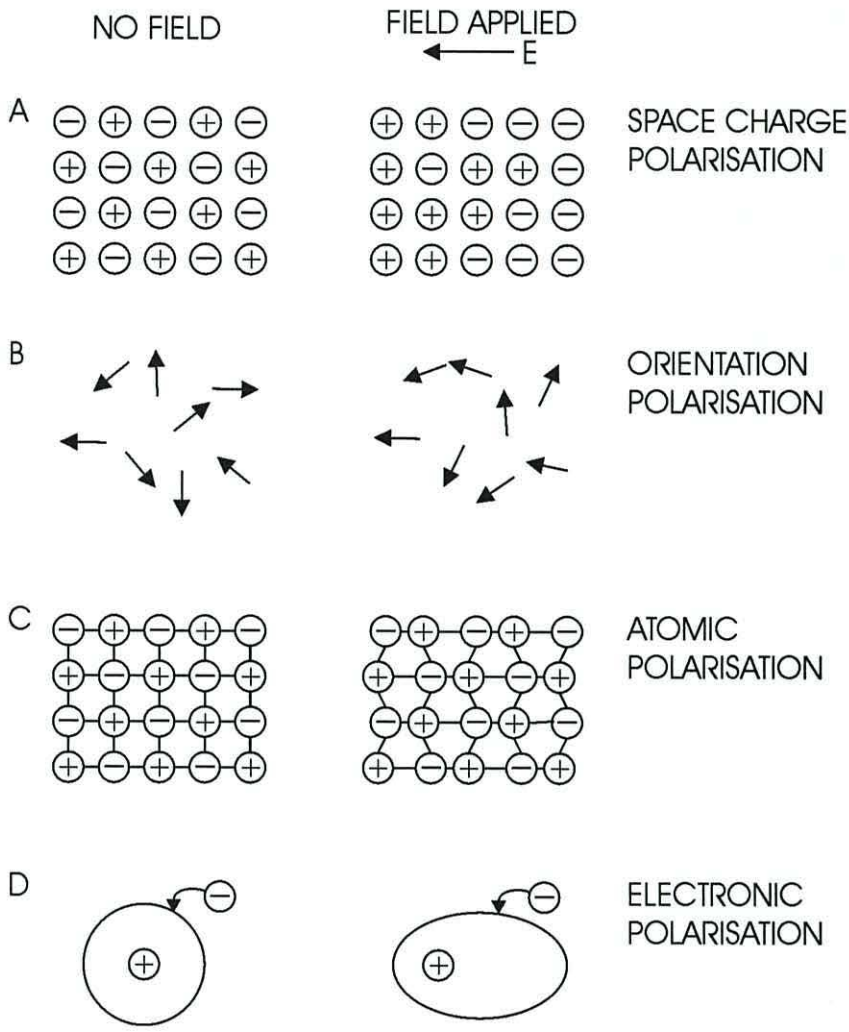

Figure 6.2 *Mechanisms for the polarisation of a dielectric [7]*

Under certain conditions, when it is possible for charges to move freely within the material but not contribute to a current flow, a space charge polarization, illustrated in Figure 6.2A, can occur. This is the case for an aqueous solution of ions, where the potential difference is below that required for electrolysis. The movement of these ionic charges creates an induced dipole moment within the material. The distribution of charge within a molecule is often asymmetrical giving rise to a permanent dipole moment. Figure 6.2B illustrates that the application of an external electric field will exert a torque on such dipoles causing them to tend to align with the field. Within a lattice made up of positively and negatively charged ions, an external field will cause the structure of the lattice to distort as in Figure 6.2C, creating a dipole. The movement of charges relative to each other also occurs within molecules, as well as crystal lattices. On the application of an external field the negatively charged electron cloud of an atom

becomes distorted relative to the positive nucleus resulting in a dipole as shown in Figure 6.2D. The overall polarisation of the material is the combination of these polarisation mechanisms. Generally, the dipoles illustrated at the top of Figure 6.2 will be of a greater strength than those at the bottom.

When an external field is applied to a dielectric, a finite amount of time will elapse before the dipole can form or existing dipoles can align with the field. This time delay occurs because the field exerts a finite force on the charges within the material and it takes a finite time for this force to move the mass with which the charge is associated. Polar molecules have a greater mass than the electron cloud of an atom and so take longer to align with an applied field.

When a low frequency alternating field is applied to a dielectric, all the dipoles are able to re-orientate themselves in phase with the applied field. However, as the frequency of the field increases, some dipoles are unable to change orientation fast enough. Once the dipoles are unable to keep time with the applied field, they do not contribute to the polarisation of the material and therefore the relative permittivity decreases. A simplified representation of the reduction in permittivity with increasing frequency for water is illustrated in Figure 6.3.

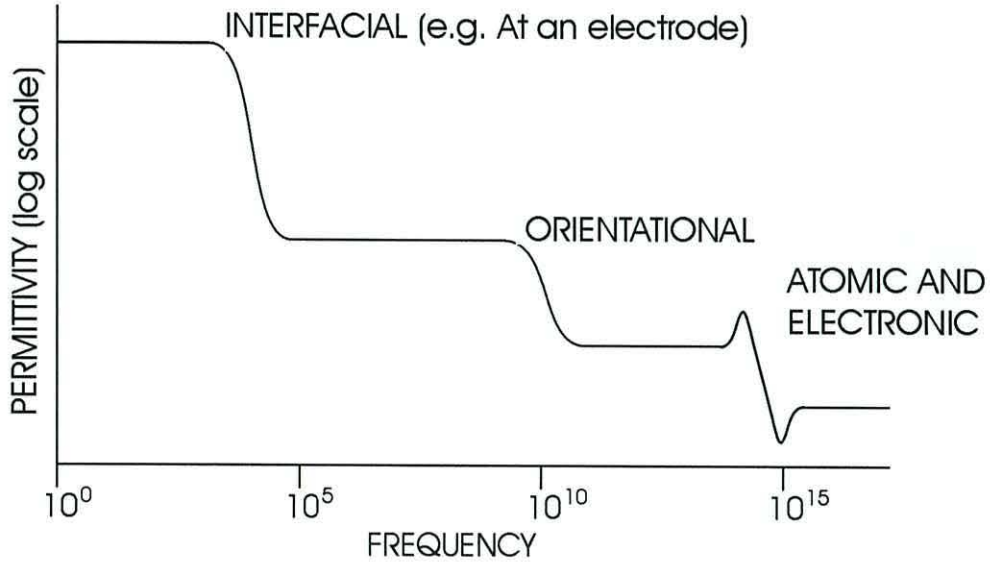

Figure 6.3 *Representation of the decrease in the permittivity of water with the frequency of the applied field.*

The bulk movement of aqueous ions in water is a comparatively slow process. The resulting dipole is only able to keep pace with the applied field up to a frequency of about 1kHz. Above this frequency the relative permittivity drops rapidly to a value of around 80, depending on temperature. The dipoles in the water molecules themselves undergo more rapid rotations but still have a significant mass to move. The relative permittivity of water remains almost constant up to 10GHz and then falls to a value of 4 as the molecular dipoles are unable to keep pace with the applied field. The electrons surrounding an atomic nucleus have little inertia and are able to respond to applied fields up to frequencies of $5x10^{14}$Hz. At higher field frequencies permittivity must be measured using electromagnetic waves. The refractive index of a material can be measured [8] and is related to the permittivity by the equation:

$$\varepsilon_r = n^2 \tag{2.6}$$

Where n is the refractive index of the material. As the temperature of a dielectric is increased its relative permittivity decreases, the permittivity of water drops from 80.37 at 20°C to 78.58 at 25°C [9]. The decrease in permittivity is caused by deflections in the dipole directions within the dielectric, caused by increased thermal agitation.

6.2.3 Complex permittivity

An ideal dielectric is a perfect electrical insulator, therefore no current flows through the material. The dielectrics used in commercial capacitors have a very high receptivity and can be considered as having no conductive losses. However, when considering a dielectric that is not a perfect insulator, it is necessary to include a conductive term. In this case the admittance Y* of a capacitor is given by [10]:

$$Y^* = G + j\omega C = \left(\frac{A}{d}\right)(\sigma' + j\omega\varepsilon') \tag{2.7}$$

Where G is the conductance of the dielectric and σ' and ε' are the real parts of the complex conductivity and permittivity respectively. The asterisk assigned to the term Y

indicates that it is a complex quantity, the remainder are scalar. To incorporate dielectric losses, the conductivity and permittivity are treated as complex quantities in the time domain, giving:

$$\sigma^* \equiv \sigma' + j\sigma'' \tag{2.8}$$

$$\varepsilon^* \equiv \varepsilon' - j\varepsilon'' \tag{2.9}$$

The complex permittivity is used when the material of interest is to be considered as a dielectric with losses. The term σ' is proportional to the power lost in the dielectric per second and the term ε'' is proportional to the power loss per cycle. Equation 2.7 can be rewritten in terms of complex permittivity only:

$$Y^* = j\omega C^* = j\omega\left(\frac{A}{d}\right)\varepsilon^* = \left(\frac{A}{d}\right)(\omega\varepsilon'' + j\omega\varepsilon') \tag{2.10}$$

or in terms of complex conductivity to give:

$$Y^* = \left(\frac{A}{d}\right)(\sigma' + j\sigma'') \tag{2.11}$$

6.2.4 Electrode double layer

When the dielectric in a capacitor consists of an aqueous solution of ions, an electrical double layer can form at the surface of each capacitor plate or electrode. A double layer is formed from an arrangement of charges and orientated dipoles adjacent to the electrode. At low frequencies this double layer significantly increases the capacitance between the electrodes, whilst at higher frequencies, such as 100kHz it is unable to form rapidly enough to effect the capacitance.

Helmholtz postulated in his model [11] of the double layer that sufficient ions are attracted to the electrode to form a layer of equal charge to that on the electrode as illustrated in Figure 6.4.

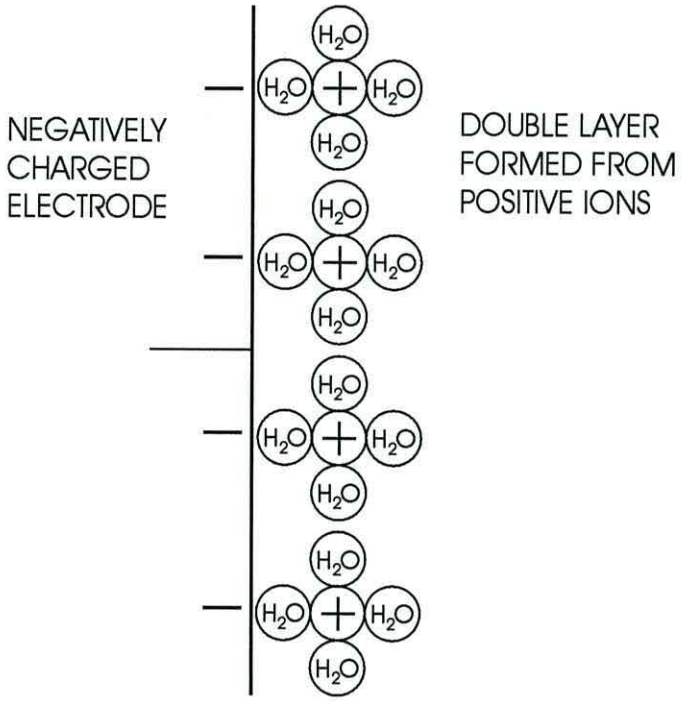

Figure 6.4 *Helmholtz model of the electrical double layer.*

As illustrated in Figure 6.4, a hydration sheath made up of polarised water molecules surrounds the ions. The radius of this hydration sheath limits the proximity of the ions to the electrode. The accumulation of opposite charges near the electrode nullifies the charges already on the electrode, allowing more charge to accumulate. This has the effect of increasing the effective permittivity of the dielectric and therefore the capacitance.

The Helmholtz model assumes that the ions in solution form a uniform sheet of charge adjacent to the electrodes. The model does not take into account thermal motions within the solution that will have a disruptive effect on the sheet of charge. In the Gouy-Chapman model [41] the sheet of charge is replaced with a diffuse layer of anions and cations. Within this diffuse layer there is an excess of ions of an opposite charge to the electrode. To simplify the model the diffuse layer of ions is considered as a number

of parallel planes of charge progressing away from the electrode into the bulk solution as illustrated in Figure 6.5.

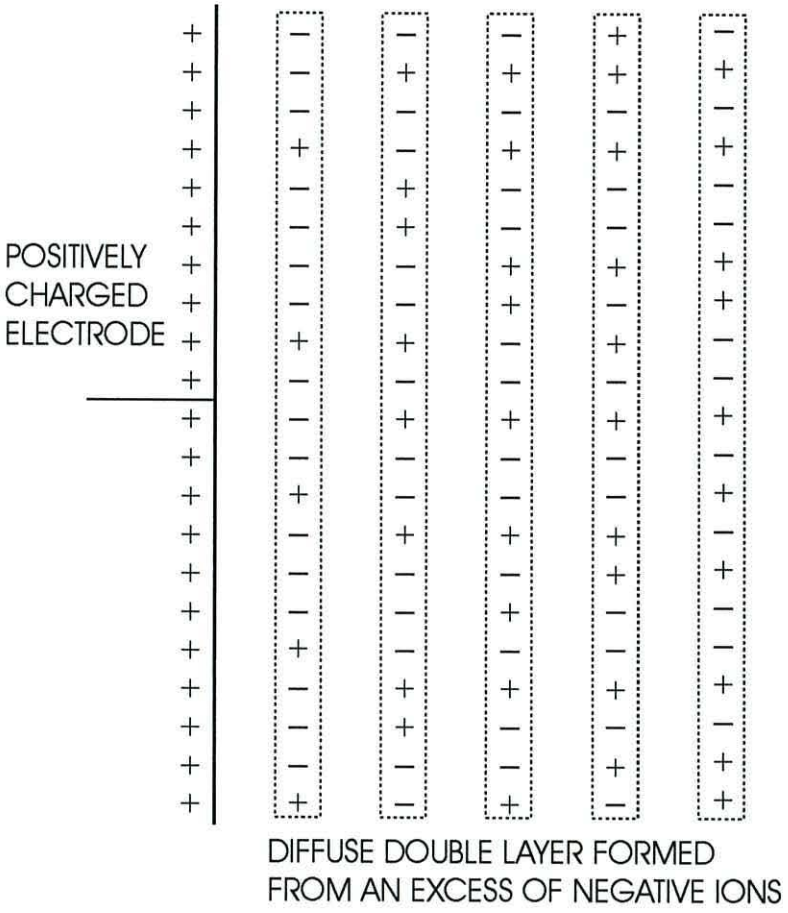

Figure 6.5 *Gouy-Chapman model of the electrical double layer.*

In this model the first plane of ions will experience the greatest effect from the charges on the electrode, so will have the largest excess of opposing charges. The charges in the first plane will then screen some of the charges on the electrode, so less of an effect will be felt by the charges in the second layer, resulting in a smaller excess of opposite charges. This screening process continues until the charge in the diffuse layer balances the charge on the electrode. At large distances from the electrode the charge distribution will be homogenous. The total excess charge in the diffuse layer matches the magnitude of the charge on the electrode.

The distance that the diffuse layer spreads into the solution depends on the charge density on the electrode and the density of ions in the solution. As the charge on the

electrode is increased more opposite charges are required to cancel them out, resulting in a thicker double layer. If however, there are a large number of opposing ions available in the solution it is more likely that they will be brought near to the surface by random thermal motions. This increase in the excess of opposing ions in each plane of ions causes the double layer to become thinner.

6.2.5 Dielectrics of more than one material

When dielectric measurements are undertaken on materials within a channel on a lab-on-a-chip device the dielectric may not be homogenous. This is the case for a suspension of cells or particles in water. This section will first consider a capacitor containing two distinct slabs of dielectric, which could represent the idealized case of two laminar fluid flow streams. Then dielectrics consisting of a suspension of particles will be considered.

Figure 6.6 illustrates a simple case where the dielectric of a capacitor is made up of two different "materials" in series. The equivalent circuit for this arrangement is also illustrated.

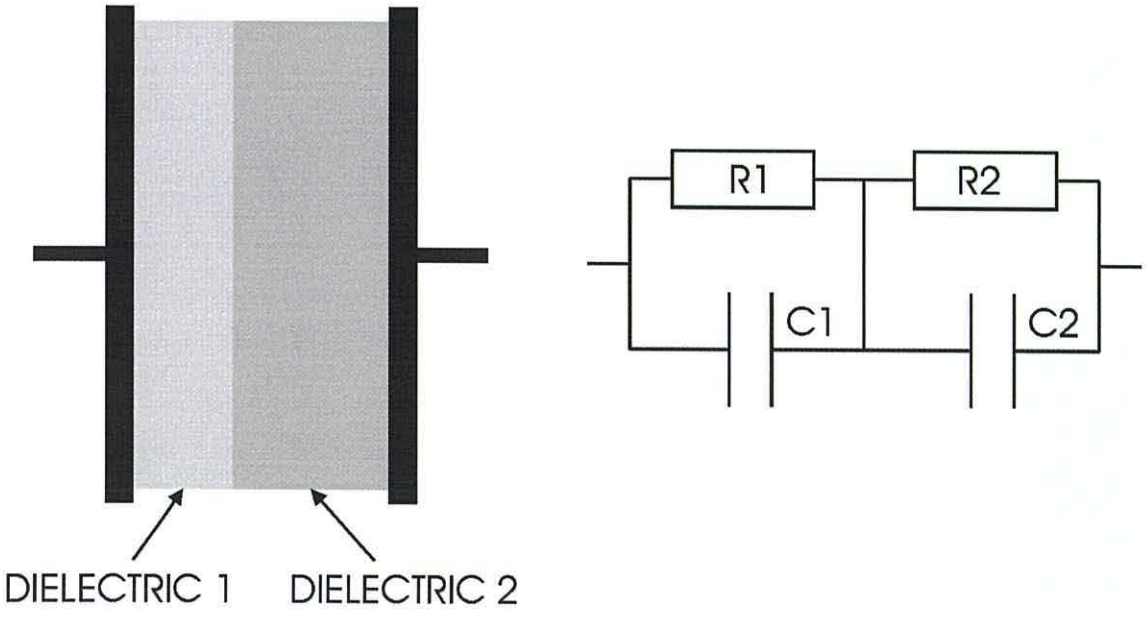

Figure 6.6 *A capacitor consisting of two separate dielectrics in series and the corresponding equivalent circuit*

Maxwell-Wagner effects [12] deal with processes at the interface of two dielectrics, such as in Figure 6.6. From consideration of the equivalent circuit it can be seen that at low frequencies the capacitive components can be considered an open circuit and the impedance of the system will be determined by the resistors. Whilst at high frequencies the impedances of the capacitors drop below that of the resistors and the overall impedance will be determined largely by the capacitors. The expressions for the series capacitance for this system at extremes of frequency are.

$$C_{f\to 0} = \frac{\left(C_1 R_1^2 + C_2 R_2^2\right)}{\left(R_1 + R_2\right)^2} \tag{3.11}$$

$$C_{f\to \infty} = \frac{C_1 C_2}{\left(C_1 + C_2\right)} \tag{3.12}$$

The externally seen capacitance converges at high frequency with a value lower than that observed at low frequencies. In the system consisting of two slabs of dielectric in series, as shown in Figure 6.6 there is a classical Debye type dispersion similar to those shown in Figure 6.3. However, in this case it is not related to the relaxation time of the dielectric. A Dedye type dispersion also appears with two capacitors and one resistor.

6.2.5.1 Particles in suspension

When biological materials such as blood are considered, two main features dominate the dielectric properties. The first of these relates to the fact that the suspending medium has a significant conductivity, due to the high concentration of ions. The other feature is the presence of suspended particles, for example platelets and cells in blood. An analytical solution for the d.c. conductivity of a dilute solution of spherical particles was developed by Maxwell [13]. The conductivity of the suspension is σ, with σ_a and σ_i being the conductivities of the medium and particles, respectively. The relationship is given by the equation:

$$\frac{(\sigma - \sigma_a)}{(\sigma + 2\sigma_a)} = \frac{p(\sigma_i - \sigma_a)}{(\sigma_i + 2\sigma_a)} \tag{3.14}$$

Where p is the particle volume fraction. A diagram of a capacitor whose dielectric consists of a suspension of particles is shown in Figure 6.7.

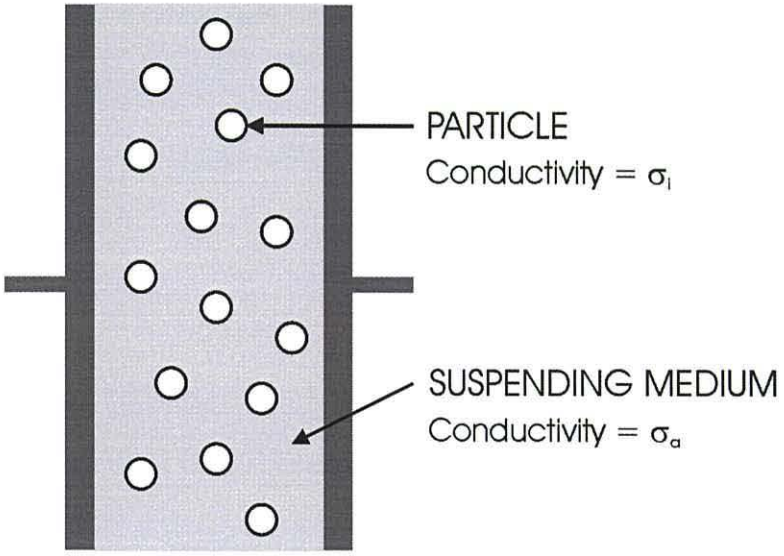

Figure 6.7 *A capacitor whose dielectric medium consists of a suspension of particles of volume fraction p.*

As mentioned previously the relationship given in Equation 3.14 is valid for dilute suspensions of particles. If the volume fraction ,p, is increased above 0.1 [14] the relationship no longer holds, due to interactions between particles. The volume fraction of particles in blood is higher, if this relationship is to be used the volume fraction must be reduced by diluting the suspension to give a particle volume fraction below 0.1.

The relationship in Equation 3.14 was developed further by Wagner [15] to cover a.c. measurements and the use of complex conductivities. It was also extended to cover non-spherical particles by Fricke [16,17], where the factor γ depends on the particle shape. The factor γ has a value of 2 for spheres and 1 for cylinders normal to the field.

$$\frac{(\sigma^* - \sigma^*_a)}{(\sigma^* + \gamma\sigma^*_a)} = \frac{p(\sigma^*_i - \sigma^*_a)}{(\sigma^*_i + \gamma\sigma^*_a)} \qquad (3.15)$$

This expression was further extended by Fricke [18] to include membrane covered spheres as illustrated in Figure 6.8 in a suspension which better represents biological cells in suspension.

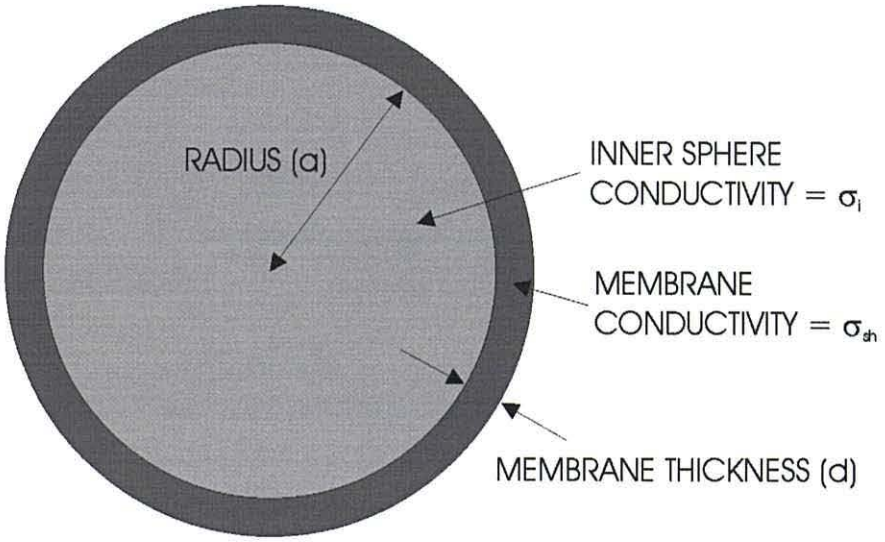

Figure 6.8 *A membrane covered sphere where membrane thickness is much less then the radius of the inner sphere.*

The overall complex conductivity of a single sphere within a sphere is given by the equation:

$$\sigma^* = \frac{\sigma^*_i - \left(2d/a\right)\left(\sigma^*_i - \sigma^*_{sh}\right)}{\left(1+d/a\right)\left(\sigma^*_i - \sigma^*_{sh}\right)/\sigma^*_{sh}} \tag{3.16}$$

Where the membrane thickness d is much less than the radius of the inner sphere a. The complex conductivity of the inner sphere is σ_i and that of the membrane σ_{sh}. The conductivity of the complete sphere can now be inserted into Equation 3.15 to give the complex conductivity of the whole suspension. The resulting equation can be solved for the special case where the membrane is dominated by capacitance C_m to give the relationships [19,20]

$$\Delta\varepsilon' = \frac{9paC_m}{4\varepsilon_0} \tag{3.17}$$

$$\sigma_s = \sigma_a\left(1-\frac{3p}{2}\right) \tag{3.18}$$

$$\tau = aC_m\left(\frac{1}{2\sigma_a}+\frac{1}{\sigma_i}\right) \tag{3.19}$$

Where $\Delta\varepsilon'$, σ_s and τ are the real part of the permittivity, the real part of the conductivity and the relaxation time constant, respectively. From these relationships it can be seen that when cells, each possessing a capacitive membrane, are introduced into a suspending medium it would be expected that the permittivity and therefore capacitance would increase, whilst the conductivity would decrease.

The situation described so far takes no account of the double layer described in the previous section, which is formed at a charged solid liquid interface. In aqueous suspensions of small particles, such as cells these double layer effects usually dominate the response up to frequencies of the order of 50KHz, depending on the medium conductivity. To take this double layer effect into account a model was developed by Schwartz [21-23], where the counter ions surrounding the particle are bound within the double layer and allowed to move laterally within it. Using this model, expressions for the relaxation time constant and the change in permittivity are:

$$\tau = \frac{a^2 e}{2\mu kT} \tag{3.20}$$

$$\Delta\varepsilon = \frac{9p}{(2+p)^2}\frac{e^2 a q_{sn}}{kT} \tag{3.21}$$

Where a, μ and q_{sn} are the particle radius, counter ion mobility and surface charge density respectively. From this model we can predict that the effective permittivity of a suspended particle can exceed that of the bulk aqueous suspending medium. This is consistent with the large changes in permittivity that can be observed.

6.3 Detection of cell suspensions

When a micro-system is used to process biological samples it is useful to be able to monitor the movement of the samples around the device. Micro-channels are normally pre-filled with a buffer solution to prevent the formation of air bubbles. For a sensor to detect biological samples it must be able to discriminate between a buffer containing the sample and the buffer. The permittivity of pure water is different that of a mixture of particles and water [24]. By measuring the effective permittivity of the fluid in the channel, it is possible to find the concentration of a specific particle type, in this case yeast cells. The permittivity of the cell suspension and of buffer varies depending on the frequency of the applied field. The variation in permittivity with frequency of the cell suspension is much greater than that of buffer. The sensitivity of this type of device can be maximised by taking measurements at a frequency where the permittivity of the cell suspension is significantly different from that of buffer. At low frequencies the aqueous buffer near the electrodes will electrolyse causing damage to the electrodes, this effect is not significant above frequencies of 1kHz.

To detect the presence of biological cells, electrode tracks were fabricated on the top and bottom of the channel to form a capacitor, the electrodes used were 10μm gold tracks running the width of the 1mm wide channel. The 200μm deep channel in Figure 6.9 was formed from a UV curing adhesive sandwiched between the two electrode substrates as described in Section 4.7.

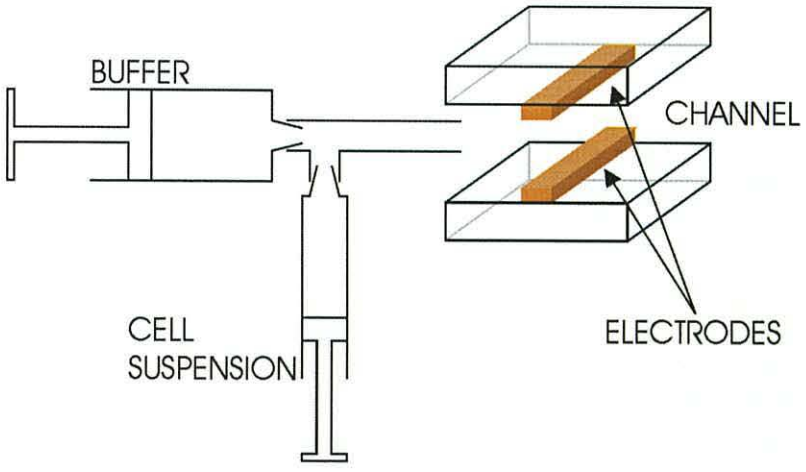

Figure 6.9 *Apparatus used to flush slugs of cell suspension between two electrodes forming a sensor.*

In the apparatus illustrated in Figure 6.9 a 100μl slug of cell suspension was injected into a pipe running to the channel and then flushed through the sensor with 1ml of clear suspending medium, at a rate of 200 ml per second. To test the device a sample of RXII yeast cells were washed four times in a solution of phosphate buffered saline (Sigma Chemical co. US.) of conductivity 250μScm^{-2}. The clear buffer solution was obtained by centrifuging a weak solution of cells. By using the supernatant at the top of the centrifuge tube this ensured the empty buffer solution had the same dielectric properties as the buffer containing the cells. The capacitance of the sensor formed across the channel was found using an A192A impedance analyser (Hewlett Packard, US) and was logged using a PICO ADC-42 analogue to digital converter (Pico Technology Limited, UK) attached to a computer. By varying the frequency at which the measurements were taken it was found that a high level of sensitivity could be achieved at a frequency of 1kHz. The experiment was repeated for different cell concentrations that were measured using a Gleman Hawkley haemocytometer.

6.3.1 Results

The graph in Figure 6.10 shows the capacitance of the device as three cell slugs of concentration $5x10^8$ cells ml^{-1} are passed through it. It can be seen that the capacitance drops as the cells pass through the device. These measurements were taken at a frequency of 1KHz.

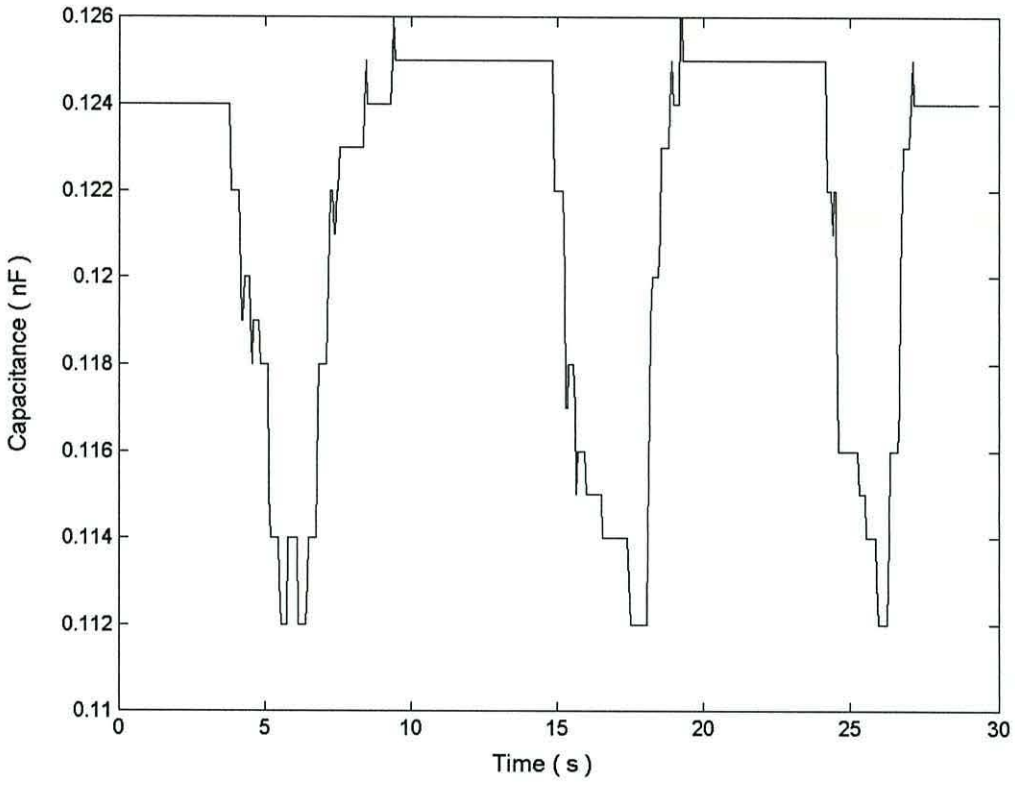

Figure 6.10 *Capacitance measured across a channel 200μm by 1mm as 3 slugs of cell suspension of concentration $5x10^8$ pass the sensor.*

The results in Figure 6.11 show the drop in capacitance of the sensor when four cell slugs of different concentrations are passed through the device.

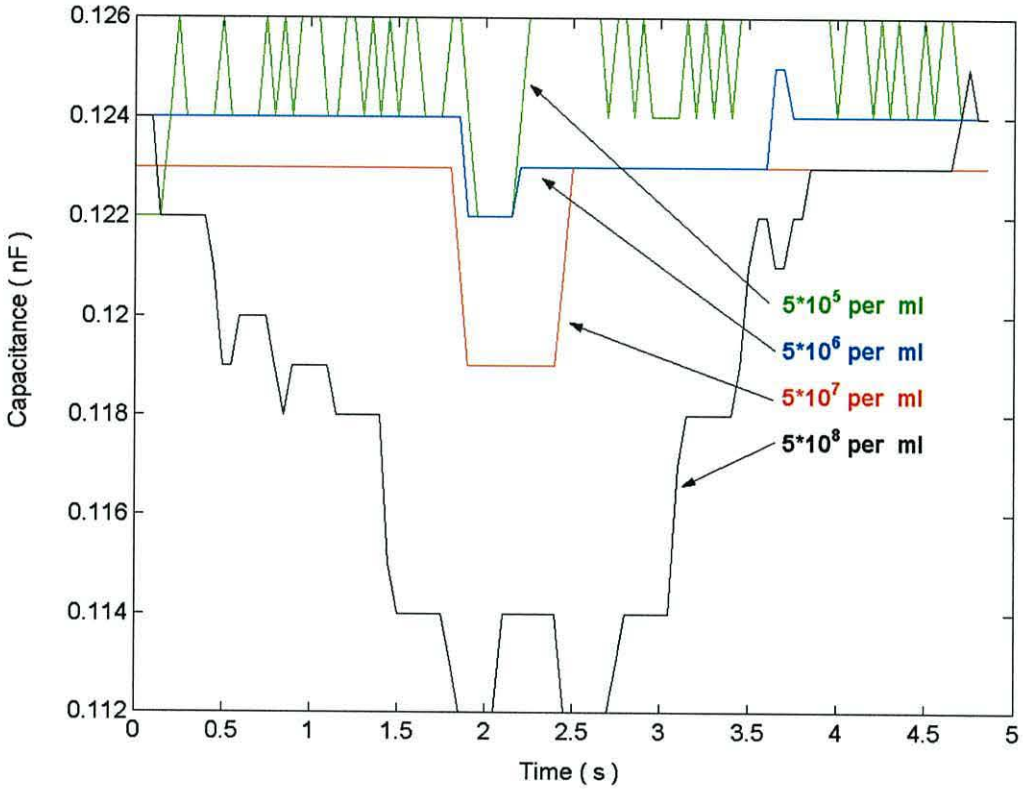

Figure 6.11 *Drop in the capacitance of the sensor for different cell concentrations.*

It can be seen from the data that the fall in the capacitance caused by each cell slug is not instantaneous. The sloping sides of each falling edge is due to the spreading of the slug, arising from the parabolic flow profile within the channel. The steps in the results are due to the output of the impedance analyser, which limits the detection sensitivity of this arrangement to concentrations above $5x10^5$ cells ml^{-1} as seen in Figure 6.11.

From the discussions in Section 6.2, it would be expected that the capacitance would increases rather than fall when particles pass through the sensing element. It can be seen from Figure 6.11 that this is not the case for these measurements.

6.3.2 Verification of the results

To verify the accuracy of these results shown in Figure 6.11 further experiments were Undertaken to confirm that the capacitance of the sensor does decrease with increased cell concentration.

To ensure that the effect is due to the presence of cells in the suspension, not changes in the conductivity due to the loss of ions from the cells, 280 $mmolL^{-1}$ manitol was introduced into the buffer to equalize the osmotic preasure between the inside and outside of the cell and reduce the loss of ions from the cell. Also the more rigorous preparation process outlined later also introduced.

Increasing both the length of the electrodes and therefore the width of the channel scaled the magnitude of the capacitance measured. Increasing the magnitude of the capacitance reducer relative size of the quantisation noise that can be clearly seen in Figure 6.11. The channel width was increased from 1mm to 6mm. In these experiments, instead of passing a slug of cell suspension through the device and constantly measuring the capacitance at one frequency, the cell concentration was kept constant and the capacitance in each case measured over a range of frequencies.

As mentioned previously, when preparing suspensions with different cell concentrations it is important to ensure that only the number of cells per millilitre are varied and not the conductivity of the medium. At the frequency of 1Khz a change in the medium conductivity will change the properties of the double layer formed at the electrodes and therefore alter the measured capacitance. The suspending medium in this case consisted of a $280mmolL^{-1}$ solution of manitol that was made up to a concentration of $260mScm^{-1}$ using phosphate buffered saline. As will be discussed in more detail in Chapter 8 the manitol increases the osmotic pressure within the solution, which reduces the loss of ions from the yeast cells. To remove any residue of the growth medium the yeast cells were washed four times and re-suspended in buffer. 0.5ml of this cell suspension was then removed and diluted with 4.5ml of the buffer to give a reduction in concentration by a factor of 10. This process was repeated twice, giving reductions in concentration of 100 and 1000. Each of these samples was then washed a further two times to ensure the conductivity of the suspending medium in each case was the same. Once this washing

had been completed the capacitance measurements were undertaken immediately. After the experiment the sample was centrifuged once more and the conductivity of the supernatant measured.

During the capacitance measurements a steady stream of particle suspension was fed through the sensor. The capacitance measurements were taken using a 4284A Precision LCR Meter (Hewlett Packerd, US) and recorded via a GPIB interface (National Instruments, US). This capacitance bridge was used for these measurements instead of the one used previously because it measures to a greater precision, however the time taken to measure each value is significantly longer, of the order of several seconds.

The conductivity and permittivity of the buffer changes with temperature. To ensure that the measured effect was not due to a temperature drift the samples were re-measured in reverse order and the same change in capacitance with concentration observed.

Figure 6.12 shows the variation in capacitance with frequency for 4 different cell concentrations.

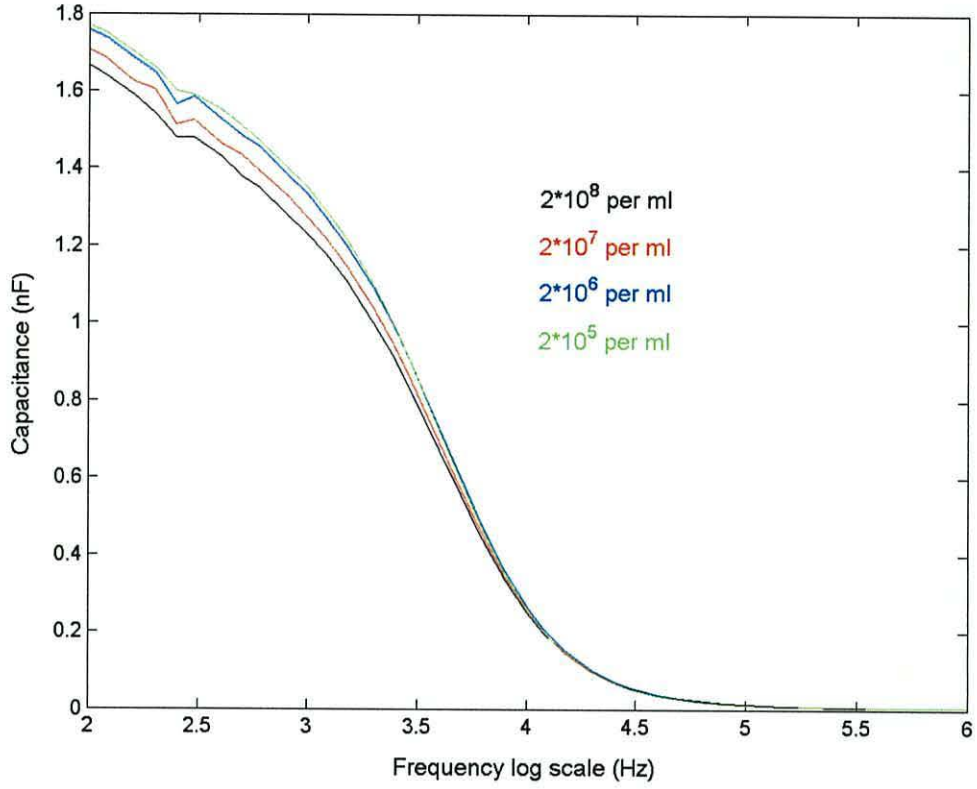

Figure 6.12 *Capacitance against frequency plots for suspensions of yeast cells of four different cell concentrations.*

At low frequencies the drop in measured capacitance with increased cell concentration can be clearly seen. Figure 6.13 shows the measured capacitance of the sensor over the frequency range 100KHz to 1MHz.

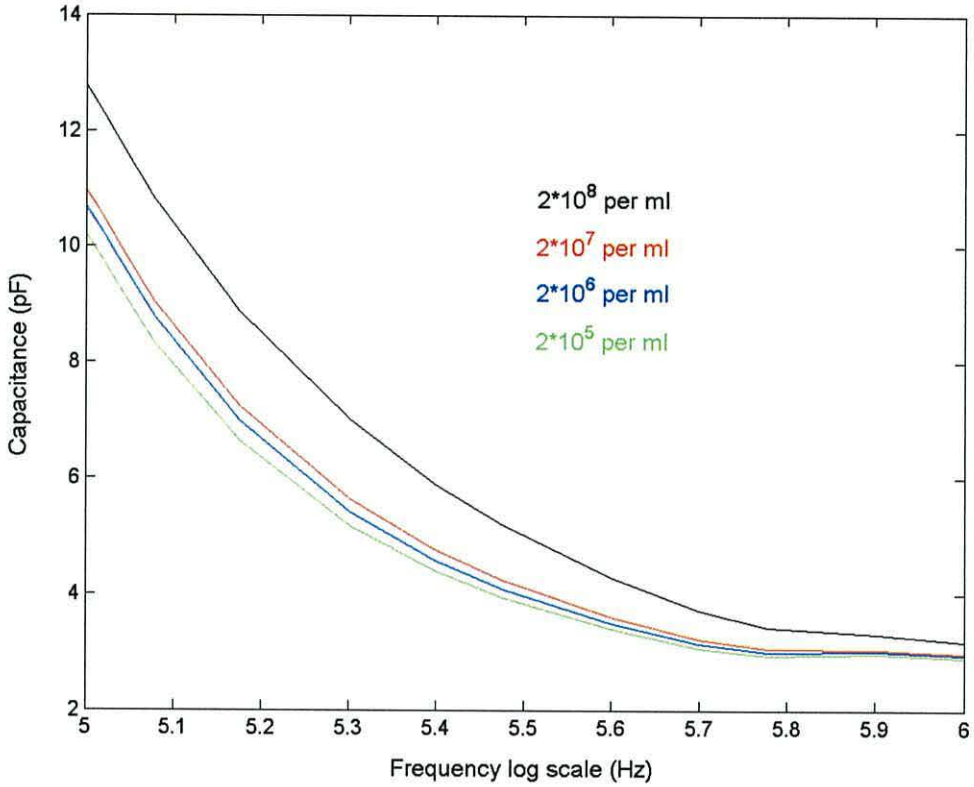

Figure 6.13 *Capacitance against frequency plots for suspensions of yeast cells of four different cell concentrations, displayed over the frequency range 100KHz to 1MHz.*

At these frequencies the order of the samples is reversed, with the measured capacitance increasing as the concentration of the cell suspension increases.

Once the capacitance measurements had been taken, the supernatant conductivity for the unused fractions of the solutions were measured. These conductivities are given in the table below.

Cell Concentration (per ml)	Supernatant Conductivity µScm-1
$2x10^8$	265
$2x10^7$	260
$2x10^6$	261
$2x10^5$	261

It can be seen from this table that there is no change in the supernatant conductivity except for the highest cell concentration where there is a slight increase.

6.3.3 Discussion

Despite extensive discussions with Prof. R. Pethig, Dr J. P. H. Burt and Dr S. Bone, a satisfactory explanation for this phenomenon at low frequencies has not yet been reached. As a simple first approximation to explain the results. The cell can be considered as a conducting sphere surrounded by an insulating cell wall. As the frequency is increased the impedance of the membrane capacitance of the cell wall will fall and the cell can be considered as a conducting sphere. The frequency at which this happens is referred to as the beta dispersion and is of the order of 1MHz. At an excitation frequency of 1Khz the insulating cell has an overall relative permittivity of approximately 4 compared to water, which has a relative permittivity of approximately 80. This dispersion occurs at the 'wrong' frequency to account for the results shown in Figure 6.12. The following explanation assumes that the polarization of the particle is lower than that of the medium at low frequencies but higher than that of the medium at high frequencies.

In this work, at low frequency, the polarisability of the yeast cell within the aqueous dielectric is less then the polarisability of the medium. Figure 6.14 shows the effect (neglecting edge effects) when only the medium is present (A), some of the medium is replaced by a particle that is less polerisable (B) and when some of the medium is replaced by a particle that is more polerisable (C) [25].

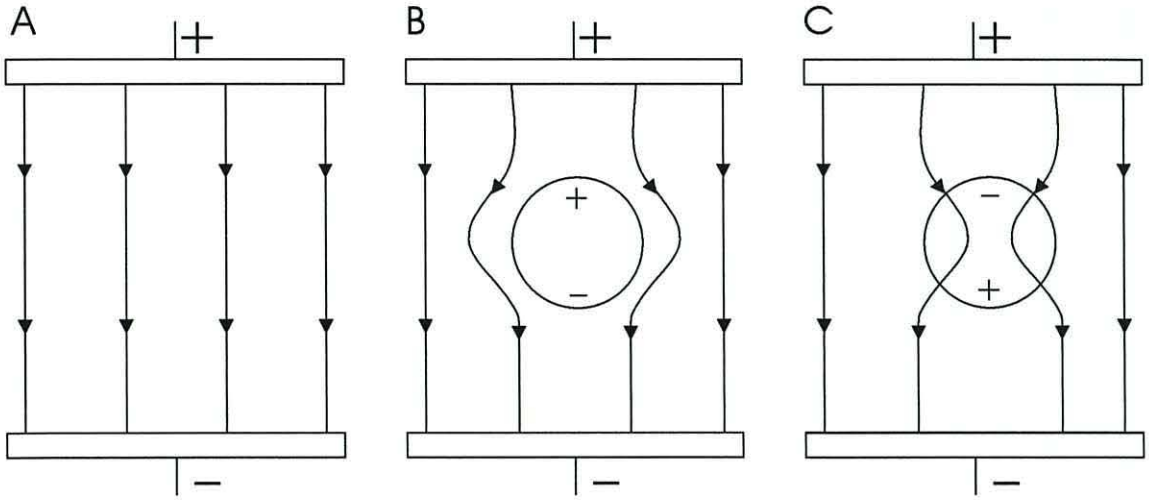

Figure 6.14 *the effect on the electric field of a particle between the electrodes. (A) when no particle is present, (B) when the particle is less polerisable than the medium and (C) when the particle is more polerisable than the medium.*

Figure 6.14A is the case when there are no particles in the fluid or the concentration is very low, the volume between the electrodes if filled with medium of relative permittivity 80. Figure 6.14B represents the case for the low frequency part of the graph in Figure 6.12, a region of relative permittivity 80 is replaced by a less polarizable cell, resulting in a reduction in the overall permittivity and therefore the capacitance. Figure 6.14C represents the case for the high frequency part of the graph, a region of relative permittivity 80 is replaced by a more polarizable cell, resulting in an increase in the overall permittivity and therefore the capacitance.

The results shown in Figure 6.12 were taken at a frequency of 1KHz. At this frequency there is a large double layer effect. This effect needs to be taken into account when analysing these results.

Normally to avoid affects due to the presence of a double layer at the electrodes and around the cells in this case, measurements are carried out at higher frequencies. However as can be seen from figure 6.12 the magnitude of the change in capacitance due to the presence of cells in suspension is a lot smaller at high frequencies.

Although a satisfactory explanation for the results has not been found they are highly repeatable.

6.4 Single particle detection

In addition to detecting suspensions of particles within a micro-system it is also useful to be able to detect individual particles. This is typically done using a micro Coulter Counter [26,27], a device that passes particles through a small aperture in a fluid filled channel with electrodes either side. A change in the resistance of the channel is measured when a particle passes through the hole.

Using a similar approach the detection electrodes used in this research were situated across the channel, a constant current was applied between the electrodes and the voltage monitored. When a particle of a different conductivity to that of the suspending medium passes between the electrodes, the resistance between them will change. To maintain a constant current the applied voltage changes. This change in voltage signifies the passage of a particle through the sensor.

Thin gold electrodes 10μm wide running across the width of the channel were fabricated onto two glass substrates. A channel 200μm deep and 500μm wide was fabricated from UV curing adhesive sandwiched between the substrates, as described in Section 4.7. The constant current between the electrodes was provided by the Wilson Current Mirror shown in the previous chapter in Figure 5.2. The voltage between the electrodes was amplified using a 741 amplifier and recorded using a computer and analogue to digital converter. To test the device, 35 glass beads of diameter 100μm were passed through the channel. Figure 6.15 illustrates this experiment.

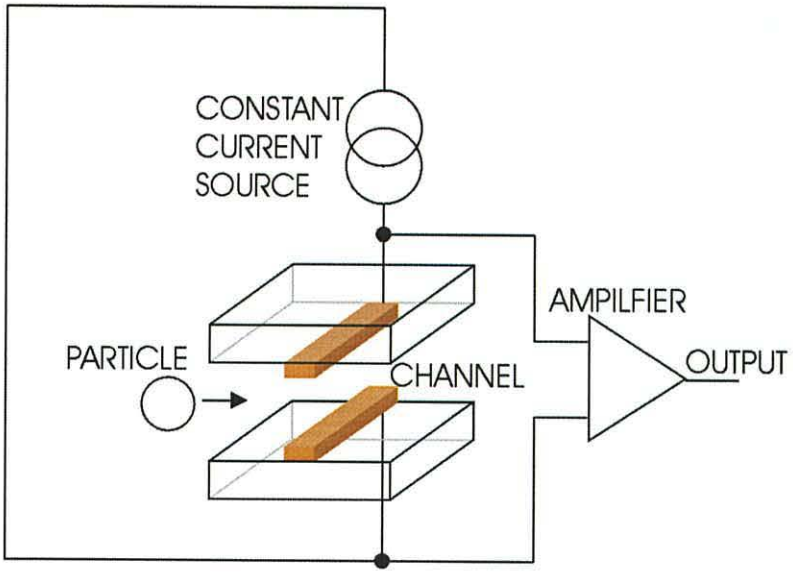

Figure 6.15 *Arrangement of the apparatus used to detect individual particles in a micro-channel.*

Figure 6.16 shows the results obtained when the 35 glass beads pass the sensor. The particles were collected to one side of the sensor, before being slowly flushed passed using a 100µl Hamilton Syringe to provide the flow.

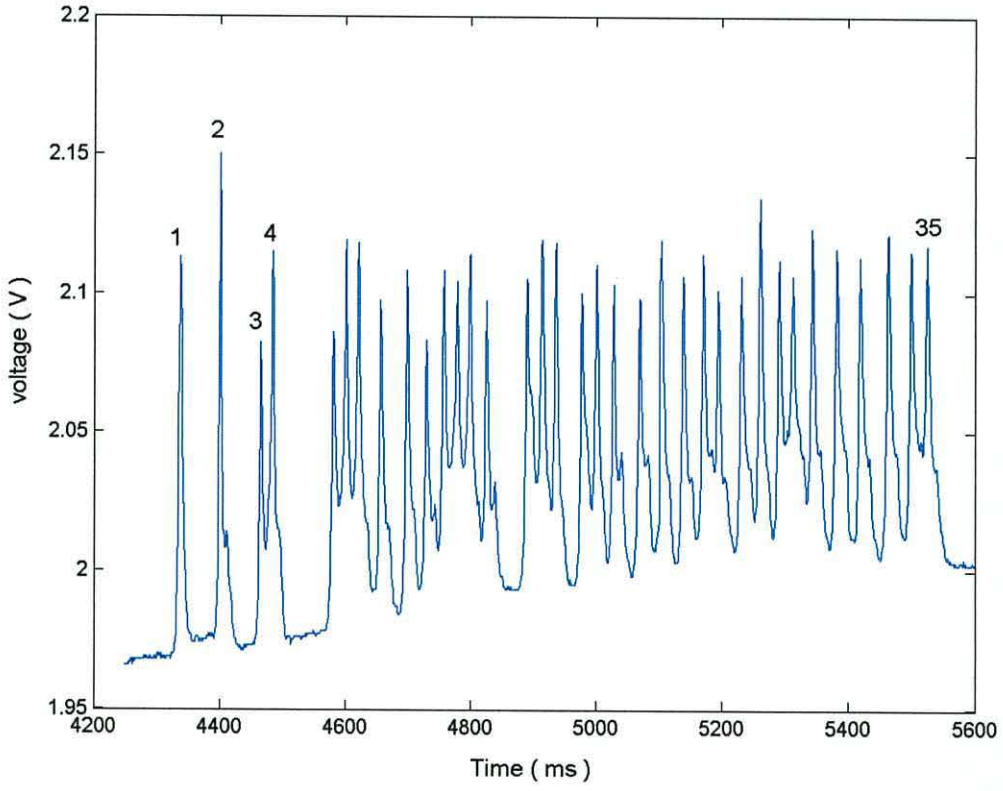

Figure 6.16 *Output produced when 35 glass beads pass through the sensing system illustrated in Figure 6.15.*

It can be seen from the results that as each of the glass beads pass the sensor there is an increase in the measured voltage. As each insulating glass bead passes the sensor it displaces some of the more conductive water, causing the resistance between the electrodes to increase. To maintain a constant current the voltage must increase as is seen by the peaks in Figure 6.16. Although the glass beads in this experiment are large, the same principle of operation applies to smaller particles. The extent of the voltage change depends on the relative size of the particle compared to the size of the channel. If the particle is large within the channel a large amount of the conducting fluid will be displaced resulting in large increase in voltage to maintain the current. However, if the particle is small the change in voltage will also be small.

6.5 Four point probe detection of single particles.

Using the approach described in Section 6.4 it was difficult to detect individual cells as they passed the sensor. In this section a four point probe detection technique is combined with a lock-in amplifier to detect individual yeast cells within a micro fabricated channel. The arrangement of the electrodes within the channel and their connections to the lock-in amplifier is shown in Figure 6.17

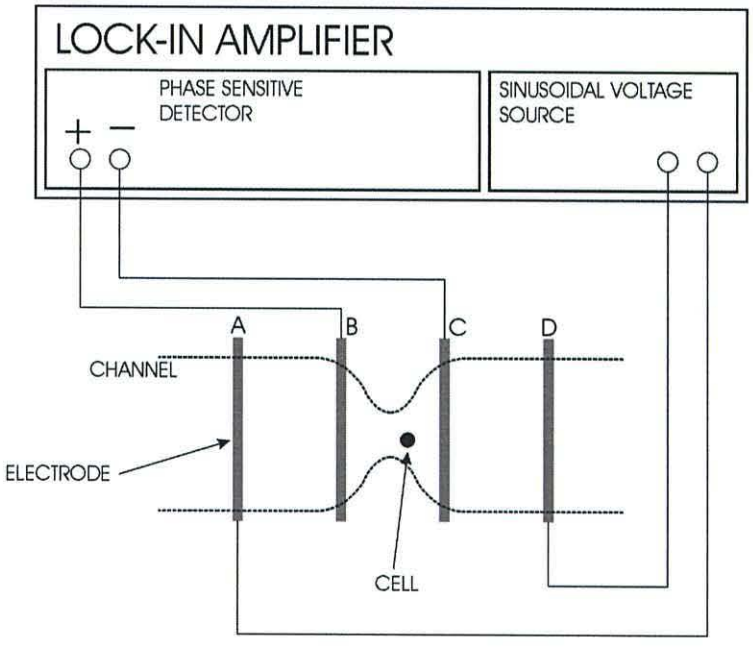

Figure 6.17 *Connections between the lock-in amplifier and the four point probe sensor used to detect individual cells*

The use of the four point probe measurement technique used here has been used elsewhere in the detection of individual particles [27,28]. It is particularly useful for this type of measurement, as it reduces the effect of contact resistance when making resistivity measurements. Conventionally a constant current is applied between the two outermost electrodes and a high impedance voltmeter is used to measure the potential between the inner two electrodes. The high impedance of the voltmeter, means that there is very little voltage drop across the contact resistance and the true potential within the channel is measured.

In this experiment instead of applying a constant current between the outer two electrodes (electrodes A and D) the sinusoidal output of the lock-in amplifier was used. The inner two electrodes (electrodes B and C) were then connected to the differential inputs of the lock in amplifier. In the arrangement shown in Figure 6.17 the potential is distributed along the channel. The potential at each of the electrodes depends on the impedance of the fluid between them. An equivalent circuit of this arrangement is shown in Figure 6.18.

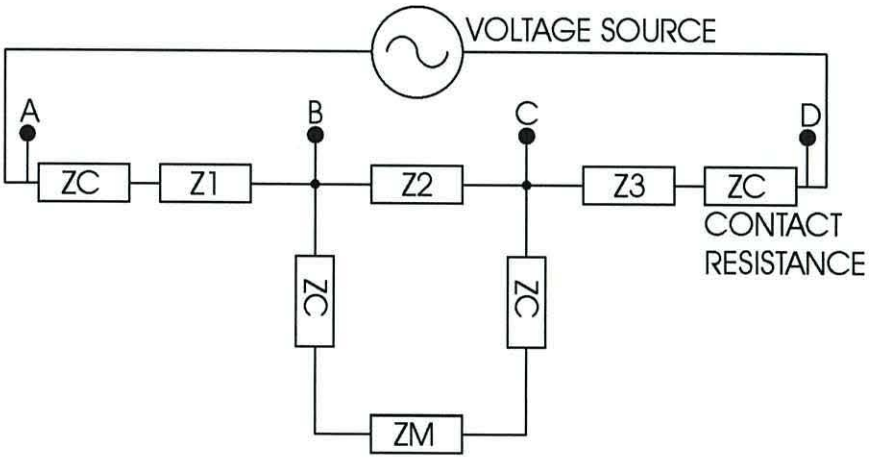

Figure 6.18 *Equivalent circuit for the electrode arrangement shown in figure 6.17*

In the equivalent circuit the impedances Z1, Z2 and Z3 correspond to the impedances of the fluid between the electrodes, whilst the impedances labelled ZC correspond to the contact resistances. The impedance ZM is the input impedance of the lock-in amplifier and is much greater than Z2 so does not effect the operation of the circuit. ZM is also much greater than ZC, so there is a negligible voltage drop across the contact

resistances at electrodes B and C. The distribution of the potential from the voltage source depends on the relative values of the impedances in series. Figure 6.19 shows a photograph of the channel structures and the arrangement of the electrodes.

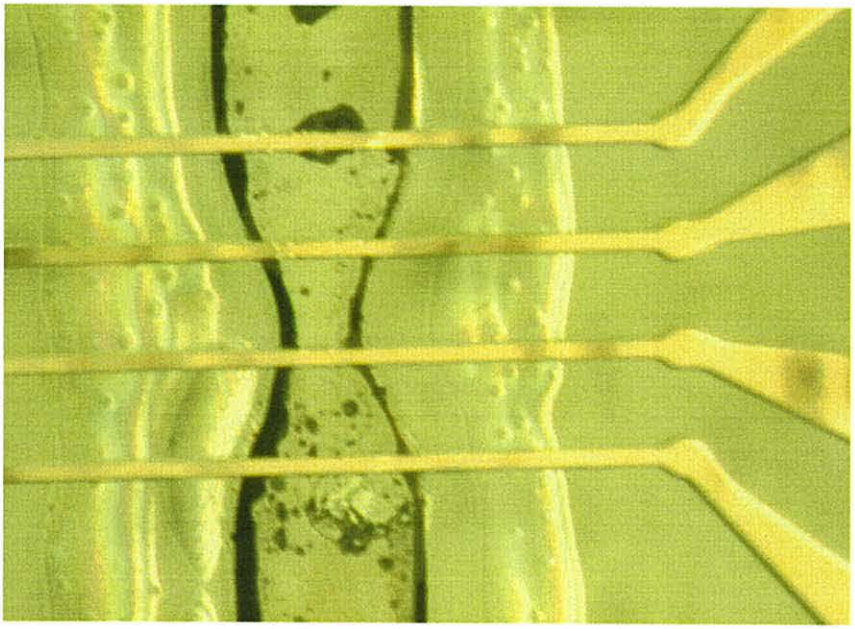

Figure 6.19 *Photograph of the four point probe sensor used to detect individual particles*

In Figure 6.19 it can be seen that the width of the channel is reduced between the centre two electrodes to maximise the change in the impedance caused by the presence of a cell. The channel was fabricated from a layer of UV curing adhesive sandwiched between two glass substrates. Spacers were placed between the substrates to give a channel height of 45μm.

When a stream of particles flows past a sensor of this type it is difficult to identify if a change in the output corresponds to the passage of a particle. To measure the effect of the presence of a particle in the sensor, a single yeast cell was moved in and out of the sensor using a syringe mounted to a micrometer barrel. The potential between the two centre electrodes was continuously logged using a GPID interface connected to the Lock-in amplifier. Figure 6.20 shows how the potential between the two centre electrodes varied as a single yeast cell was moved in and out of the area between the two centre electrodes.

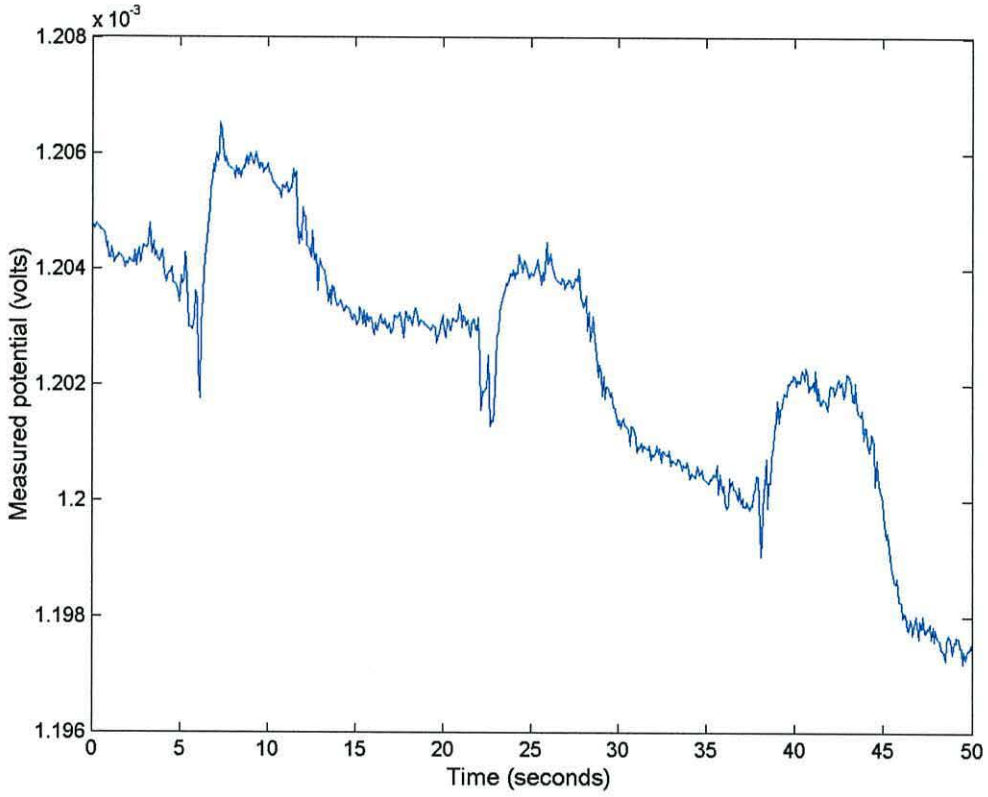

Figure 6.20 *Variation in the potential between the two centre electrode as a yeast cell is move in and out of the sensing area*

The results shown in Figure 6.20 were taken for a yeast cell suspended in a solution of 280 mmolL^{-1} manitol which had been made up to a conductivity of 200μScm^{-1} using phosphate buffered saline. The excitation waveform from the lock-in amplifier was a 10KHz 100mV r.m.s sinusoidal voltage waveform. This frequency was chosen as a significant change in voltage with the passage of a cell was detected. Coulter counters traditionally operate at dc. However the use of a lock-in amplifier requires that a alternating waveform is used. Although, the model of lock-in amplifier used is capable of operating down to 5mHz, at this frequency it takes a long time for the output to stabilise.

From Figure 6.20 it can be seen that there is a drift in the voltage with time. This does not present a problem, since only the magnitude of the change when a cell passes through the sensing area is required. The voltage drift can be removed by introducing a high pass filter into the circuit. This can be implemented either physically or digitally once the samples have been taken. There was only a small variation in the size of the yeast particles that passed through the device. However, some cells clumped together to

form a larger particles. Figure 6.21 shows the potential between the centre electrodes when a croup of three yeast cells were moved in and out of the sensing area.

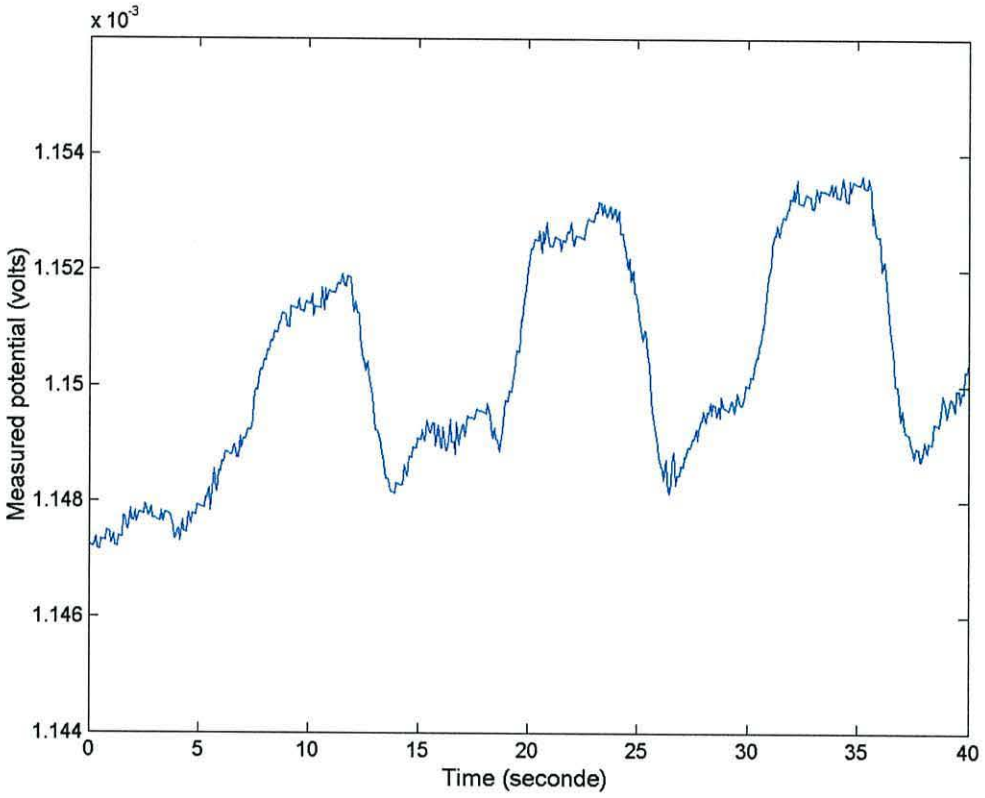

Figure 6.21 *Variation in the potential between the two centre electrodes as a group of three yeast cells is moved in and out of the sensing area*

The change in potential when a single cell entered the area between the two centre electrodes was approximately 2μV. However, when a larger particle consisting of three yeast cells entered the area between the electrodes there was a change in potential of approximately 4μV.

In Figure 6.21 a reduction in the potential below the reference level can be seen either side of the peak. This could be due to a drop in the impedance between the two outer electrodes as the cell passes through the area between them. This reduction in the impedance will result in a greater fraction of the overall potential being dropped over this section. As a result the potential between the two centre sensing electrodes is reduced. This is a similar effect to that seen in a flow cytometer developed elsewhere, which measures the relative impedances of the fluid between three electrodes in series [2].

6.6 Summary

The main aim of this chapter was to develop simple sensors that could be incorporated into the micro-channels described in Chapter 3 to detect the presence of particles. As with the flow sensor in the previous care was taken where possible to minimise the complexity of the associated detection circuitry.

To detect slugs of particle suspensions passing through a channel, electrodes were fabricated on the upper and lower surfaces of the channel. The capacitance between these electrodes was measured to provide an indication of the permittivity of the fluid in the channel. When a cell suspension passed the sensor there was a change in the capacitance between the electrodes. The magnitude of the change depended on the concentration of the cells. The measurements were carried out at a frequency of 1kHz as this produced the largest change in the capacitance. At this frequency the formation of a double layer on the electrodes still occurs. The measured capacitance is therefore likely to be a combination of effective permittivity of the material in the channel and effects caused by the double layer. To check the accuracy of these measurements the capacitance of the sensor was measured over a range of frequencies for different cell concentrations. From these measurements it was found that the device was most sensitive at the lower frequencies in the range measured. Using this approach it was possible to detect cell concentrations of 5×10^5 cells ml^{-1} for yeast.

To detect individual, large particles a design based on the Coulter Counter was developed. Instead of locating electrodes either side of a small aperture as in the case of a Coulter Counter, electrodes were located on the upper and lower surfaces of a narrow channel. A constant current was applied between these electrodes and the voltage monitored. When a glass bead passed between the sensors the resistance between the electrodes increased, resulting in an increase in the voltage to maintain the constant current. Although high resistance glass beads were used the same effect should occur with biological particles, as at dc they can be considered to be insulating spheres due to the formation of a double layer around the particle. Using this type of sensor it was possible to clearly distinguish 35 glass beads as they passed the sensor.

Using the sensor described it was difficult to detect individual cells, due to their small size compared to the dimensions of the channel. To produce a more sensitive device that was capable of detecting small particles within a relatively large channel, the four point probe technique was combined with a phase sensitive detection using a lock-in amplifier. Using this approach it was possible to clearly distinguish when a particle entered the sensing area. It was also possible to distinguish between single yeast cells and groups of cell clumped together. A group of three cells produced a voltage pulse of twice the magnitude to a single cell.

The sensors described in this chapter have all been fabricated using photolithography to pattern a layer of gold on a glass substrate. The intended application for the sensors is in lab-on-a-chip devices, which use gold electrodes on glass to manipulate particles by dielectrophoresis. As the sensors are fabricated in the same way as the DEP electrodes they can be added to the same photo mask and fabricated with little extra effort or cost. Although the sensor elements themselves can effectively be produced with little added effort, additional control circuitry is required. In this chapter the interface electronics largely consist of simple constant current sources, oscillators and amplifiers. The exception to this is the use of a lock in amplifier. However simple circuits do exist for the phase sensitive detection of signals [29]. The sensor developed here for the detection of individual particles does not have the performance of these developed elsewhere [26,27]. However the channel structure is much larger allowing it to be more easily incorporated into a lab-on-a-chip device.

The detection methods outlined in this chapter did not require the use of any imaging equipment to monitor the micro-system. Commercial microscope systems are often bulky and expensive and it is often necessary to optically monitor what is happening on a device. The following chapter will deal with the development of low cost microscope systems for use with lab-on-a-chip devices.

6.7 Refrences

[1] 'Development of a microfluidic device for fluorescence activated cell sorting' J. Kruger, K. Singh, A. O'Neill, C. Jackson, A. Morrison and P. O'Brien, *Journal of Micromechanics and Microengineering* **12** (2002) 486-494

[2] 'Impedance spectroscopy cell analysis in microchannels' S . Gawad, S. Metz, L. Schilld and P. Renaud, *Micro Total Analysis Systems 2001* 253-255

[3] 'A microfabricated fluorescence-activated cell sorter' A. Y. Fu, C. Spence, A. Scherer, F. H. Arnold and S. R. Quake, *Nature Biotechnology* **17** (1999) 1109-1111

[4] 'Micromachined flow cytometers with embedded etched optic fibres for optical detection' C-H Lin and G-B. Lee, *Journal of Micromechanics and Microengineering* **13** (2003) 447-453

[5] 'Micro flow cytometers with buried SU8/SOG optical waveguides' C-B. Lee C-H Lin and G-L. Chang, *Sensors and Actuators A* **103** (2003) 165-170

[6] 'Physics' Patrick Fullick. *Heinemann Educational Publishers. 1994, Oxford, UK.*

[7] 'Dielectrics and Waves' Arthur R. Von Hipple. *Chapman and Hall Ltd. 1954, London, UK.*

[8] 'Optics' Eugene Hecht and Alfred Zajac. *Addison-Wesley Publishing Company. 1974, London. UK.*

[9] 'Table of dielectric constants of pure liquids' Arthur A. Maryott and Edgar R. Smith. *National Bureau of Standards Circular 541. 1951 Washington, US.*

[10] 'Bioimpedance and Bioelectricity Basics' S. Grimnes and O. G. Mertinsen, *Academic Press 2000 London, UK.*

[11] 'The Physical Chemistry of Membranes' Michael E. Starzak. *Academic press. 1984 Orlando, US.*

[12] 'The Maxwell-Wagner dispersion in a suspension of ellipsoids' H. Fricke, *Journal of Physical Chemistry* **57** (1953) 934-937

[13] 'Treatisen on electricity and magnetism' J. C. Maxwell, *Oxford University Press Oxford, UK*

[14] 'Dielectric and electronic properties of biological materials' R. Pethig, *John Wiley and sons Chichester, UK*

[15] 'Explanation of the dielectric fatigue phenomena on the basis of Maxwell's concept' W. Wagner, *Arch Elektro technologies (berlin)* **2** (1914) 271

[16] 'A mathematical treatment of the conductivity and capacity of depressive systems. I the electrical conductivity of a suspension of homogeneous spheroids' H. Fricke *Physics Review* **24** (1924) 575-587

[17] 'A mathematical treatment of the conductivity and capacity of depressive systems. II The capacity of a suspension of conduction spheroids surrounded by a none conduction membrane for a current of low frequency'H. Fricke *Physics Review* **26** (1925) 678-681

[18] 'The complex conductivity of a suspension of stratified particles of spherical cylindrical form' H. Fricke *Journal of Physical Chemistry* **59** (1955) 168

[19] 'Electrical properties of tissue and cell suspensions In: Lawrence J H, Tobias CA (eda) Advances in biological and medical physics vol 4 147-209' H. P. Schwan *Academic Press 1957 New York, US*

[20] 'Dielectric properties of tissue' K. R. Foster and H. P. *Schwan CRC Critical Reviews in Biomedical Engineering* **17** (1989) 25-104

[21] 'A theory of the low frequency dispersion of colloidal particles in electrolyte solution' G. Schwartz, *Journal of Physical Chemistry* **66** (1962) 2636

[22] 'On dielectric relaxation due to chemical rate processes' G. Schwartz, *Journal of Physical Chemistry* **71** (1967) 4021-4030

[23] 'Dielectric relaxation of biopolymers in solution' G. Schwartz, *Advanced Molecular Relaxation Processes* **3** (1972) 281

[24] 'Dielectric Spectroscopy of Colloidal Suspensions' D. F. Myers and D. A. Saville, J. Colloid and Lnterface Science 131 (1989) 448-460

[25] 'Dielectrophoresis: Using inhomogeneous AC electrical fields to separate and manipulate cells' R. Pethig, *Critical Reviews in Biotechnology* **16** (1996) 331-348

[26] 'Quantatative sensing of nanoscale solids using a microchip coulter counter' O. A. Saleh and L. L. Sohn *Review of Scientific Instruments* **72** (2001) 4449-4451

[27] 'Design and fabrication of a micromachine coulter counter' M. Koch, E. G. R. Evans and A. Brunnschweiler, *Journal of Micromechanics and Microengineering* **9** (1999) 159-16

[28] 'Microchip coulter particle counter' U. Larsen G. Blankenstein and S. Ostergaare, *Proceedings in Transducer 1997* 1319-1322

[29] 'Electronics, Noise and signal recovery' E. R. Davies *Academic Press 1993 London, UK*

Chapter 7

Imaging

7.1 Introduction

The sensors described in Chapters 5 and 6 can be used to monitor the movement of fluid, cells and particle suspensions within micro-systems. When detailed information about specific types of particles in a sample is required, for instance when searching for specific particles in a sample of drinking water, it is possible to use optical microscope systems.

The commercial microscope systems used to observe particles within lab-on-a-chip type devices are often bulky and expensive. When observing micro-systems it is often not necessary to observe fine detail, for example when monitoring the collection of large groups of cells around a electrode due to dielectrophoresis (DEP) [1]. In these situations it is possible to use a basic microscope, which is inexpensive to produce. This chapter documents the development of a number of low cost microscope systems with reduced or zero optics for use with lab-on-a-chip devices. The microscope systems are developed to be simple, low cost devices, which are capable of producing images of a high enough quality for the specific application.

In commercial micro fluidic systems the part of the system in contact with the sample is often in the form of a disposable cartridge, which fits into some kind of analysis machine [2,3]. The disposal of equipment that has come into contact with the sample eliminates the possibility of cross-contamination. The simple microscope systems described in this chapter could be applied to disposable devices. An area of research applicable to disposable systems is the use of micro-lens arrays, which can be fabricated in polymers using inkjet printing, These lenses can be used to focus sources of illumination on a device.

One application where it is often necessary to observe a micro-system is when particles are manipulated using electrokinetics. Three specific methods of particle manipulation through electrokinetics are electrorotation, dielectrophoresis and travelling wave dielectrophoresis [6]. When observing each of these processes the resolutions required are different. It is necessary to observe fine detail when monitoring the rotation of a particle in electrorotation but a lower resolution can be tolerated when monitoring the accumulation of particles during positive dielectrophoresis.

This chapter first reviews how simple commercial microscopes operate and how the quality of an image is influenced by the wavelength of the illuminating light and diffraction at the lens. Most CMOS cameras are provided with a lens, Section 6.5 describes how that lens can be reversed to form a low cost microscope capable of resolving small details. To incorporate the optical elements of the microscope into a cartridge type micro system the lens was fabricated in PDMS, which also forms the fluidic channels on the device as described in Section 7.6. When PDMS is used the lens is susceptible to damage. To produce a more durable device Section 7.7 describes how a lens was fabricated on the underside of the device using clear epoxy.

In situations where it is not necessary to resolve fine details it is possible to remove the lens, placing the device directly onto the imaging array. In Section 7.9 this approach is used to find the DEP spectrum of live yeast cells, illustrating that useful measurements can be taken using low quality images.

7.2 Background

This section provides an introduction to some of the ideas and concepts used in the research described in this section. Section 7.2.1 briefly describes the optical arrangement used in this chapter. Sections 7.2.2 and 7.3.3 describe the illumination sources used and the effect the aperture size has on the resolution of a lens system.

7.2.1 Imaging using an objective lens and camera array

In a conventional bench top optical microscope the objective lens produces a virtual image of the sample, within the microscope the ocular (or eyepiece) lens is necessary to view this image plane [7,8]. It is also possible to view the image directly if a screen is inserted at the image plane within the microscope. Instead of using a physical screen an imaging array can be inserted at the image plane to view the image on a TV monitor as shown in Figure 7.1.

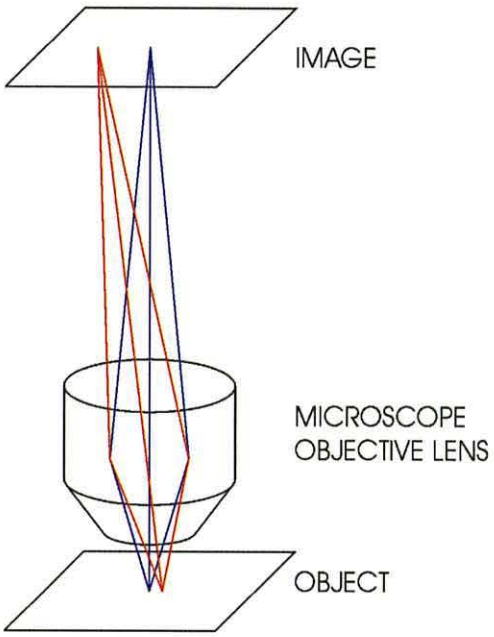

Figure 7.1 *Microscope composed of a commercial objective lens and an imaging array.*

Individual sensor pixels within an imaging array are typically between 5 and 10 μm in size. Therefore, fine detail may be resolved at low magnifications. The wavelength of visible light limits the smallest observable features to around 0.5μm. Due to this limitation, when using this arrangement little benefit is gained by having magnifications greater than x20. In the remainder of this chapter the performance of different lens systems used in this arrangement are investigated.

7.2.2 Illumination

The source of illumination for most bench top microscopes consists of a tungsten filament bulb or if ultra violet light is used to highlight fluorescent particles then, a mercury discharge tube is used. Within a lab-on-a-chip device it is often not necessary to have accurate colour reproduction of the particles so other sources of illumination may be considered.

Light emitting diodes (LEDs) are highly efficient light sources and produce very little heat compared to a tungsten filament bulb, thus reducing the rate of evaporation of fluid from a test device. The most common colour of LED's is red. However, shorter wavelengths, such as blue are also available. The shorter wavelength allows the

maximum possible resolution of the microscope image to be improved. To provide a high intensity source of illumination diode lasers may also be used. Although lasers are available in colours other than red, there is a substantial increase in price as the wavelength decreases. Both LED's and lasers provide a point source of illumination and additional optics must be incorporated into the microscope design where illumination of a large area is necessary. Alternatively, electro luminescent foils may also be used for uniform illumination over a large area. The illumination source used with the microscope arrangements shown here was a commercially available blue LED.

7.2.3 Diffraction at an Aperture

In addition to being limited by the wavelength of the light used the maximum achievable resolution of a lens system is also limited by the systems numerical aperture [8]. For a single lens the extent of the diffraction is dependent on the diameter of the lens and the wavelength of the light. Diffraction is not the only resolution limiting effect when using a single lens. For a large lens much more significant distortion will come from imperfect focusing of the light rays due to spherical, chromatic and other lens aberrations

Instead of considering diffraction at a circular aperture, the simpler case of diffraction at a slit will be used to explain the diffraction process. Figure 7.2 illustrates the effect of diffraction at a slit, where the length of the slit is much greater than its width.

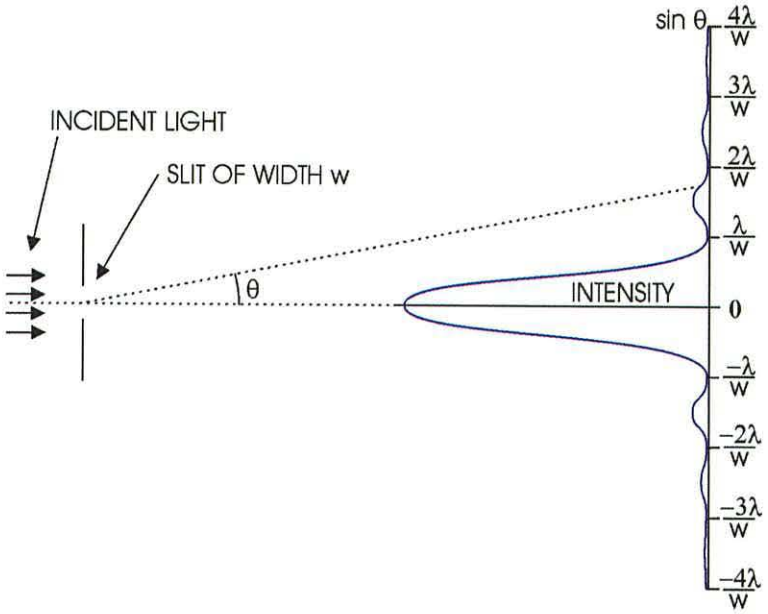

Figure 7.2 *Intensity distribution caused by diffraction at a long slit.*

The curve shown in Figure 7.2 illustrates the normalised intensity distribution produced by diffraction at a single slit of width w. The high and low points in the distribution are a result of constructive and destructive interference respectively, of the light coming through the slit. The equation of the curve is [8,9]:

$$\frac{I(\theta)}{I(0)} = \left(\frac{\sin\left(\pi w \sin\theta / \lambda\right)}{\pi w \sin\theta / \lambda} \right)^2 \tag{7.1}$$

$$\frac{I(\theta)}{I(0)} = \left(\mathrm{sinc}\left(\pi w \sin\theta / \lambda\right)\right)^2 \tag{7.2}$$

Where I(θ)/I(0) is the normalised intensity distribution and w, θ and λ are the slit width, the angle of measurement and the wavelength of the light respectively. The minima in the intensity distribution are given by:

$$\sin\theta = \frac{n\lambda}{w} \tag{7.3}$$

Where n is an integer corresponding to the number of the minima counting outwards from the straight through position. The limit of the blurring caused by diffraction can be

considered to be the first minimum, as the central peak in the intensity distribution is much brighter than the peaks either side. The intensity distribution for a circular aperture is slightly different to that of a slit, the first minimum being located at [9]:

$$\sin\theta = \frac{1.22\lambda}{d} \tag{7.4}$$

Where d is the diameter of the aperture. The aperture diameter required to achieve a certain resolution at the image plane depends on the wavelength of the light used and the geometry of the lens system. Figure 7.3 shows the diameter of the circle of light formed in the image plane when a point source of light is projected onto an image plane 10mm from the lens. The curves are plotted for wavelengths in the range 300nm to 800nm The aperture size is varied between 0.1 and 10mm.

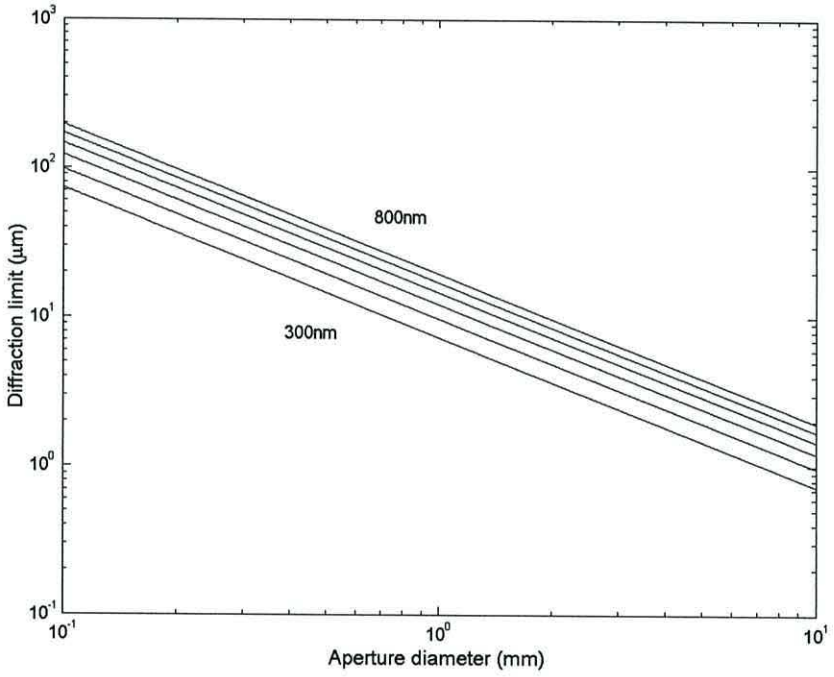

Figure 7.3 *Variation in the diffraction limit of a lens system for different sized apertures and wavelengths of light.*

From Figure 7.3 it can be seen that the size of the lens aperture required depends on the application. For a very small lens there would be significant blurring of the image due to diffraction, making it unsuitable for high resolution image enlargement. The applications described in this section are aimed at imaging the contents within the channel, for these reason relatively large lenses typically 3 or 6mm in diameter have been used.

The unsuitable nature of small lenses for image enlargement is reflected in the applications of micro lenses reported in the literature where the lenses are used primarily to collimate divergent light, for example either from a optical fiber [10] (lens diameter = 260μm) or LED [11] (lens diameter = 50μm). Although individual micro lenses are unsuitable for the image enlargement described in this chapter they are suitable for image reduction as used in photolithography [12,13]. Diffraction is not a problem in these applications due to the small distance between the lens and substrate.

7.3 Reversed camera lens

The objective lenses in commercial microscopes are of a high quality and are therefore also expensive. When tracking particles across a travelling wave electrode array or monitoring particles accumulated on a set of DEP electrodes, it is not necessary to resolve fine details within individual particles. In these situations the low resolution image produced by a lens of a reduced quality is sufficient to monitor the position of particles.

The integrated lens found on many simple computer "web cams" can be reversed and used as a simple objective lens. Such lenses are readily available and inexpensive. Figure 7.4A illustrates this type of lens in use as a camera and in Figure 7.4B the lens is reversed to form an objective lens.

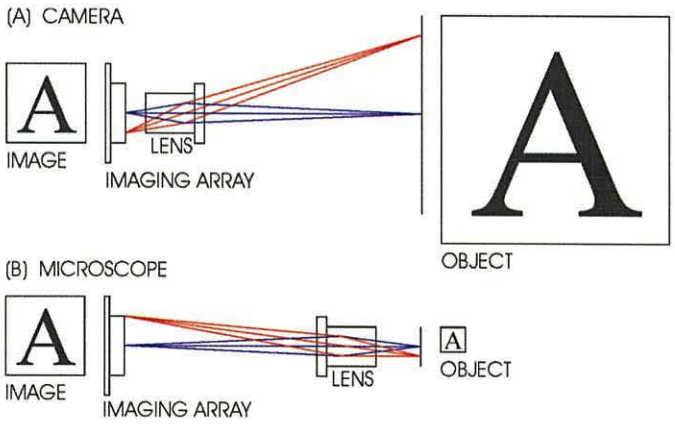

Figure 7.4 *The use of a simple lens and imaging array to form (A) a camera (B) a microscope.*

As mentioned previously the dimensions of the pixels on a CMOS imaging array are typically between 5 – 10 microns in size. As a result, small features can be resolved with low magnifications. A magnification factor of 10 would ideally allow features between 0.5 - 1 micron to be resolved. However, this level of quality is unlikely to be achieved due to the limitations in the resolving power of the lens and limitations imposed by the wavelength of the illuminating light.

At low magnifications it is possible to have a large working distance between the lens and the specimen allowing for easier use. A low magnification also increases the depth of field of the microscope system, making it more robust to slight errors in focusing. If the depth of field can be made sufficiently large to compensate for slight errors in the positioning of the sample, then it is easier to incorporate a microscope into the type of cartridge system described in Section 7.1. Figure 7.5 shows the image produced when a set of interdigitated castellated electrodes are viewed using the microscope arrangement shown in Figure 7.4B. The area of the electrodes represented by this image is 240μm across.

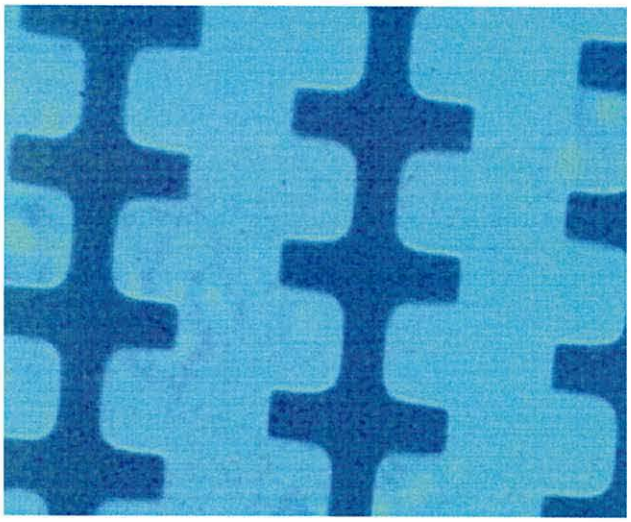

Figure 7.5 *Image of the electrode structure shown in Figure 6.8 produced using a reversed low cost camera lens as shown in figure 7.4B*

It can be seen that this approach provides a reasonable quality image. The magnification between the electrode and the imaging array is x11, above this magnification little improvement was seen in the quality of the image.

7.4 PDMS moulded lenses

One approach used to fabricate a channel structure is the use of the mouldable polymer PDMS (polydimethylsiloxane) [14] as described in Section 2.2.2.3. PDMS is optically clear and can be used to reproduce fine details of less than 100nm, making it suitable for producing optical elements. Figure 7.6 illustrates how a simple lens can be incorporated into a PDMS channel structure to form a microscope system.

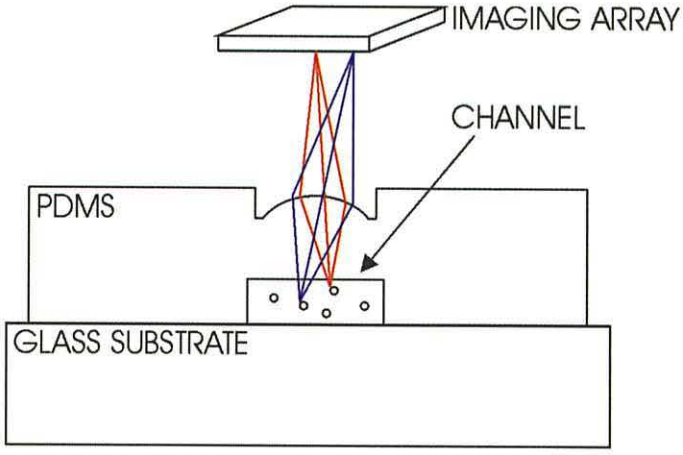

Figure 7.6 *Simple lens and channel system formed in PDMS.*

The structure illustrated in Figure 7.6 was fabricated by allowing PDMS to cure whilst sandwiched between two moulds. To produce an optical element of a high quality the mould for the lens was constructed using a commercially available concave glass lens mounted on a microscope slide. In this case the channel mould was fabricated using Loctite 358 UV curing adhesive (Loctite, UK) on top of a microscope slide. The surface of the UV adhesive will not completely set if exposed to oxygen. To overcome this problem the UV adhesive was sandwiched between the glass substrate and an acetate cover before the channel was photo patterned. Once the adhesive had been cured in the area of the channel, the remaining adhesive was removed with propanol and the acetate layer pealed from the adhesive. The flat surface of the acetate was transferred to the UV curing adhesive, which in turn was transferred to the upper surface of the channel formed in the PDMS. It was essential to produce a flat upper surface to the channel, as any roughness would distort the image.

To remove any small air bubbles from the PDMS before it was used with the moulds, it was degassed under vacuum for 30 minutes. The presence of the vacuum causes any small bubbles to expand making them more buoyant, therefore increasing the speed that they leave the PDMS.

The distance between the curved lens surface and the channel was large enough to allow the lens to focus on the particles and form an image on the CMOS imaging array.

In Figure 7.6 both the substrate and PDMS are transparent, allowing some light to pass directly from the illumination source to the imaging array, without passing through the lens. This stray light significantly affected the quality of the image resulting in a very low contrast.

To overcome this problem black carbon powder was added to a thin layer of PDMS that covered the surface of the device around the lens. The manufacturing steps to produce this improved device are illustrated in Figure 7.7. Once the opaque layer had cured, optically clear PDMS was applied on top and the channel mould was added. Once the second layer had cured, the PDMS was removed from the mould and applied to a glass substrate.

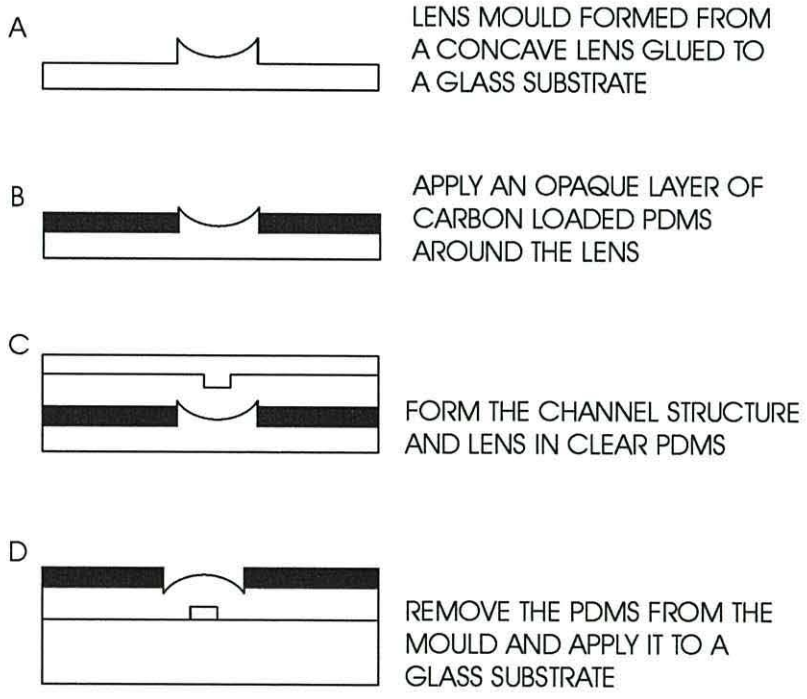

Figure 7.7 *Fabrication of a channel structure and lens using PDMS.*

The image in Figure 7.8 was taken using a moulded PDMS lens produced using the process in Figure 7.7. To take the image, the channel structure was placed on top of the electrodes.

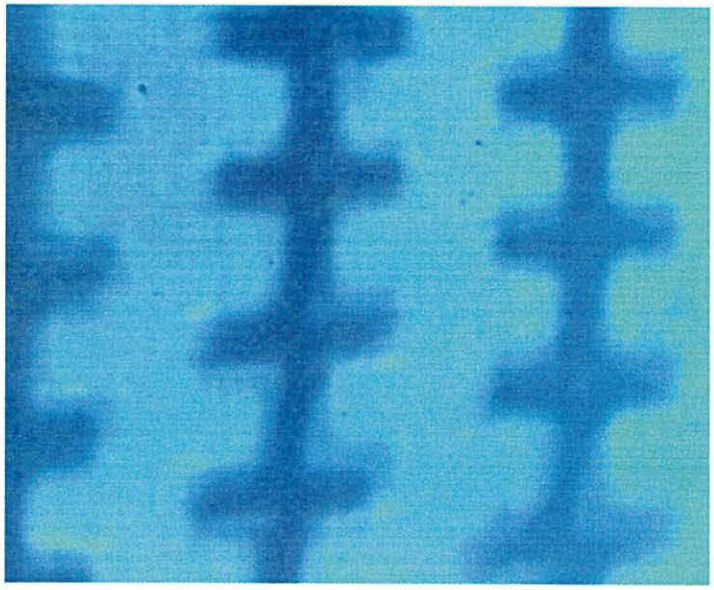

Figure 7.8 *Image of interdigitated castellated electrodes produced using a lens incorporated into a PDMS channel structure*

As expected, the image is of a lower quality than that achieved using the camera lens. When a single lens element is used, distortions in the image are caused by chromatic and spherical aberrations. Chromatic aberrations are due to different wavelengths of light being diffracted by different amounts, resulting in the lens having a range of focal lengths for different colours of light. Spherical aberrations are caused by the fact that spherical lenses, such as the one used here, do not focus light passing through the centre of the lens at the same point as light passing through the circumference of the lens. The multiple elements in a compound lens reduce these aberrations.

Once cured, PDMS forms a soft elastic material onto which dust and other contaminates can easily adhere. These contaminants are difficult to remove without damaging the optically flat surface. The image of the electrodes in Figure 7.8 does not contain the right angles of the original image. This could be due to a physical distortion of the whole lens, resulting in non uniform stretching of the image. This effect has been reported elsewhere in PDMS micro lens arrays[15], where distortion of the PDMS has resulted in beam deflections of 5^{O}. In that research shape deformation was found to be

the dominant factor in determining the optical properties of the lens . PDMS is supplied as a two part resin consisting of a liquid resin to which a catalyst is added to form a solid alastomer. To increase the rigidity of the PDMS the amount of catalyst added was doubled. This resulted in a tougher material that was more resistant to mechanical damage. However, the firmer composition of PDMS made it more difficult to release from between the moulds.

7.5 Araldite 2020 moulded from PDMS

The PDMS lens used in the previous section was susceptible to damage and could change shape if mechanically stressed. To eliminate this problem a harder, less adhesive lens was fabricated from Araldite 2020 epoxy resin (Ciba Speciality Chemicals, UK). Araldite 2020 is an optically clear, two-part resin with a low viscosity and curing time, dependant on temperature, of several hours. The low viscosity and long curing time of this resin aids the removal of small air bubbles caused during the mixing of the two components.

Another possible approach that was considered was to mould the lens from UV curing adhesive. However, Loctite 358 is not as transparent as Araldite 2002. Figure ~~6.16~~ 7.9 shows the extent to which Araldite 2020, UV curing adhesive and PDMS transmit light. Water is included for reference purposes.

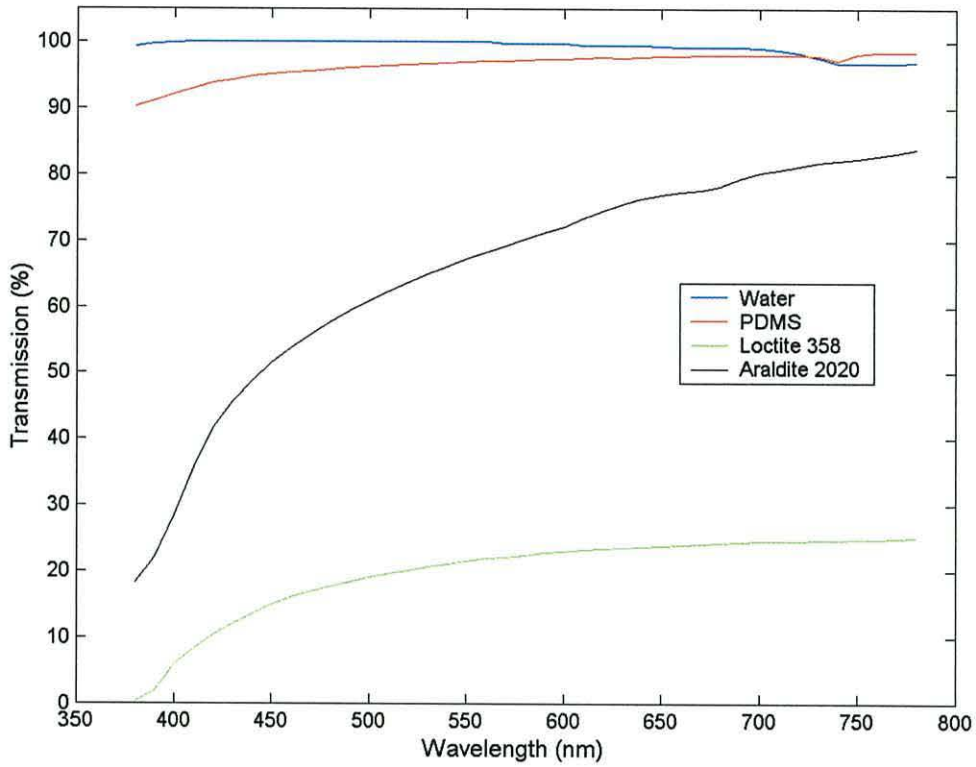

Figure 7.9 *Transmission of light at optical wavelengths through Araldite 2020, Loctite 358, PDMS and ultra pure water.*

It can be seen from Figure 7.9 that Araldite 2020 is not as clear as PDMS. However, it is significantly more transparent than the Loctite 358 UV curing adhesive. Unfortunately Araldite 2020 resin adheres well to glass, thus preventing direct moulding from a concave glass lens. Therefore an intermediate mould stage was used. where a glass lens was first used to produce a PDMS negative lens, which was in turn used to mould the Araldite 2020.

An advantage of using PDMS to form channel structures is that once on the substrate it can be removed for cleaning and then reattached, a process that can be repeated several times. There is no natural adhesion between cured Araldite 2020 and glass, therefore it must be either moulded in contact with the glass or bonded once cured. Both of these approaches make the formation of unobstructed channels difficult. Due to this problem other methods to produce the channel structures, such as those described in Chapter 4 were used and the Araldite 2020 lenses was fabricated on the underside of the substrate as shown in Figure 7.10.

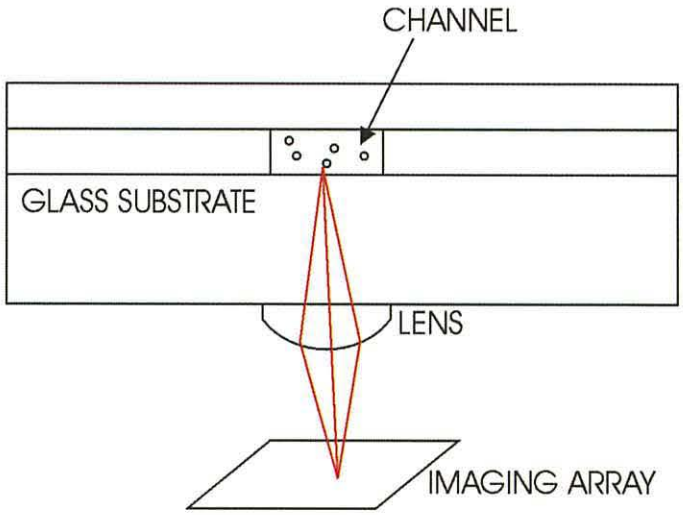

Figure 7.10 *Fabrication of a lens from Araldite 2020 on the underside of a device.*

The stages involved in producing a lens from Araldite 2020 are illustrated in Figure 7.11. Due to the intermediate step in the moulding process it is necessary to start with a convex lens of the same type required in the final structure. The template lens is covered in PDMS, which had been degassed under vacuum for 30 minutes to remove air bubbles. Once cured the PDMS copy of the template was removed to form the mould for the Araldite 2020. The two components that form the Araldite 2020 resin were thoroughly mixed to form a completely homogenous solution. If the two components were not sufficiently mixed, banding could be observed in the cured resin. The resin was degassed and poured over the PDMS mould, then the glass substrate along with any channel structures were placed on top. The resin was then left to cure over night. Contact with the Araldite 2020 caused the PDMS mould to fog but this did not affect the quality of the araldite copy. The PDMS mould was removed from the substrate revealing the moulded lens.

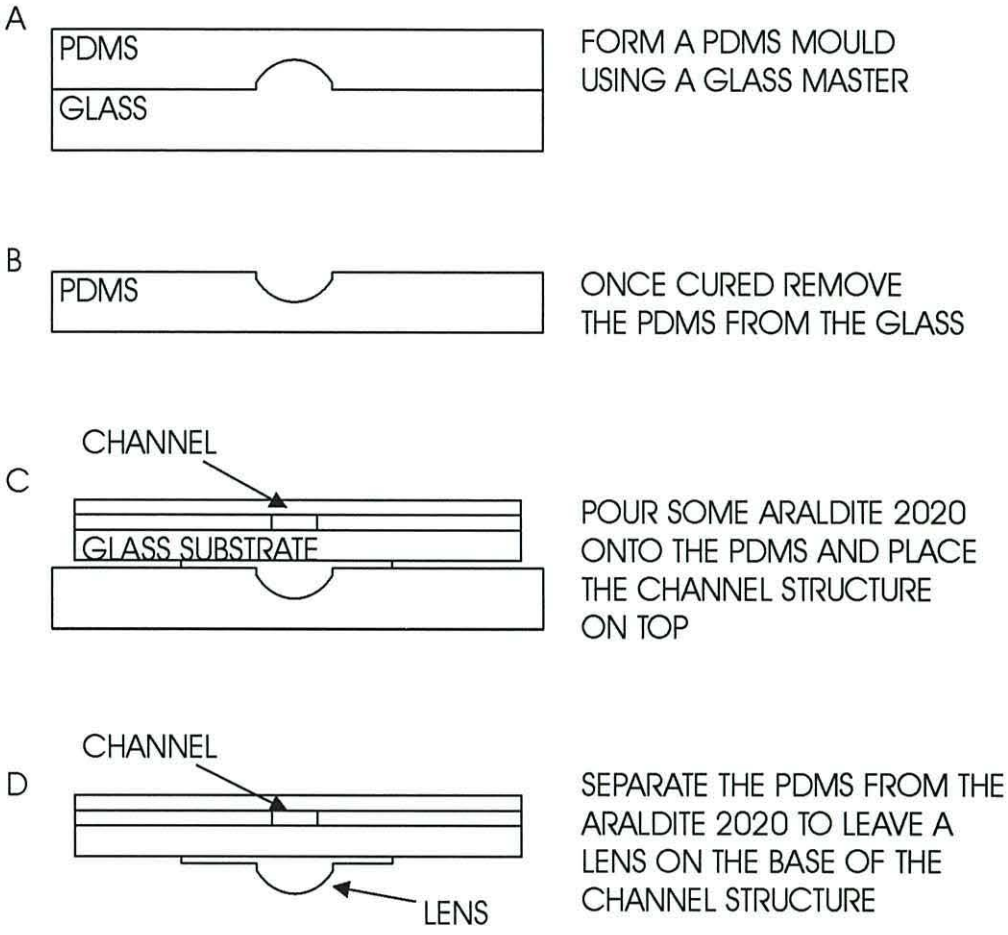

Figure 7.11 *Stages involved in fabricating a lens form Araldite 2020.*

Figure 7.12 is an image of a set of electrodes taken using a lens fabricated from Araldite 2020. To produce the image the electrodes were placed in contact with the substrate onto which the lens had been fabricated.

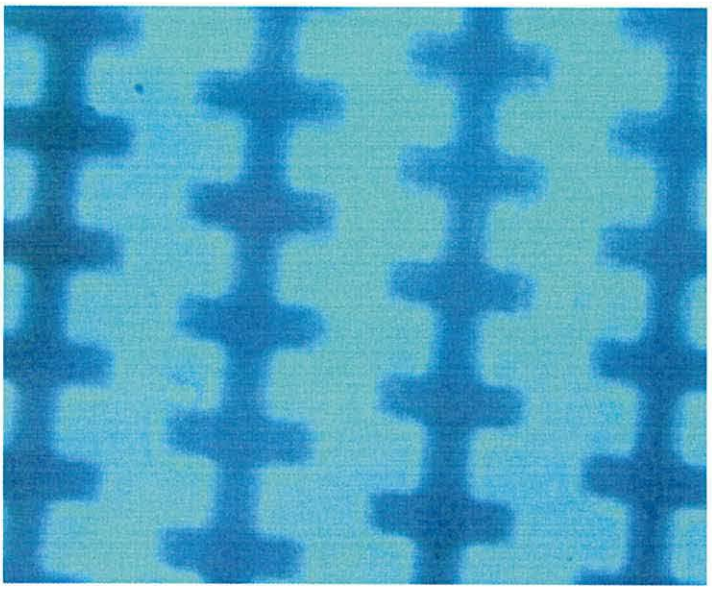

Figure 7.12 *Image of interdigitated castellated electrodes taken using a lens fabricated from Araldite 2020 on the underside of the substrate.*

The image quality is similar to that for a PDMS lens but the Araldite 2020 lens was much more resistant to damage and easier to clean. The rigid nature of the lens prevented the stretching of the image that can be observed in Figure 7.8.

During the curing process resins generate heat. When large volumes of Araldite 2020 above 50 ml were mixed there was insufficient surface area to allow the heat generated to dissipate properly. The heat increased the temperature of the resin, which in turn increased the rate of reaction and further increased the heat generated. Due to this cyclic process the temperature rapidly increased. The rapid reaction between the resin and the hardener reduced the curing time to less then 30 minutes, resulting in insufficient time for all the small air bubbles to leave the solution. To eliminate this problem the ratio of resin to hardener was reduced below the recommended ratio of 3:1, to a new ratio of 6:1. The reduction in the concentration of the hardener reduced the initial rate of reaction and therefore reduced the heat generated. By limiting the amount of heat generated internally the curing time was increased, allowing sufficient time for any bubbles to leave the solution. Despite the reduction in the amount of hardener the resin was still rigid once cured.

In some cases gas was expelled from the PDMS mould, which formed small bubbles in the Araldite 2020 lens. To reduce the occurrence of these bubbles, the gas was driven

off by curing the PDMS at a temperature of 100°C. At this temperature the PDMS cured much more rapidly, forming firm elastomer within an hour for volumes of the order of 50ml.

7.6 DEP measurements using contact imaging

The aim of the research discussed in this section is to demonstrate that useful measurements can be taken using low quality images. The application that was chosen was the measurement of the dielectric properties of yeast by monitoring their collection around a set of DEP electrodes. As it is not necessary to view fine details the electrode array was placed directly onto the image sensor and illuminated using a LED positioned 30cm away to provide a degree of collimation. This collimated light projected a shadow of the array onto the sensor as shown in Figure 7.13.

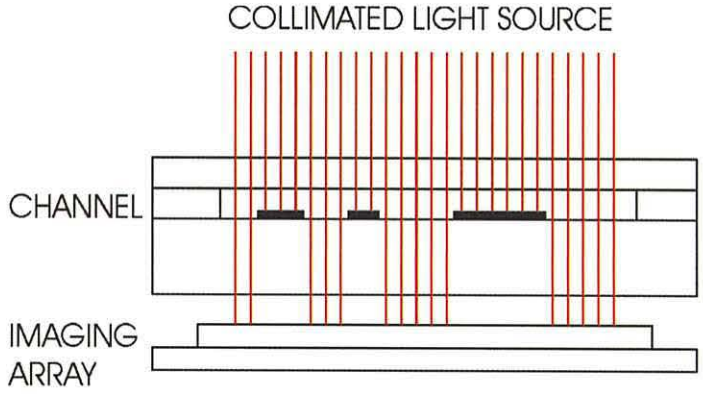

Figure 7.13 *Formation of an image using contact imaging.*

The quality of the image produced using contact imaging is mainly limited by the resolution of the imaging array. If the distance between the object and the array is large, errors will also occur due to diffraction at the edge of the features and if the light is not completely parallel then blurring will occur due to the multiple ray paths. Both of these causes of blurring are illustrated in Figure 7.14.

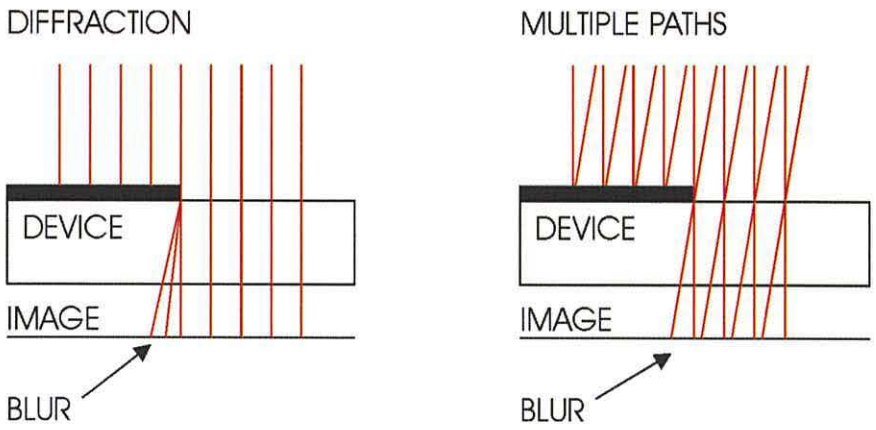

Figure 7.14 *Effects of blurring in contact imaging caused by diffraction and the multiple paths produced by a non collimated source.*

Figure 6.15 shows a set of castellated DEP electrodes imaged using contact imaging. Although it is difficult to resolve individual cells, the electrodes and groups of cells are clearly visible in the series of images shown later in Figure 7.16.

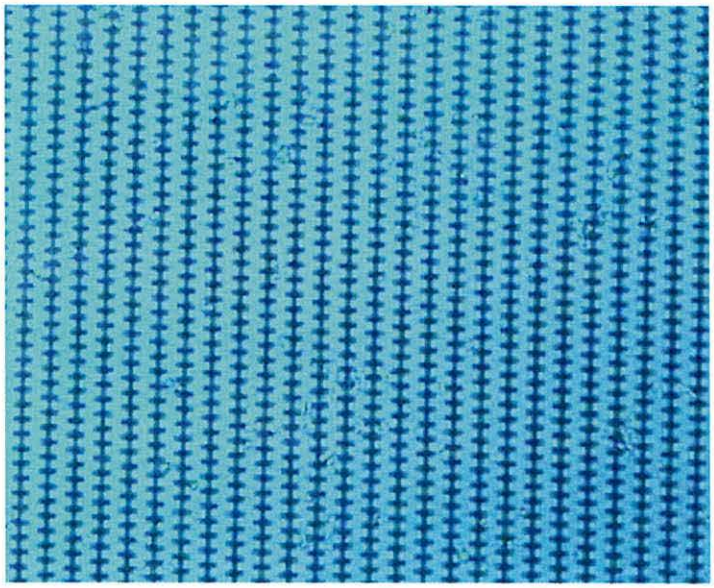

Figure 7.16 *Image of interdigitated castellated electrodes produced using contact imaging as shown in Figure 7.13.*

When cells are collected above a set of interdigitated castellated electrodes, they will form chains across the gap between the high field regions on the electrodes [16]. The formation of these groups of particles will make the device more opaque when viewed from above. To assess the strength of the DEP force exerted on the particles, a suspension of cells was continuously passed over a set of DEP electrodes. The rate at

which cells collect gives an indication of the DEP force they experience. Once the field was turned on the cells began to collect, which reduced the amount of light that could pass through the device to the imaging array. To maximise the resolution of the image a short wavelength blue-green LED was used for illumination. This approach of measuring the amount of light absorbed by particles collected using DEP electrodes has been used previously [10,11]. However, an advantage of using an imaging array instead of a single photo sensor is that dark areas of the image formed by the electrodes can be ignored. Using this approach only pixels that occupy the areas between the electrodes were used to measure the intensity. By maximising the change in the measured signal in this way the effect of noise is reduced. The flow through the device was provided by a Miniplus 3 peristaltic pump (Gilson, France). To minimise the volume of cell suspension required, the piping from the pump and the device were combined into a closed system with no large reservoir. The processing of the image produced by the array was undertaken using the image processing toolbox, which accompanies Matlab.

7.6.1 Results

Figure 7.16 shows a montage of the images taken at 5 second intervals when a suspension of live yeast cells in solution of conductivity 20uScm^{-1} were passed over a set of DEP electrodes. A 10kHz 6v r.m.s. signal was applied to the electrodes at the start of the experiment, this was then removed after the 15th sample to allow the cells on the electrodes to be washed away, then re-connected after the 20th sample. The flow rate over the electrodes was adjusted so that it was just sufficient to move the cells when no field was applied.

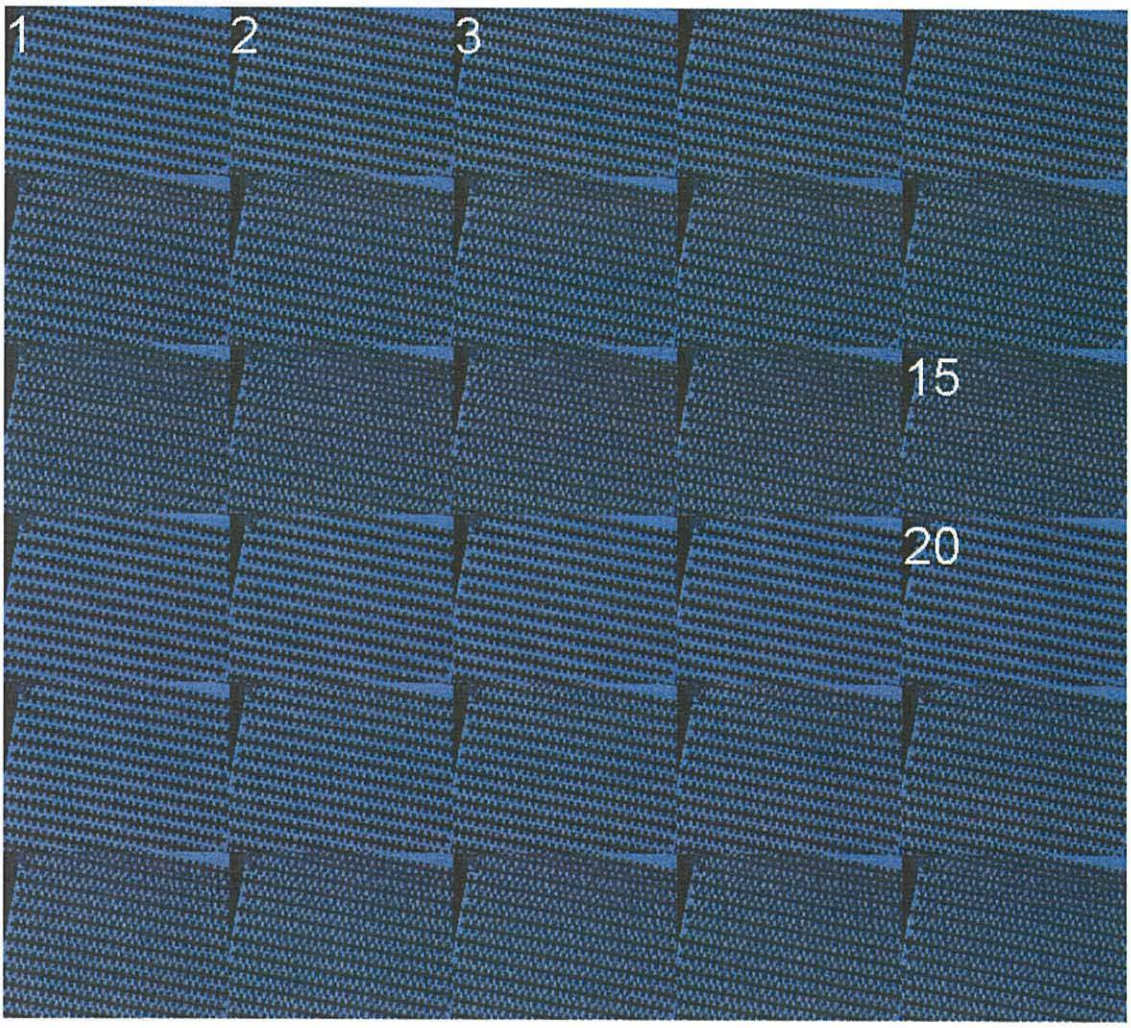

Figure 7.16 A *montage of a series of 30 images captured at 5 second intervals. The sequence of the images is from left to right starting in the top left hand corner as indicated by the numbers. The signal to the electrodes is turned on at the first image, turned off at the 15th image and then turned on again at the 20th image.*

Figure 7.17 illustrates the variation in the intensity of the selected pixels for the red, green and blue channels of the imaging array. The sudden rise in the intensity is due to switching off the applied field, causing the cells to be cleared from the electrodes.

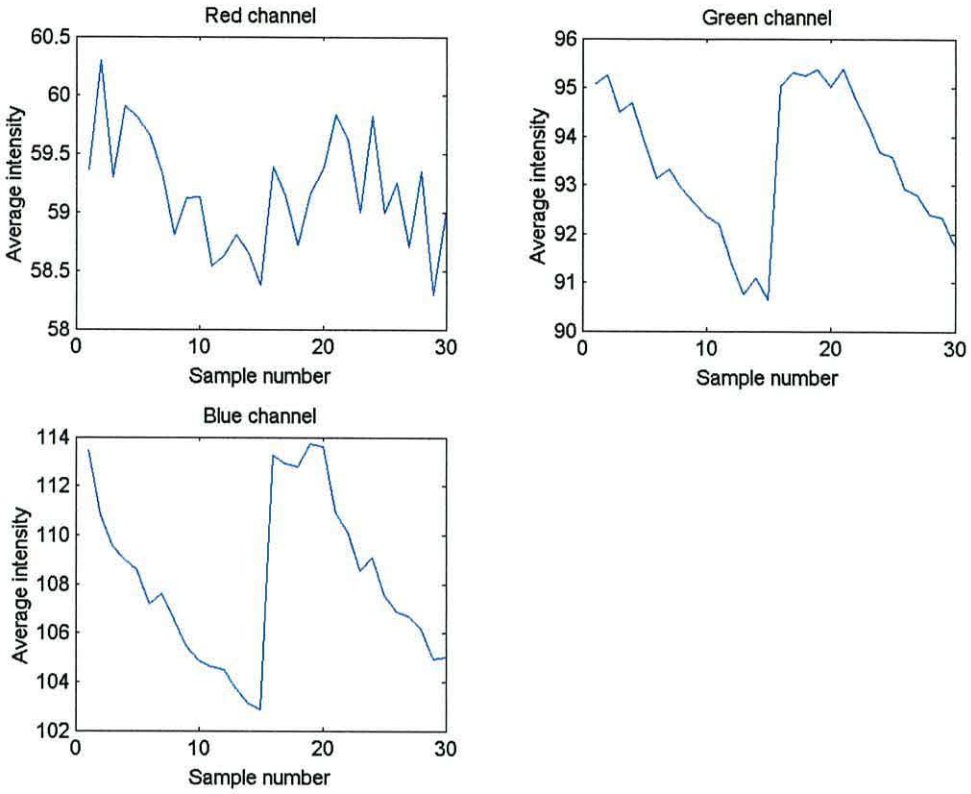

Figure 7.17 *Variation in the intensities of the red, green and blue channels for the areas not covered with electrodes in the series of images shown in Figure 7.16.*

As expected due to the use of a blue LED the greatest range and least noise is achieved using the blue channel from the imaging array. To allow some cells to collect even when the DEP force is low, the flow rate was only just greater than that required to move the cells across the device. When the cross sectional area of the pipe leading to the device was greater than the cross sectional area of the chamber, there was a lower flow rate in the pipe. This low flow rate allowed the cells to settle out in the pipe, reducing the number that passed over the electrodes. Figure 7.18 shows the effect this had on the accumulation of the cells over the electrodes.

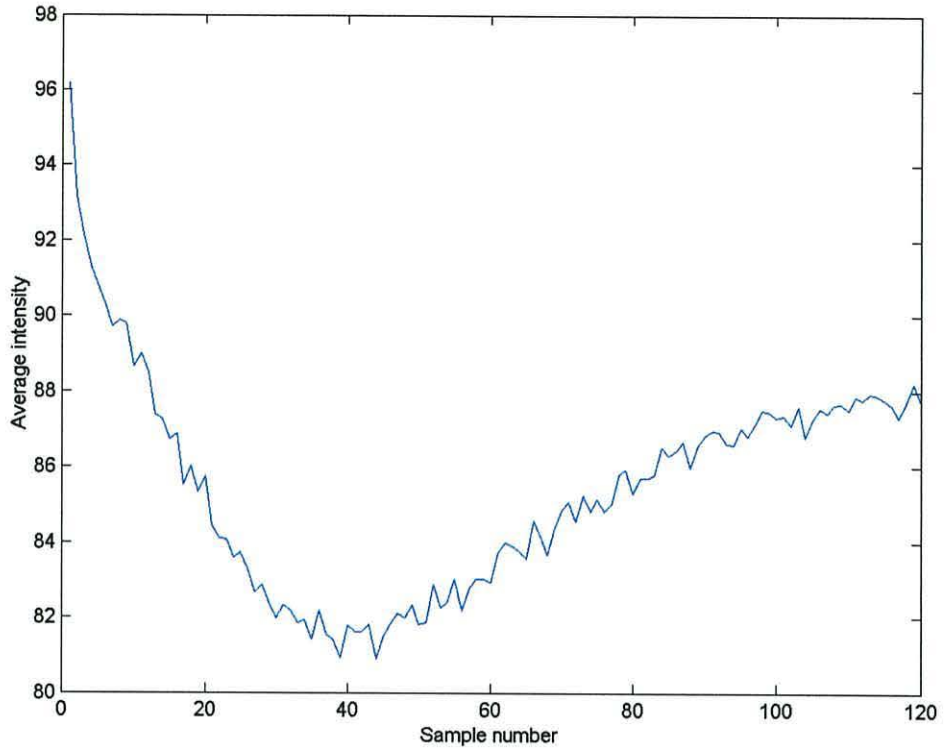

Figure 7.18 *Change in the transmission through a set of DEP electrodes due to particle collection, where the flow rate in the pipe leading to the electrodes is smaller than that over the electrodes.*

In Figure 7.18 the values up to around the 20th sample correspond to the device becoming more opaque, due to the collection of cells between the electrodes. As the cells settle out in the pipe leading to the device, clear solution passes over the electrodes. This solution washes away some of the cells already in the electrodes, as can be seen from the 40th sample onwards. To overcome this problem the diameter of the pipe leading from the peristaltic pump to the device was reduced.

To produce a spectrum showing the variation in the DEP force with frequency the initial gradient, showing a drop the transmission through the device, was found for a number of different frequencies. The gradient was found automatically by using Matlab to fit a straight line to the first 20 samples. The DEP spectrum produced in this way for live yeast in a solution of conductivity 20mScm^{-1} is shown in Figure 7.19.

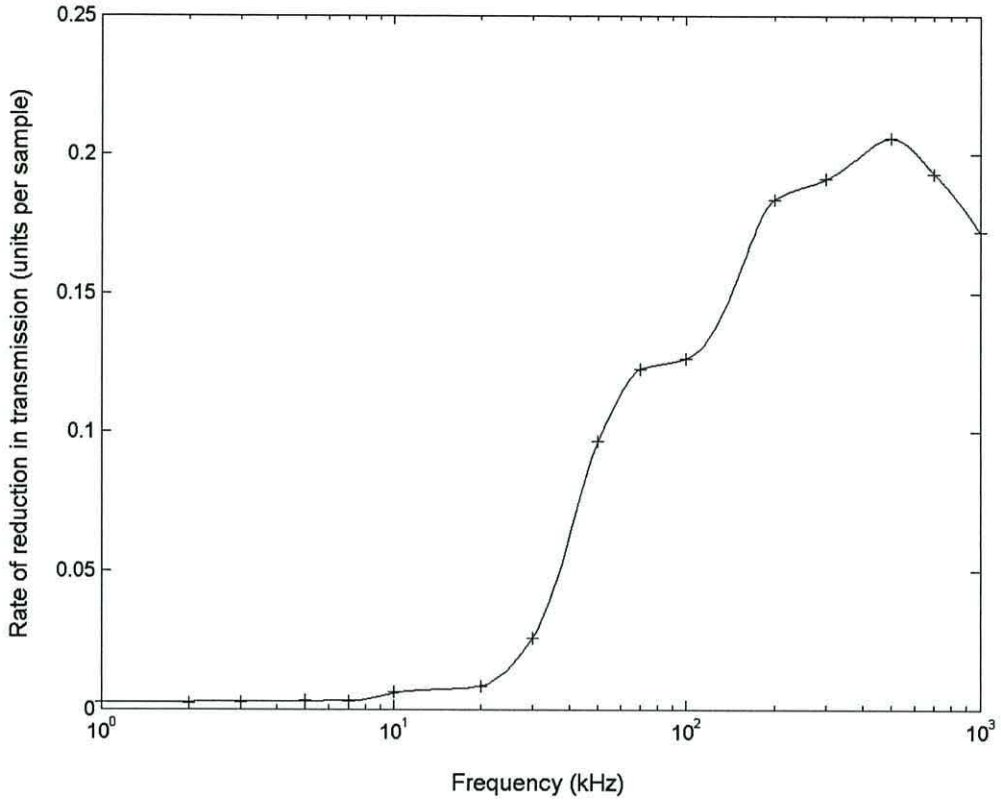

Figure 7.19 *DEP spectra for live yeast in medium of conductivity 10μScm^{-1}, produced using contact imaging*

The results shown in Figure 7.19 correspond well with previously measured spectrums for viable yeast cells above DEP electrodes [17,18]. These results illustrate that it is possible to make useful measurements of the dielectric properties of cells, despite using simple microscope systems that produce low quality images.

7.7 Summary

The main aim of this chapter was to develop simple microscope systems that can be combined with lab-on-a-chip devices to produce useful images of the particles within the device. The quality of the image required from a microscope system depends on the application. When carrying out electro rotation a high degree of resolution is required to detect details of individual particles. However, when monitoring the collection of large groups of particles around DEP electrodes a lower resolution is sufficient.

The integrated lens that was supplied with the CMOS "web cam" used in this work was reversed to form a low cost objective lens. Although the image is not as good quality as could be achieved using a microscope objective lens, it was still possible to resolve fine detail. This research showed that it is possible to produce reasonable quality images using low cost optics.

A commonly used approach when manufacturing devices incorporating micro-channels for the analysis of biological samples is to fabricate the parts in contact with the sample on a disposable cartridge. This cartridge is then interfaced to the more expensive control and sensing equipment. If optical observations of the device are required some sort of microscope must be incorporated into the system. To achieve this a device was developed which incorporated a simple lens within a channel structure. This lens was used to project a magnified image of the channel onto an imaging array. Initially, PDMS was used to form the channel structure and the lens, as it is optically clear and can be moulded precisely to form the optical surface of the lens. Using this approach it was possible to produce reasonable quality images of the contents of the channel.

Although PDMS can be used to accurately mould lenses it is still flexible once cured allowing mechanical stress to deform the shape of the lens. PDMS also has a slightly adhesive surface once cured, which can causes dust and particles to collect on its surface. Due to the soft nature of the PDMS it is difficult to remove this material without damaging the optically flat surface of the lens. To overcome these problems a lens element was fabricated from the optically clear epoxy Araldite 2020. This material is not as well suited to the fabrication of channel structures as PDMS, therefore the lens element was fabricated on the lower surface of the substrate, whilst the channel was fabricated on the upper surface using different processes. The image produced by this type of lens was of a similar quality to that produced using a PDMS moulded lens element. However, the lens was more resistant to mechanical damage and the image was not distorted due to stretching of the lens.

To illustrate that useful results could be produced using a low quality image the DEP spectrum for live yeast in a medium of conductivity $10\mu Scm^{-2}$ was measured. A process of contact imaging was used to produce the image, whereby the DEP electrodes are

placed directly on the imaging array and illuminated from above. Using this approach it is not possible to clearly resolve individual cells. As the cells collected between the electrodes due to DEP the amount of light passing through the device reduced. Instead of simply averaging the intensity across the device using a single photo sensor [17], only the areas not obscured by the electrodes were averaged, thus minimising the effect of noise. By measuring the rate of change in the intensity when signals of different frequencies were applied to the electrodes it was possible to produce a DEP spectrum, which corresponded well with those produced previously in other work. This research here has proved that it is possible to produce simple microscope systems for incorporation into lab-on-a-chip devices, which are capable of producing useful images.

When samples such as cell suspensions are used in lab-on-a-chip devices it is important that they are correctly prepared. This preparation involves the removal of unwanted particles such as those that could block the channel. Where DEP electrodes are incorporated into the channel the conductivity of the suspending medium must also be accurately controlled. Chapter 8 describes some of the approaches that are currently used to prepare samples. To change the conductivity of samples, diffusion can be used to remove ions but not larger particles. An existing approach used to do this has been developed to meet a specific application using computer simulation tools.

7.8 References

[1] 'Positive and negative dielectrophoretic collection of colloidal particles using interdigitated castellated microelectrodes' R. Pethig, Y. Huang, X-B. Wnag and J. P. H. Burt, *J. Applied Physics D* **24** (1992) 881-888

[2] 'i-Stat company web site (1/9/2002)' http://www.i-Stat.com

[3] 'Caliper company web site (1/9/2002)' hppt//www.calipertech.com

[4] 'Deposition of micropatterned coating using an ink-jet technique' R. Danzedrink and M. A. Aegerter, Thin Solid Films 351 (1999) 115-118

[5] 'Deposition of optical microlens arrays by ink-jet processes' R. Danzedrink and M. A. Aegerter, Thin Solid Films 392 (2001) 223-225

[4] 'Dielectrophoresis: using inhomogeneous AC electrical fields to separate and manipulate cells' R. Pethig, *Critical Reviews in Boitechnology* **16** (1996) 331-348

[7] 'Biology, third edition' Neil A. Campbel, *The Benjamin/Cummings Publishing Company, Inc. 1993 California, US.*

[8] 'Optics' Eugene Hecht and Alfred Zajac. *Addison-Wesley Publishing Company. 1974, London. UK.*

[9] 'Optics' F. G. Smith and J. H. Thomson, John Wiley and Sons ltd. 1988, Chichester, UK.

[10] 'A surface micromachnned optical scanner array using photoresist lenses fabricated by a thermal reflow process' H. Toshiyoshi, G-D. J. Su, J. LaCosse and M. C. Wu, *Journal of Lightwave Technology* **12** (2003) 1700-1708

[11] 'Mushroom microlenses: optimised microlenses by reflow of multiple layers of photoresist' P. Heremans, J. Genoe, M. Kuijk, R. Vounckx and G. Borghs, *IEEE Photonics Technology Letters* **9** (1997) 1367-1369

[12] 'Reduction Photolithography using microlens arrays: applications in grey scale photolithography' H. Wu, T. W. Odom and G. M. Whitesides, *Journal of Analytical Chemistry* **74** (2002) 3267-3273

[13] 'Connectivity of features in microlens array reduction photolithography: generation of various patterns with a single photomask' H. Wu, T. W. Odom and G. M. Whitesides, *Journal of the Americam Chemical Society* **124** (2002) 7288-7289

[14] 'Rapid prototyping of Microfluidic systems in Poly(dimethylsiloxane)' D. C. Duffy, J. C. McDonald, O. J. A. Schueller and G. M. Whitesides, *J. Analytical Chemistry* **70** (1998) 4974-4984

[15] 'Analysis of elastic micro optical components under large deformation' K. Hoshino and I. Shimoyama, *Journal of Micromechanics and microeingineering* **13** (2003) 149-154

[16] 'Positive and negative dielectrophoretic collection of particles using interdigitated castellated microelectrodes' R. Pethig, Y. Huang, X-B. Wang and J. P. H. Burt, *J. Applied Physics D* **24** (1992) 881-888

[17] 'Applications of a new optical techniques for measuring the dielectrophoretic behaviour of micro-organisms' J. E. R. Price, J. P. H. Burt and R. Pethig, *Biochemica and Biophysica Acta* **964** (1988) 221-230

[18] 'Optical technique for measuring the positive and negative dielectrophoretic behaviour of cells and colloidal suspensions' M. S. Tallary and R. Pethig *IEE Proceedings in Science, Measurement and Technology* **141** (1994) 395-399

Chapter 8

Sample Conductivity Reduction

8.1 Introduction

The fabrication of channel structures and sensors to process aqueous suspensions of cells has been described in Chapters 4 to 6. These suspensions were pre-prepared and contain little or no contaminants. However, when a raw sample is taken from the environment, it is likely to contain a broad range of substances in addition to the particles of interest. Such contaminants could be in the form of particulates of varying size or dissolved compounds, such as ionic salts. Where these contaminants could interfere with the operation of a micro-device they must be removed before the sample enters the micro-system. Ionic contaminant compounds can change the conductivity of a fluid sample, thus interfering with any dielectric measurements or dielectric processes within the device.

Section 8.2 provides an overview of the types of contaminants that are found in a typical sample and considers how they are normally removed. An example of when sample preparation is essential is in the case of dielectric based operations on blood [1]. The natural ionic concentration and therefore conductivity of blood is too high to allow useful dielectric measurements to be undertaken within a micro device, therefore the conductivity must be reduced. For cell studies, this is normally achieved using the time consuming and labour intensive process of repeatedly centrifuging and washing the sample [2-4]. This is a process that is difficult to automate or integrate into a micro-fluidic device. However, methods have been developed to reduce the concentration of a sample using H shaped microfabricated channel structures [5]. The H-filter allows the blood to flow adjacent to a stream of low conductivity buffer solution. As the flow is laminar the two streams can be separated without any physical mixing occurring between the two flows. However, as the dissolved ions have a high diffusion coefficient, a proportion of them move from the blood to the buffer reducing the ionic concentration in the blood and therefore its conductivity. A device based on the same principle has also been developed to undertake analytical measurements on small molecules in blood plasma [6]. By allowing the small molecules to diffuse into an adjacent flow stream containing the reagent it is not necessary to separate the cells and plasma.

The physical processes involved in the operation of a H-filter are described in Section 8.3. The requirements of the design are defined in Section 8.4 and analytical methods are used to provide a starting point for a computational analysis. The specifications of the finite element simulation are described in detail in Section 8.5, including the equations to be solved and the boundary conditions.

The basic H-filter design is refined in Section 8.6 using the computer simulation package FEMLAB (Comsol ltd, Sweden) to produce a system capable of the large reduction in concentration required for dielectrophoretic studies of blood. To assess a possible fabrication route and the validity of the design a demonstration H-filter was fabricated and tested in section 8.7. There was a good match between the results obtained experimentally and those produced by the computer model.

8.2 Existing methods of sample preparation

The types of unwanted substances in a sample taken from the environment vary depending on the type of sample and its source. For example, if a water sample is taken from a river to look for a specific organism, such as the pathogen cryptospriduim that can cause sickness in humans [7], the sample will contain a wide range of particulate contaminants. These will vary from small creatures a few millimetres in size to bacteria less than 1μm in size. There will also be dissolved minerals and salts that may affect the conductivity of the sample. Alternatively, if a blood sample is taken, the presence of large particulate contaminants is not a problem as none are present in the blood stream. However, the ions contained in blood plasma significantly increase the conductivity. If measurements on blood cells are to be taken using dielectrophoresis [8] the medium conductivity typically needs to be lower than that of whole blood. Therefore ions must be removed from the blood sample. When removing contaminants from a sample it is clearly important not to damage or remove the particle of interest.

8.2.1 Particulate contaminants

Large, dense particles, such as grit, can be removed from a sample by allowing it to settle but smaller and less dense particles will tend to remain in suspension. Assuming

the size of the target particle is known, particulate contaminants of a different size can be removed by passing the sample through two filters. The first with pores slightly larger than the particle and the second with pores slightly smaller. The particle of interest, along with any similar sized particles, will be collected on the second filter and can be removed by back flushing the filter with clean re-suspension medium. If a large volume of raw sample is passed through the filters this has the effect of concentrating the sample.

To remove particles of a different density to the desired particle, the particles can be added to a solution with a controlled density intermediate between the densities of the particles to be separated. Where a particle settles in such a system depends on its density. This approach is commonly used to separate red and white blood cells [9]. Centrifuging the particle suspension will accelerate the process.

Separation of particles based on their dielectric properties can be carried out using positive and negative dielectrophoresis. Under controlled conditions the desired particles will be attracted towards electrodes, whilst others will be repelled [10] or vice versa. The process of dielectrophoresis is ideal for micro systems as it operates optimally when microelectrodes are used.

8.2.2 Dissolved contaminants

A common approach to remove dissolved contaminants from a particulate sample is to centrifuge the sample so that a pellet of material is formed at the bottom of the centrifuge tube. The suspending medium (supernatant) is then removed and replaced with a new medium of a controlled composition [11]. Re-suspension of the particles from the pellet is then achieved by physical agitation. This process is not usually completely effective as some of the original suspending medium will remain trapped in the pellet and it is routine to repeat this process several times. The composition of the liquid used to re-suspend the pellet depends on the application. If animal cells are used in an electrokinetic application it may be necessary to re-suspend the particles in a low conductivity, indigestible, sugar solution such as sucrose [12] to maintain the same osmotic pressure and prevent the cells from rupturing. This is explained in more detail

in Section 8.4.1. In electrokinetic studies the control of the sample conductivity is one of the most labour intensive parts of sample preparation. The research described here uses computer aided design and simulation tools to investigate the feasibility of simplifying the sample preparation process using the H-filter concept.

In the case of cells in blood it is necessary to significantly reduce the conductivity of the suspending medium by a factor of approximately 10,000 from 1.55 Sm^{-1} to 0.5 mSm^{-1}. Reduction of the suspending medium conductivity by re-suspension of the cells can lead to a loss of cells. For investigation of rare cell types, such as foetal cells in maternal blood (1 in 10^9 cells) used in the early detection of Downs syndrome [13], this loss of cells must be minimised.

8.3 H-filter operation

A reduction in the suspending medium conductivity can be achieved using a so called H-filter, originally developed by J. P. Broody and P. Yager [5] and currently under commercial development by Micronics Inc. [14,15]. As illustrated in Figure 8.1 the structure has two inlets and two outlets. The sample enters via inlet A, whilst a buffer of a different ionic strength enters at inlet B. The two streams of fluid are in physical contact as they travel the length of the central channel and then separate before arriving at their respective outlets. Whilst the two fluid streams are in contact diffusion can occur across the boundary.

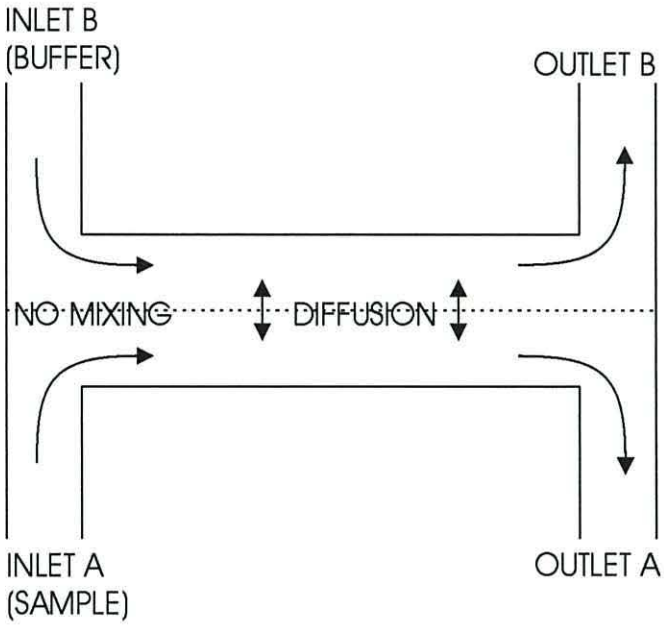

Figure 8.1 *Operation of a H-filter. Diffusion can occur between the sample and the buffer but the two liquids do not mix.*

The nature of fluid flow in a channel is determined by the Reynolds number [16] which is given by the equation :

$$\mathrm{Re} = \frac{\rho u D}{\mu} \tag{8.1}$$

Where ρ, μ, u and D are the density, dynamic viscosity, velocity and characteristic length of the fluidic system respectively. For a channel with a circular cross section the characteristic length D is the diameter. However, microfluidic channels are seldom circular, so the hydraulic diameter D_h is used which is given by the equation.

$$D_h = \frac{4A}{C} \tag{8.2}$$

Where A and C are the area and circumference of the channel respectively. For a long channel the flow will be laminar for Reynolds numbers below 1000 [17]. Due to their small dimensions, most microfluidic systems have Reynolds numbers less than 10 and operate well within the laminar regime. No turbulence occurs within the micro channel and so the two streams of liquid do not mix with each other as they travel through the device.

Although there is no mixing of the fluid, diffusion can occure across the channel. The rate at which particles diffuse in a given medium depends on their size. A small particle will generally diffuse more rapidly than a larger one. The fluid velocity is controlled so that there is sufficient time for the target particles to diffuse from one stream to the other. A simple expression for the typical distance L that a particle travels in time t is given by [18]

$$L = \sqrt{Dt} \tag{8.3}$$

Where D is the diffusion coefficient of the particle in the suspending medium and is given by the equation [19]

$$D = \frac{RT}{N} \times \frac{1}{3\pi\mu d} \tag{8.4}$$

Where R is the gas constant ($8.31*10^7$ $JK^{-1}mol^{-1}$), N is Avagadros number ($6.02*10^{23}$ mol^{-1})[20], and T, μ and d are the absolute temperature, the viscosity of the suspending medium and the particle diameter respectively. Diffusing particles undergo random, Brownian, motions. For a one dimensional system, the probability of finding a particle of diffusion coefficient, D, a distance, x, from its starting point after time, t, is given by the normalised probability density function, y(x). The function y(x) is normalised for a constant area under the curve of unity instead of the peak value and is given by the relationship[5].

$$y(x) = \frac{1}{\sqrt{4\pi Dt}} \exp\left(-\frac{x^2}{4Dt}\right) \tag{8.5}$$

This relationship forms a gaussian distribution centred on the starting point of the particle.

When a H-filter is used with blood, the two particles types of interest are the blood cells themselves and the ions within the plasma, which play a significant role in increasing

the conductivity. In this research sodium ions are considered, as they are the most common ion found in blood plasma [21]. The diffusion coefficient for a sodium ion in water is $1x10^{-9}m^2s^{-1}$ compared to $6.8x10^{-14}m^2s^{-1}$ for a red blood cell [5]. The typical distance covered in one second through diffusion is 32μm for a sodium ion, compared to 0.26μm for a red blood cell. As mentioned previously, the probability distribution of finding a particle a given distance from its starting position after a period of time is gaussian in shape. Therefore, there is a chance that a given particle could diffuse significantly further than the typical diffusion length. Solutions of the normalised probability density function (equation 8.5) are illustrated in Figure 8.2 for 3 different particles. The particles used and their diffusion coefficients were, a sodium ion ($D=1000x10^{-12}m^2s^{-1}$), a hemoglobin molecule ($D=70x10^{-12}m^2s^{-1}$) and the protein myosin ($D=10x10^{-12}m^2s^{-1}$). A red blood cell was not included with main part of the figure as its low diffusion coefficient ($D=0.068x10^{-12}m^2s^{-1}$) results in a high sharp peak, restricting the remaining curves to the lower 10% of the graph. The insert shows the graph re-plotted with the inclusion of a red blood cell. From the curves shown on the graph it can be seen that the distance a particle diffuses increases significantly as its diffusion coefficient increases and therefore size decreases.

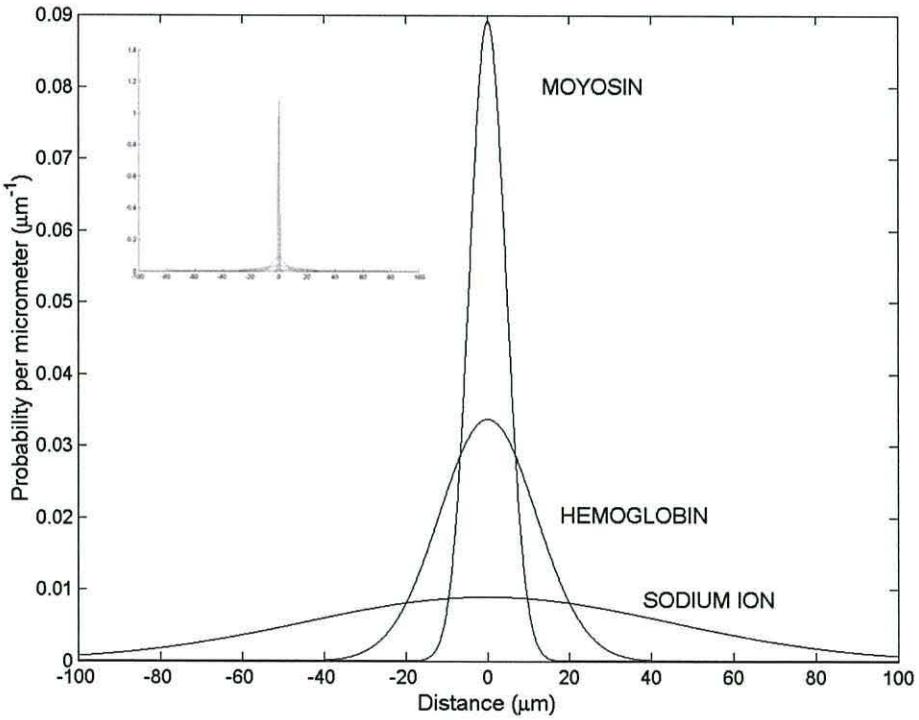

Figure 8.2 *Normalised probability density functions for myosin, hemoglobin and sodium inns after diffusion for 1 second in water. The insert shows the graph re-plotted with the inclusion of a red blood cell.*

When performing dielectrophoretic measurements on blood it is generally necessary to first reduce the samples conductivity. This can be done using a H-filter to selectively remove the ions that have a high diffusion coefficient. If blood is delivered to one inlet channel and a buffer to the other, the ions will diffuse from the blood into the buffer, thus reducing the electrical conductivity of the blood. As mentioned previously, the dimensions of the channel and the time that the two fluids are in contact must be controlled to allow a reasonable portion of the ions in the blood to diffuse into the buffer stream. However, there should not be significant movement of the blood cells.

Figure 8.3 illustrates a two dimensional (2D) simulation of the movement of blood and a buffer through a H-filter. The average velocity at each inlet is 100µm/sec, which results in the two fluids being in contact for 10 seconds. The modelling of this system will be discussed in more detail in the next section. The arrows indicate the direction and magnitude of fluid flow. It can be seen that the flow streamlines across the centre of the device are parallel, indicating that there is no turbulent mixing. They also have the parabolic profile characteristic of laminar flow.

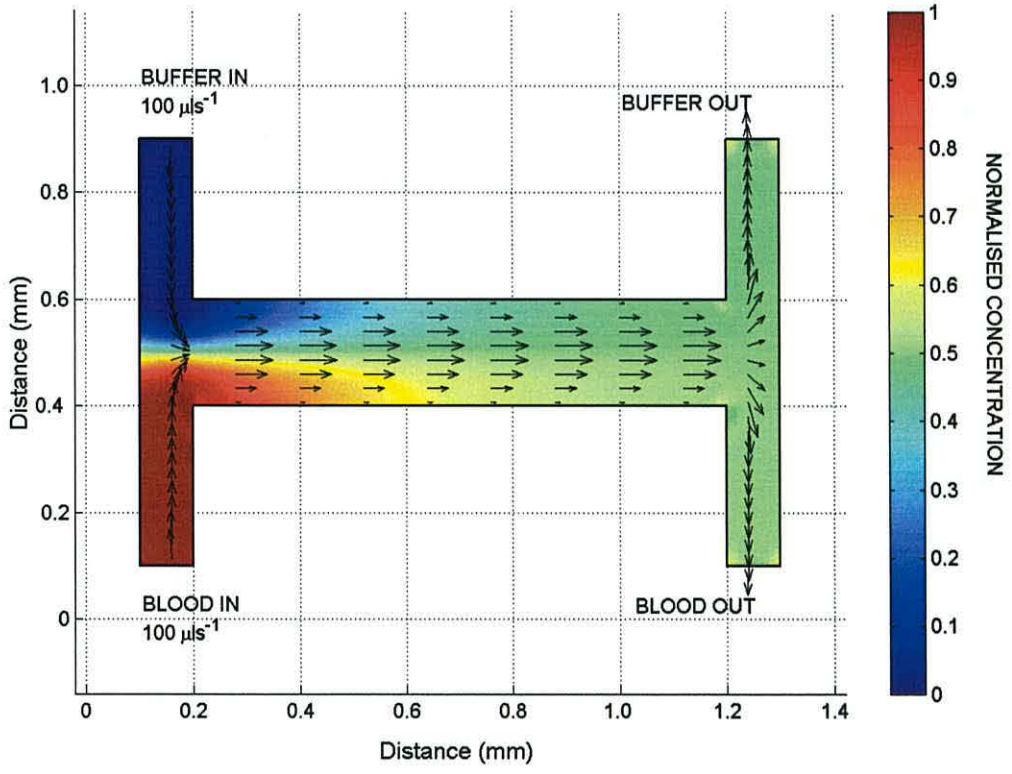

Figure 8.3 *Femlab simulation of a basic H-filter showing the concentration of sodium ions and the direction of the fluid flow.*

The colour map shows the concentration of the sodium ions. It can be seen that the sodium ions diffuse across from the blood stream to the buffer stream resulting in a reduced concentration at the blood outlet.

8.4 Requirements and design

The conductivity of a raw sample of particles in suspension can be too high for some applications. This section and the following section deal with the design of a microfluidic system to reduce the ionic concentration and therefore conductivity of a particle suspension. The design and construction of micro-fabricated prototypes is a costly and time-consuming process. It has been stated [22] that a typical commercial micro-device will require at least 10 design and manufacture iterations. To improve the efficiency of micro-device design there has, in recent years, been a large increase in the use of computer aided design tools. The research in this chapter has been undertaken primarily as a computer aided design and simulation based feasibility study. The final device designs arrived at in this thesis represent micro-devices that are ready for manufacture, with a high degree of confidence that the resulting physical devices would meet all the design criteria.

8.4.1 Target Application

The target application for this research is the dielectrophoretic study of cells within a blood sample. To enable this, the electrical conductivity of the blood sample must be reduced by a factor of 10,000, from approximately 1.5 Sm^{-1} to 0.15mSm^{-1}. To simplify the design process all ionic conductivity has been considered to be derived from sodium ions. This assumption is valid, as the diffusion rate of any ion is much greater than that of a blood cell. To illustrate, red blood cells have a diffusion coefficient of $6.8x10^{-14}m^2s^{-1}$, whilst the diffusion coefficient for a sodium ion is $1x10^{-9}m^2s^{-1}$ [5]. In addition, the main dissolved salt in blood is sodium chloride [21]. The system to be designed must reduce the sodium ion concentration whilst retaining the blood cells.

By rearrangement of equation 8.3 the typical time t for a particle to diffuse a distance L is given by the equation

$$t = \frac{L^2}{D} \tag{8.5}$$

To ensure cells remain in the same flow stream throughout the process, the distance diffused by the red blood cells should be less than half their diameter. Although a platelet is smaller than a red blood cell and diffuses more rapidly, this has not been chosen as the smallest cell of interest as they are not really cells at all but fragments of larger cells from in bone marrow [9]. A red blood cell has a diameter of ~6μm and typically takes 130 seconds to diffuse 3μm. The motion of a particle through diffusion follows a random path and in 130 seconds some particles will have moved significantly further then 3μm. To minimise the number of particles that are lost, the time the blood and pure water are in contact is reduced to 10 seconds. During this time the red blood cells and sodium ions diffused typical distances of 0.82μm, and 100μm respectively. The diffusion distance of the red blood cell is significantly less than half its diameter preventing the particle from being lost. The sodium ions diffuse a significant distance of 100μm in 10 seconds, resulting in a reasonable proportion being removed from the blood plasma. As the sodium ions typically only diffuse 100μm in 10 seconds it is not necessary to fabricate a central channel significantly larger than this dimension.

So far only the typical diffusion length of the particles has been considered. The probability density function for the diffusion distance has a gaussian shape. To find the distribution of a group of particles after diffusion has occurred the original distribution can be convolved [23] with the probability density function. This approach assumes that the probability density function is not distorted by the localised concentration. This for instance would not be the case for fluids where the viscosity and therefore diffusion coefficient increases with concentration, such as saturated sugar solutions.

The initial concentration profile selected consisted of a 100μm layer of particles in medium, adjacent to 900μm of medium with no particles. The diffusion of the particles across the medium was found by convolving the initial concentration with the

probability density function for that particle after a given time. The process was repeated for diffusion times from 2 seconds to 20 seconds in 2 second steps. It is important to remember that these results are for a static system and are intended only as a guide. Figure 8.4 shows the distribution of sodium ions after they have been allowed to diffuse for different amounts of time. The probability density function and the initial concentration profile were discreditised into 0.1μm steps in order to carry out the convolution numerically.

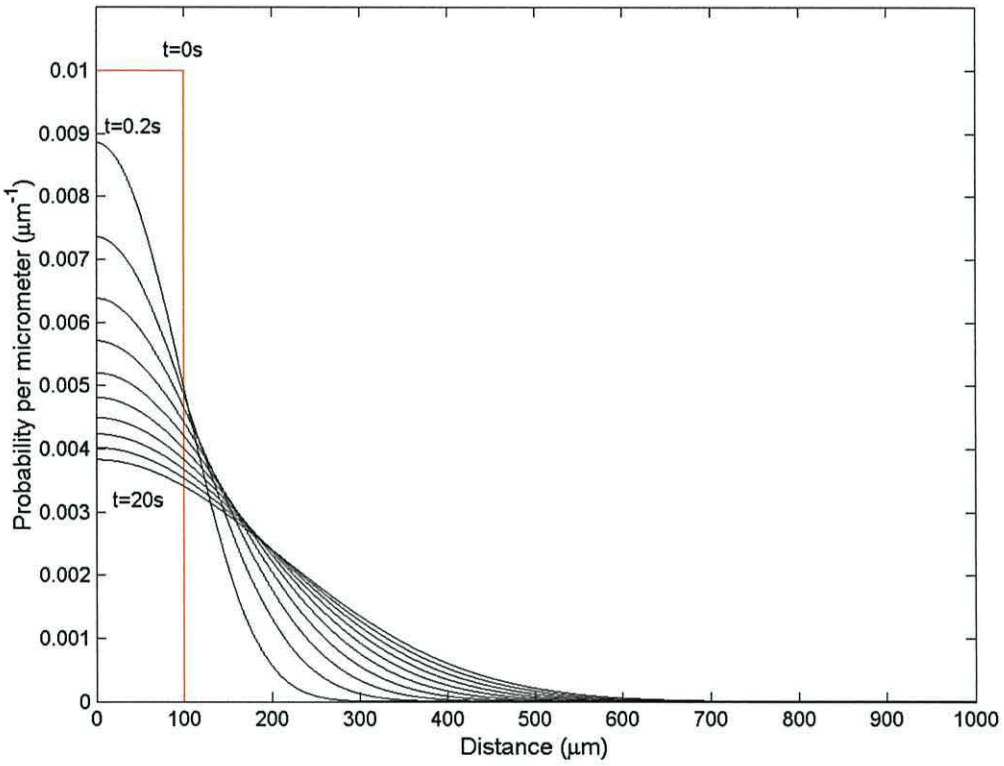

Figure 8.4 *Diffusion of sodium ions away from a region of high concentration after diffusion times form 2 to 20 seconds in 2 second steps.*

From Figure 8.4 it can be seen that the sodium ions rapidly diffuse away from the high concentration region. After 10 seconds more than half the ions have left their original volume, which is marked in red. The same process illustrated in Figure 8.4 was repeated for red blood cells, which have a much lower diffusion coefficient. The results are illustrated in Figure 8.5.

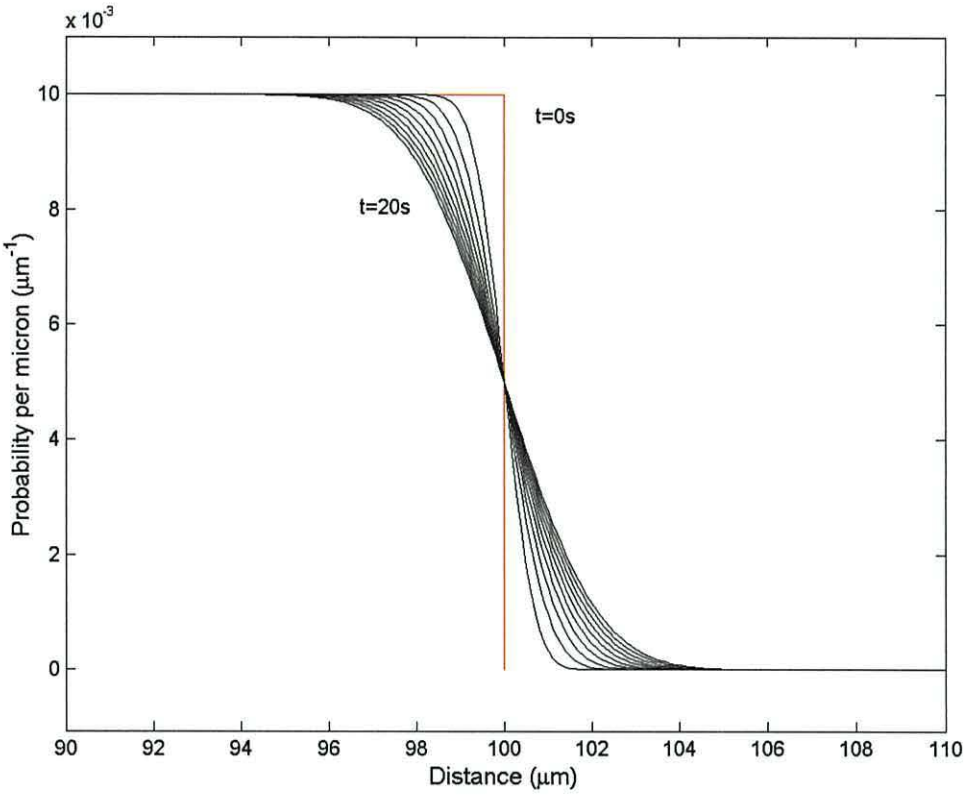

Figure 8.5 *Diffusion of red blood cells away from a region of high concentration after diffusion times form 2 to 20 seconds in 2 second steps.*

Only a small part of the concentration profile has been shown in Figure 8.5. As would be expected the diffusion of the red blood cells is much slower. For the H-filter design illustrated in Figure 8.1 cells that diffuse a distance greater than half their diameter would be lost from the sample stream. In the case of red blood cells this corresponds to 3μm. Through integration to find the area under the curve either side of the 103mm position after a diffusion time of 10 seconds, the fraction of particles lost was found to be 0.0017%. This is an idealised example but provides an indication of the operation of the H-filter. It is likely that physical vibration of the system and fluctuations in the flow will have a greater effect on the red blood cells than diffusion.

An initial channel width of 100μm (200μm where the buffer and sample combine) was chosen, as this is similar to the diffusion distance of the sodium ions. If a significantly larger channel were used, ions adjacent to the wall would be less likely to diffuse into the other flow stream. It is also a convenient dimension to fabricate channels through either photolithography or laser micro machining.

The solute concentration within a blood cell is greater than the solute concentration in the plasma. This difference creates an osmotic pressure within the cell, which allows it to retain its shape [9]. If the solute concentration within the plasma is significantly reduced the osmotic pressure may increase to a level where the cell will lyse. To maintain the solute concentration within the plasma, the ions can be replaced with a non-ionic solute, such as the sugar sucrose [24]. As the sugar is non-ionic, it will not significantly change the conductivity of the suspending medium but will prevent the red blood cells from lysing. This replacement with sugar is achieved by forming the buffer in Figure 8.2 from a sugar solution. As the ions diffuse out of the blood, the dissolved sugar molecules diffuse in. This process is only necessary with relatively fragile animal cells and would not be so critical with more robust cells, such as yeast.

8.5 Construction of the finite element model

Analytical solutions for the concentration profile within a H-filter exist for simple geometries and flow profiles [18]. However, these solutions are complex and valid only for specific applications. To model a wider range of possible arrangements a finite element approach has been used. The modelling was undertaken using the software package FEMLAB.

In this problem there are two connected physical proccesses that must be solved simultaneously. They are the physical movement of the fluid within the channel and the diffusion of material through the fluid. To find the concentration profile, mass movement through flow and diffusion must both be taken into account. The movement of mass by diffusion is governed by Fick's second law, whilst physical fluid movement is governed by the Navier-Stokes equations. Section 8.5.1 describes Fick's second law and shows how this equation is converted to the form used in the finite element model. The version of the Navier-stokes equations used is also provided. The boundary conditions chosen for the problem are then outlined in Section 8.5.2.

In the formulation of this model it has been assumed that the flow profile in the channel is not affected by the concentration of dissolved or suspended material. As will be covered later, this results in the viscosity term in the Navier-Stokes equations remaining constant. Also a simplified version of the Navier-stokes equations for incompressible

fluids has been used, which assumes that the density, viscosity and thermal conductivity of the fluid remain constant. Adding an additional mass transfer term to the diferential equations governing the diffusion incorporates the change in the concentration due to fluid flow.

8.5.1 Partial differential equations

This section will first discuss the equations relating to diffusion and then those relating to fluid flow. Fick's second law of diffusion states that for a constant diffusion coefficient, D, the rate of change in concentration with time, is proportional to the rate at which the concentration gradient changes with distance in a given direction, x. This can be expressed by the equation:

$$\frac{\partial C}{\partial t} = D\frac{\partial^2 C}{\partial x^2} \tag{8.6}$$

Where C is the concentration at a given point. If the diffusion coefficient is not constant, but instead varies with concentration, the more general form given by the following equation must be used.

$$\frac{\partial C}{\partial t} = \frac{\partial}{\partial t}\left(D\frac{\partial C}{\partial t}\right) \tag{8.7}$$

In a real system it is necessary to consider diffusion in all three dimensions. Assuming the diffusion coefficient is independent of the direction equation (8.6) becomes,

$$\frac{\partial C}{\partial t} = D\frac{\partial^2 C_x}{\partial x^2} + D\frac{\partial^2 C_y}{\partial y^2} + D\frac{\partial^2 C_z}{\partial y^2} \tag{8.8}$$

This can be re written

$$\frac{\partial C}{\partial t} = D\nabla^2 \vec{C} \tag{8.9}$$

Where the right hand side in equation 8.8 is equal to the right hand side in equation 8.9. The arrow over the concentration indicates that it is a vector quantity. At present this expression does not take into account any change in concentration due to fluid movement, u. To include this a convective term is added to the relationship to give.

$$\frac{\partial C}{\partial t} = \nabla.\left(D\nabla\vec{C} + \vec{C}\vec{u}\right) = \vec{N} \tag{8.9}$$

The concentration flux vector (**N**) on the right hand side of the expression now contains both a diffusive and convective contribution. When solving this problem the steady state condition is of interest, this means there is no change in the concentration profile with time. Therefore there is no concentration flux and left hand side of the equation is set to zero to give.

$$\nabla.\left(D\nabla\vec{C} + \vec{C}\vec{u}\right) = 0 \tag{8.10}$$

This is the partial differential equation that is used in the simulation package. A steady state solution for the fluid movement is also required. The incompressible Navier-Stokes equations give

$$-\eta\nabla^2\vec{u} + \rho\left(\vec{u}.\nabla\right)\vec{u} + \nabla p = 0 \tag{8.11}$$

$$\nabla.\vec{u} = 0 \tag{8.12}$$

Where η, u, ρ and p are the viscosity, velocity density and pressure of the fluid respectively. Equation 8.11 expresses that the momentum gain within the system is in steady state. From left to right the terms relate to rate of momentum gain through viscous transfer, convection and pressure forces, the zero on the right indicated these are balanced. Equation 8.12 expresses that the velocity of the fluid at every given point

does not change. The process of solving these equations for a given geometry and boundary conditions is carried out by the software package FEMLAB.

8.5.2 Boundary Conditions

To solve a group of differential equations it is necessary to define the boundary conditions of the problem. In doing so the values of the result are fixed at the edge of the simulation space and the result calculated so that these values remain valid. The solving process is iterative. An initial solution is improved upon repeatedly until the error between iterations falls below a defined value. Two physical processes are being solved at the same time in this simulation. Therefore, it is necessary to define two sets of boundary conditions. One set relating to the diffusion and the other relating to the fluid flow.

As a result of the low flow velocity in the channel and its small dimension, the structure has a low Reynolds number and therefore the flow is laminar. In laminar flow the fluid immediately adjacent to the channel wall is stationary (velocity, u=0), this forms the fluid flow boundary condition for all the main channel walls and is commonly known as 'no-slip'. Two different approaches are commonly used to define the flow at the inlet of a finite element model. One approach is to define a parabolic flow profile where the fluid is stationary at both channel walls. The approach used in this work defines a flat velocity profile across the channel but allow the fluid to slip along the channel walls for a short length. This short section of slip boundary allows the natural flow profile to become established without causing a contradiction where the boundary settings meet. It can be assumed that a parabolic flow will be established within a distance equivalent to the width or height of the channel [25]. Therefore it is safe to assume that the flow profile is fully established before the inlet channels meet. constant pressure was defined at the outlet boundary. To change proportion of the fluid that goes to each outlet these pressures were adjusted relative to each other. Figure 8.6 illustrates the boundary conditions relating to the fluid flow part of the model.

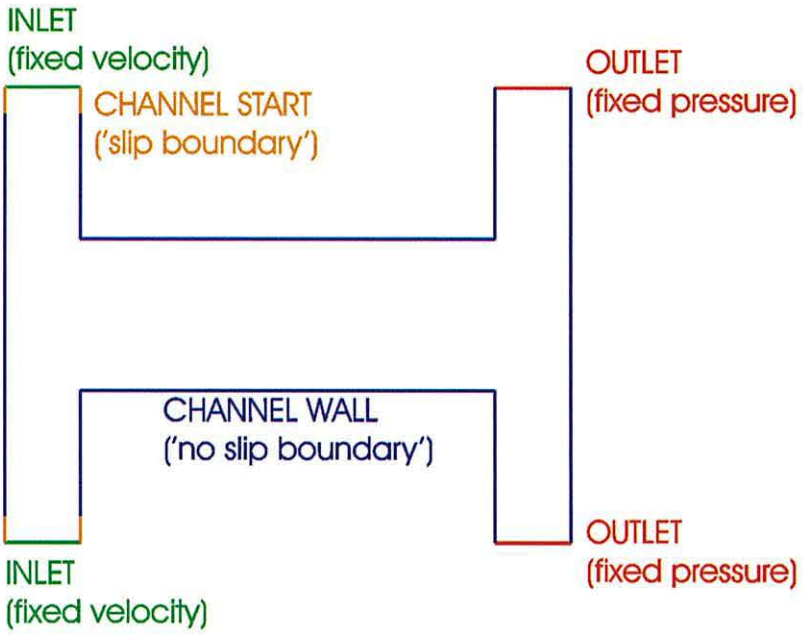

Figure 8.6 *Boundary conditions applied to the fluid flow part of the H-filter model.*

The channel walls of the H-filter are impermeable to any diffusing material within the fluid flow. This defines the boundary condition at the walls of the channel that states there is no concentration flux (**N**) in the direction normal (**n**) to the boundary (**N.n**=0). The concentrations at the inlets are given constant values irrespective of flow by defining the concentration at that boundary. The concentration at the outlet should be the same as if the channel continued beyond the boundry. This is achieved by setting the diffusive concentration flux across the boundary to be equal to the convective concentration flux due to fluid flow. These boundary conditions are illustrated in Figure 8.7.

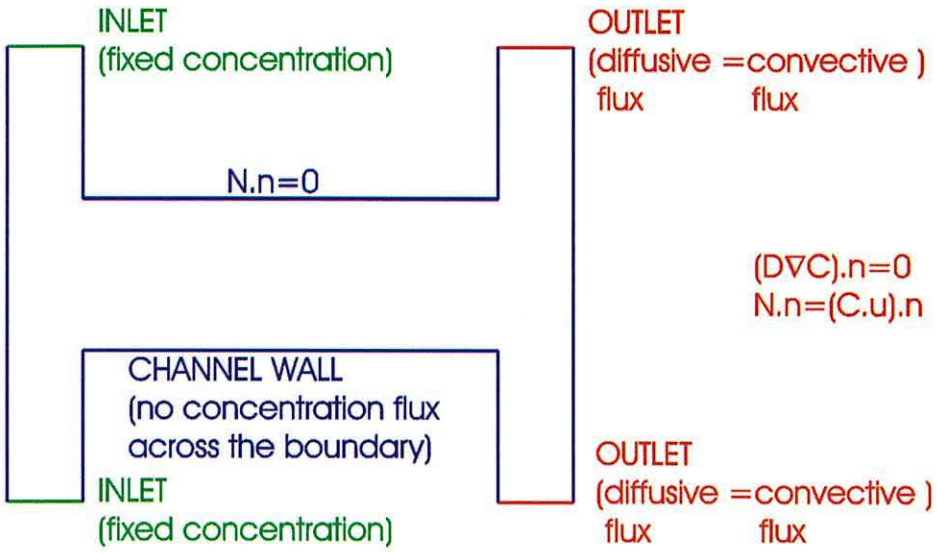

Figure 8.7 *Boundary conditions applied to the Diffusion part of the H-filter model*

Once the equations governing the physical processes and the boundary conditions have been defined, it is possible to solve the model to show the steady state result. In some situations a steady state will not exist, for example if the boundary conditions have been poorly defined and the flow into a system is different from the flow out. A steady state will also not be achieved if the system is unstable and oscillates.

The precise operation of a finite element analysis program varies depending in the methods used [26]. In brief the problem space is broken down into a mesh of small elements with the boundary conditions kept constant at the edge. The solution at each node is then calculated by solving the partial differential equations for each element. To reduce the computational complexity of the problem an initial approximation to the solution is made and then the process iterated until the error between successive solutions reaches a specified value. Once stable values are achieved at each node, interpolation can be used to find an approximate solution value at any point in the problem space. The accuracy of a solution depends largely in the resolution of the finite element mesh used.

8.6 Finite element modelling

This section contains the different geometries that were simulated and describes how the basic H-filter design was adapted to improve the reduction in sodium ion concentration. Section 8.6.1 first compares the results from two and three dimensional models. The flow profile through the channel is then optimised in section 8.6.2. Before diffusion and fluid flow are modelled simultaneously in Section 8.6.3. Sections 8.6.4 to 8.6.6 then optimise the design to achieve the concentration reduction set out in Section 8.4.

8.6.1 Comparison of two and three-dimensional simulations

For all the simulations in this section a two-dimensional (2D) representation of the H-filter has been used. This approach is less computationally intensive and assumes that the shape of the structure extends a long distance out of or into the plane of the simulation, compared to the channel width. Figure 8.8 illustrated the 2D simulation of the flow profile within a H-filter. This is a plan view of the filter shape used in the three dimensional (3D) simulation shown later in Figure 8.9.

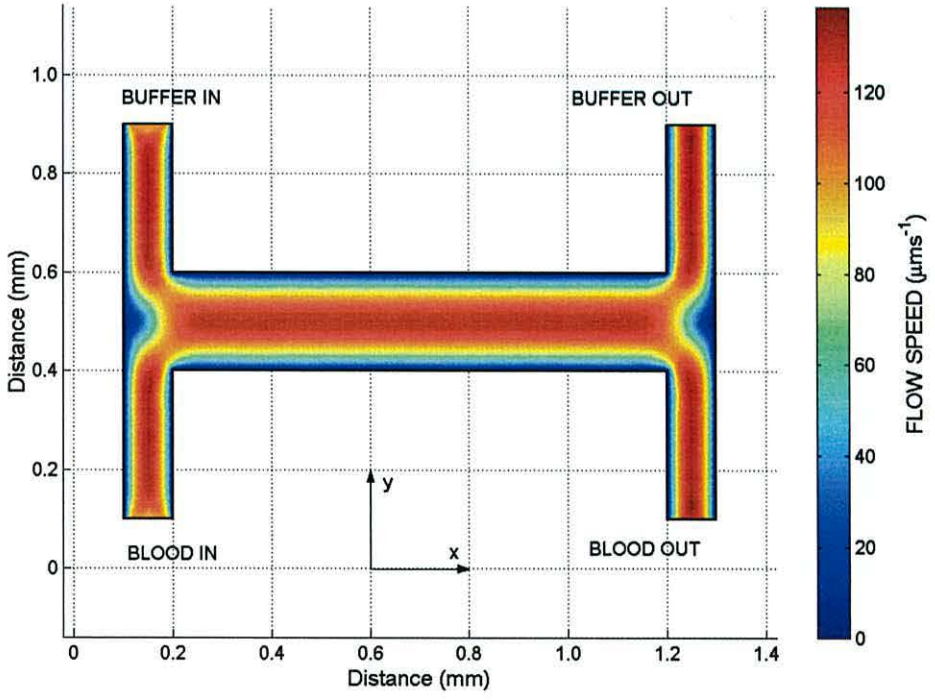

Figure 8.8 *2D simulation of the fluid flow in a simple H-filter.*

In this simulation a parabolic flow profile can be seen with stationary fluid at the channel walls and rapid flow in the centre of the channel. The average flow velocity is $100\mu ms^{-1}$ but due to the parabolic flow profile, the peak flow velocity is significantly larger at $130\mu ms^{-1}$. The flow profile will be described in more detail in Section 8.6.2.

Figure 8.9 illustrates a 3D simulation of the channel in Figure 8.3, the plan view has been extended 100μm out of the plane of the image in the z direction to produce a 3D structure.

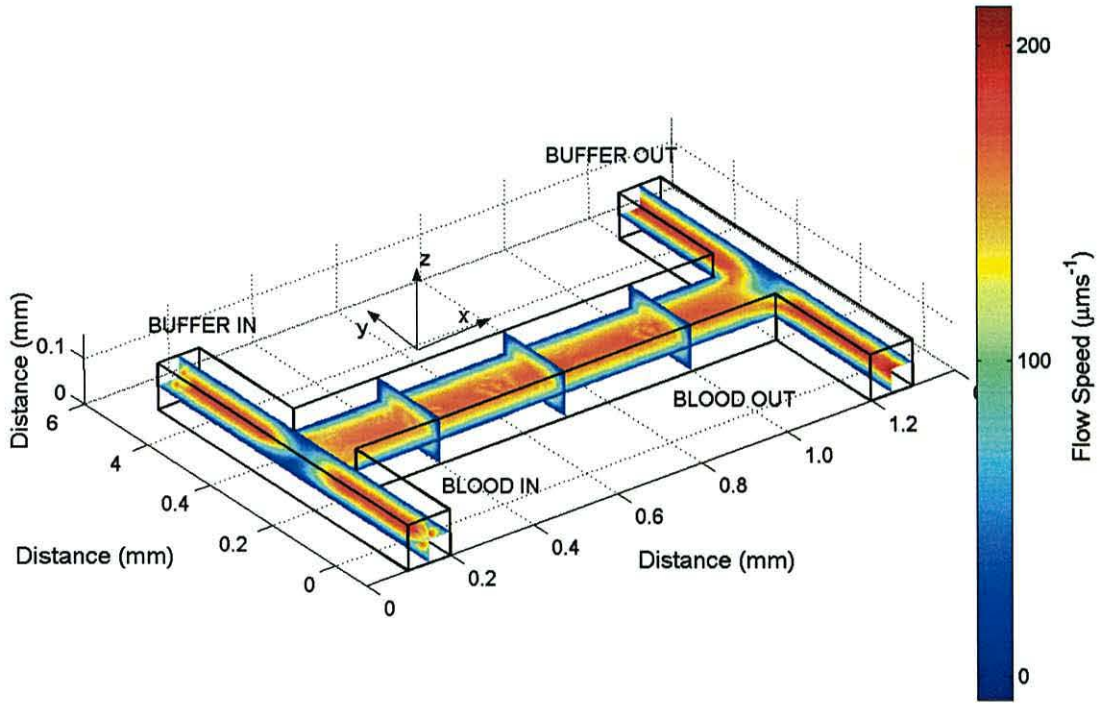

Figure 8.9 *3D simulation of the fluid flow in a simple H-filter.*

The overall parabolic shape of the flow profile in the 3D model is generally similar to the 2D model, but certain details are different. In the 3D model the flow rate at the upper and lower surfaces of the channel is taken into account and as specified by the boundary condition is stationary. In the 2D model it was assumed that the flow rate was constant at all heights for a given point in the channel, in comparison the 3D simulation shows an overall 3D parabolic flow profile. For comparative purposes Figure 8.10

shows the flow velocities for both the 2D and 3D models. In each case the velocities are plotted for a line in the y direction across the middle of the centre channel.

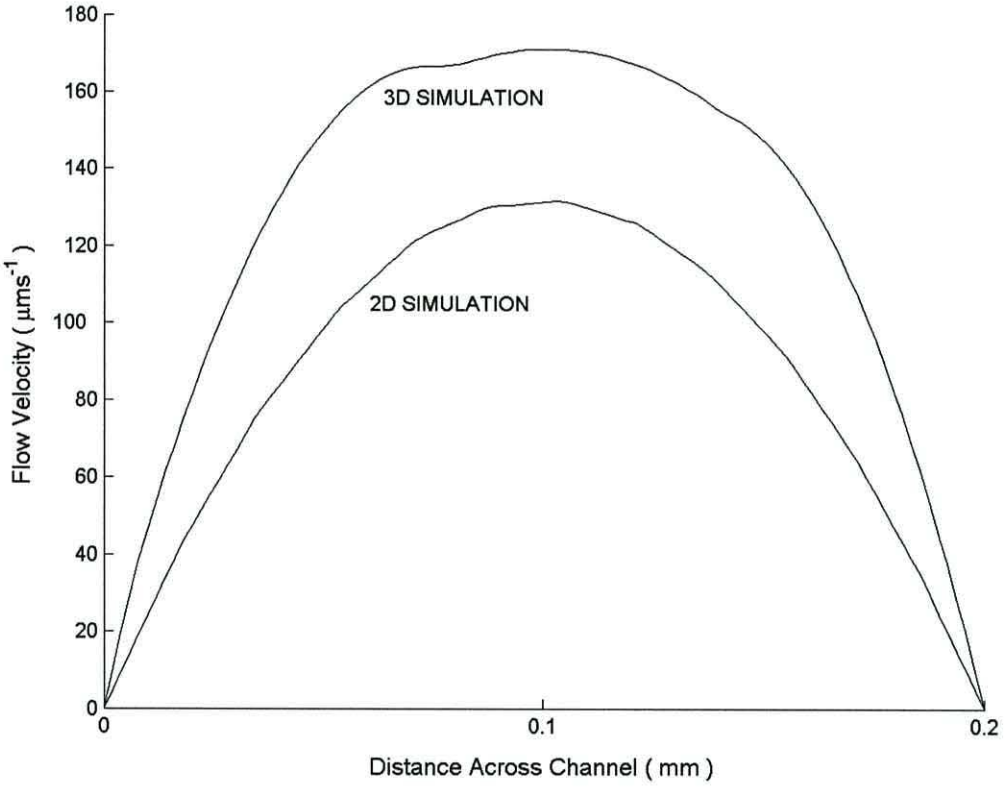

Figure 8.10 *Flow velocities calculated using 2D and 3D simulations of a H-filter.*

The finite element process causes the lack of smoothness due to the discrete nature of the approximation. This can be observed in both curves. From consideration of these curves it can be observed that the flow profiles for the two simulations have a similar shape. However, the stationary fluid at the upper and lower surfaces of the channel in the 3D model results in a greater central flow rate to maintain the same average flow through the channel. The 2D model more closely matches the 3D model when the height of the 3D model is increased. The flattening of the flow profile for the 3D case is caused by the upper and lower surfaces of the channel. For wide shallow channels this flow profile would be almost completely flat across the centre section with each end going to zero in a parabolic profile.

Although the 2D model is a less accurate representation of the system than the 3D model, it provides a useful indication of its operation. As long as the height of the real system is large compared to the width, the results produced by a 2D model are acceptable.

8.6.2 Curved channel profile to reduce stationary fluid

The simulation result in Figure 8.8 illustrate that there are regions of near stationary fluid at either end of the central channel of the H-filter, where the blood and buffer meet or separate. These volumes of near stationary fluid could result in particles becoming trapped at either end of the channel. It is therefore necessary to reduce the size of this volume to a minimum. From the simulation result in Figure 8.8 it can be seen that the natural path of the moving fluid is curved. To reduce the stationary volume the right angles in the H-filter were replaced by curved corners as illustrated in Figure 8.11. The radius was chosen to produce a gradual change in the direction of the fluid, whilst being small enough to minimise the thin channel wall where the two inlets meet.

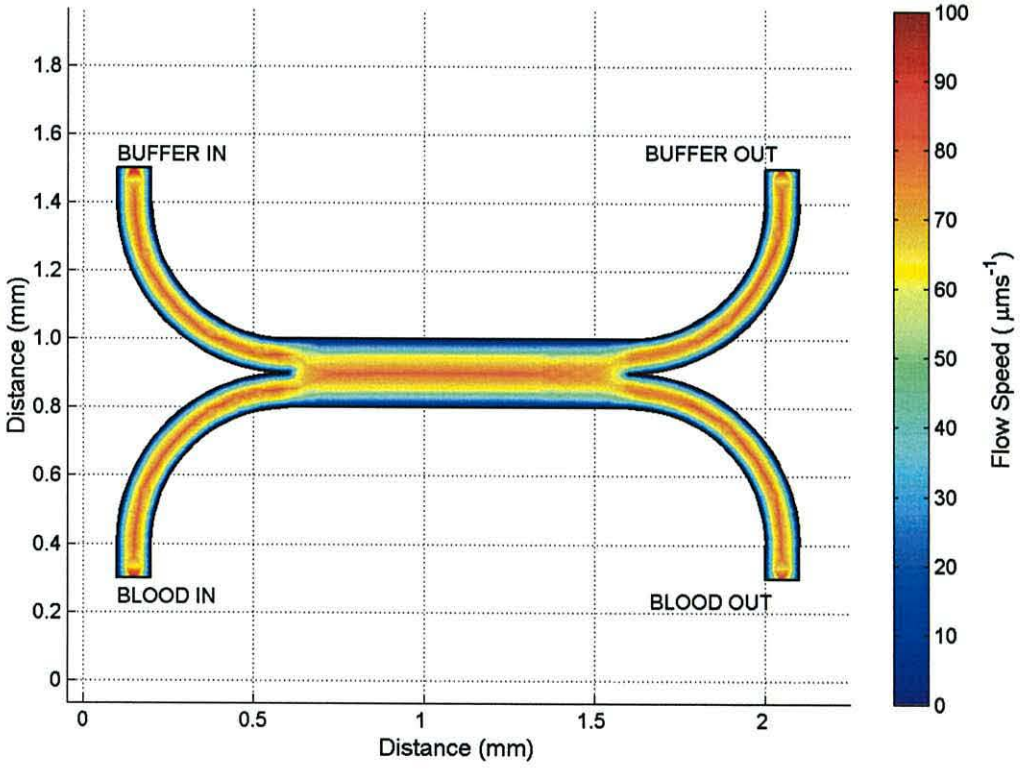

Figure 8.11 *Flow profile through a H-filter with curved corners.*

From the simulation results it is evidant that the areas of stationary fluid at either end of the central channel are no longer present, resulting in minimal "dead volume" throughout the device.

8.6.3 Simultaneous simulation of diffusion and fluid flow

When using the FEMLAB simulation package it is possible to combine two physical processes, in this case flow and diffusion, into a single model as described in Section 8.5. This approach was used to model the diffusion of sodium ions from one flowing stream to the other. A normalised concentration of sodium ions of 1 was defined at the blood inlet and a concentration of 0 was defined at the buffer inlet. Figure 8.12 illustrates the variation in the concentration of sodium ions along the length of the channel.

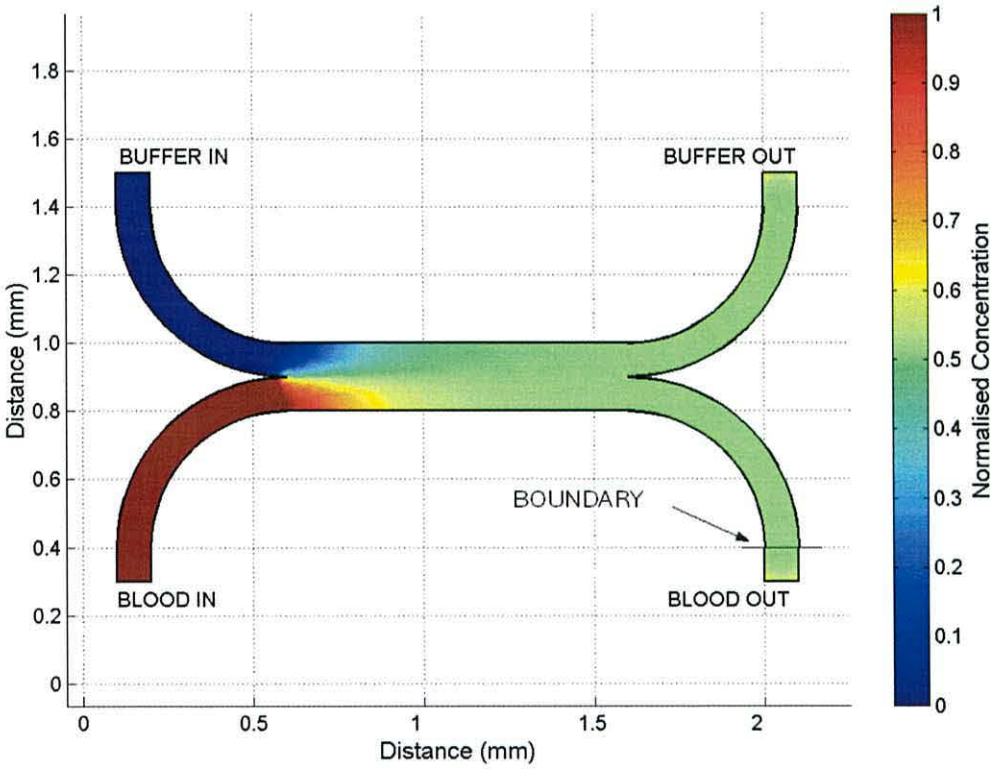

Figure 7.12 *Computer simulation illustrating the diffusion of sodium ions in a H-filter.*

Using Equation 8.3 the typical diffusion distance for sodium ions in 10 second was calculated to be 100μm. However from observation of the simulation results the ions appear to diffuse more rapidly. This effect is accounted for by the parabolic flow profile within the channel, which causes ions at different positions in the channel to have different velocities. As can be seen from Figure 7.9 the flow velocity in the centre of the channel is $130\mu ms^{-1}$ so ions in this fluid region pass through the centre channel in less than 10 seconds. However, once an ion has diffused a slight distance into the buffer stream, the flow rate drops due to the parabolic flow profile. This drop in velocity increases the time spent in the channel allowing the particle to diffuse further. This process only applies to sodium ions leaving the blood. Larger particles are not lost through this mechanism as once they are in the central rapid section of the flow profile they will reach the outlet before they can diffuse into the slower fluid.

The average concentration of the sodium ions in the blood at the outlet is found by integrating across the channel, slightly before the outlet and dividing this value by the width of the channel. A boundary before the end of the channel is used to eliminate the slight errors, visible in Figure 8.12, that occur in the solution at the outlet due to the coarseness of the finite element mesh. Using this approach the concentration of sodium ions in the processed blood was found to be 52% of that at the inlet. This is as expected for full diffusion giving near equal concentration at both outlets but it is significantly less than the required reduction in concentration.

8.6.4 Dissimilar flow volumes through H-filters

In the case discussed in Section 8.6.3 both the blood and the buffer have the same flow rate through the device. The maximum dilution of the blood occurs when the ions are distributed uniformly through the two fluids. In this situation the maximum factor by which the concentration can be reduced is 50%.

To further reduce the concentration of the sodium ions in the blood it is necessary to pass more buffer through the device than blood. Increasing the dimension of the channel supplying the buffer is one approach to this requirement as illustrated in Figure 8.13. Although this approach increases the total amount of fluid available into which the

sodium ions can diffuse, the concentration at the outlet only drops to 41% of that at the inlet, which represents only a slight improvement over the previously achieved 52%.

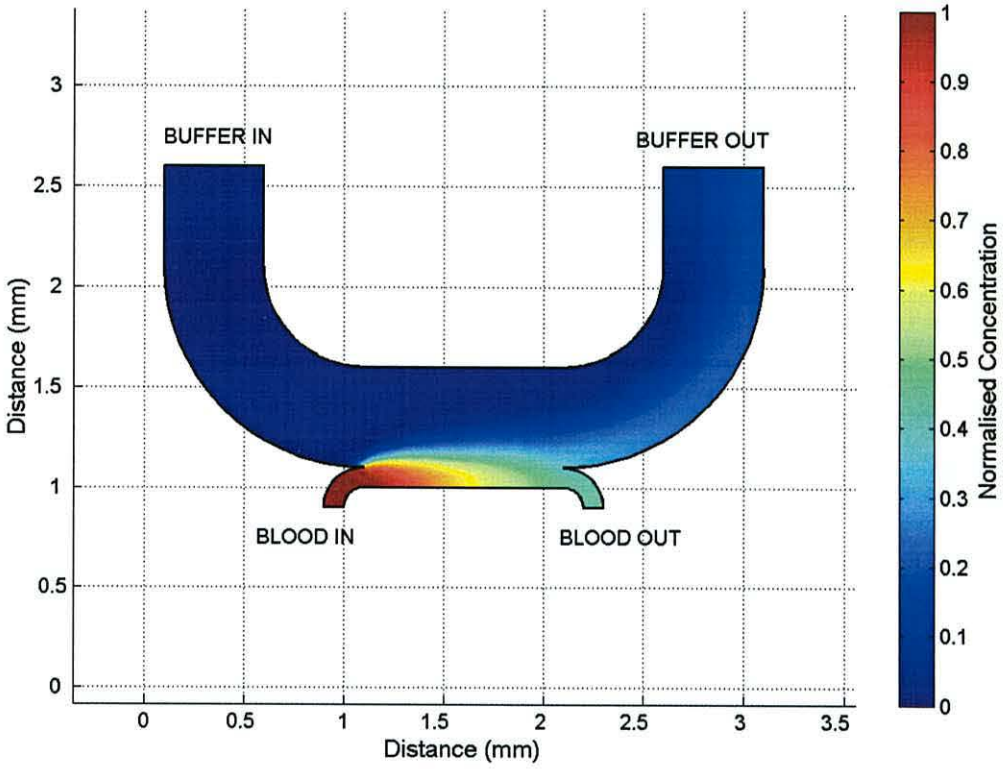

Figure 8.13 *Simulation of the concentration of sodium ions in a H-filter, where there is a 5:1 ratio between the size of the buffer and sample inlets.*

From the simulation results in Figure 8.13 it can be seen that the diffusion distance of the ions into the buffer limits the achievable reduction in the concentration. The ions have insufficient time to diffuse into the buffer in the upper half of the channel.

Instead of changing the channel dimensions, it is also possible to increase the flow of the buffer relative to the blood. In this situation the blood flow profile will distort, forming a thinner stream along the side of the channel. To maintain the same volume transport, the velocity of the blood stream increases. The arrows in Figure 8.14 illustrate this effect when the flow rate of the buffer is ten times that of the blood.

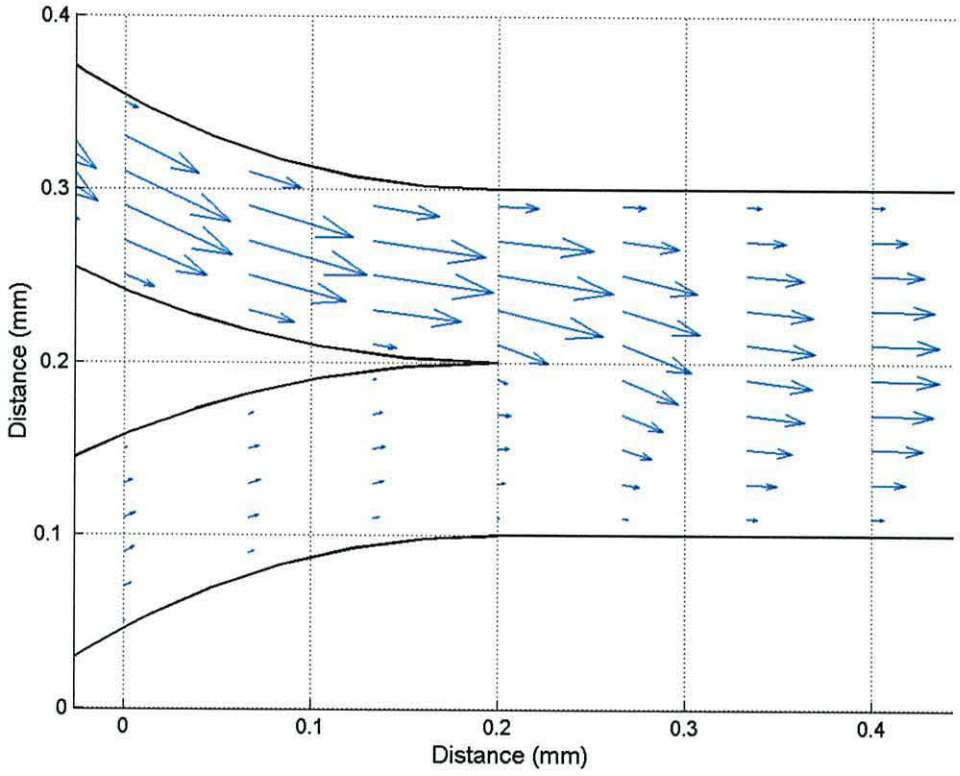

Figure 8.14 *An enlarged section of a simulation showing the flow profile in a H-filter, where there is a 10:1 ratio between the inlet velocity of the buffer and sample.*

When in Figure 8.14, the two fluid streams make contact, the two parabolic flow profiles combine to form a larger, parabolic flow profile. The average velocity of this fluid is governed by the amount of fluid entering from the two inlets. In the case where the inlet channels are of the same width the combined flow rate is the average of the two inlet flow rates, which for this example is $600\mu ms^{-1}$. The direction of the arrows in Figure 8.14 illustrates that the blood travels along the lower surface of the central channel. This flow is relatively slow compared to the main bulk of the fluid, allowing more time for the ions to leave the blood.

The diffusion distance is proportional to the square root of the time taken. As a simple, worst case, approximation we can consider a flat rather than parabolic flow profile giving a uniform velocity of $600\mu ms^{-1}$ across the channel. The time spent in the channel is then 1.6 seconds, which results in a typical diffusion distance for sodium ions of 40μm. Even though the time in the channel has been reduced by a factor of 0.16 the diffusion distance has only fallen by a factor of 0.4. This effect combines with the

reduced width of the fluid stream and the removal of the ions by the rapidly flowing buffer to produce an improved reduction in the ionic strength of the blood. Figure 8.15 shows a simulation of the sodium ion concentration in a H-filter, where the flow of the buffer is ten times greater than that of the blood.

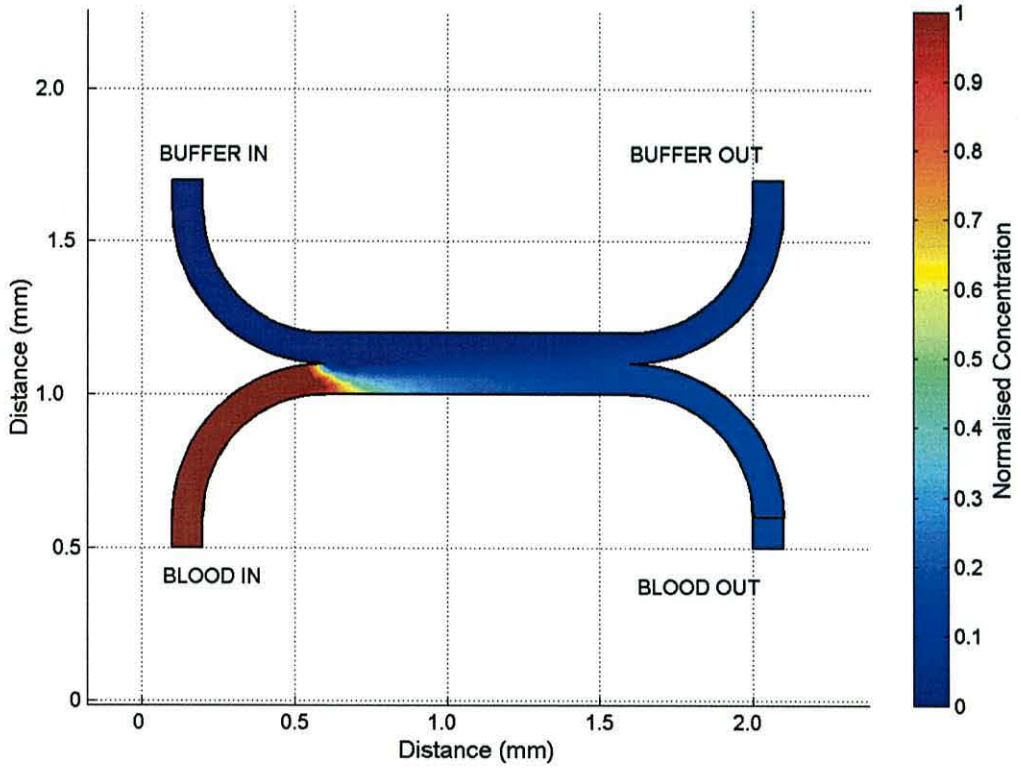

Figure 8.15 *Simulation showing the sodium ion concentration in a H-filter where there is a 10:1 ratio between the inlet velocities of the buffer and sample.*

For the simulation results shown in Figure 8.15, where the flow rate of the buffer is 10 times greater than that of the blood, the concentration of the sodium ions in the blood has been reduced to 16% of the initial value. This is a significant improvement in comparison to identical flow rates, where the concentration was reduced to 52% of the initial value. The extent to which the concentration is reduced depends on the ratio between the flow rates of the buffer and blood. Figure 8.16 illustrates how the concentration of the ions in the blood varies for different ratios of flow rates. The average flow velocity of the blood was kept constant at $100\mu ms^{-1}$ and the flow velocity of the buffer varied between $100\mu ms^{-1}$ and $10{,}000\mu ms^{-1}$.

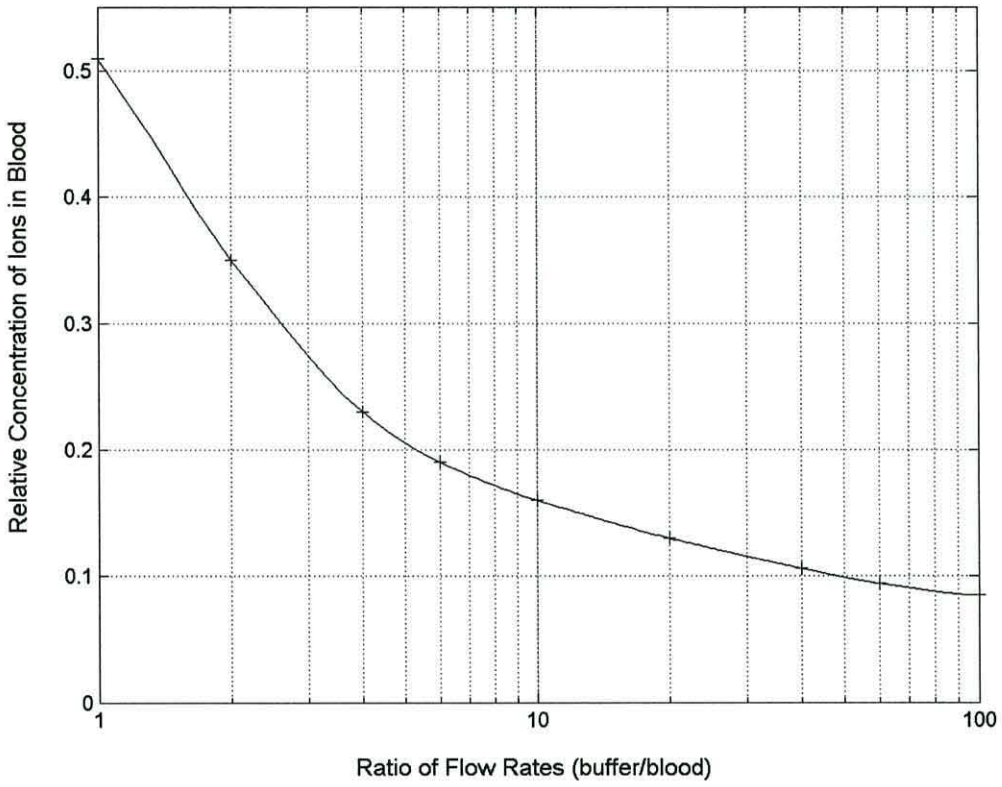

Figure 8.16 *Variation in the concentration of sodium ions at the outlet for different ratios of flow rates of buffer and sample ranging from 1:1 to 100:1.*

In Figure 8.16 as the ratio of the flow rates increases the ion concentration in the blood at the outlet decreases. However, the degree of improvement with increasing flow rate is not linear and reduces with increasing flow rates. When the flow ratio is doubled from 1:1 to 2:1 the ion concentration is reduced by 47%. However, if the ratio is doubled between 10:1 and 20:1 the ionic concentration at the outlet is only reduced by 22%.

To ensure that the blood is neither lost to the buffer outlet nor has buffer added to it, the flow rates at the outlet must exactly match those at the inlet. When the ratio of the two flow rates is high, a small percentage error between the flow rates at the outlet and inlet of the buffer can significantly effect the composition of the blood at the outlet. For a 100:1 ratio of the flow rate of buffer to blood, a 1% difference between the buffer outlet and inlet can result in a significant change in flow at the blood outlet. If the flow rate at the buffer outlet is 1% less than the inlet, the excess buffer will result in the blood being diluted with an equal volume of buffer. However, if the flow at the buffer

outlet is 1% greater than the inlet, the extra fluid comes from the blood inlet leaving none to pass through to the blood outlet.

The choice of ratio of flow rates is a compromise between high ratios giving a high level of dilution and lower ratios being easier to control. The benefit gained from increasing the ratio of flow rates decreases as the ratio increases so little benefit is gained from using ratios greater than 10:1.

8.6.5 Three Input H-filters

In the H-filter described in Section 8.6.4 the buffer that is used to remove the ions only makes contact along one interface with the blood. To improve the efficiency of the H-filter buffer, can be passed along both surfaces of the stream of blood as illustrated in Figure 8.17.

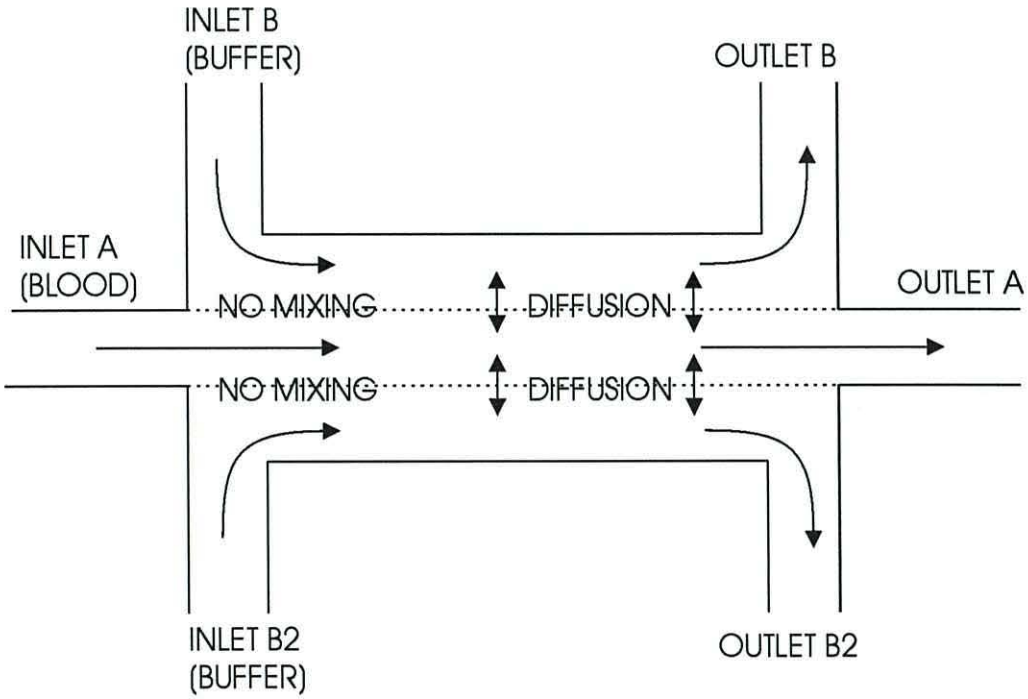

Figure 8.17 *H-filter design with buffer flowing along both sides of the sample.*

A simulation of the concentration of sodium ions in the channel for a flow ratio between the buffer and blood of 10:1 is shown in Figure 8.18.

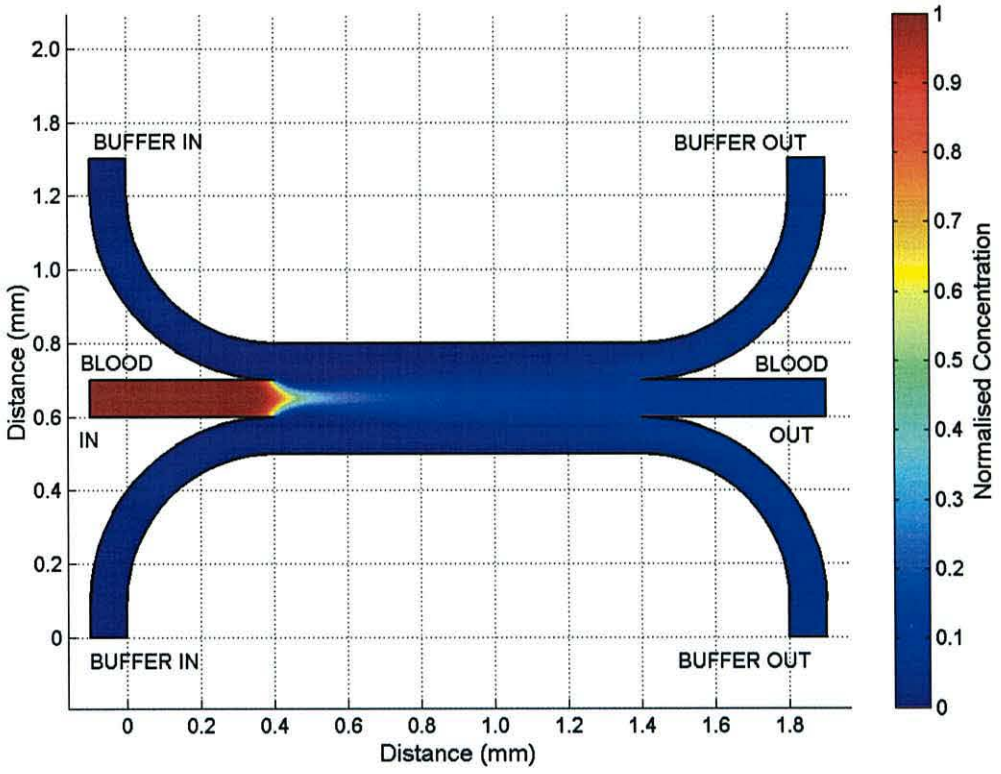

Figure 8.18 *Simulation showing the concentration of sodium ions in a H-filter with buffer on both sides of the sample. The ratio between the inlet velocities of the buffer and sample is 10:1.*

From the simulation results, it can be seen that where the blood and buffer meet, the blood is channelled into a thin stream. Once this stream arrives at the end of the central channel it slows down and expands to fill the channel once more, this effect is more obvious in Figure 8.19. In Figure 8.18 the sodium ions diffuse into the buffer and are removed to the outlets labelled 'buffer out'. The concentration of the sodium ions in the blood at the outlet is 11% of that at the inlet. This compares to a reduction to 16% of the initial value when the buffer only made contact with the blood on one surface. Due to the channels either side of the blood there is twice the volume of buffer flowing through the H-filter. This situation is comparable to a ratio of flow rates of buffer and blood of 20:1 in the single sided filter, where the concentration of ions in the blood was reduced to 13%, which is less effective then channelling buffer on both sides of the sample.

From this simulation it appears that the blood is spreading out along the length of the channel. However, it should be remembered that this graph shows ion concentration and this is simply the effect of the ions diffusing into the buffer. Because the flow in the

channel is laminar the fluid stream that enters the channel at the inlet labelled 'blood in' leaves through the outlet labelled 'blood out'. This effect is more obvious when the diffusion of haemoglobin is considered, this is a larger molecule with a diffusion coefficient of $70x10^{-12}m^2s^{-1}$. The result of the simulation is illustrated in Figure 8.19.

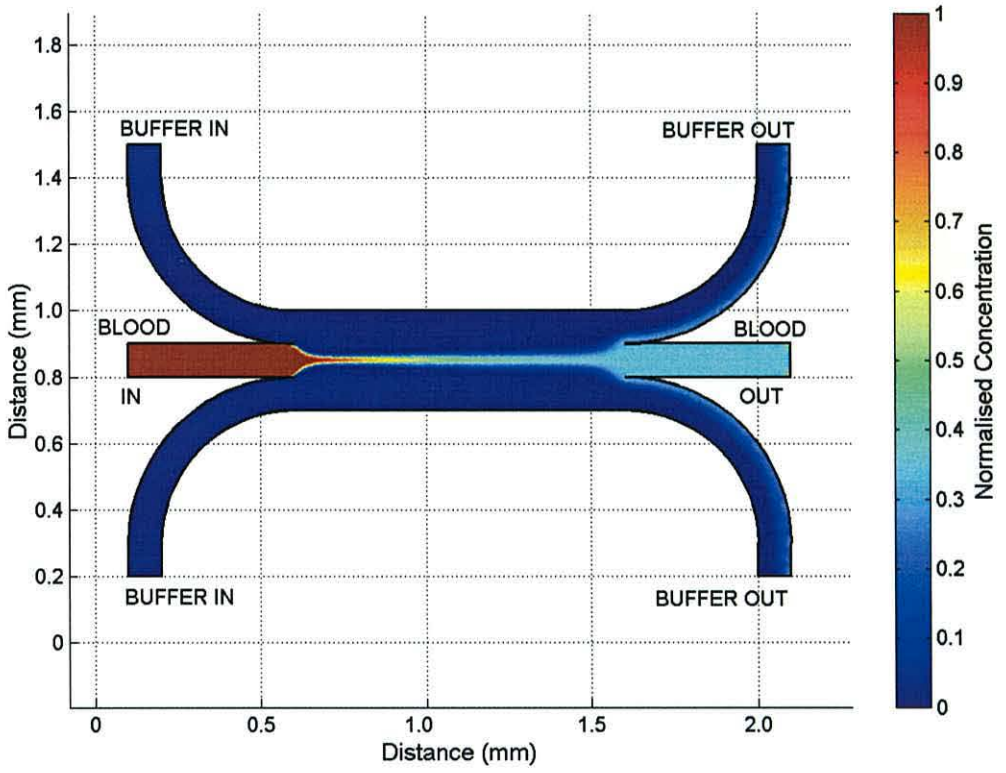

Figure 8.19 *Simulation illustrating the concentration of haemoglobin in a H-filter with buffer on both sides of the sample. The ratio between the inlet velocities of the buffer and sample is 10:1*

Haemoglobin is nevertheless a relatively small particle compared to a red blood cell so there is significant diffusion of the molecules into the buffer. The concentration of the haemoglobin in the blood stream at the outlet is 35% of that at the inlet.

With a reduced diffusion coefficient the changes in the concentration over a given distance become smaller. Limitations due to the mesh size and numerical precision in the simulation result in errors when small diffusion distances are encountered. Reducing the mesh size can improve the accuracy but the computing resources available limit this process.

Table 8.1 lists some particles, their diffusion coefficients in water [5] and the extent to which the H-filter in Figure 8.18 reduces their concentration. Particles were chosen with a range of different diffusion coefficients. For diffusion coefficients below 5 it was difficult to achieve an accurate result due to errors in the simulation. A graphical representation of these results is illustrated in Figure 8.20

Particle	**Diffusion Coefficient (10^{-12} m^2s^{-1})**	**Dilution Factor**
-	10,000	0.070
Hydrogen ion	9,000	0.071
Sodium ion	1,000	0.106
-	100	0.295
Haemoglobin	70	0.349
Myosin	10	0.823
Tobacco mosaica virus	5	0.908
Platelet	0.16	
Red blood cell	0.068	

Table 8.1 *Diffusion coefficients of selected particles and the extent to which their concentration is reduced using the H-filter in Figure 8.18.*

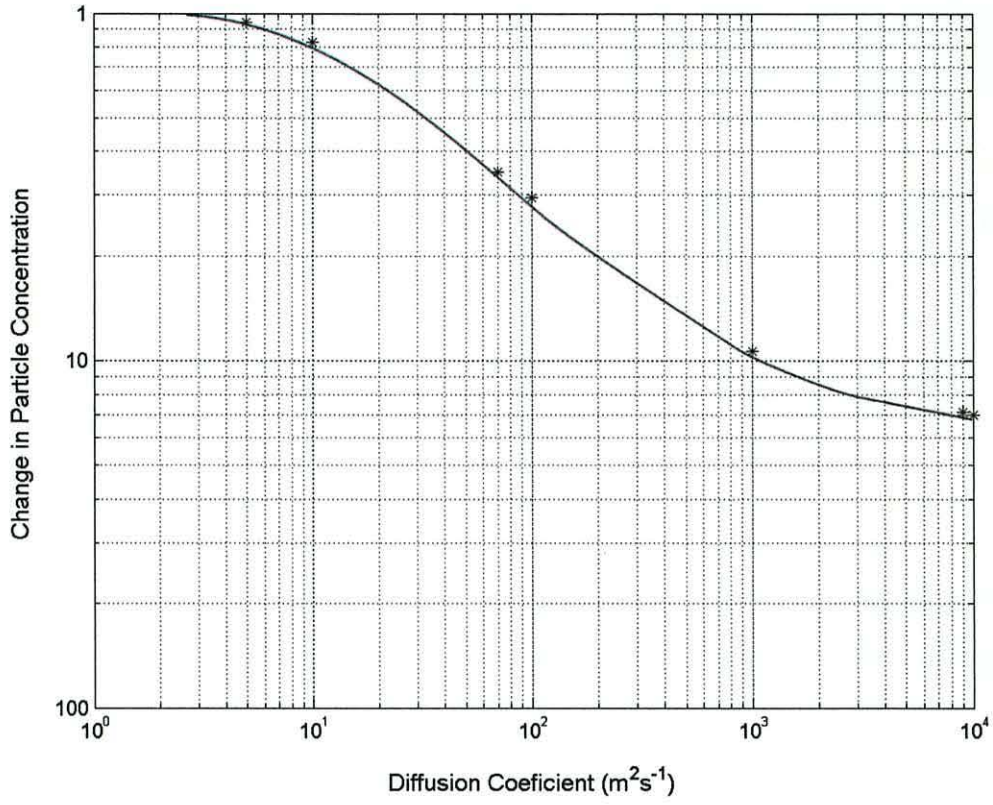

Figure 8.20 The *change in particle concentration at the outlet of the H-filter for different diffusion coefficients.*

The diffusion coefficient of a hydrogen ion is $9000x10^{-12}m^2s^{-1}$, which relates to a decrease in concentration to 0.071 of the original concentration at the inlet. This value gives an indication of the maximum possible dilution achievable with this design. It is not possible to have a concentration at the outlet greater than that at the inlet. As the diffusion coefficient is reduced, the concentration of the particles at the outlet approaches the concentration at the inlet.

8.6.6 Connecting H-filters in series

The reduction in the concentration of the sodium ions to 11% achieved using the design in Section 8.4.6 is significantly less than the reduction to 0.001% required by the design in Section 8.4.1. To further reduce the ion concentration several H-filters can be connected in series. A simulation of four H-filters of the type described in Section 8.6.5 connected together is illustrated in Figure 8.21. Due to the wide range of concentrations

in the simulation it is difficult to visualise the result in a single diagram. To overcome this problem the results were re-plotted for different concentration ranges from 0-1 to 0-0.0000001. The factor by which the scale bar should be multiplied is adjacent to each simulation.

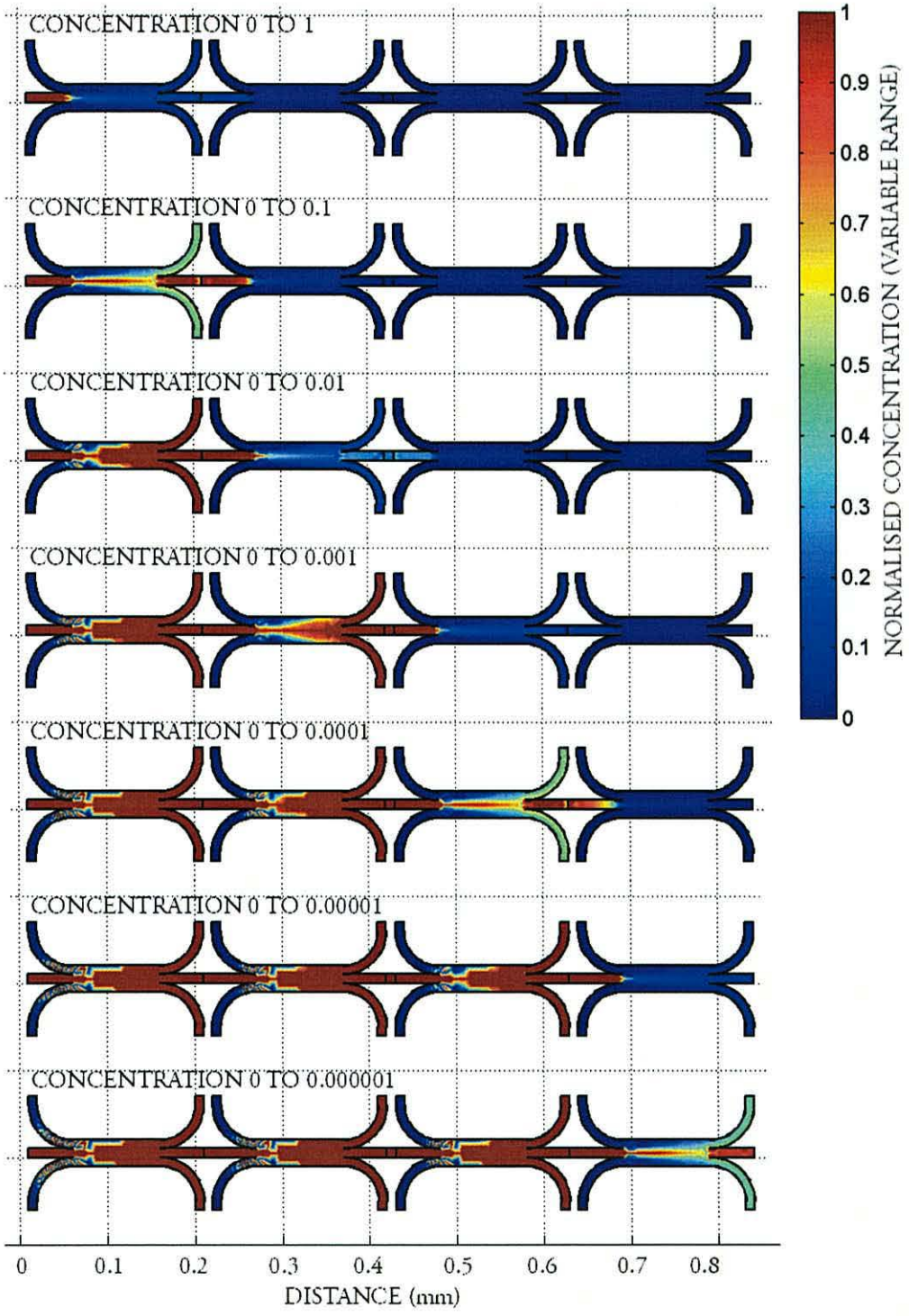

Figure 8.21 *Simulation of 4 H-filters connected in series. Due to the wide range of concentrations the results were plotted 7 times each over different ranges to allow the lower concentrations to the right of the figure to be visualised. The values on the colour bar should be scaled for each image.*

Figure 8.21 illustrates the reduction in the concentration of the sodium ions in the blood as they pass through four H-filters in series. As the concentration range is reduced, small errors in the simulation become more visible to the left of the figure. To give an indication of how the concentration changes through the device, the values of concentration were plotted along a horizontal line through the centre of the blood channel. The variation in the concentration of the sodium ions (diffusion coefficient $1000x10^{-12}m^2s^{-1}$) along the filters in series is shown in Figure 8.22 along with two other lines produced when diffusion coefficients of $9000x10^{-12}$ m^2s^{-1} (hydrogen ion) and $70x10^{-12}$ m^2s^{-1} (haemoglobin) were used in the same simulation.

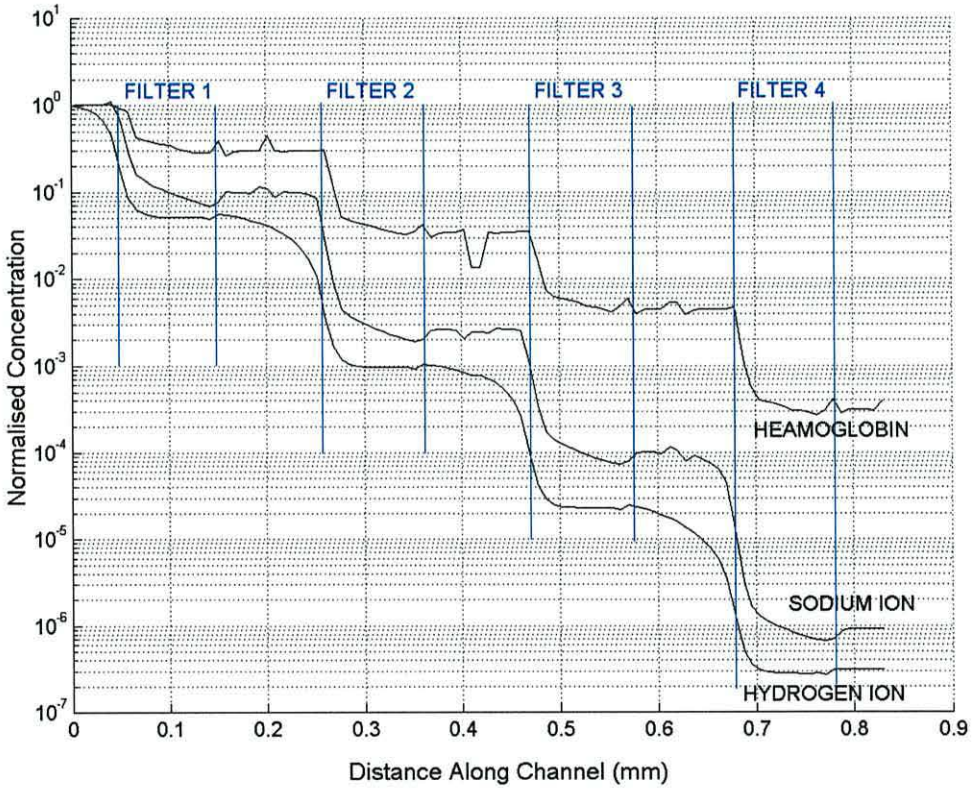

Figure 8.22 *Variations in the concentrations of hydrogen ions, sodium ions and haemoglobin along the length of the four H-filters in series shown in Figure 8.21.*

In Figure 8.22 the flatter sections of the graph correspond to the areas where the blood is flowing between H-filters and the rapid drops in concentration correspond to sections where the blood is in contact with the buffer. The difference in diffusion coefficients between sodium ions and haemoglobin increases the error in the simulation result, as

rounding errors become more significant at lower diffusion coefficients. This error is evident in the unevenness of the graph for haemoglobin, compared to the graph for hydrogen ions. The reduction in the concentration of the sodium ions over the four H-filters is 0.0001 %.

In the design requirements in Section 8.4.1 it was stated that a reduction factor of 10,000 in the concentration of the ions in blood is required to allow dielectrophoretic studies to be undertaken. This reduction factor corresponds to a fall in the conductivity to 0.01% of its original value, which is amply satisfied by the design in Figure 8.21.

In order to implement the design in Figure 8.21 it is necessary to incorporate a pumping mechanism into the system, which may have errors that cause the actual flow rates to differ from those modelled. Although the modelling process is not completely accurate it gives a useful indication of the operation of the system, which can be used to refine the design without building and testing prototypes.

8.7 Testing

The work described in this chapter is primarily a computer modelling based feasibility study. However, in order to check the credibility of the results obtained some experiments were carried out. The design shown in Figure 8.21 is complicated to implement as 9 inlet pressures and 9 outlet pressures must be accurately controlled. To show the performance of the design a single repeat unit was manufactured and tested. The manufacturing process used is described in Section 8.7.1 and the experimental set up described in Section 8.7.2. The fluid flow profile through the device was investigated using dyes as described in Section 8.7.3 and the conductivity reduction achieved at the outlet measured in section 8.7.3.

8.7.1 H-filter Fabrication

The fabrication approach used was that of sandwiching a layer of UV curing adhesive between two glass slides, as described in Chapter 4. Initially an exact copy of the geometry shown in Figure 8.18 was fabricated. However, when the channels were flushed through under high pressure to remove any trapped air the narrow walls where the channels meet were distorted. To overcome this problem the channels were combined at a sharper angle. The change in the geometry did not have any noticeable effect on the flow in the central section of the H-filter. The mask used to produce the H-filter used in these experiments is shown in Figure 8.23.

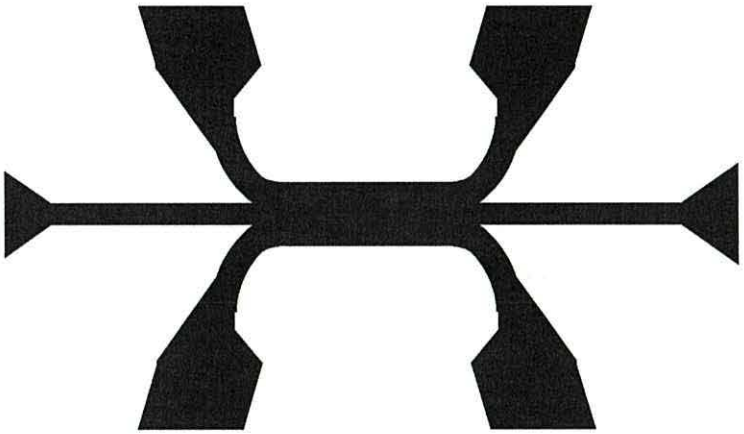

Figure 8.23 *Diagram of the photo mask used to produce the H-filter channel structure for these experiments.*

The closer a photo mask is to a photo-sensitive material the higher the achievable resolution. The resolution limit, R, for proximity printing is given by [22].

$$R = \frac{3}{2}\sqrt{\lambda s} \tag{8.13}$$

Where λ is the wavelength of the light and s is the distance between the mask and photo-sensitive material. When conventional microscope slides are used to sandwich the adhesive, there is a distance of 0.7mm between the mask and the adhesive compared to the channel width of 100μm. The resolution limit at this distance is 20μm, which is a reasonable fraction of the channel width. In addition the light source of the mask aligner

used in this research is not completely collimated, there is a collimation error of 3° that causes additional blurring of the mask by 36μm. The combined effect of these two processes made it difficult to resolve the channel when a 0.7mm thick substrate was used.

To overcome this problem one side of the structure was formed from a large cover slip of thickness 120μm. At this distance the blurring due to diffraction at the edge is 8μm and the blurring due to the error in the collimation of the light source is only 6μm. With the mask in closer proximity to the adhesive a well defined channel was produced as shown in Figure 8.24. To fully cure a layer of adhesive 400μm thick, a 40 second exposure at an energy density of $15mJcm^{-2}$ was used. In this application ideally projection printing would be used as this can produce a high-resolution image at a distance, however this facility was not available.

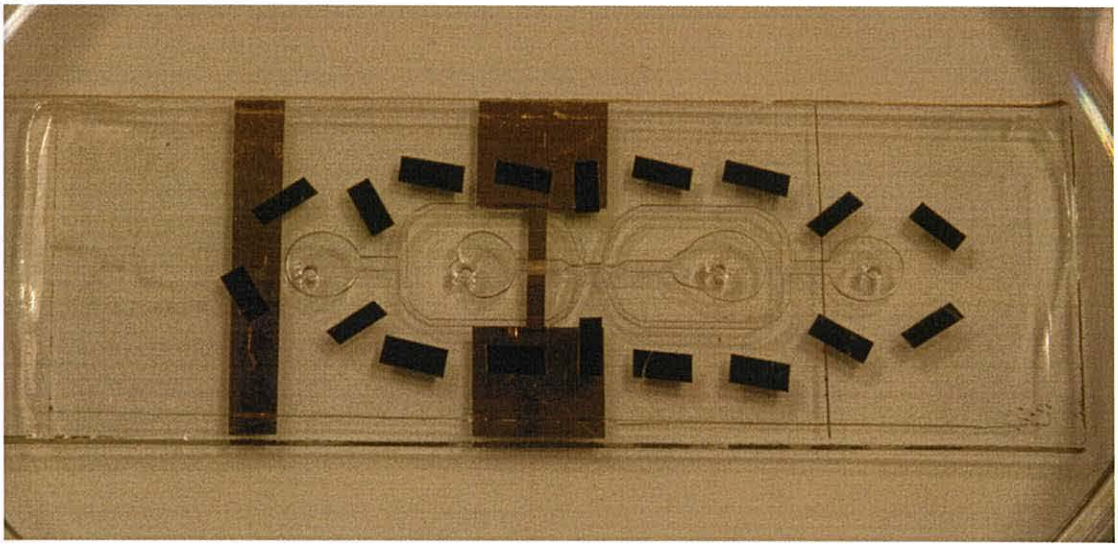

Figure 8.24 *H-filter structure fabricated from UV curing adhesive sandwiched between a microscope slide and a 120μm thick cover slip.*

The approach of using UV curing adhesive sandwiched between two slides produced structures with near vertical sidewalls and reasonably smooth channel walls. The LIGA process described in Chapter 2 of this thesis is ideally suited to high aspect ratio structures of this type. Once a nickel master has been produced many channel structures can be produced at low cost through thermoplastic replication. A disadvantage of LIGA is the long set-up time.

8.7.2 Experimental setup

From the simulation work it was found that small changes in the inlet and particularly the outlet pressure of the device resulted in significant changes in the flow profile. This is particularly true when the flow rate of the buffer is significantly larger than the flow rate of the sample. To have a high degree of control of the pressures and flow rates at the inlet and outlets of the device the set-up shown in Figure 8.25 was used. Initially syringe pumps were used but the flow from these was too pulsatile to provide a controlled flow.

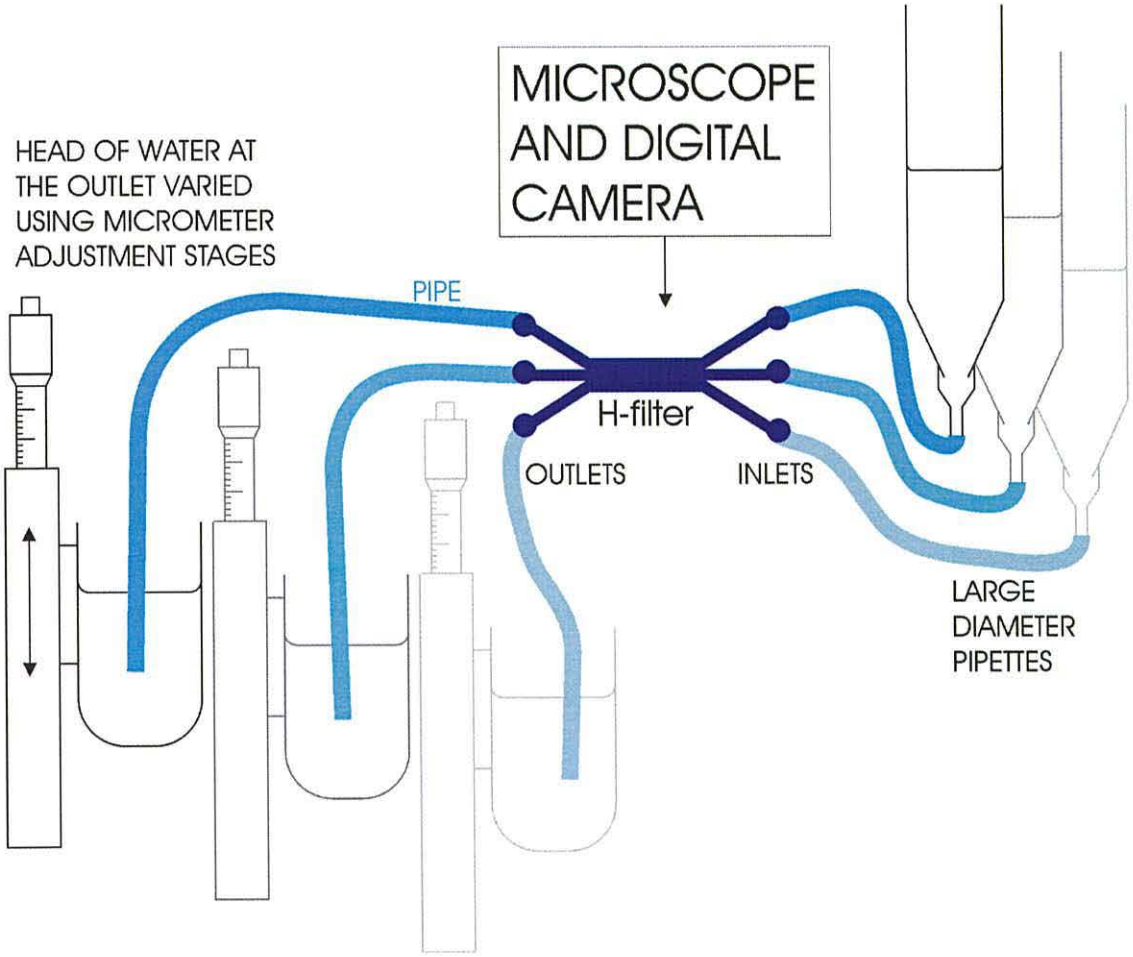

Figure 8.25 *Diagram showing the setup used to test the H-filter designed in this work.*

The fluid flow in to the device was controlled by varying the head of water supplied through 0.3mm diameter syringes from large diameter pipettes. The syringes were used to improve the control of the inlet flow by reducing the change in flow rate produced for a given change pressure or head of fluid, thus allowing more accurate adjustments to be made. Large diameter pipettes were used to ensure that as the fluid flowed through the device there were no a significant changes in the fluid head. It was essential that the pipettes and fluid were both free from any large fibre contaminants, since due to the shape of the H-filter, these could be funnelled into the central section and become trapped making the device useless. The outlet flow rate and therefore pressure must be controlled accurately. To achieve this, containers were mounted on micrometer adjustment stages (Micro-controle, France) to accurately vary the head of water at the outlet and therefore the backpressure. The images shown in this chapter were captured using a Eclipse ME600 microscope (Nikon, Japan) and a DXM1200 digital camera (Nikon, Japan).

8.7.3 Fluid flow results

The experiments carried out were divided into two parts. Firstly two dyes were passed through the channel at reasonably high flow rates to investigate the flow profile within the channel. High flow rates were used to limit the diffusion that occurred between the flow streams. Magenta dye was fed to the sample inlet, whilst Cyan dye was fed to the two buffer inlets. By adjusting the relative pressures at the inlets the relative flow rates were controlled. This produced a stream of red dye between two blue streams. The pressures of the two buffer outlets were then adjusted to centralize the dye in the outlet channel as shown in Figure 8.26A. The back pressure at the outlet was then gradually increased until the flow stream expanded to fill the outlet channel as shown in Figure 8.26B and Figure 8.26C.

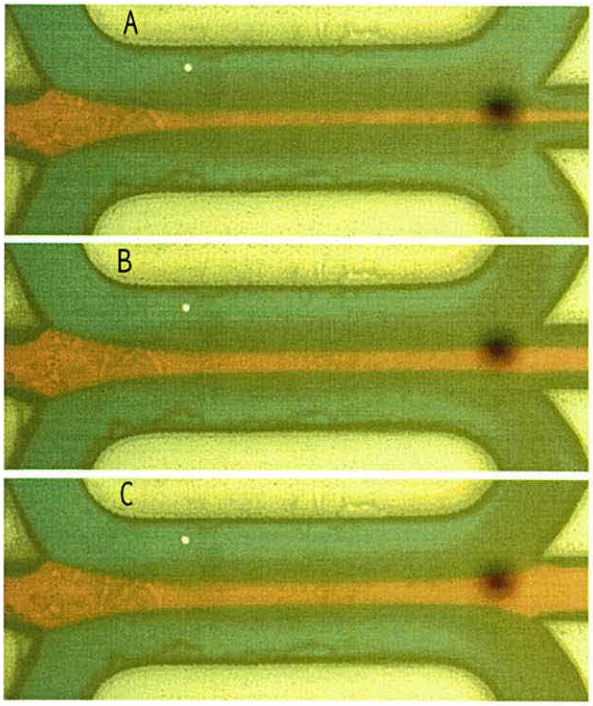

Figure 8.26 *Once the pressures at the two buffer outlets have been adjusted to centralize the sample stream (as shown in A) the back pressure at the outlet is increased (as shown in B) until only the sample stream is leaving through the sample outlet (as shown in C).*

Once the flow through the device had been established, the relative flows at the different inlets were found by timing the rate at which the levels in the pipettes decreased. Due to the small change in the levels there was a large potential for error in this measurement. An attempt was made to collect the dye from the outlets but movement of the pipes disrupted the flow in the channel. The flow profile in Figure 8.26 corresponds to a ratio between the buffer and sample of 3:1 (6:1 if both buffer inlets are included). Figure 8.27 illustrates the flow profile achieved when flow rates at all the inlets are equal.

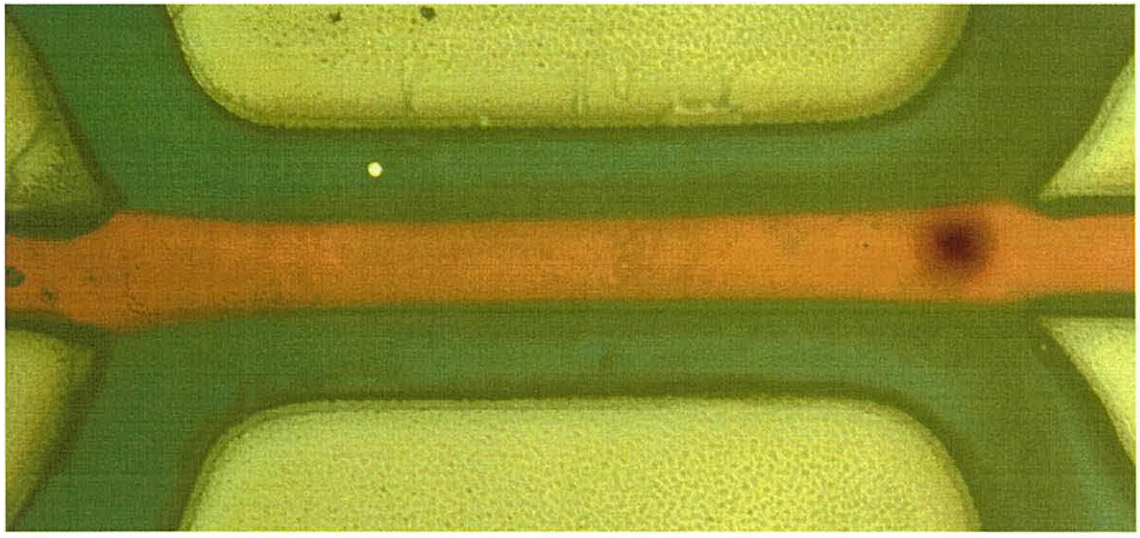

Figure 8.27 *Flow profile through the H-filter when the flows at all the inlets are equal.*

In Figure 8.27 it appears that as the magenta (sample) fluid leaves the device to the right, Cyan dye is also drawn along the walls of the sample outlet channel. Figure 8.28 illustrates that this is not the case. When the flow expands into the wider section of the channel to the right, the dark areas adjacent to the walls do not expand as would be expected in laminar flow.

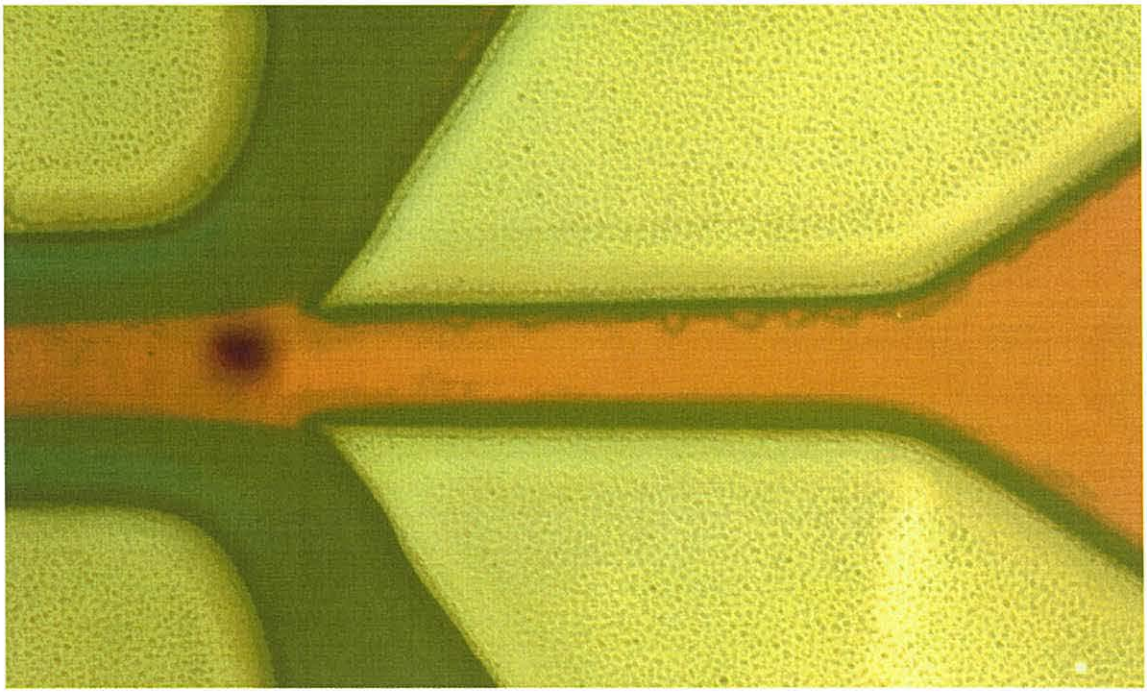

Figure 8.28 *When the magenta dye spreads out to fill the wider channel to the right the dark areas do not change width indicating that they are artefacts of the channel wall, not cyan dye from the buffer flow stream.*

The dark areas to either side of the channel are a result of the large height of the channel and the shallow depth of field of the microscope, they are the out of focus section of the channel wall.

8.7.4 Conductivity reduction results

To assess the effectiveness of the H-filter developed in this research it was necessary to measure the conductivity of the solution at the outlet. In a macro system this can be achieved by collecting a set volume and then using a standard conductivity probe. In this case the flow rate through the device was very low. The channel was 100μm wide and 400μm high with an average flow velocity of $100mms^{-1}$. This results in a flow volume through the channel of $4x10^{-6}mls^{-1}$. The volume between the electrodes of a conductivity probe is typically around 1ml. At this flow rate it would take just under 3 days to collect enough fluid to take a measurement, which is obviously not practical. To overcome this problem a set of interdigitated gold electrodes were fabricated in the channel immediately, after the outlet of the device. This section of the channel was 500μm wide and the sensor was within 5mm of the H-filter. A corresponding volume of $1x10^{-3}ml$ would take 250 seconds to replenish, assuming the flow profile was flat and not parabolic. To allow the fluid over the sensor to be completely replaced the measurement of conductivity was taken after 20 minutes (1200 seconds) of steady flow, after this time the value of conductivity was constant. An image of the H-filter and the interdigitated gold electrodes are shown in Figure 8.29.

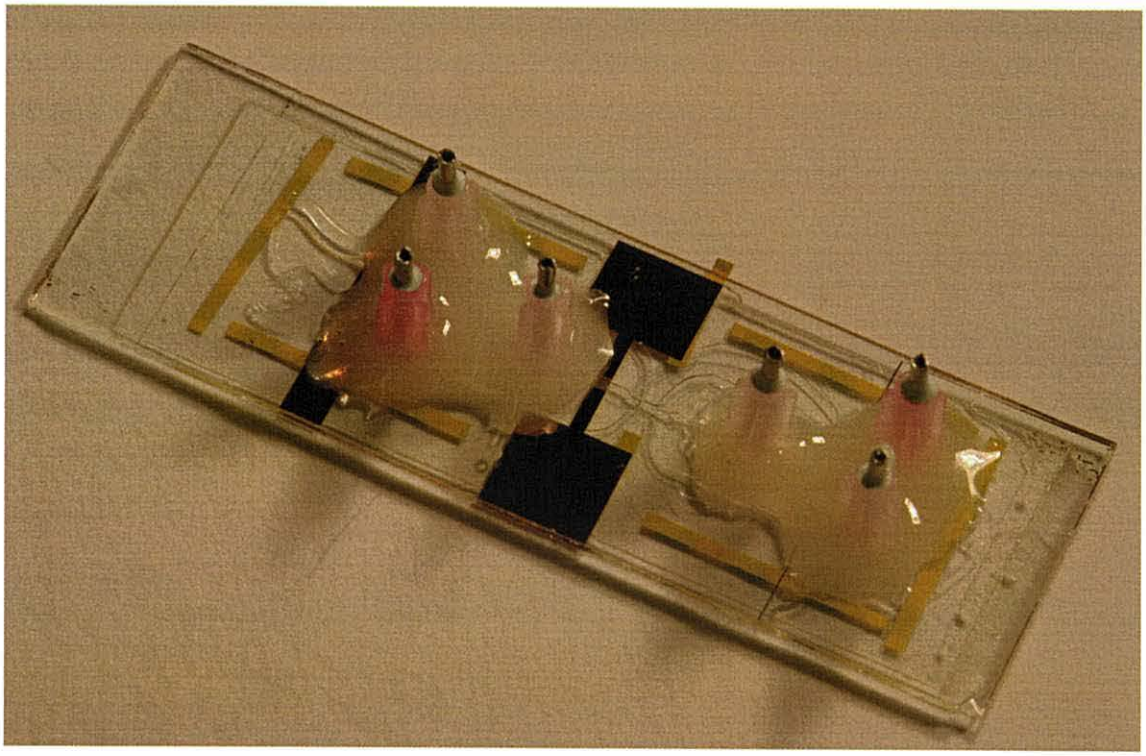

Figure 8.29 *H-filter structure used in these experiments showing the iterdigitated electrodes within the channel used to measure the conductivity of the solution at the outlet.*

To measure the conductivity the electrodes within the channel were directly connected to a Whatnan CDM4010 conductivity meter (Jenway ltd. UK). The electrodes in the channel did not have the same cell constant as the probe provided with the meter. To overcome this problem the electrodes in the channel were calibrated by passing different fluids of known conductivity through the channel. It was not possible to use the temperature probe attached to the conductivity meter with the fluid directly therefore it was assumed that the liquid in the channel was at room temperature. However, this may not have been the case due to heating of the device by the microscope light source. To limit the effect on temperature a x5 objective was used and only a low level of illumination was required. Instead of using red blood cells, yeast cells were used as these are far more robust whilst still of a similar size.

At the low flow rates specified in the design the flow profile through the channel was very sensitive to changes in the pressures at the fluid ports and any vibrations. The absence of any particles in the buffer solution made it difficult to adjust the relative flow velocities. To overcome this problem the pressure at the sample inlet was increased to force particles back up the buffer inlets. Once the pressure was returned to a lower level the particles flowed back into the H-filter and could be used to judge the flow velocity

from the buffer inlets. The protocol used to set up the flows within the device was the same as that used for the coloured dyes. Figure 8.30 shows yeast cells travelling through the device when the flow velocities at the sample and buffer inlet are the same.

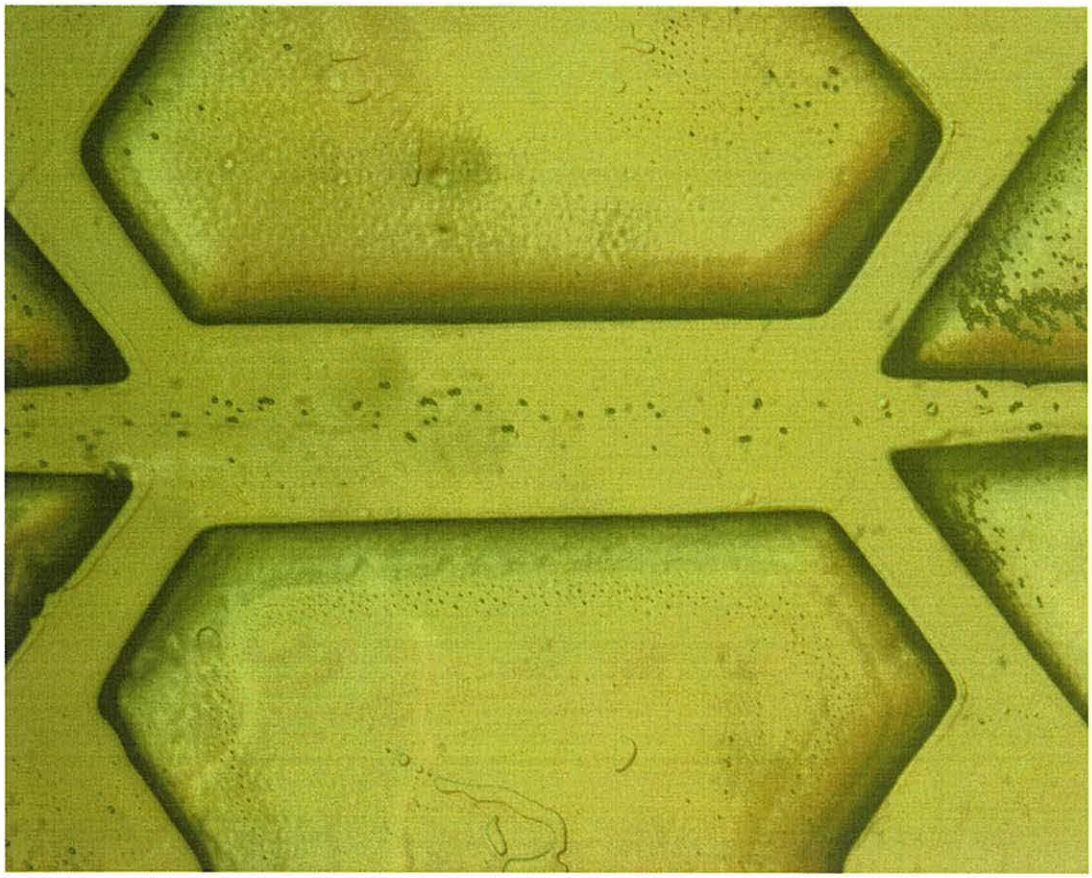

Figure 8.30 *Yeast cells travelling through a H-filter. The flow rates at the inlets are the same.*

From Figure 8.30 it can be seen that the UV curing adhesive has separated from the glass substrate allowing yeast cells to become trapped outside of the main channel area. This was not detectable when dyes were passed through the channel and did not noticeably effect the flow in this case.

It was not possible to achieve the high ratio between the buffer and sample flow specified in the modelling work. The best that could be achieved with the equipment available was a ratio of buffer to sample of 4:1 (8:1 considering both sides). As the flow of buffer was increased above this ratio the pressure of the buffer became very close to the pressure of the sample fluid and the sample stream was forced back towards the inlet.

The conductivity of blood is approximately 1.5 Sm^{-1}. This conductivity was too high to measure using the electrode structure within the channel. Instead the conductivity of the cell suspending medium was 0.01 Sm^{-1} or 100 μScm^{-1}. Once the flow was established it remained stable as long as there were no vibrations. After 20 minutes at a flow ratio between the buffer and sample of 4:1 the conductivity at the outlet was measured to be 16μScm^{-1}. This corresponds to a drop in conductivity by a factor of 6.3.

8.7.5 Comparison of simulation and experimental results

It was not possible experimentally to achieve the 10 to 1 ratio between the flow rates of the sample and buffer that was specified in the computer model. To compare the model results with those achieved experimentally the H-filter model was re-solved for a 1 to 4 ratio between the flow rates of sample and buffer. The results of this model are shown in Figure 8.31.

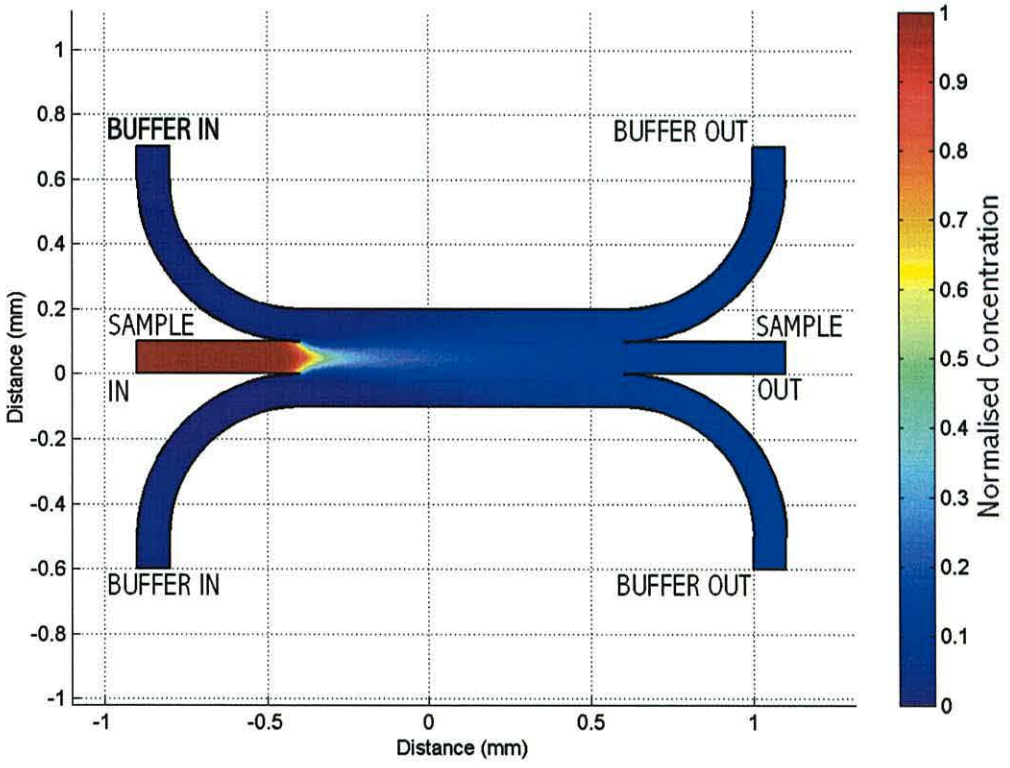

Figure 8.31 *Simulation showing the normalised concentration of sodium ions in a H-filter with buffer on both sides of the sample. The ratio between inlet velocities of the buffer and sample is 4:1.*

Due to the low concentration of ions in the main part of the channel it is difficult to judge the concentration from the scale bar. To give a clearer indication of the change in concentration Figure 8.32 shows the concentration profile measured on a line running along the centre of the channel from the sample inlet to outlet.

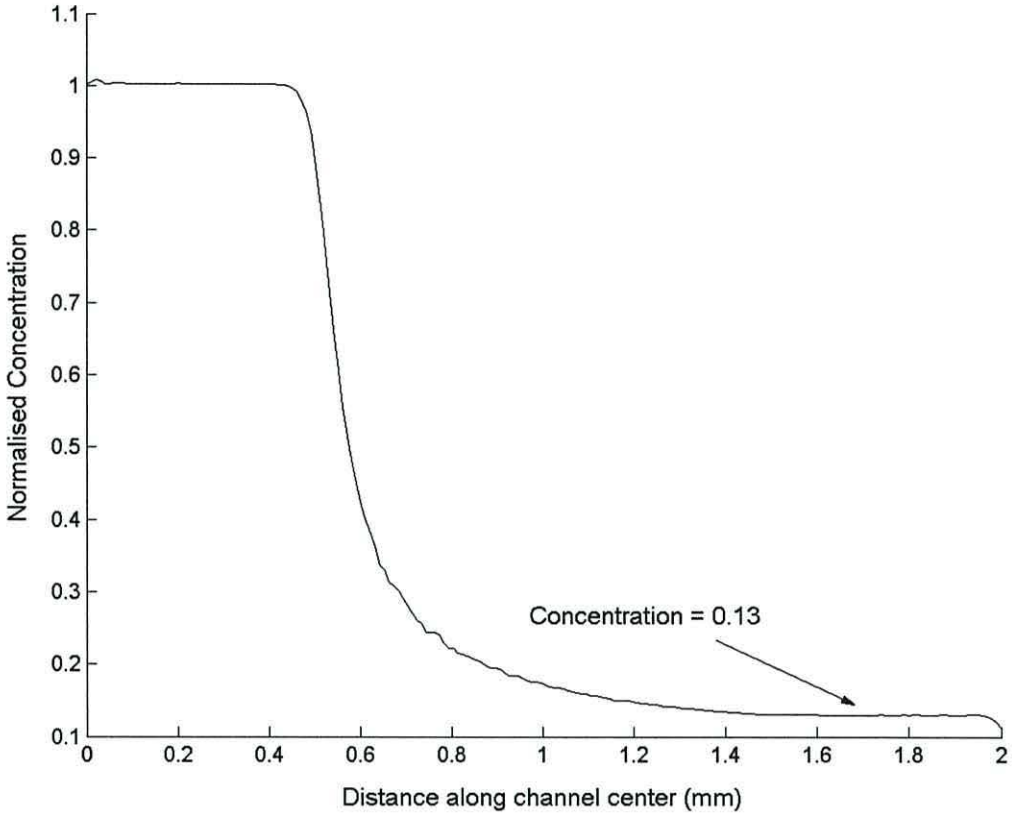

Figure 8.32 *The concentration profile measured along a line down the centre of the H-filter shown in Figure 8.31.*

From the graph in Figure 8.32 it can be seen that the concentration of sodium ions in the sample drops rapidly when the sample and buffer streams meet. By the time that the sample has reached the outlet the normalised concentration predicted by the computer model has dropped to 0.13. This corresponds to a predicted reduction in concentration of 7.7 times. Allowing for experimental error this drop in concentration is very similar to the reduction factor of 6.3 measured experimentally.

8.7.6 Discussion of experimental and theoretical results

The experimental and theoretical results correspond well for the H-filter design described in this chapter. The 18% difference between the measured results and those calculated could be due solely to errors in setting up the experiment, however other effects may also have an influence.

To prevent the yeast cells from settling out of solution in the pipes leading to the device an indigestible sugar manitol was added to the buffer to make them more buoyant. The addition of the sugar increased the viscosity of the fluid. From equation 8.4 it can be seen that this slight increase in viscosity of the fluid would decrease the diffusion coefficient. From the computer model a doubling of the viscosity and therefore halving of the diffusion to $500x10^{-12}m^2s^{-1}$ results in a new concentration at the outlet of 0.17, compared to that of 0.16 found experimentally.

Another possible reason for the difference between experimental and theoretical results could be due to the use of a two dimensional simulation. The graph in Figure 8.10 shows that the fluid flow in the centre of the channel is greater for the three dimensional simulation than the two dimensional. The faster movement of the fluid results in less time for the ions to diffuse into the buffer, which accounts for the higher than expected conductivity at the outlet. Alternatively a two dimensional simulation neglects the effects at the top and bottom of the channel. In reality the fluid near these boundaries moves more slowly and therefore there is more time for the ions in the sample to diffuse into the buffer. This would cause the measured conductivity in practice to be less than that found in theory, which is not the case.

When setting up the experiment the flows were adjusted such that no yeast cells were lost to the buffer stream and cell velocities at the inlet and outlet were the same. Due to this adjustment it is not possible to comment on the diffusion of the yeast cells. However, from general observation the cells followed the streamlines of the fluid.

Previous work by other groups [27] has shown that it is possible to produce thin streams of fluid sheathed by a buffer. From these cases it is likely that there is no physical phenomena that prevents high ratios between the buffer and the sample as specified in

the model. In this research the available equipment limited the ratio achievable and through the use of better flow control, higher ratios should be achieved. One possible approach is to use electro-osmotic pumping to move the fluid in the H-filter. However, this approach would require careful analysis as the electrical double layer and therefore the flow rate is effected by ionic concentration [28].

8.8 Summary

Using the simulation package FEMLAB a design was produced incorporating a series of H-filters to reduce the conductivity of blood to a level suitable for dielectrophetic measurements to be undertaken. To assess the feasibility of producing high aspect ratio channel structures the design was fabricated in UV curing adhesive sandwiched between two glass substrates. To successfully use the design the flow rates in and out of the device must be accurately controlled. Assuming this can be achieved the device should be able to reduce the conductivity of a sample of blood to a useful level in a few seconds. This is a significant improvement over the current approach of repeated centrifuging and washing of the cells which takes at least 10 minutes compared to 40 seconds for the design illustrated in Figure 8.21. The accuracy of the model was tested by fabricating one repeat unit of the final device and testing it with yeast cells suspended in a saline and manitol solution. Although it was not possible to achieve the high flow ratios between sample and buffer specified in the design there was a good correlation between the theoretical and experimental results.

8.8.1 Future work

The work contained within this chapter describes the development of the H-filter design to a specific problem. However, the flexibility of the H-filter can potentially be increased by combining it with other technologies, such as dielectrophoresis.

Dielectrophoresis can be used to selectively move particles based on their dielectric properties and the properties of the medium in which they are suspended. If electrode arrays are fabricated on the walls of the H-filter they can be used to exert a force on the

particles in the flow streams. The magnitude and direction of this force depends on the complex permittivity of the particle and the complex permittivity of the suspending medium [8,25]. Figure 8.33 shows the DEP spectra for live and dead yeast calculated using a multi shell model [29].

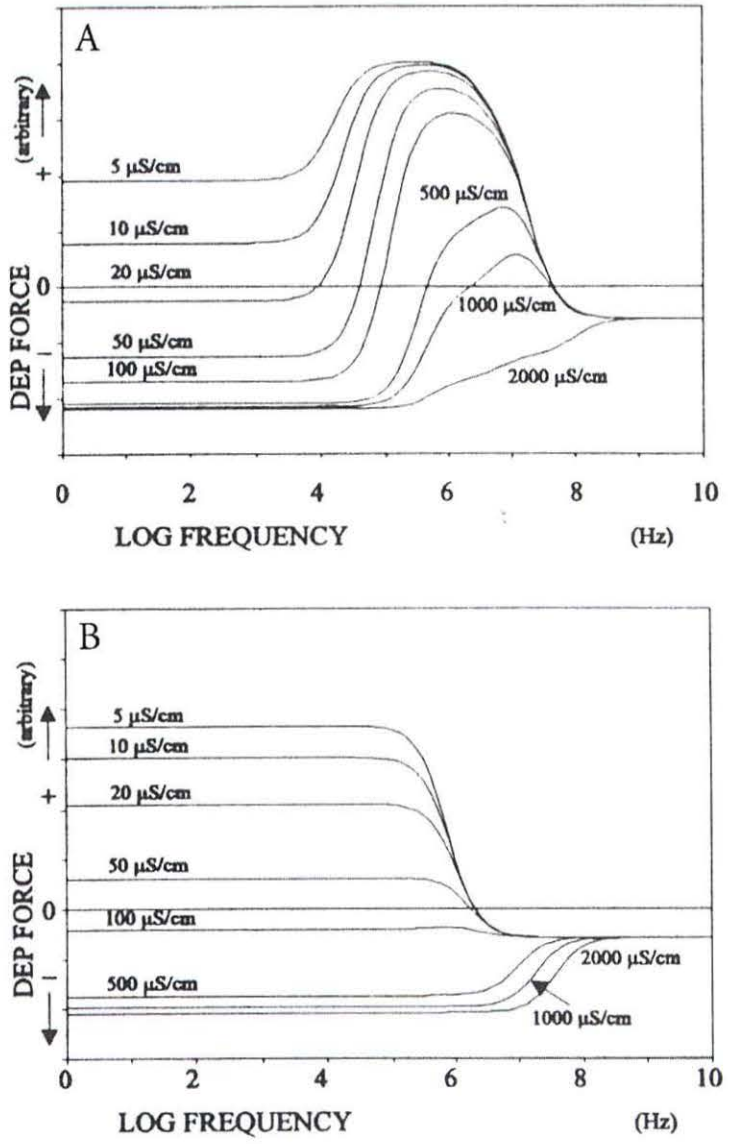

Figure 8.33 *(A) shows the DEP spectra for live yeast in various medium conductivities with a constant permittivity of 78 (water).*
(A) shows the DEP spectra for dead yeast in various medium conductivities with a constant permittivity of 78 (water)[16].

To illustrate the principle of how DEP force could be used to separate mixed cell types using a H-filter a specific example will be considered. The conductivity of a solution containing a mixed population of yeast cells can be changed to a specific value using

the series of H-filters shown in Figure 8.21. It can be seen from the graphs in Figure 8.33 that if the conductivity of the suspending medium is set to $50\mu Scm^{-1}$ then at frequencies around 1kHz the live yeast will experience a negative DEP force, whilst the dead yeast will experience a positive DEP force. However, if the frequency is set to 10MHz this situation will be reversed, with the live yeast experiencing a positive DEP force and the dead yeast experiencing a negative DED force. A cell suspension can be passed through a H-filter with electrodes on the channel walls where the other inlet also supplies a medium of conductivity $50mScm^{-1}$ If the electrodes on the wall adjacent to the particle suspension are energised at 1kHz, live yeast will be repelled whilst dead yeast are attracted to the wall. To further separate the two yeast populations the electrode on the other wall can be energised at 1MHz to attract live yeast and repel dead yeast. This process is illustrated in Figure 8.34.

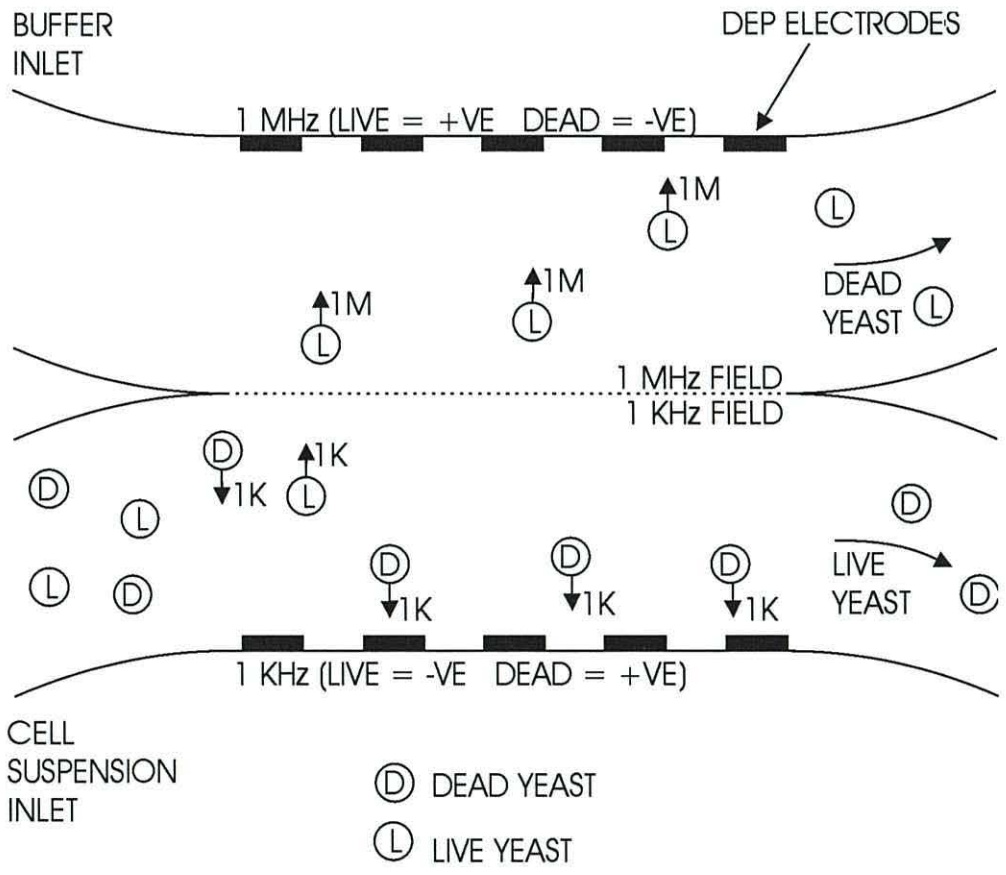

Figure 8.34 *Separation of live and dead yeast using positive and negative dielectrophoresis within a H-filter.*

The dielectric spectra for every cell is different. Therefore the design of this type of device will vary depending on the two particles to be separated. In the example in Figure 8.34 the conductivity of the medium at the second inlet was the same as that of the medium containing the cells. This does not have to be the case and under some circumstances an improvement in the separation may be achieved using different conductivities. Due to the potential to achieve rapid separation of cell populations it is a worthwhile challenge to develop these devices and characterise their operation for various particles and flow rates.

8.8 Refrences

[1] 'Isolation of cultured cervical carcinoma cells mixed with peripheral blood cells on a bioelectronic chip' J. Cheng, E. L. Sheldon, L. Wu, M. J. Heller and J. O'Connell, *Journal of Analytical Chemistry* **70** (1988) 2321-2326

[2] 'Dielectrophoretic spectra of single cells determined by feedback-controlled levitation' K. V. I. S. Kaler and T. B. Jones, *J. Biophysics* **57** (1990) 173-182

[3] 'Selective dielectrophoretic confinement of bioparticles in potential energy wells' X-B. Wang, Y. Huang, J. P. H. Burt, G. H. Markx and R. Pethig, *J. Applied Physics D* **26** (1993) 1278-1285

[4] 'Dielectrophoretic separation of cells: Continuous Separation' G. H. Markx and R. Pethig, *Biotechnology and Bioengineering* **45** (1995) 337-343

[5] 'Diffusion based extraction in a microfabricated device' J. P Brody and P. Yager, *Sensors and Actuators A* **58** (1997) 13-18

[6] 'A rapid diffusion immunoassay in a T-sensor' A. Hatch, A. E. Kamholz, K. R. Hawkins, M. S. Munson, E. A. Schilling, B. H. Weigl and P. Yayer, *Nature Biotechnology* **19** (2001) 461-465

[7] 'Development of electrorotation Assay for Analytes in water' A. D. Goater (1999) *University of Wales PhD Thesis*

[8] 'Dielectrophoresis: Using inhomogeneous AC electrical fields to separate and manipulate cells' R. Pethig, *Critical Reviews in Boitechnology* **16** (1996) 331-348

[9] 'Biology, third edition' Neil A. Campbel, *The Benjamin/Cummings Publishing Company, Inc. 1993 California, US.*

[10] 'Positive and negative dielectrophoretic collection of colloidal particles using interdigitated castellated microelectrodes' R. Pethig, Y. Huang, X-B Wang and J. P. H. Burt, *J. Applied Physics D* **24** (1992) 881-888

[11] 'Laboratory Techniques in biochemistry and molecular biology: vol 18 methods of cell separation' P. T. Sharpe, Editors R. H. Burdon and P. H. van Knippenberg, *Elsevier 1988 Oxford, UK.*

[12] 'Dielectrophoresis of human red cells in microchips' C. Xu, Y. Wang. M. Cao and Z. Lu, *Electrophoresis* **20** (1999) 1829-1831

[13] 'Trophoblasts circulating in maternal blood as candidates for prenatal genetic evaluation' S. Yagel, P. Shpan, M. Dushnik, N. Livni and S. Shimonovitz, *Human Repoduction* **9** (1994) 1184-1189

[14] 'Lab-on-a-chip sample preparation using laminar fluid diffusion interfaces-computational fluid dynamics model results and fluidic verification experiments' B. H. Weigl, R. L. Bardell, N. Kesler, K. J. Morris, *J. Analytical Chemistry* **371** (2001) 97-105

[15] 'Micronics company web site (1/9/2002)' http://www.micronics.net

[16] 'Microfluidic Technology and Applications' Michael Koch, Alan Evans and Arthur Brunnschweiler, *Research studies press ltd. 2000, Hertfordshire, UK*

[17] 'Simulation of microfluid systems' R. Zengerle and M. Richter, *J. Microtechnology and Microengineering* **4** (1994) 192-204

[18] 'United States Patent number 5,932,100: Microfabricated differential extraction device and method' P. Yager, J. P. Brody, M. P. Holl, F. K. Forster and P. C. Galambos.

[19] 'Whole blood diagnostics in standard gravity and microgravity by use of microfluidic structures (T-sensors)' B. H. Weigl, J. Kriebel, K. J. Mayes, Todd Bui and P. Yager, *Microchimica Acta* **131** (1999) 75-83

[20] 'Keye and Laby, tables of chemical and physical constants, sixteenth edition' Longman, Essex, UK.

[21] 'Bio-inorganic chemistry' Robert W.Hay. *John Wiley and Sons (1987) Chichester, UK.*

[22] 'Fundamentals of microfabrication' Mark Madou, *CRC press, 1997, Boca Raton, Florida, US*

[23] 'Advanced modern engineering mathematics' Glyn James. *Addison-Wesley Publishing Company (1993) Wokingham, UK.*

[24] 'Separation of human brest cancer cells from blood by differential dielectric affinity' F. F. Becker, X. B. Wang, Y. Huang, R. Pethig, J. Vykoukal and P. R. C. Gascoyne, *Preceedings of the National Academy of Science USA* **92** (1995) 860-864

[25] 'AC Electrokinetics: colloids and nanoparticles' Hywel Morgan and Nicholas G. Green, Editor R. Pethig *Research Studies Press ltd. Hertfordshire, UK.*

[26] 'Applied CFD Techniques: An introduction based on finite element methods' Rainald Lohner, *John Wiley and Sons ltd. Chichester, UK*

[27] 'Development of a nicrofluidic device for flurescence activated cell sorting' J. Kruger, K. Singh, A. O'Neill C. Jackson, A. Morrison and P. O'Brien. *Journal of Micromechanics and Microengineering* **12** (2002) 486-494

[28] 'Bioimpedance and Bioelectricity basics' S. Grimnes and O. G. Martinsen, *Academic Press 2000 London, UK.*

[29] 'DEP-FFF: field-flow fractionation using non-uniform electric fields' G. H. Markx, J. Rousselet and R. Pethig, *J. Liquid. Chromatography and Related Technology* **20** (1997) 2857-2872

Chapter 9

Conclusion

The aim of this thesis is to describe developments made in key areas of lab-on-a-chip technologies, namely device fabrication, integrated electrical sensing, external imaging and sample pre-conditioning.

When using travelling wave electrode arrays to manipulate particles one of the main causes of device failure was found to be the occurrence of open circuits at the via-hole connections between layers. A number of approaches were investigated to overcome this problem, including the fabrication of single layer electrode structures to move biological particles. The approach described here maintains the typical travelling wave electrode geometry but eliminates the need for via-holes by fabricating alternate electrodes on different physical layers over their entire area, using a polyimide insulating layer. When this approach was used, adjacent electrodes were at different heights. Through computer simulation of the field above the electrode it was found that there was only a slight distortion and reduction in the electric field strength above the electrode array. Increasing the magnitude of the electrical signals applied to the device would compensate for this. To assess the performance of this new electrode structure the electrical equivalent circuit was considered and measurements taken using an impedance analyser. From these measurements it was found that the performance of the new design was similar to that of designs previously developed.

Also described are three design approaches that were developed to produce the micro-fluidic channels used throughout this work. In the first approach the channel structure was produced through photopatterning of dry film laminate resist. Once the laminate had been baked a cover was attached using an UV curing adhesive. This approach produced strong channels, however prolonged exposure to water was found to cause the structure to delaminate. In an alternative approach, channels were machined in dry film laminate using an Exitech 8000 series excimer laser micro machining system. Once machined the cover was directly bonded to the laminate, since it remained naturally adhesive. Using this approach it was possible to produce complex, high resolution channel geometries. To overcome the need to use expensive laser machining systems, a third approach was developed where the upper and lower glass substrate were separated by shims and the area between them filled with UV curing adhesive. The adhesive was then selectively exposed to form the channel structure, before excess adhesive was flushed out with a solvent. Due to the nature of the manufacturing process

there was a significant distance between the mask and the adhesive during exposure, which was found to affect the final resolution of devices. A significant advantage of this fabrication process was the ability to fabricate devices with electrodes on both upper and lower surfaces. This was problematic using laser machining as the mechanically aggressive nature of the machining process could damage electrodes fabricated under the dry film laminate.

A series of sensors were designed for incorporation into the developed micro-fluidic channels. Particular attention was paid to minimising the complexity of the sensor and associated interface electronics. The principle of fluid flow measurement, using a hot wire anemometer has been extended for use in these channels. For ease of manufacture the hot wire was fabricated in the form of a thin gold track on one surface of the channel. A constant electrical current was applied across the track and the cooling effect of the fluid measured as a change in the potential across the track. When a single track was used, it was found to be very sensitive to changes in the fluid temperature.

Temperature compensation was integrated into the sensor by using 4 similar tracks in a Wheatstone Bridge arrangement. Any ambient changes in fluid temperature effected the entire device resulting in no change in the sensor output. However, the cooling affect of the flowing fluid on the tracks perpendicular to the flow was greater than that for the tracks parallel to the direction in flow. This asymmetry in the resistances making up the bridge resulted in an output signal that varied with flow rate. From experimentation it was found that the sensitivity increased rapidly as the current through the bridge increased. A doubling of the current from 5 to 10 mA resulted in an increase in the output voltage by a factor of 8. Due to increased cooling of the entire device the rate of increase in output voltage decreased as the flow rate increased.

Initially the Wheatstone Bridge flow sensor was driven by passing a d.c. current through the device between opposite corners and measuring the potential between the other two corners. Using this approach it was possible to detect flow velocities in in the range of mms^{-1}. To increase the sensitivity of the bridge, phase sensitive detection with a lock-in amplifier was used. Flow velocities in the range $2500\mu ms^{-1}$ to $10\mu ms^{-1}$ could be measured. By transforming the signal form the lock-in amplifier into the frequency domain it was possible to detect small pulsitile flows with an average velocity of

$0.65\mu ms^{-1}$. The maximum temperature of the Wheatstone Bridge was calculated as 7.5°C above ambient temperature for the maximum current used of 45mA. At this low overheat ratio it is unlikely that biological particles within the channel will be damaged.

To generate a steady flow through a micro channel for varying backpressures a sensor and pump were incorporated into a simple feedback loop. When the backpressure was increased by increasing the head of water at the outlet, the speed of the pump increased to maintain the flow rate.

In addition to measuring flow, sensors were also developed in Chapter 6 to detect the presence of individual particles and particle suspensions within a micro-channel. Suspensions of yeast were detected by measuring the capacitance between two electrodes on either side of a channel through which the suspension was passed. The quantisation levels in the output of the impedance analyser used for measurement limited the sensitivity. However, it was still possible to detect cell concentrations of $5x10^5$ per ml. The nature of the change in capacitance was unexpected but the results were found to be highly repeatable. Individual particles were detected using an approach similar to a Coulter Counter. Using the same electrode arrangement employed to detect particle suspensions, a constant current was applied through the channel. The presence of a large 100μm particle was detected as an increase in the potential between the electrodes. This increase was necessary to maintain the current as the resistance increased due to the presence of the insulating particle.

Through the combination of a four point probe sensor and a lock-in amplifier the presence of individual yeast cells were detected as they passed the sensor. Using this approach it was possible to differentiate between particles of different sizes. A single yeast cell resulted in a change in the output of the sensor by 2mV whilst a group of 3 resulted in a change of 4mV.

In Chapter 7 a series of simple optical systems for the visualisation of lab-on-a-chip devices are described. Particular attention is given to the use of reduced or zero optics to form microscope systems. To resolve smaller features lens elements were incorporated into the channel structures.

Initially the lens elements were fabricated in the silicone elastomer PDMS, as this material is optically clear and can also be used to form the channel structure. To form structures that were more resistant to damage the PDMS was replaced by Araldite 2020, which whilst tougher was slightly less transparent. Using lenses fabricated from these materials, reasonable quality images could be produced by projecting an image onto a CMOS imaging array connected to a computer. To demonstrate how low quality images can be used to take useful measurements, a dielectrophoretic spectra for live yeast was measured. The results obtained corresponded well to previous work.

An important area in lab-on-a-chip research is sample preparation. The final area of work was a computer modelling process to design a micro-fabricatable sample pre-conditioning stage to reduce the conductivity of blood to a level suitable for dielectrophoretic measurements to be undertaken. The design was based on a H-filter. Initial work refined the geometry of the H-filter to minimise the areas of stationary fluid within the device. By combining the physical processes of diffusion and fluid flow into a single model it was possible to design the H-filter to give a high reduction in the conductivity of the blood. By increasing the volume of buffer solution that passes through the filter without increasing the volume of blood it was possible to achieve a significant drop in the ionic concentration of the blood. As the ratio of the flow rates between the buffer and the blood increased, the rate of improvement in the performance of the device decreased, indicating a practical flow ratio limit for buffer to blood of 10:1. In a typical H-filter the buffer only makes contact with the sample on one side. To increase the efficiency of the filter, the buffer was passed down both sides of the blood flow stream. Using a single H-filter it was found impractical to attempt to achieve the required reduction in ionic concentration of 10,000. To achieve this desired level of reduction four H-filters were connected in series to gave a 100,000 reduction in the concentration in sodium ions. This provides a significant safety margin to allow for any errors in the simulation. To assess the validity of the computer model one repeat unit of the final design was fabricated and tested. Although it was not possible to achieve the flow ratio specified in the design the conductivity of a sample was reduced by a factor of 6.3 for a buffer to sample ratio of 4:1 (8:1 if both sides are considered). This result was in good agreement with the computer model. At the end of this chapter an area of possible future work is outlined whereby electrodes are incorporated into a H-filter to selectively move particles using dielectrophoresis.

Publications

'Measurement of Fluid and Particulate Flow in Microchannels', J. A. Drysdale and J. P. H. Burt. Oral presentation at *the first European Workshop on Electrokinetics and Electrohydrodynamics in Microsystems*, 6-8th September (2001), Glasgow, UK

'Parasite Viability by Electrorotation', C. Dalton, A. D. Goater, J. Drysdale and R. Pethig, *Colloids and Surfaces A : Physicochemical and Engineering Aspects* **195** (2001) 263-268

'Development of a Micro Systems for Circular Chormatography using Wavelet Trancform Detection' J. C. T. Eijkel, C. Dalton, C. J. Hayden, J. A. Drysdale, Y. C. Kwok and A. Manz, *Miocro Total Analysis Systems 2001* (2001) 541-542

'An Automated Method for Dielectrophoretic Measurements including Electric Field Corrections' A. D. Goater, J. A. Drysdale and J. P. H. Burt, *Journal of Electrostatics* Submitted